Doctoral School of Chemical Engineering and Material Sciences

University of Pannonia

Submitted for the degree of
Doctor of Philosophy
of the University of Pannonia, Hungary

Author: Datao Xu
Supervisor: Dr. habil. Gusztáv Fekete and Dr. András Kovács

Dissertation Title: Landing strategy optimization for lower limb injury risk reduction: Combining computational biomechanical modeling and machine learning

DOI:10.18136/PE.2025.941

Veszprém
2024

LANDING STRATEGY OPTIMIZATION FOR LOWER LIMB INJURY RISK REDUCTION: COMBINING COMPUTATIONAL BIOMECHANICAL MODELING AND MACHINE LEARNING

Thesis for obtaining a PhD degree in the Doctoral School of Chemical Engineering and Material Sciences of the University of Pannonia

in the branch of Material Sciences and Technologies

Written by Datao Xu

Supervisor: Dr. habil. Gusztáv Fekete
Co-supervisor: Dr. Kovács András

propose acceptance (yes / no)

…….……...……
Dr. habil. Gusztáv Fekete
Supervisor

propose acceptance (yes / no)

…….……...……
Dr. Kovács András
Co-supervisor

As reviewer, I propose acceptance of the thesis:

Name of Reviewer: Dr. yes / no

…….……...……
(1st reviewer)

Name of Reviewer: Dr. yes / no

…….……...……
(2nd reviewer)

The PhD-candidate has achieved ….....% at the public discussion.
Veszprém,

…….……...……
(Chairman of the Committee)

The grade of the PhD Diploma …..... (…….. %)
Veszprém,

…….……...……
(Chair of the UDHC)

Submitted with 186 pages and 242 references

The Dissertation contains 69 Figures, and 19 Tables

Supervision

Dr. habil. Gusztáv Fekete	*Supervisor*	PhD supervisor, Doctoral School of Chemical Engineering and Material Sciences, University of Pannonia. Associate Professor at Vehicle Industry Research Center, Széchenyi István University
Dr. András Kovács	*Co-supervisor*	PhD supervisor, Doctoral School of Chemical Engineering and Material Sciences, University of Pannonia

Acknowledgements

As I write this final part of my dissertation, I am about to the end of my student career. Standing on the threshold of graduation, looking back, everything seems to be vivid in my mind and I can't help but moisten my eyes with emotion. Three years of doctoral career is hard but full of laughter and joy. At this moment when it is coming to an end, my heart is full of reluctance for student life and deep nostalgia for the University of Pannonia. Looking back on these three years of doctoral study, some too many people have helped me and too many people to thank.

First and foremost, I would like to express my sincere appreciation to my supervisor, Prof. Dr. habil. Gusztáv Fekete, for his consistent guidance, support, and encouragement throughout this research endeavor. His extensive expertise and insightful suggestions have played a critical role in shaping the outcome of this study, and his unwavering confidence in my abilities has served as a constant source of motivation. Moreover, I would like to extend my deepest gratitude to my co supervisor, Dr. András Kovács, for his invaluable advice, constructive critiques, and unwavering backing. His relentless pursuit of excellence and generous knowledge sharing have significantly enriched this work and contributed to its success.

I am profoundly grateful to Prof. Dr. Yaodong Gu for providing me with the opportunity to pursue my doctoral degree and for his comprehensive support during both my master's and doctoral studies. Your unwavering belief in my capabilities and exceptional guidance as a mentor has left an indelible impression on me. Your enthusiastic support was always there to uplift me whenever I encountered obstacles. It has been an honor to have you as my supervisor.

Many other academic, secretarial and technical members of staff have facilitated the realization of this thesis and I express them all my gratitude. I acknowledge the Faculty of Engineering, University of Pannonia (PE), Savaria Institute of Technology, Eötvös Loránd University (ELTE) and Faculty of Sports Science, Research Academy of Grand Health, Ningbo University (NBU) for the facilities and support provided.

I am very fortunate to work in a group full of talented people who have not only helped me with my research but also given me invaluable advice and support. Thanks to all the professors, colleagues, and PhD students for their helpful assistance, comments, and suggestions during my research work. Thanks to everyone who took part in the studies of this dissertation, your time was much appreciated. Many other administrative, academic, secretarial, and technical members of staff have facilitated the realization of this dissertation and I express to them all my sincere gratitude.

I cannot overlook the unwavering support of my family. Despite the physical distance that separated us, their unshakable belief in me never wavered. Their love and encouragement have been the cornerstone of my inner strength.

Lastly, I would like to acknowledge the financial assistance provided by the Stipendium Hungaricum Programme, Tempus Public Foundation, and China Scholarship Council (CSC).

Content

Abstract

Landing is one of many fundamental sports techniques, that can commonly be associated or accompanied by sports injuries, such as anterior cruciate ligament (ACL) injury, lateral ankle sprain (LAS), etc. Different landing patterns can expose lower limb joints and ligaments to different loading modes. A successful landing is defined as the body being able to cushion the impact load well enough to maintain body balance and avoid injury. In actual motion monitoring, most current studies of ACL forces during landing have been conducted using biomechanical models such as musculoskeletal models and in vivo studies. However, the establishment of such a model usually requires a large and complex base of knowledge, and the simulation calculation process is usually time-consuming and costly. In recent years, an increasing number of studies have favored the use of machine learning methods to model and predict the complex "input-output" relationship, to address the computational difficulty and cost of important variables in biomechanics.

The first research question of this thesis: Previous studies on the impact of fatigue factors on the lower limb biomechanics during landing tasks often only investigated the effect of fatigue factors on ACL injury risk from some indirect indicators, rather than starting from the perspective of the dynamic loading forces within the ACL itself. However, the limitation is that it cannot explore the exact mechanism of the fatigue factor increasing ACL injury risk from the internal force itself. In addition, it is unclear whether changes in the ankle during after-fatigue landing are associated with an increased risk of ACL injury.

The first research objective of this thesis: To accurately calculate ACL internal dynamic load forces by constructing a musculoskeletal modeling. In addition, this study aims to explore whether there are detectable and recognizable differences in ankle joint kinematics, lower limb joint energy dissipation (joint work) and ACL load force between before-fatigue and after-fatigue landing, as well as to explore the possible relationship between them.

The first research results and conclusions of this thesis: The ACL dynamic load force will increase during after-fatigue single-leg landing (SL), which suggested that the lower limb neuromuscular fatigue factor would increase the risk of ACL injury. There was a significant difference in ankle motion patterns between before-fatigue and after-fatigue SL. Therefore, the increased risk of ACL injury during after-fatigue SL is related to the decrease of ankle initial contact angle (AICA) and ankle range of motion (AROM), and the relationship between AICA, AROM and peak ACL force (PAF) is highly negatively correlated, the relationship with TED is highly positively correlated. I concluded that lower limb neuromuscular fatigue increases the ACL dynamic loading force during SL, thereby increasing the risk of ACL injury. This result is associated with a smaller AICA (plantarflexion angle) and AROM movement pattern of the ankle joint during after-fatigue SL. By increasing the AICA and AROM during SL, the energy dissipation of the lower limb joints can be increased and the PAF reduced, thus reducing the impact loads on the lower limb joints and reducing lower limb injuries, including ACL injuries.

The second research question of this thesis: In clinical landing injury screening, clinical experts mainly performed quantitative description and analysis from the perspective of biomechanics. However, traditional approach has the inherent limitation of losing a large amount of effective information when extracting low-dimensional single-time point discrete variables from high-dimensional time-continuous variables. Meanwhile, the landing patterns are different in the situation of different injury conditions, different control/intervention conditions, and whether there is lower limb injury, which will cause great difficulties for clinical experts in clinical diagnosis. In recent years, the relevant application of explainable machine learning (XML) in clinical diagnosis has increased the trust of experts in this field in the traceability of ML methods, and has been accepted by more and more researchers.

The second research objective of this thesis: To investigate whether XML can help with landing pattern recognition and to what extent it can aid in the interpretation of prediction results. This work firstly compared the classification recognition performances of several classical classification models on two class landing tasks, and then constructed the XML model based on the neural network model with the best recognition performance combined with LRP to explain the model classification recognition results. The current study proposed two approaches to assess the computed interpretability results: 1) assessment from a statistical perspective; and 2) assessment from a clinical perspective. For statistical evaluation, a Statistical Parametric Mapping (SPM) technology based on random field theory was used to detect statistical differences in the input signals, and then to verify whether interpretability results are reasonable based on statistical differences. For clinical evaluation, interpretable results were analyzed clinically by experienced experts in the field to assess their compatibility with clinical features.

The second research result and conclusion of this thesis: Both three classification algorithm models achieved high recognizability in the nine classification tasks, and the classification performance level of artificial neural network (ANN) for the input signal is particularly outstanding in comparison to the other two models. From the classification performance, I found that based on the knee data as input signals the classification performance was better. There is a greater difference in sagittal landing patterns between classes in the three planes. For the detailed results of relevance score (RS) distribution, I found that the early landing phase contributed more to landing pattern recognition between classes. For each joint, the largest summed contribution rate of RS was knee joint, followed by in the ankle joint and hip joint. For each plane, the largest summed contribution rate of RS was sagittal plane, followed by the transversal plane and frontal plane. In conclusion, I highlighted the applicability of XML methods that can interpret the results of ML decisions for clinical landing analysis, and their great promise for future application and implementation.

The third research question of this thesis: During landing, the knee has the highest risk of injury, and the most common is the non-contact ACL injury, with more than 80% of its injuries occurring during landing tasks. It is also true that ankle sprains, on the other hand, are one of the most common injuries associated with landing, and more than 80% of ankle sprains occur in the lateral. At present, whether ankle joint motion patterns

(AICA, AROM) during landing affect joint energy dissipation and the degree of shock load cushioning across the lower limb, or even if there is some association with lower limb injury, remains to be further explored. In assessing the ACL injury mechanism, traditional models mainly set ligaments as having linear force-length characteristics and consider them independent of strain rate.

The third research objective of this thesis: To more realistically revert and simulate the ACL injury mechanics, this study developed a knee musculoskeletal model that reverts the ACL ligament to a nonlinear short-term viscoelastic mechanical mechanism (strain rate-dependent) generated by the dense connective tissue (DCT) as a function of strain. This work was specified: (1) The peak vertical ground reaction force (PVGRF), total energy dissipation (TED), peak ankle sagittal moment, peak knee sagittal moment, and peak hip sagittal moment were used to assess the overall injury risk of the lower limb, and explored their relationships with AICA, AROM. (2) The peak ankle inversion angle (PAIA), and peak ankle inversion moment (PAIM) was used to assess the LAS risk, and hypothesized the positive correlation between them and AICA, AROM. (3) The ACL model was developed and constructed to calculate ACL dynamic loading forces, and then the PAF was used to assess the ACL injury risk, and hypothesized the negative correlation between them and AICA, AROM. (4) The feasible ankle motion patterns were explored to balance the LAS and ACL injury risk based on the interaction between PAIA and PAF.

The third research result and conclusion of this thesis: The AICA exhibits a negative correlation with PVGRF and PAF, a positive correlation with TED and PAIA. The AROM exhibits a positive correlation with TED and PAIA. The results indicated that the LAS risk is negatively correlated with ACL injury risk. Based on the determined intersection points, I found that 30° to 40° of AICA and 50° to 70° of AROM were the more appropriate range to balance the injury risk between them. This range can be referenced by individuals during SL, but it should also be adjusted according to the person's ankle dorsiflexion ability and the level of muscle function around the ankle joint. In addition, it is also necessary to strengthen the training of the muscles, the medial and lateral tissues, ligaments around the ankle joint, so as to increase the AICA and AROM to reduce lower limb injury risk while avoiding ankle joint injury.

The fourth research question of this thesis: During landing, the knee, which serves as the pivotal joint connecting the ankle and hip, is the most susceptible to damage. When the biomechanical mechanisms of internal loads on the human body are explored in the context of the complex external mechanical environment, the current solutions in the field are mainly achieved by finite element analysis (FEA) techniques and musculoskeletal modeling simulations. Previous research has demonstrated that increasing the ankle plantarflexion (ankle initial contact angle: AICA) may increase ankle energy dissipation during landing, thereby reducing the landing impact on the other joints. At present, it is unclear whether increasing the ankle plantarflexion angle during landing would change the knee loading mechanism and further affect ACL injury risk.

The fourth research objective of this thesis: To explore the effects of different ankle plantarflexion angles during SL on knee impact loading and ACL injury risk. The

biomechanical properties of the knee joint were planned to be quantified based on musculoskeletal modeling and finite element analysis (foot-ankle-knee integration model). This study employed a joint impact force to evaluate the impact loads on the knee at various landing angles, and calculated the joint negative work to assess the ability of the knee to dissipate the energy impact. Additionally, the ACL internal load forces (musculoskeletal modeling) and ACL stress (finite element analysis) were simulated and calculated to evaluate the ACL injury risk. Meanwhile, landing optimization strategies are further proposed to reduce knee-related injuries based on the possible findings.

The fourth research result and conclusion of this thesis: As the ankle plantarflexion angle increased during landing, both the peak knee vertical impact force and ACL force decreased significantly. The maximum von Mises stress of ACL, meniscus, and femoral cartilage decreased as the ankle plantarflexion angle increased. The overall range of variation in ACL stress was small and was mainly distributed in the femoral and tibial attachment regions, as well as in the mid-lateral region. The current findings revealed that the use of larger ankle plantarflexion angles during landing may be an effective solution to reduce knee impact load and the risk of rupture of the medial femoral attachment area in the ACL.

The fifth research question of this thesis: In actual motion monitoring, most current studies of ACL forces during landing have been conducted using biomechanical models such as musculoskeletal models and in vivo studies. However, the establishment of such a model usually requires a large and complex base of knowledge, and the simulation calculation process is usually time-consuming and costly. In recent years, an increasing number of studies have favored the use of machine learning methods to model and predict the complex "input-output" relationship, to address the computational difficulty and cost of important variables in biomechanics.

The fifth research objective of this thesis: To develop a highly accurate and easy-to-implement ACL dynamic load force prediction model, which has low input variable demands (sagittal joint angles), excellent generalization capabilities and superior performance in terms of high accuracy. This study first combines long short-term memory (LSTM) algorithm to construct the prediction model, and then introduces a metaheuristic optimization algorithm (SSA) to optimize the prediction model based on existing machine learning models, and further optimizes the prediction results by combining the discovered linear relationship between AICA, AROM and PAF to achieve accurate prediction of the ACL dynamic load force during SL using simple and easy-to-measure kinematic data.

The fifth research result and conclusion of this thesis: By substituting AICA and AROM as independent variables in the SSA-extreme learning machine (ELM) prediction model, the model shows excellent prediction performance because of very strong correlation. Based on the equal scaling by combining results of SSA-ELM and SSA-LSTM, the prediction model achieves excellent performance in ACL force prediction of the overall waveform. Therefore, my study proposed a method for constructing a highly accurate and easy-to-implement ACL dynamic load force prediction model, which has low input variable demands (sagittal joint angles),

excellent generalization capabilities and superior performance in terms of high accuracy.

The sixth research question of this thesis: Previous studies in estimating continuous kinematic variables have usually calculated the informative features of a single group from the surface electromyography (EMG) signals of each muscle, and used them as regular features in that motion pattern. However, the features extracted from a single surface EMG channel are extremely sensitive to noise, amplitude cancellation and electrode shifts, which would increase estimation errors. By revealing the neuromuscular control mechanism behind the motor system, muscle synergy can detect movement intention comprehensively and accurately, and its application is expected to help patients in clinical rehabilitation. Adaptive neuro-fuzzy inference system (ANFIS) has the advantages of optimizing membership functions through independent learning and adjusting fuzzy logic rules to establish output functions that adapt to various rules.

The sixth research objective of this thesis: To develop a movement intention detection technology for estimating each joint continuous kinematic variable based on the lower limb muscle synergy pattern, with a view to developing applications for more efficient exoskeleton-assisted rehabilitation training. More specifically, this study extracted the lower limb muscle synergy patterns of healthy subjects and patients through non-negative matrix factorization (NNMF), and then mapped the lower limb muscle synergy patterns to each joint continuous motion variable using the developed ANFIS non-linear regression model. It is hypothesized that the proposed ANFIS model driven by the NNMF-extracted muscle synergy patterns will be able to accurately and reliably estimate lower limb joint movements, and that the effectiveness will also be radiated to patient subjects.

The sixth research result and conclusion of this thesis: Six muscle synergies were determined to construct the muscle synergy pattern driven ANFIS model. Three fuzzy rules were determined in most estimation cases. Combining the results of the four error indicators across the estimated variables indicates that the current model has excellent estimated performance in estimating lower limb joint movement. The estimation errors between the healthy and patient groups are consistent. The proposed model of this study can accurately and reliably estimate lower limb joint movements, and the effectiveness will also be radiated to the patient group. This revealed that the models also have certain advantages in the recognition of motor intentions in patients with relevant movement disorders.

In conclusion, lower limb neuromuscular fatigue will increase the ACL dynamic loading force during SL, thereby increasing the risk of ACL injury. This result is associated with a smaller AICA (plantarflexion angle) and AROM movement pattern of the ankle joint during after-fatigue SL. The use of larger ankle plantarflexion angle during SL may be an effective solution to reduce knee impact load and the risk of rupture of the medial femoral attachment area in the ACL. By increasing the AICA and AROM during SL, the energy dissipation of the lower limb joints can be increased and the PAF reduced, thus reducing the impact loads on the lower limb joints and reducing lower limb injuries, including ACL injuries. However, this may increase the LAS risk. AICA in the approximate range of 30° to 40° and AROM in the approximate range of

50° to 70° is likely to balance the association between the LAS and ACL injury risk. It is essential to strengthen the training of the muscles, the medial and lateral tissues, ligaments around the ankle. This can reduce lower limb injury risk while avoiding ankle joint injury when AICA and AROM are increased. The findings of this work can provide new insights for the optimization of landing strategies and thus provide important theoretical support for the development of lower limb injury prevention training or related rehabilitation programs.

Additionally, the current study proposed a method for constructing a highly accurate and easy-to-implement ACL dynamic load force prediction model, which has low input variable demands (sagittal joint angles), excellent generalization capabilities and superior performance in terms of high accuracy. In the future, we plan to combine our proposed ACL force prediction model with a subject-specific musculoskeletal model, and use it as an effective and accurate ACL injury risk assessment tool. Furthermore, it will be promoted and applied to a wider range of sports training and injury monitoring to improve the body's sports performance and reduce sports injuries. Furthermore, I further proposed a movement intention detection technology for estimating each joint continuous kinematic variable. It was demonstrated that the proposed ANFIS model driven by the NNMF-extracted muscle synergy patterns will be able to estimate the joint movements of the lower limb accurately and reliably, and that this effectiveness will also be radiated to patients. Future work from this study can be applied to sports rehabilitation in the clinical field by achieving more flexible and precise movement control of the lower limb assisted equipment to help the rehabilitation for patients.

Abbreviations

ACL: Anterior cruciate ligament
ACTED: Ankle contribution to total energy dissipation
AED: Ankle energy dissipation
AF: After-fatigue
AI: Artificial intelligence
AICA: Ankle initial contact angle
ANFIS: Adaptive neuro-fuzzy inference system
ANN: Artificial neural network
AROM: Ankle range of motion
BF: Before-fatigue
CT: Computerized tomography
DCT: Dense connective tissue
ELM: Extreme Learning Machine
EMG: Electromyography
FEA: Finite element analysis
FEM: Finite element model
HCTED: Hip contribution to total energy dissipation
HED: Hip energy dissipation
KCTED: Knee contribution to total energy dissipation
KED: Knee energy dissipation
KNN: K-nearest neighbor
LAS: Lateral ankle sprain
LRP: Layer-wise relevance propagation
LSTM: Long short-term memory
MAPE: Mean absolute percentage error
ML: Machine learning
MRI: Magnetic resonance imaging
MSE: Mean square error
MVC: Maximal voluntary contraction
NNMF: Non-negative matrix factorization
NRMSE: Normalized RMSE
PAF: Peak ACL force
PAIA: Peak ankle inversion angle
PAIM: Peak ankle inversion moment
PAM: Peak ankle sagittal moment
PHM: Peak hip sagittal moment
PKM: Peak knee sagittal moment
PRE: Session rating of perceived exertion
PVGRF: Peak VGRF
R^2: Square of correlation coefficient
RMSE: Root mean square error
SCA: Subtractive clustering algorithm
SL: Single-leg landing
SPM: Statistical parametric mapping
SSA: Sparrow search algorithm
SVM: Support vector machine
TED: Total energy dissipation
VAF: Variability accounted for
VGRF: Vertical ground reaction force
XML: Explainable machine learning

List of Figures

List of Tables

1. Introduction

1.1 Overview of the fatigue factor's effect on landing injuries

Landing is one of the fundamental daily exercise techniques (Figure 1). Single-leg landing (SL) support is more conducive to stopping, changing direction, and jumping after landing, mainly due to the ability of the non-supported leg to respond quickly and sufficiently after a full landing. So, SL is more commonly used in daily exercises [1-3]. Different landing patterns can expose lower limb joints and ligaments to different loading modes [3-5]. Landing is also commonly associated with or accompanied by lower limb injuries, such as anterior cruciate ligament (ACL) injury, patellar tendinitis, and ankle sprain, among which ACL injury is one of the most common [1, 6-9]. ACL plays an important role in stabilizing the knee joint, which is specifically manifested in restricting the anterior movement of the tibia to the femur during lower limb flexion and preventing excessive internal and external inversion of the knee [10]. ACL injuries can have significant impacts on the individual levels of exercise and quality of life, and also induce other pathological changes in the knee joint. [8, 11].

Figure 1 Illustration of various landing motions [3].

A successful landing is defined as the body being able to cushion the impact load well enough to maintain body balance and avoid injury [1, 12]. Successful landing support requires the body to have sufficient muscle strength, joint stability and postural balance to trigger the body's protective mechanisms [1, 13]. There are a variety of factors that can affect successful landings, and lower limb muscle fatigue may affect the body's landing pattern and lead to an increased risk of ACL injury [14-17]. When the body is in a state of lower limb muscle fatigue, it will exhibit less knee and hip flexion, greater ground reaction force (GRF), and greater knee valgus angle during landing [1, 3, 15, 18]. When landing with less knee and hip flexion, the body may land in a more upright position. It will increase the ground reaction forces, knee joint contact forces, which increases the impact on the ACL [1, 19]. Also, greater knee valgus angles can lead to increased ACL force [3]. Therefore, fatigue factors potentially increase the risk of ACL injury.

However, previous studies on the impact of fatigue factors on the lower limb

biomechanics during landing tasks often only investigated the effect of fatigue factors on ACL injury risk from some indirect indicators, rather than starting from the perspective of the dynamic loading forces within the ACL itself [14, 20-22]. For example, previous studies analyzed the lower limb joint kinematics of athletes during ACL injury through competition videos, and concluded that 'hard' landings and functional knee valgus collapse increase the risk of ACL injury [7, 8, 12]. This discrimination method has gradually become a consensus and has been accepted in the field of biomechanics. However, the limitation is that it cannot explore the exact mechanism of the fatigue factor increasing ACL injury risk from the internal force itself. The reasons for this limitation are mainly the high cost of constructing biomechanical models and the large errors in the calculation results in the past, thus lacking a certain degree of practicality and accuracy [1, 9]. The inability to accurately explore ACL loading during exercise makes it difficult for researchers to accurately recognize the injury mechanism and risk degree of related movements, and reducing the effectiveness of injury prevention and sports monitoring. Therefore, based on constructing the musculoskeletal model and accurately calculating the ACL internal dynamic load force, it is vital to develop a predictive model that can quickly and accurately predict ACL loading during landing.

The ankle joint and surrounding tissues play an important role in absorbing high-impact loads during landing, especially in the SL support, which can withstand the impact force of approximately 2-5 times the body weight [23, 24]. Insufficient shock absorption of the ankle joint will increase the energy consumption requirement of the proximal lower limb joint [23, 25, 26]. The degree and relative contribution of joint energy dissipation (negative joint work) to lower limb joint shock absorption was thought to be altered by adjusting the ankle initial contact angle (AICA) in the sagittal plane (dorsiflexion and plantarflexion) during SL [25, 27, 28]. The AICA also affects the ankle range of motion (AROM) and GRF, which are associated with the risk of lower limb injury [1, 25, 29]. Previous studies have reported that the smaller AICA (peak plantarflexion angle) and sagittal range of motion occur during after-fatigue SL [9, 20, 23, 29]. The AICA affects the redistribution of energy dissipation in the lower limb joints during SL, which may increase the injury risk of the lower limb [6, 28]. However, it is unclear whether changes in the ankle during after-fatigue SL are associated with an increased risk of ACL injury. Therefore, this study aims to explore whether there are detectable and recognizable differences in ankle joint kinematics, lower limb joint energy dissipation (joint work) and ACL load force between before-fatigue and after-fatigue SL, as well as to explore the possible relationship between them.

In overview, this work mainly has the following research objectives: (1) To calculate the ACL dynamic load force during SL through musculoskeletal modeling simulations to investigate whether fatigue factors increase the risk of ACL injury; (2) To explore whether there are recognizable differences in the ankle motion patterns between before-fatigue and after-fatigue SL, and further explore the relationship between AICA, AROM and lower limb energy dissipation and peak ACL force.

1.2 Application of explainable machine learning to clinical diagnosis

Landing maneuvers are frequently used in clinical injury screening, which include: 1) Assessment and screening of functional valgus collapse (an indicator of ACL injury) [30]; 2) Assessment of dynamic postural stability in ACL reconstruction where impaired sensorimotor control and mechanical stability can be identified among athletes [31]; 3) Screening for patients with chronic ankle instability [32], and so on. In clinical injury screening, clinical experts mainly performed quantitative description and analysis from the perspective of biomechanics, which includes biomechanical data such as kinematics (joint angle, spatiotemporal parameters, etc.), kinetics (ground reaction force, joint moment, etc.), and muscle status (muscle activation degree, muscle force, etc.). However, the quantitative descriptive analysis traditionally used in clinical screening is usually only for discrete variables at a specific time point, such as peak angle, peak force, peak moment, etc. Although this traditional approach has successfully solved many clinical injury screening problems, it also has the inherent limitation of losing a large amount of effective information when extracting low-dimensional single-time point discrete variables from high-dimensional time-continuous variables [33, 34]. This is because in many cases it is not clear whether and to what extent a single pre-selected variable adequately represents the characteristics of that class of landing pattern. At the same time, the landing patterns are different in the situation of different injury conditions, different control/intervention conditions, and whether there is lower limb injury, which will cause great difficulties for clinical experts in clinical diagnosis. Therefore, a new method is urgently needed to explore the deeper characteristics of different landing patterns itself, to improve the effectiveness and accuracy of clinical injury screening.

Artificial intelligence (AI) and machine learning (ML) technologies are becoming more sophisticated as the economy and society develop, and their use in various industries to improve the efficiency of decision-making has also greatly reduced the burden on humans [35, 36]. The healthcare industry is one of the many sectors that benefit from this, with AI and ML playing an important role in medical image-assisted diagnosis, pattern recognition of patient symptoms, identification of cancer tissue, etc [37-39]. This trend is also being recognized in the field of clinical gait analysis, where it has been successively used in gait pattern recognition and classification of patients with stroke [40], Parkinson's disease [41], cerebral palsy [42], osteoarthritis [43], and different functional gait disorders [44, 45]. At the same time, advances in motion capture technology, mechanics sensing technology, and signal processing technology have made it possible to collect diverse and fine-grained human biomechanical data, providing the prerequisites for the application of big data-driven ML methods in the field of clinical biomechanics [33, 45, 46]. Although machine learning techniques have been very successful in solving a variety of clinical classification tasks and providing new insights from complex systems, they also suffer from an important limitation: black box effect [46, 47]. That is, they all have the disadvantage of being black boxes and rarely provide and explain useful information about the reasons for making a particular decision [46, 48]. This opaque operation and decision-making of most non-linear ML methods lead to a problem: the results of predictive recognition are hard to understand

and uninterpretable, and this in turn undoubtedly affects the efficiency of ML applications in medical clinical diagnosis [49, 50].

Based on this, the demand for ML methods for the interpretability of decision results in the field of clinical diagnosis continues to grow, and explainable machine learning (XML) has received increasing attention in recent years [50, 51]. XML mainly refers to a series of machine learning methods that help the decisions and behaviors of artificial intelligence technology to be understood by humans, and which aims to illustrate how non-linear ML models work and the reasons for such predictive results [51]. The relevant application of XML in clinical diagnosis has increased the trust of experts in this field in the traceability of ML methods, and has been accepted by more and more researchers [52, 53]. In recent years, an XML based on Layer-wise Relevance Propagation (LRP) has been proposed to address the problem of lack of interpretability of ML prediction results, which mainly measures the contribution and relevance of each input variable to the overall prediction results through backward propagation [48, 54]. As shown in Figure 2, with its unique advantages in interpreting both linear and non-linear ML models, this method has been successfully applied to classification and recognition tasks in different scenarios, including clinical gait analysis, and has also been validated for its good interpretability performance in clinical diagnosis tasks [46, 49, 55-60]. Whether XML can bring new challenges and opportunities for the application of landing pattern recognition in clinical diagnosis is not yet known. In other words, it is debatable whether XML can lead to new insights beyond the traditional "yes" or "no" simple discriminatory results.

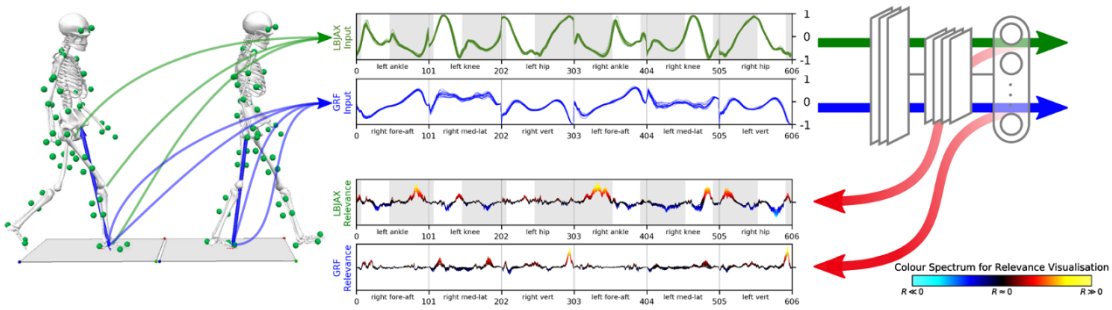

Figure 2 Illustration of data acquisition and analysis by XML [34].

Therefore, this work aims to investigate whether XML can help with landing pattern recognition and to what extent it can aid in the interpretation of prediction results. This work firstly compared the classification recognition performances of several classical classification models on two class landing tasks, and then constructed the XML model based on the neural network model with the best recognition performance combined with LRP to explain the model classification recognition results. At the same time, considering that biomedical signals are more abstract compared with signals such as image text, the evaluation of interpretability results is full of challenges [49, 58, 61]. To solve these challenges, the current study proposed two approaches to assess the computed interpretability results: 1) assessment from a statistical perspective; and 2) assessment from a clinical perspective. For statistical evaluation, a Statistical

Parametric Mapping (SPM) technology [62] based on random field theory was used to detect statistical differences in the input signals, and then to verify whether interpretability results are reasonable based on statistical differences. For clinical evaluation, interpretable results were analyzed clinically by experienced experts in the field to assess their compatibility with clinical features. Finally, our work mainly addresses the following two research questions: (1) which areas of input signals in the two class landing patterns are most relevant to the landing pattern recognition? (2) To what extent do these regions of input signals identified as most relevant for landing pattern recognition remain consistent with statistical evidence and clinical consensus assessment?

1.3 Overview of ankle movement patterns and lower limb injury risk during landing

During landing, as the key joint connecting the ankle and hip, the knee has the highest risk of injury [4, 5, 63]. The most common is the non-contact ACL injury (Figure 3), with more than 80% of its injuries occurring during landing tasks [1, 3, 9, 64]. As one of the main ligaments around the knee joint, the ACL is crucial for maintaining stability in the knee joint [10, 65]. After an ACL rupture, the patients experience a general decrease in their exercise level and quality of life. Even after prompt treatment, only 55% of patients return to their daily competitive sport level within the first year [66]. More seriously, ACL ruptures also frequently lead to other pathologic changes, such as osteoarthritis of the knee [9, 67-69].

It is also true that ankle sprains (Figure 3), on the other hand, are one of the most common injuries associated with landing, and more than 80% of ankle sprains occur in the lateral [70, 71]. Lateral ankle sprain (LAS) causes structural damage to the lateral collateral ligaments (anterior tibiofibular ligament and calcaneofibular ligament) of the ankle joint [71, 72]. These structural injuries may cause joint pain, swelling, and related dysfunction. In severe cases, they can also cause re-sprains of the ankle joint and progress to chronic ankle instability [70, 72]. An increased ankle inversion angle is recognized as one of the important biomechanical factors causing LAS [71, 72]. Ankle inversion is the inward rotation of the ankle joint that turns the sole toward the midline of the body. When the ankle is in greater plantarflexion and inversion, it is considered to be at greater risk for LAS [72-74].

During the landing process, the lower limbs undergo a transfer of load impact pattern from the distal to the proximal: foot-ankle to knee, knee to hip [4, 6, 64]. The ankle joint and its surrounding muscles and tissues have a crucial function in absorbing the load impact during landing, serving as the initial point for the transfer of this impact [64]. Research has shown that they can withstand impact forces ranging from 2 to 5 times the individual's body weight during a SL [12, 24, 64, 75]. Previous studies have suggested that increasing the ankle initial contact angle (AICA) during landing may increase ankle energy dissipation [28, 64], and a greater ankle range of motion (AROM) has also been thought to increase the time to the peak point of vertical ground reaction force (VGRF) [1, 2], thereby reducing the impact on the lower limb [64]. However, whether ankle joint motion patterns (AICA, AROM) during SL affect joint energy

dissipation and the degree of shock load cushioning across the lower limb, or even if there is some association with lower limb injury, remains to be further explored. It is undeniable that AICA and AROM during SL can be adjusted to a large extent by human autonomic awareness. Consequently, guiding individuals to consciously adjust their ankle movement patterns during landing based on the discovered laws is anticipated to decrease the incidence of lower limb injuries. [64, 76].

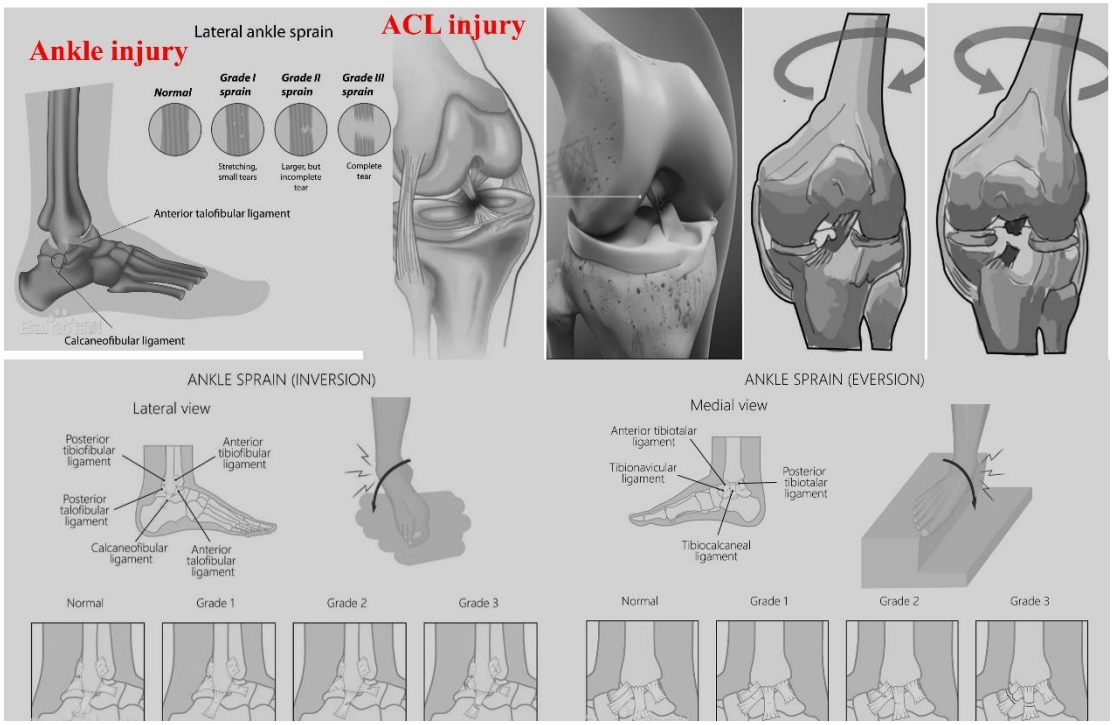

Figure 3 Illustration of ankle injury and ACL injury [64].

In assessing the ACL injury mechanism, traditional models mainly set ligaments as having linear force-length characteristics and consider them independent of strain rate [77-79]. However, ligaments (Figure 4), as dense connective tissue (DCT), are characterized by short-term viscoelastic strain, which affects the force-length characteristics [78, 80]. Hence, to more realistically revert and simulate the ACL injury mechanics, this study developed a knee musculoskeletal model that reverts the ACL ligament to a nonlinear short-term viscoelastic mechanical mechanism (strain rate-dependent) generated by the DCT as a function of strain. By implementing the structural constitutive model, this study calculated the compressive stress on the ligament at different strains [80, 81].

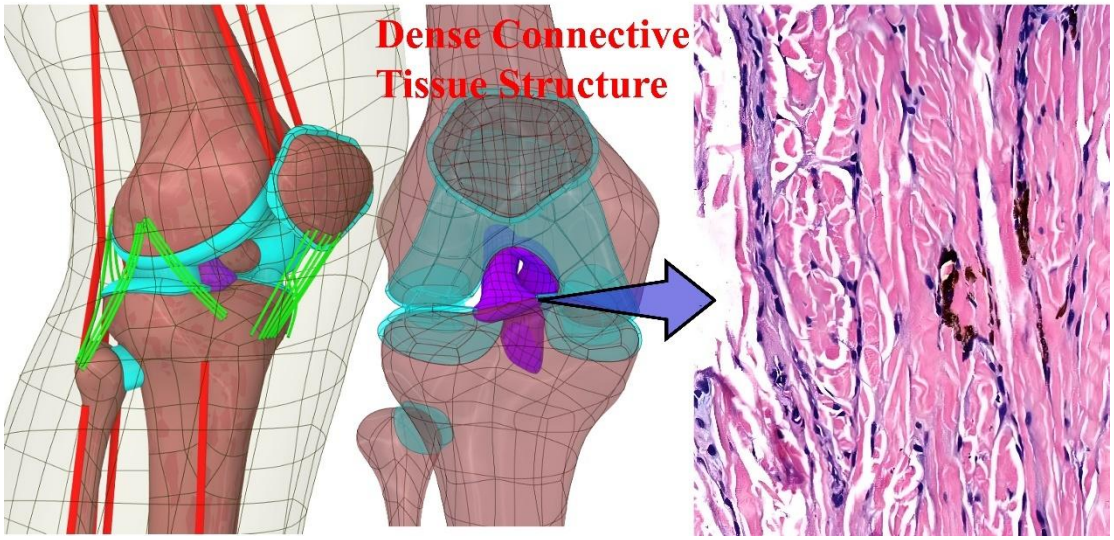

Figure 4 Illustration of the ligament dense connective tissue structure [80].

Therefore, this study aims to explore an optimized landing strategy to reduce the injury risk of the lower limb. This study hypothesized that the variations in ankle motion patterns (AICA, AROM) during SL would be associated with the injury risk of the lower limb. Among these, by appropriately increasing AICA and AROM during SL, the overall injury risk of the lower limb, particularly ACL injury, can be minimized, but this increases the LAS risk. Furthermore, there is an "optimal" ankle movement pattern that can balance the association between the LAS and ACL injury risk, allowing for minimization of the overall injury risk.

During landing, when the body undergoes a greater VGRF, the impact on the joints of the lower limbs is greater [82, 83]. Among them, the degree to which the joints and soft tissues of the lower extremities are subjected to loads increases if the landing impact is not effectively dissipated [19, 64]. To be exact, insufficient energy dissipation in the lower extremity joints will increase the injury risk [64]. The moment is the torsional effect that the forces around the joint produce, and a larger moment implies greater stress on the muscles and ligaments surrounding the joint [1, 74]. These changes in biomechanical outcomes are thought to lead to an increased risk of lower limb injury [74, 83, 84]. Furthermore, the greater the loading force on the ACL, the greater the risk of ACL tears and strains [64, 84].

Therefore, the following works are specified: (1) The peak VGRF (PVGRF), total energy dissipation (TED), peak ankle sagittal moment (PAM), peak knee sagittal moment (PKM), and peak hip sagittal moment (PHM) were used to assess the overall injury risk of the lower limb, and explored their relationships with AICA, AROM. (2) The peak ankle inversion angle (PAIA), and peak ankle inversion moment (PAIM) was used to assess the LAS risk, and hypothesized the positive correlation between them and AICA, AROM. (3) The ACL model was developed and constructed to calculate ACL dynamic loading forces, and then the peak ACL force (PAF) was used to assess the ACL injury risk, and hypothesized the negative correlation between them and AICA, AROM. (4) The feasible ankle motion patterns were explored to balance the LAS and ACL injury risk based on the interaction between PAIA and PAF.

1.4 Overview of ankle initial contact angle and knee injuries during landing

Landing is an important sport technique that is used in almost all human movements [1, 2, 28, 63]. The single-leg landing (SL) support is preferred over the double-leg landing support due to its superior ability to facilitate rapid pauses and shifts of direction after landing [1, 3, 28, 85]. As a result, it is commonly utilized in exercises [1, 3]. From the distal to the proximal areas, the lower limbs undergo a transfer of load impact patterns during landing: from the foot-ankle to the knee, then from the knee to the hip [4, 6, 85]. The absence of energy dissipation by the joint during landing is a primary factor contributing to musculoskeletal injuries that are associated with load transfer [63, 86]. In the case of the commonly employed SL support, only the support leg absorbs the energy shock, which raises the likelihood of injury to the landing limb [63, 85, 86]. As the primary joint transmitting impact load, the ankle joint and its accompanying muscles and tissues have an essential function for transferring impact loads during landing [64]. Especially in SL supports, the ankle joint can withstand an impact force close to five times the individual's body weight [12, 24, 64, 75]. Inadequate shock absorption in the ankle joint leads to an increase in the energy requirements of the other proximal joints [12, 28]. More precisely, the decrease in the dissipation of energy in the ankle (negative work) enhances the level of impact load in the other joints [19, 64]. Among them, the injury risk also undoubtedly increases when the knee's impact load is increased [64].

During landing, the knee, which serves as the pivotal joint connecting the ankle and hip, is the most susceptible to damage [4, 5, 63]. When the knee joint is exposed to large impact loads for long periods of time, injuries associated with it inevitably occur, such as non-contact anterior cruciate ligament (ACL) injuries, meniscus injuries, patella fractures or dislocations, and cartilage injuries [1, 64, 87]. Of these, the most notable is ACL injury, which is one of the most popular injuries accompanying landing tasks (80% injury rate) and often incurs the most severe repercussions [1, 3, 9]. After an ACL rupture, patients experience a general decrease in their exercise level and quality of life. Even after prompt treatment, only 55% of patients return to their daily sports level within the first year [66]. Furthermore, ACL ruptures can lead to additional pathological alterations in the knee joint, such as knee osteoarthritis and meniscus-induced injury [9, 67-69, 88]. Therefore, it is critically important to estimate knee forces accurately and efficiently, even ACL internal loading, during landing to assess the risk of knee-related injury and to propose timely preventive measures to prevent injury.

When the biomechanical mechanisms of internal loads on the human body are explored in the context of the complex external mechanical environment, the current solutions in the field are mainly achieved by finite element analysis (FEA) techniques and musculoskeletal modeling simulations (Figure 5) [5, 77, 89]. Both of these methods are also expected to successfully evaluate the knee and ACL internal loading mechanisms during landing. The FEA technique is a computational method to demonstrate the mechanical response of biological systems under complex loading conditions [90-92]. It allows complex physical problems to be transformed into simple mathematical models, and then computer simulations are used to obtain the stress and

strain parameters of the human body under loading conditions, to assess the knee and ACL stress distribution during landings on the ground. As shown in Figure 6, OpenSim is an open-source software platform for musculoskeletal modeling and has become a mainstream analysis tool for human biomechanics research due to its proven applicability and accuracy [64, 78, 89]. By constructing an ACL model in OpenSim, ACL dynamic loading forces during landing can be accurately calculated [64, 77, 93].

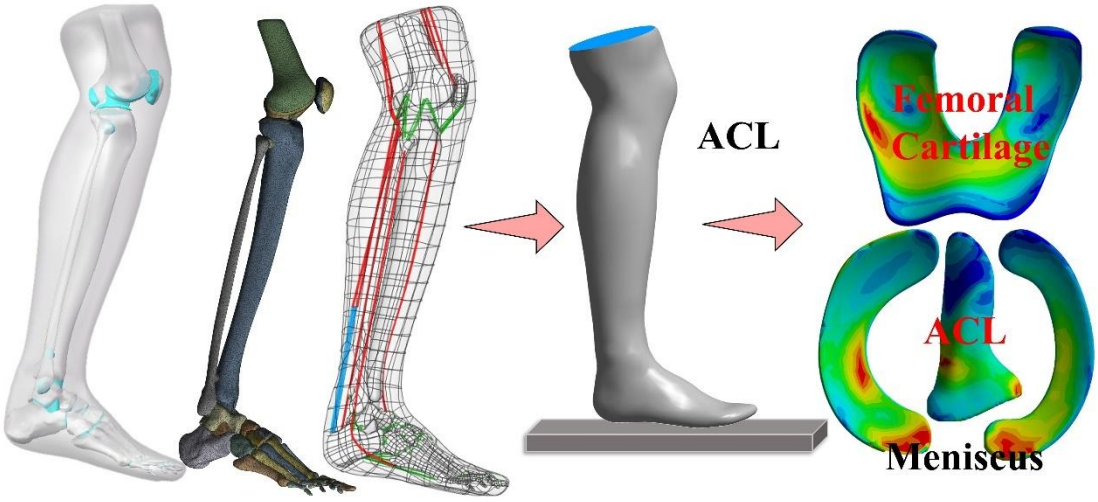

Figure 5 Illustration of the finite element analysis [85].

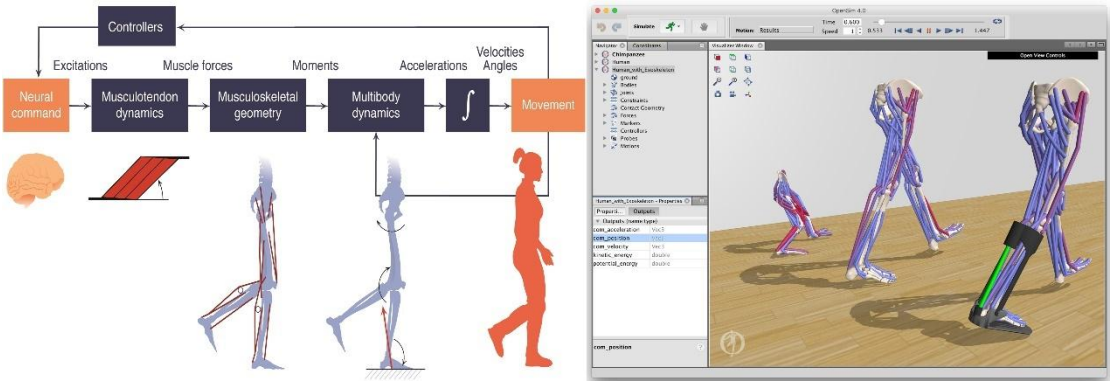

Figure 6 Illustration of OpenSim-based musculoskeletal modeling simulation [94].

In assessing the ACL injury mechanism, traditional models mainly set ligaments as having linear force-length characteristics and consider them independent of strain rate [77-79]. However, ligaments, as dense connective tissue (DCT), are characterized by short-term viscoelastic strain, which affects the force-length characteristics [78, 80, 85]. Hence, to more realistically revert and simulate the ACL injury mechanics, this study developed a knee musculoskeletal model that reverts the ACL ligament to a nonlinear short-term viscoelastic mechanical mechanism (strain rate-dependent) generated by the DCT as a function of strain [85]. By implementing the structural constitutive model, this study calculated the compressive stress on the ligament at different strains [80, 81, 85].

Previous research has demonstrated that increasing the ankle plantarflexion (ankle initial contact angle: AICA) may increase ankle energy dissipation during landing, thereby reducing the landing impact on the other joints [28, 64]. Nevertheless, more research needs to be done on how ankle plantarflexion (AICA) affects the lower limb's ability to dissipate joint energy and absorb shock loads during single-leg landings, as well as any possible links between this and knee injuries. Unquestionably, ankle plantarflexion during landing can be adjusted to a large extent by individual autonomic awareness. Consequently, it is expected that instructing individuals to consciously adjust their ankle movement patterns during landing, according to the discovered rules, would reduce the occurrence of knee-related injuries [64, 76].

At present, it is unclear whether increasing the ankle plantarflexion angle during landing would change the knee loading mechanism and further affect ACL injury risk. Therefore, this work aims to explore the effects of different ankle plantarflexion angles during SL on knee impact loading and ACL injury risk. The biomechanical properties of the knee joint were planned to be quantified based on musculoskeletal modeling and finite element analysis (foot-ankle-knee integration model). Meanwhile, landing optimization strategies are further proposed to reduce knee-related injuries based on the possible findings.

1.5 Application of machine learning in predicting lower limb biomechanical variables

In actual motion monitoring, most current studies of ACL forces during landing have been conducted using biomechanical models such as musculoskeletal models and in vivo studies [93, 95-97]. However, the establishment of such a model usually requires a large and complex base of knowledge, and the simulation calculation process is usually time-consuming and costly. In recent years, as shown in Figure 7, an increasing number of studies have favored the use of machine learning methods to model and predict the complex "input-output" relationship, to address the computational difficulty and cost of important variables in biomechanics [46, 98-100]. When predicting time series data in biomechanical variables, the prediction model relies not only on the current input, but also needs to combine the input at the previous or follow time as a reference. Therefore, a recurrent neural network with a special structure called long short-term memory (LSTM) network has been widely used to predict the variables such as the GRF, the knee joint contact forces, and the coordination variability in the field of biomechanics [98, 99, 101].

However, one issue to consider when predicting biomechanical variables based on machine learning is that manually setting the hyperparameters of a neural network model for a specific data set often results in slow convergence, failure to converge, and overfitting of the model, thus affecting its predictive performance [102, 103]. Recently, more and more studies have focused on finding the optimal parameter solution by combining metaheuristic algorithms, thus solving intractable problems in various engineering fields [104-106]. Specifically, the metaheuristic algorithm provides a practical and elegant solution to complex problems. The sparrow search algorithm (SSA) is a novel metaheuristic algorithm, which is mainly inspired by the foraging and anti-

predation behaviors of sparrows [107]. The performance of the SSA has been tested through experiments on 19 benchmark functions and compared with the performance of other classical intelligent algorithms. Simulation results show that SSA is superior to other algorithms in terms of accuracy, stability, robustness and convergence speed, and has been implemented in a large number of studies [107]. Therefore, this study intends to use SSA to find the optimal parameters of the prediction model in predicting the ACL dynamic load forces to achieve an accurate prediction of the ACL forces.

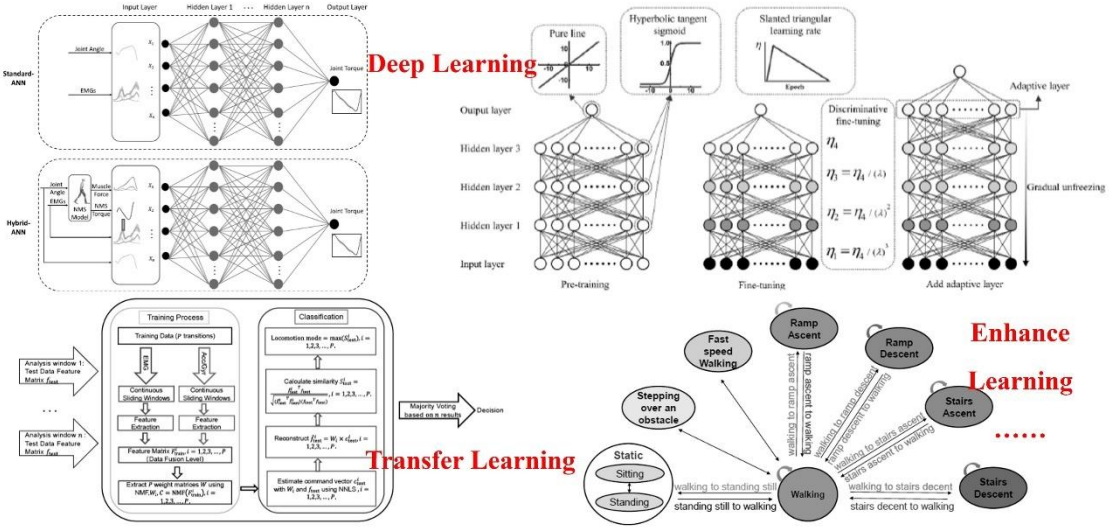

Figure 7 Illustration of the machine learning prediction model [108].

It is difficult to have a recognizable intersection relationship between the trend of the ACL force and the corresponding set of independent variables near the point in time when the peak ACL force (PAF) occurs, which may lead to a larger prediction error near of the PAF. In addition, when assessing the risk of ACL injury, the trend in ACL force near the time point when the PAF occurs (during the 10%-35% landing phase) is the stage that is mainly focused on [1-3, 96]. It has been reported that this stage is a high-risk time window for ACL injury to occur [7, 8]. Therefore, how to design an optimal prediction model that can accurately predict the trend during the 10%-35% landing phase is a difficulty requiring a solution in the current research field. Therefore, this study intends to further optimize the model by constructing the PAF prediction model twice based on the explored relationship between ankle kinematics and PAF, finally achieving an accurate and effective prediction of the ACL force during SL.

1.6 Application of surface electromyographic signals in estimating lower limb joint movements

For related patients with movement disorders, the main clinical focus is on exercise rehabilitation to help recover lost motor function and enhance sports performance, etc [109-111]. In this regard, lower limb-powered exoskeletons and orthoses have been extensively developed for sports rehabilitation to improve the efficacy of pathological rehabilitation [112, 113]. In exoskeleton-assisted rehabilitation training, the active participation of the human user plays a crucial role in stimulating

neuromuscular recovery [114, 115]. In other words, the basis for achieving seamless control of exoskeletal robots and orthoses is the accompanying accurate inference of the user's movement intentions, which is currently a difficult and challenging task in this field [112-116]. At the present stage, the user's movement intention information is mainly obtained through surface electromyography (EMG) signals [117]. Surface EMG is generated by muscle contraction and can be used as a tool to detect movement intention before the user making the actual movement, thus being widely used in rehabilitation robots and human-machine interfaces, etc [118-120].

As shown in Figure 8, there are two main ways to detect the user's motion intention based on surface EMG signals: 1) identifying different motion patterns of human limbs based on feature extraction and classification algorithms; 2) estimating continuous kinematic variables (joint angles, force, torques, etc.) [113, 114, 121]. For the first one, the researchers have mainly developed feature extraction and classification algorithms with high accuracy to analyze the surface EMG signal to recognize the different movement patterns of the limb. However, this way can only identify a limited number of discrete movement patterns from the surface EMG signal, such as walking on a flat surface, sitting down/standing up, walking uphill/downhill, etc. [112, 122, 123]. The recognition results of this method are more suitable for use as trigger control for exoskeleton robots, as it inevitably affects human-machine coordination and smoothness during movement [124]. In the second way, surface EMG signals are used to estimate continuous time-series-based kinematic variables [125, 126]. Implementations of the second approach are divided into two main types: 1) model-based neuro driven musculoskeletal models [127]; 2) model-free machine learning algorithms such as artificial neural networks and support vector machines [124, 125]. By recognizing the expected motion trajectory from the surface EMG signal, this approach can be used as a control command for exoskeleton robots to achieve smooth motion control [113, 125, 128].

Previous studies in estimating continuous kinematic variables have usually calculated the informative features of a single group from the surface EMG signals of each muscle, and used them as regular features in that motion pattern [112, 129]. For example, a feature matrix will be constructed based on the extraction of time-domain features (root mean square amplitude, waveform length, maximum fractal length, etc.) from individual surface EMG channels. However, one issue that needs to be examined is that the features extracted from a single surface EMG channel are extremely sensitive to noise, amplitude cancellation and electrode shifts, which would increase estimation errors [118, 130, 131]. More critically, the inability to effectively detect individual surface EMG signals makes it difficult for the surface EMG features extracted from specific movement patterns to reflect the real physiological phenomenon. This is particularly true in specific patients, as evidenced by the failure or ineffectiveness of surface EMG signal capture in selected muscles under motor deficits [110, 112, 132]. This directly leads to an increase in the error between the estimated continuous movement variables and the expected results, thus hindering the use of rehabilitation robots in clinical practice [133, 134].

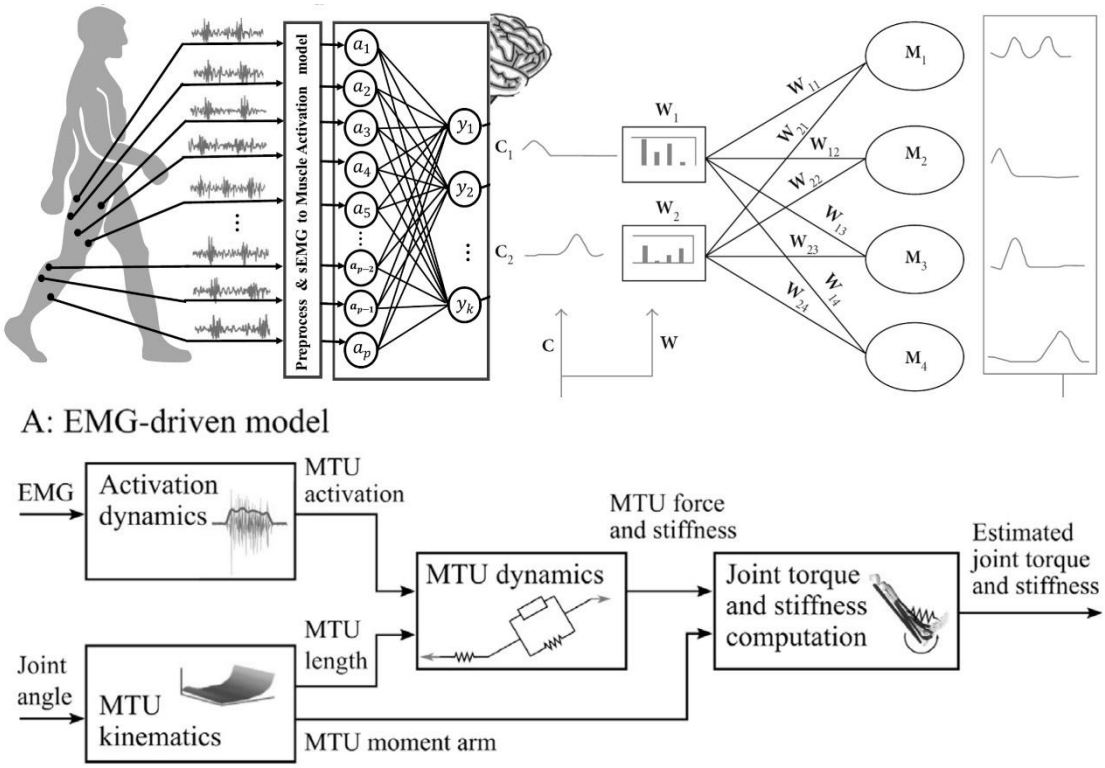

Figure 8 Illustration of lower limb joint motion estimation based on surface EMG signals [108].

How the central nervous system efficiently and sequentially controls the peripheral neuromusculoskeletal to achieve target movements is a fundamental question in the field of neuroscience and movement science research. Among them, the existence of muscle synergy makes efficient and orderly control possible [135, 136]. Muscle synergy is a collection of neural control information, which contains the coordinate information between each muscle to reveal the coordination of muscle recruitment [135, 136]. At the macroscopic level, muscle synergies reflect the shared neural drive of motor units between muscles. In recent years, muscle synergy has been proposed for applications in the analysis of motor mechanisms in healthy subjects and patients, as well as in exoskeletal rehabilitation robots and human-machine interfaces to detect movement intention [137-142]. By revealing the neuromuscular control mechanism behind the motor system, muscle synergy can detect movement intention comprehensively and accurately, and its application is expected to help patients in clinical rehabilitation.

In terms of mathematical operations, extracting muscle synergy is an approximate decomposition of the original muscle activation matrix into the product of the muscle synergy matrix and the activation coefficient matrix [142, 143]. Many algorithms can implement muscle activation matrix decomposition, which includes non-negative matrix factorization (NNMF), principal component analysis, factor analysis, vector quantization, etc. Compared with other methods, the left-right matrix factors acquired by decomposing the muscle activation matrix based on NNMF have a non-negative characteristic, which enhances the interpretability of the issue [143, 144]. In addition, NNMF has many advantages such as simplicity in implementation, interpretability in

decomposition form and results, and low storage consumption [143, 144].

When estimating continuous kinematic variables based on muscle synergy patterns, there is a high degree of non-linear correlation between them [125, 128]. Therefore, a non-linear modeling tool that can handle complex information should be developed when mapping muscle synergy patterns to kinematic variables. As one such tool, the adaptive neuro-fuzzy inference system (ANFIS) has been successfully applied to identify different human motion patterns and estimate continuous joint movements [145-147]. ANFIS combines the autonomous learning mechanism of artificial neural networks with the fast inference capability of fuzzy logic inference systems, which has capable of fast processing of large-scale non-linear data and evolutionary learning [145, 148]. It also has the advantages of optimizing membership functions through independent learning and adjusting fuzzy logic rules to establish output functions that adapt to various rules [145, 148]. Therefore, ANFIS is expected to be efficient and accurate in detecting human movement intentions, both for healthy subjects and patients, when used as a modeling tool for mapping muscle synergy patterns to kinematic variables.

This study aims to develop a movement intention detection technology for estimating each joint continuous kinematic variable based on the lower limb muscle synergy pattern, with a view to developing applications for more efficient exoskeleton-assisted rehabilitation training. More specifically, this study extracted the lower limb muscle synergy patterns of healthy subjects and patients through NNMF, and then mapped the lower limb muscle synergy patterns to each joint continuous motion variable using the developed ANFIS non-linear regression model. It is hypothesized that the proposed ANFIS model driven by the NNMF-extracted muscle synergy patterns will be able to accurately and reliably estimate lower limb joint movements, and that the effectiveness will also be radiated to patient subjects.

1.7 Aims and objectives

The 1st research question:

Previous studies on the impact of fatigue factors on the lower limb biomechanics during landing tasks often only investigated the effect of fatigue factors on ACL injury risk from some indirect indicators, rather than starting from the perspective of the dynamic loading forces within the ACL itself. However, the limitation is that it cannot explore the exact mechanism of the fatigue factor increasing ACL injury risk from the internal force itself. In addition, it is unclear whether changes in the ankle during after-fatigue landing are associated with an increased risk of ACL injury.

Therefore, my 1st objective is:

To accurately calculate ACL internal dynamic load forces by constructing a musculoskeletal modeling. In addition, this study aims to explore whether there are detectable and recognizable differences in ankle joint kinematics, lower limb joint energy dissipation (joint work) and ACL load force between before-fatigue and after-fatigue landing, as well as to explore the possible relationship between them.

The 2nd research question:

In clinical landing injury screening, clinical experts mainly performed quantitative description and analysis from the perspective of biomechanics. However, traditional approach has the inherent limitation of losing a large amount of effective information when extracting low-dimensional single-time point discrete variables from high-dimensional time-continuous variables. Meanwhile, the landing patterns are different in the situation of different injury conditions, different control/intervention conditions, and whether there is lower limb injury, which will cause great difficulties for clinical experts in clinical diagnosis. In recent years, the relevant application of explainable machine learning (XML) in clinical diagnosis has increased the trust of experts in this field in the traceability of ML methods, and has been accepted by more and more researchers.

Therefore, my 2nd objective is:

To investigate whether XML can help with landing pattern recognition and to what extent it can aid in the interpretation of prediction results. This work firstly compared the classification recognition performances of several classical classification models on two class landing tasks, and then constructed the XML model based on the neural network model with the best recognition performance combined with LRP to explain the model classification recognition results. The current study proposed two approaches to assess the computed interpretability results: 1) assessment from a statistical perspective; and 2) assessment from a clinical perspective. For statistical evaluation, a Statistical Parametric Mapping (SPM) technology based on random field theory was used to detect statistical differences in the input signals, and then to verify whether interpretability results are reasonable based on statistical differences. For clinical evaluation, interpretable results were analyzed clinically by experienced experts in the field to assess their compatibility with clinical features.

The 3rd research question:

During landing, the knee has the highest risk of injury, and the most common is the non-contact ACL injury, with more than 80% of its injuries occurring during landing tasks. It is also true that ankle sprains, on the other hand, are one of the most common injuries associated with landing, and more than 80% of ankle sprains occur in the lateral. At present, whether ankle joint motion patterns (AICA, AROM) during landing affect joint energy dissipation and the degree of shock load cushioning across the lower limb, or even if there is some association with lower limb injury, remains to be further explored. In assessing the ACL injury mechanism, traditional models mainly set ligaments as having linear force-length characteristics and consider them independent of strain rate.

Therefore, my 3rd objective is:

To more realistically revert and simulate the ACL injury mechanics, this study developed a knee musculoskeletal model that reverts the ACL ligament to a nonlinear short-term viscoelastic mechanical mechanism (strain rate-dependent) generated by the

DCT as a function of strain. This work was specified: (1) The peak VGRF (PVGRF), total energy dissipation (TED), peak ankle sagittal moment, peak knee sagittal moment, and peak hip sagittal moment were used to assess the overall injury risk of the lower limb, and explored their relationships with AICA, AROM. (2) The peak ankle inversion angle (PAIA), and peak ankle inversion moment (PAIM) was used to assess the LAS risk, and hypothesized the positive correlation between them and AICA, AROM. (3) The ACL model was developed and constructed to calculate ACL dynamic loading forces, and then the peak ACL force (PAF) was used to assess the ACL injury risk, and hypothesized the negative correlation between them and AICA, AROM. (4) The feasible ankle motion patterns were explored to balance the LAS and ACL injury risk based on the interaction between PAIA and PAF.

The 4th research question:

During landing, the knee, which serves as the pivotal joint connecting the ankle and hip, is the most susceptible to damage. When the biomechanical mechanisms of internal loads on the human body are explored in the context of the complex external mechanical environment, the current solutions in the field are mainly achieved by finite element analysis (FEA) techniques and musculoskeletal modeling simulations. Previous research has demonstrated that increasing the ankle plantarflexion (ankle initial contact angle: AICA) may increase ankle energy dissipation during landing, thereby reducing the landing impact on the other joints. At present, it is unclear whether increasing the ankle plantarflexion angle during landing would change the knee loading mechanism and further affect ACL injury risk.

Therefore, my 4th objective is:

To explore the effects of different ankle plantarflexion angles during SL on knee impact loading and ACL injury risk. The biomechanical properties of the knee joint were planned to be quantified based on musculoskeletal modeling and finite element analysis (foot-ankle-knee integration model). This study employed a joint impact force to evaluate the impact loads on the knee at various landing angles, and calculated the joint negative work to assess the ability of the knee to dissipate the energy impact. Additionally, the ACL internal load forces (musculoskeletal modeling) and ACL stress (finite element analysis) were simulated and calculated to evaluate the ACL injury risk. Meanwhile, landing optimization strategies are further proposed to reduce knee-related injuries based on the possible findings.

The 5th research question:

In actual motion monitoring, most current studies of ACL forces during landing have been conducted using biomechanical models such as musculoskeletal models and in vivo studies. However, the establishment of such a model usually requires a large and complex base of knowledge, and the simulation calculation process is usually time-consuming and costly. In recent years, an increasing number of studies have favored the use of machine learning methods to model and predict the complex "input-output" relationship, to address the computational difficulty and cost of important variables in

biomechanics.

Therefore, my 5th objective is:

To develop a highly accurate and easy-to-implement ACL dynamic load force prediction model, which has low input variable demands (sagittal joint angles), excellent generalization capabilities and superior performance in terms of high accuracy. This study first combines LSTM algorithm to construct the prediction model, and then introduces a metaheuristic optimization algorithm (SSA) to optimize the prediction model based on existing machine learning models, and further optimizes the prediction results by combining the discovered linear relationship between AIC, AROM and PAF to achieve accurate prediction of the ACL dynamic load force during SL using simple and easy-to-measure kinematic data.

The 6th research question:

Previous studies in estimating continuous kinematic variables have usually calculated the informative features of a single group from the surface EMG signals of each muscle, and used them as regular features in that motion pattern. However, the features extracted from a single surface EMG channel are extremely sensitive to noise, amplitude cancellation and electrode shifts, which would increase estimation errors. By revealing the neuromuscular control mechanism behind the motor system, muscle synergy can detect movement intention comprehensively and accurately, and its application is expected to help patients in clinical rehabilitation. ANFIS has the advantages of optimizing membership functions through independent learning and adjusting fuzzy logic rules to establish output functions that adapt to various rules.

Therefore, my 6th objective is:

To develop a movement intention detection technology for estimating each joint continuous kinematic variable based on the lower limb muscle synergy pattern, with a view to developing applications for more efficient exoskeleton-assisted rehabilitation training. More specifically, this study extracted the lower limb muscle synergy patterns of healthy subjects and patients through NNMF, and then mapped the lower limb muscle synergy patterns to each joint continuous motion variable using the developed ANFIS non-linear regression model. It is hypothesized that the proposed ANFIS model driven by the NNMF-extracted muscle synergy patterns will be able to accurately and reliably estimate lower limb joint movements, and that the effectiveness will also be radiated to patient subjects.

2. Materials and methods

2.1 Ethics statement

As shown in Figure 9, this study was approved by Ningbo University's Ethics Committee (Approval Number: RAGH20220608), and all subjects provided and signed written informed consent. Before participating in the formal experiment, all subjects were given a detailed explanation of the experiment's objectives, prerequisites and steps.

宁波大学
NINGBO UNIVERSITY
中国 浙江 宁波市江北区风华路818号 邮编：315211
No 818. Fenghua Road, Ningbo, Zhejiang, China 315211
电话 Tel：(086)-574-87600253
传真 Fax：(086)-574-87604161

The application **"Landing strategy optimization for lower limb injury risk reduction: Combining musculoskeletal modeling and deep learning"** that you submitted to this office in regard to the use of human subjects in the proposal referenced above has been reviewed by the Secretary, the Chair, and two members of the **Ethics Committee of Ningbo University.**

In addition: the research has been approved for the inclusion of human subjects, for waiver of the consent process (for the one being assessed), for a waiver of the assent process (for the one being assessed), for a waiver of the parental permission process (for the one being assessed) and for a waiver of the **Health Insurance Portability and Accountability Act (HIPAA) Research Authorization** (entire research study for the one being assessed).

Date of IRB Approval: Jun, 16, 2022
Date of IRB Approval Expiration: Jun, 16, 2024
Approval Number: RAGH20220608

If applicable, informed consent (and **HIPAA Research Authorization**) must be obtained from subjects or their legally authorized representatives and documented prior to research involvement. The **IRB**-approved consent form and process must be used. Changes in the research (e.g., recruitment procedures, advertisements, enrollment numbers, etc.) or informed consent process must be approved by the **IRB** before they are implemented (except where necessary to eliminate apparent immediate hazards to subjects).

This approval is valid for **two years** from the date of **IRB** review when approval is granted or modifications are required. The approval will no longer be in effect on the date listed above as the **IRB** expiration date. A continuing review application must be approved within this interval to avoid expiration of **IRB** approval and cessation of activities. A final report must be provided to the **IRB** and all records relating to the research (including signed consent forms) must to retained and available for audit for at least 3 years after the research has ended.

It is the responsibility of all investigators and research staff to promptly report to the **IRB** any serous, unexpected and related adverse events and potential unanticipated problems involving risks to subjects or others.

This approval is issued under

Jianshe Li
Chairman of the Ethics Committee of Ningbo University

Ningbo University

Human Informed Consent Form

Instructions to the Student Researcher(s): An informed consent/assent/permission form should be developed in consultation with the Adult Sponsor, Designated Supervisor or Qualified Scientist.
This form is used to provide information to the research participant (or parent/guardian) and to document written informed consent, minor assent, and/or parental permission.

- When written documentation is required, the researcher keeps the original, signed form.
- Students may use this sample form or may copy ALL elements of it into a new document.

If the form is serving to document parental permission, a copy of any survey or questionnaire must be attached.

Student Researcher(s): _____
Title of Project: _____

I am asking for your voluntary participation in my science fair project. Please read the following information about the project. If you would like to participate, please sign in the appropriate area below.
Purpose of the project:

If you participate, you will be asked to:

Time required for participation:

Potential Risks of Study:

Benefits:

How confidentiality will be maintained:

If you have any questions about this study, feel free to contact:

Adult Sponsor/QS/DS: _____ Phone/email: _____

Voluntary Participation:
Participation in this study is completely voluntary. If you decide not to participate there will not be any negative consequences. Please be aware that if you decide to participate, you may stop participating at any time and you may decide not to answer any specific question.
By signing this form I am attesting that I have read and understand the information above and I freely give my consent/assent to participate or permission for my child to participate.

Adult Informed Consent or Minor Assent Date Reviewed & Signed: _____

Research Participant Printed Name: Signature:

Parental/Guardian Permission (if applicable) Date Reviewed & Signed: _____

Parent/Guardian Printed Name: Signature:

Figure 9 The ethics form and human informed consent form.

2.2 Experiments and methods for objective 1

The work procedure is presented in Figure 10, which was mainly divided into four parts: 1) Collect the biomechanics data during the landing phase between before-fatigue and after-fatigue; 2) Build the musculoskeletal model based on Visual 3D (C-Motion Inc., Germantown, US) and OpenSim (Stanford University, Stanford, CA, USA) software to simulate and calculate the ACL force ; 3) Explore the internal relationship between the AIC, AROM and joint energy dissipation, PAF based on the SL patterns difference between before-fatigue and after-fatigue.

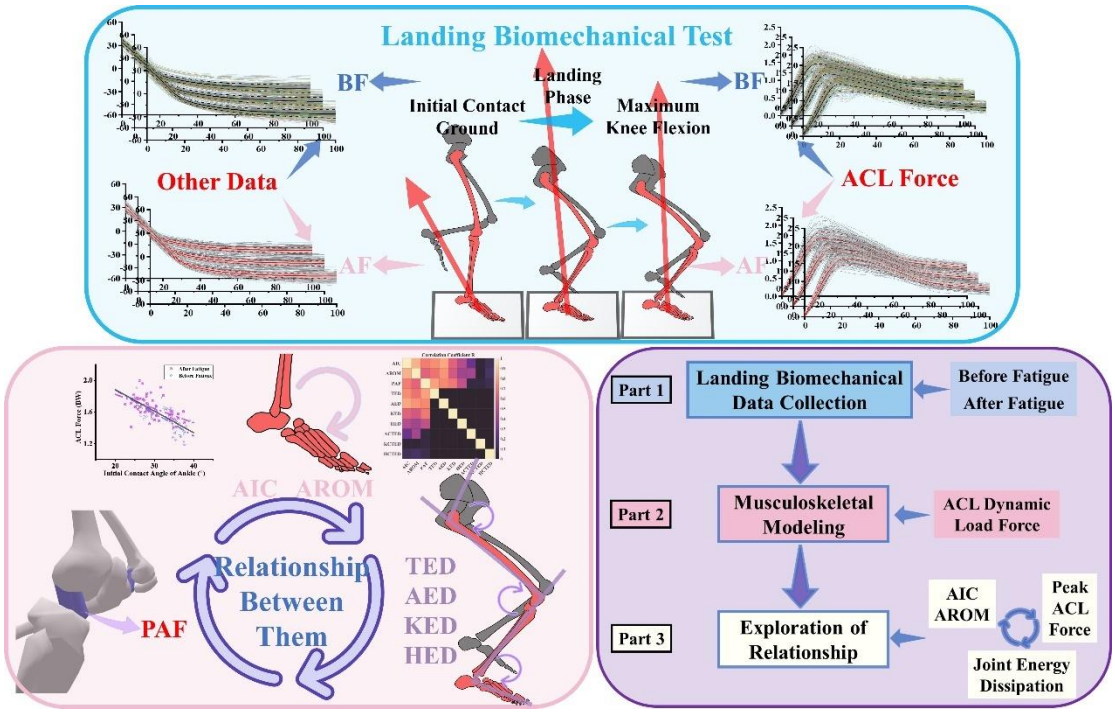

Figure 10 Overview of the whole work procedure of this study.

2.2.1 Participants

A total of 56 healthy male subjects (age: 22.56±5.13 years; body mass: 82.62±13.38 kg; height: 1.85±0.11 m) were recruited for this study. To be eligible, participants had to have no history of severe lower-extremity surgery or any other injury variables that would interfere with the study within the previous six months. The experiment's goals, requirements, and procedures were explained to the participants.

2.2.2 Experimental protocol and procedures

The Vicon motion capture device with 8 infrared cameras (Vicon Metrics Ltd., UK) was used to obtain three-dimensional lower limb joint kinematic data at a 200 Hz sampling frequency. Meanwhile, the ground reaction force (GRF) data were obtained synchronously using a 1000 Hz AMTI force plate installed in the ground (AMTI, Watertown, UAS). This study performed musculoskeletal modeling of the lower limbs based on the pipeline that had been constructed from previous models, by adjusting the built-in parameters to apply with the current study musculoskeletal modeling requirements [78, 149]. Thirty-eight reflective markers were placed on the subject's body to track movement (Figure 11A). Meanwhile, six Electromyographic (EMG) sensors (Delsys, Boston, MA, USA) with 1000 Hz frequency were used to measure the muscle activations. As presented in Figure 11B, six muscles (rectus femoris, vastus medialis, vastus lateralis, tibialis anterior, lateral gastrocnemius, and medial gastrocnemius) were selected to verify the accuracy of the constructed musculoskeletal model based on previous studies [89, 150]. During EMG signal acquisition, this study first treated the skin surface with alcohol cleaning and wiping to ensure that the electrodes could adhere well and record muscle activity accurately [64]. The EMG sensors were then placed jointly by two experimental operators to ensure that their

electrodes were placed in the middle of the target muscle and aligned with the orientation of the muscle fibers [36]. Besides the use of EMG patches, this study used a bandage for secondary fixation of the EMG sensors to ensure that the electrodes would remain stable and in close contact with the muscles. Before starting the formal data acquisition, this study also performed signal testing to ensure that the electrodes were properly placed and could accurately record muscle activity. For the adjacent muscles, such as the soleus and lateral gastrocnemius, two experimental operators simultaneously observed the EMG signal data during the acquisition in real time. For the observed abnormal fluctuation signal, it is considered an acquisition failure, and the acquisition will be carried out after debugging and checking again. The maximal voluntary contraction (MVC) for selected six muscles was also collected to standardize the muscle activation [89].

The experiment was divided into three parts: 1) Landing biomechanical test of BF; 2) Fatigue intervention; 3) Landing biomechanical test of AF (Figure 11C). The BF and AF biomechanical test process was the same. The drop landing was selected as the landing test maneuver, and the whole test process is outlined in Figure 11D. As a general landing test maneuver, drop landing maximizes the revivification of landing properties, and has been used in a large number of studies [6, 19]. The dominant leg was chosen as the analytical limb in this study, and a total of 39 reflective markers (12.5 mm diameter standard) were affixed to the pelvic and lower limb (Figure 11A). The placement of reflective markers in all subjects was performed by the same experimenter and checked by another experimenter. All subjects were required to wear tights, leggings, and uniform shoes, and warmed up for 10 minutes by running at their own pace in the laboratory, then they acquainted themselves with the experimental procedure. After the reflective markers and EMG sensors were affixed, subjects were asked to stand on the force plate in a standard anatomical posture with their feet open, shoulder width apart, arms open to 45° oblique downward, and they were visually ahead and kept motionless until the experimenter completed static data collection.

For the landing biomechanics, a 40 cm high jump platform was placed directly in front of the force plate, and the subject stood on the jump platform with his hands on his hips. After hearing the "begin" signal from the experimenter, the subject moves the dominant leg forward, and leans forward to fall vertically from the jump platform at no initial speed synchronously. Subjects were instructed to land with their dominant leg as close to the center of the force plate as possible, and then land on one leg for support and balance. A successful experiment was defined as the subject's ability to balance on the dominant leg for 3 seconds without any tendency to fall. 5 successful landing trial datasets were collected for each subject both before-fatigue (BF) and after-fatigue (AF) landing test. The subjects rested for at least 30 seconds between each session in landing test of BF, and their heart rates were monitored using a wireless Polar table to ensure their heart rates had recovered before the next testing.

Fatigue intervention was performed immediately after the completion of the BF landing biomechanical test. The current study adopts the continuous close chain action in the whole process to better maintain and control the state of lower extremity muscle fatigue (Figure 11C). All subjects loaded the barbell with their knees bent to 90° to

squat, the weight of the barbell was set to 1/3 of the subject's body weight, and the frequency of squatting was set to 50 times/min [151, 152]. During the fatigue intervention, two experimenters assisted the subjects to carry out the fatigue intervention. The experimenter first selected the barbell plate according to the body weight of the subjects. Then, the experimenter set the metronome at a frequency of 50 times/min, and the subjects performed weight-bearing squats according to the rhythm of the metronome. Throughout the fatigue intervention, the subjects were protected and verbal encouragement was given to keep them going.

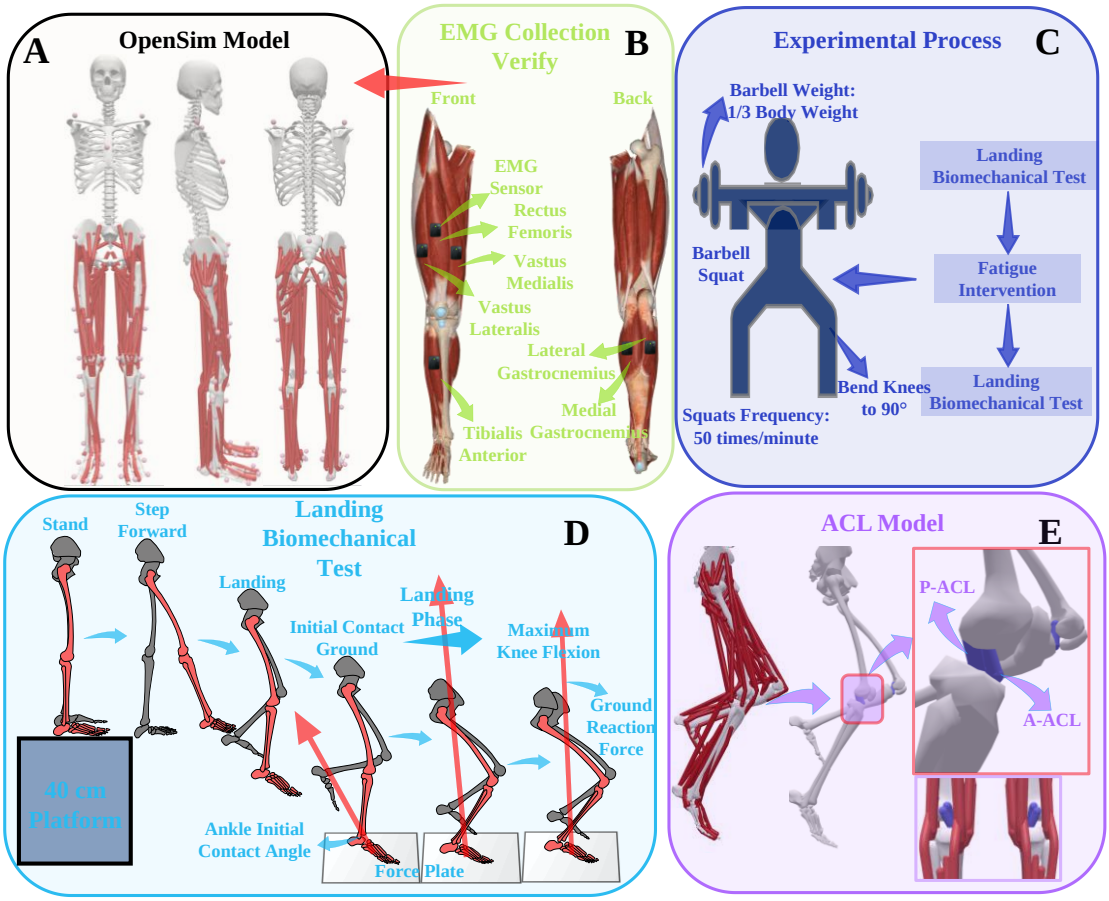

Figure 11 Overview of the musculoskeletal model and whole study experimental procedure. (A) Illustration of the position of the reflective marking points about the constructed musculoskeletal model. (B) Illustration of the position of the EMG test on human lower limbs, which aims to verify the accuracy of the established musculoskeletal model. (C) Illustration of the whole experimental process, which includes three main steps: 1) SL biomechanics test of before-fatigue; 2) Fatigue intervention; 3) SL biomechanics test of after-fatigue. (D) Illustration of the process of SL biomechanics test. The landing phase was from initial contact with the ground to maximum knee flexion. (E) Illustration of the constructed ACL physiological model in OpenSim musculoskeletal model. The ACL was attached to the medial front of the tibial intercondylar eminence and extended to the medial side of the lateral condyle of the femur.

When the subject meets any one of the following three criteria, the subject was considered to be fatigued and can begin the landing test: 1) Subjects cannot complete 2 effective squats or cannot keep up with 4 consecutive squats; 2) According to the session rating of perceived exertion (PRE) to determine the subjects' subjective fatigue. PRE is divided into 6 to 20 levels, level 6 is defined as quiet, and level 20 is defined as very tired [21]. In this study, fatigue was defined as an RPE level above 17 [153]; 3) Heart rate reaches 85% of maximum heart rate, and maximum heart rate was defined as the 220 minus subject's age [15]. The subject's heart rate is monitored in real time to determine if the subject is constantly fatigued.

Landing tests of AF was performed as soon as the subject was determined to be maximally fatigued. The landing test requirements were the same as BF, but there was no rest time between each session in the landing test of AF. Meanwhile, the subjects were asked to perform the squat jump three times in a row between each test to maintain the fatigue effect [154]. The time to complete the landing movement and the immediate heart rate were recorded throughout the test, and the results are shown in Table 1.

Table 1 The physical state of athletes during the experiment.

	Complete time (s)	Heart Rate (times/min)	PRE Level
Landing Tests Before-Fatigue Intervention	287±79.1	82.3±6.9	8.0±0.5
Fatigue Intervention	123.6±23.5	165.6±10.1	17.0±1.5
Landing Tests After-Fatigue Intervention	169.6±68.4	172.3±9.8	17.5±1.1

2.2.3 Data initial collection and processing

Linear envelope is a smoothing technique commonly used in the processing of EMG data to extract the low-frequency trends of the signal and filter out the high-frequency noise to provide a more intuitive representation of the level of muscle activity [108]. In the current study, the linear envelope of the collected EMG raw signal was band-pass filtered with a Butterworth fourth-order filter in the frequency range of 10-400 Hz, followed by full-wave rectification, and finally low-pass filtered with a 6 Hz cut-off frequency (based on the determined most appropriate signal-to-noise ratio). At the same time, the EMG signal was normalized by dividing the EMG amplitude by the maximum root mean square amplitude, which was then divided by MVC to obtain the degree of each muscle activation [89]. Muscle activation level is the degree of muscle contraction during an exercise cycle, usually quantified by an electromyographic signal. It characterizes the degree of muscle engagement and workload during various movements or static postures, reflecting the strength of activation signals sent from the nervous system to the muscle. Finally, the muscle activation results of collecting by the EMG sensor and obtained by musculoskeletal modeling simulation were compared to verify the effectiveness and accuracy of the musculoskeletal model.

Vertical GRF greater than 10N was used to establish the initial contact force point [1, 3]. The landing phase was defined as from the initial contact force point to the

maximum knee flexion [1, 2]. The data was initially processed in Vicon Nexus software: 1) Name the captured reflective markers; 2) fix the missing reflective markers in this stage; 3) delete the redundant and wrong reflective markers. Data were collected for a total of 5 s, including 2 seconds before and 3 seconds following the initial contact with the ground [19].

Then, the exported C3D files from Vicon Nexus were imported into Visual 3D 6.7.3 (C-Motion Inc., Germantown, US) software for further modeling process [89]. In this step, joint kinematics (joint angle) and joint kinetics (joint moment) were calculated by using the built-in inverse kinematics and inverse dynamics algorithms in Visual3D. Based on Winter's study of the selected filter frequency [155], the most appropriate signal-to-noise ratio was determined by carrying out the residual analysis of data in subsets. Based on this, fourth-order zero-phase lag Butterworth low-pass filters with frequencies of 10 and 20 Hz were used to filter the kinematic and kinetic data [155].

Finally, the ankle, knee, hip joints sagittal angle and power, each muscles activation were then imported into MATLAB R2022a (Visual R2022a, MathWorks, United States) to expand into 101 data point curves (0%-100% landing phase). The whole process of data processing was realized by self-written MATLAB scripts.

2.2.4 ACL Modeling and Properties Setting

The processed kinematic and kinetic data were exported in "$.osim$" format via Visual3D and then imported into OpenSim for musculoskeletal modeling to create the ACL physiological model. The lower limbs will have a large impact during the landing phase, especially in the early landing stage, the acceleration and ground reaction force of each segment will change dramatically, resulting in non-convergence in the optimization process. Therefore, several attempts were made to reproduce the landing using the Reduce Residuals Algorithm (RRA) and Computed muscle control (CMC) for each segment. As presented in Figure 11E, the ACL was attached to the medial front of the tibial intercondylar eminence and extended to the medial side of the lateral condyle of the femur. Since the main purpose of the current study to establish the ACL physiological model is to calculate the internal ACL loading forces, it is only necessary to assume that the endpoints are fixed without considering the actual adhesion mechanisms. The structure of the passive soft tissue of the ACL was mainly achieved by inhibiting the activation of the contractile element.

ACL force is determined by the mechanical properties of the ACL, which include its force-strain property and its stiffness (physiological cross-sectional area). The ACL strain varies with the knee valgus angle under different flexion conditions. Based on the simulation results after CMC, it can be seen that ACL strain is a function of knee kinematics, that is, the function of the muscle optimization process. Therefore, this work sets the ratio of passive ACL strain to flexion-extension and varus-valgus angle to 15% by adjusting the ACL material properties of the passive fiber strain at the maximum isometric force [78, 93, 96, 156]. As a maximum tolerance ratio, 15% is reasonable because the range of 9% to 15% has been shown to cause ACL rupture and microfiber damage [96, 157]. If a passive ACL strain characteristic is specified as less than 1% in an individual model, additional adjustments are made to the models to

ensure that the strain limit can be accurately controlled. For the contact area between ligament and bone (junction of ligament together with bones), the maximum strain was limited to 2.5-3.0% to ensure that the isometric force could start from the lowest value in the simulation [93]. The length of bony osteoligamentous (tendons) and ligaments (muscles) will be examined during CMC based on the determined ACL strain when the presence of deformation of the entire muscle-tendon unit [78]. The linear elastic stiffness of the ACL was set at 240 N/mm based on a cadaveric study by Woo et al. on humans aged 22-35 years [157]. The constant stiffness can be specified as a material property, because it is characteristic only in the region of transition from low strain to high stiffness at high strain based on the Gaussian law [78].

2.2.5 Recognition and difference of landing pattern variable Between BF and AF and correlation analysis

This study first needs to reveal the changes in joint energy dissipation and ankle joint movement patterns (AICA and AROM) during after-fatigue SL, and then further determine the relationship between joint energy dissipation and ankle joint movement patterns. Further, based on the relationship between joint energy dissipation and ACL force, the relationship between ankle motion pattern and ACL force was finally deduced. Therefore, this study first extracted and calculated the variable of AIC, AROM, PAF, total energy dissipation of lower limb (TED), ankle energy dissipation (AED), knee energy dissipation (KED), hip energy dissipation (HED), ankle contribution to total energy dissipation (ACTED), knee contribution to total energy dissipation (KCTED), hip contribution to total energy dissipation (HCTED).

The AROM is defined as the difference between the maximum plantarflexion and the dorsiflexion. The joint energy dissipation is the joint negative (eccentric) work, and the joint work was computed by the integral of joint power over time [6]. The joint contribution to total energy dissipation was calculated as the percentage of each joint in the total energy dissipation [6]. The current study only considered joint work in the sagittal plane, as the lower limb energy dissipation is mainly concentrated in the sagittal plane during single-leg landing [6, 12].

For the variables of AIC, ROM, PAF, AED, KED, and HED, this study performed the Paired-samples T-test for the mean value of each sample (112 datasets) to test differences between before-fatigue and after-fatigue. Also, considering the large original dataset (560 original datasets), this study combined machine learning algorithms to determine the recognizability of the two classes of data with each other [46, 158]. Three classical and widely used classification and recognition algorithm models were conducted: 1) Support vector machine (SVM); 2) K-nearest neighbor (KNN); 3) Artificial neural network (ANN). A total of 112 samples dataset ($56_{Before-Fatigue} + 56_{After-Fatigue}$) of each class is randomly distributed uniformly to avoid errors during model training. Meanwhile, the data from the five successful trials for each subject were placed in the same subset during model training to ensure that the model performance was not affected by the same subject's data in different subsets.

Pearson correlation analysis and linear regression analysis were performed to

explore the relationships between them. As presented in Table 2, the interpretation of the correlation was defined according to previous studies [159]. When the correlation coefficient is less than 0.1, it is defined as no correlation.

Table 2 Interpretation of Pearson's correlation coefficients.

Square of the Correlation Coefficient R^2	Interpretation of the Correlation
[0.00, 0.01)	Negligible
[0.01, 0.16)	Weak
[0.16, 0.49)	Moderate
[0.49, 0.81)	Strong
[0.81, 1.00]	Very strong

2.2.6 Classification and recognition algorithm model

SVM has many unique advantages in solving nonlinear, small-sample, high-dimensional data pattern recognition problems. Given training sample set $D = (x_1, y_1), (x_2, y_2), \dots, (x_m, y_m), y_i \in (-1, +1)$, the essence of classification is to find a partition hyperplane in the sample space to separate samples of different categories. For the SVM, the model corresponding to the hyperplane partition in the feature space can be expressed as $f(x) = \omega^T \phi(x) + b$. Where the $\omega = (\omega_1; \omega_2; \dots; \omega_d)$ is the normal vector that determines the direction of the hyperplane; the b is the displacement term, which determines the distance between the hyperplane and the origin; the $\phi(x)$ represents the eigenvectors after the x map. By setting the kernel function $\kappa(x_i, y_i) = \phi(x_i)^T \phi(x_j)$, the support vector expansion can be obtained:

$$f(x) = \omega^T \phi(x) + b = \sum_{i=1}^{m} \alpha_i y_i \phi(x_i)^T \phi(x) + b = \sum_{i=1}^{m} \alpha_i y_i \kappa(x, x_i) + b \quad (1)$$

In this study, the linear kernel functions ($\kappa(x, x_i) = {x_i}^T x_j$) were used to turn the input feature's data into a higher-dimensional space. At the same time, the soft margin idea was used to cope with the possibility of misclassifications. The soft margin should make the samples that do not meet the constraints as small as possible while maximizing the margin, then the optimization objective can be expressed as: $min_{\omega,b,\xi_i} \frac{1}{2}||\omega||^2 + C\sum_{i=1}^{m} \xi_i$. Where the ξ_i is the slack variables, and the C $(C = 1)$ is a regularization constant [160, 161]. For the selection of C values in SVM, it is a balance between model complexity and generalization ability.

K-nearest neighbor (KNN) algorithm was selected as the learning algorithm for fitness evaluation. The KNN was first proposed by Cover and Hart in 1968, and it is mainly used in character recognition, text classification, image recognition, and other fields [162]. The algorithm idea of the KNN is that if a sample is most similar to k samples in the dataset, and most of the K samples belong to a certain category, then the sample also belongs to that category [162, 163]. Let the eigenspace χ be the n-dimensional vector space R^n of real numbers, $x_i, x_j \in \chi \subseteq R^n$, $i = 1,2, \dots, N$, $x_i =$

$(x_i^{(1)}, x_i^{(2)}, \ldots, x_i^{(n)})^T$, $x_j = (x_j^{(1)}, x_j^{(2)}, \ldots, x_j^{(n)})^T$, and the L_p distance of x_i, x_j is defined as:

$$L_p(x_i, x_j) = \left(\sum_{l=1}^{n} |x_i^{(l)} - x_j^{(l)}|^p \right)^{\frac{1}{p}} \quad (2)$$

Where the p is a variable parameter, when $p = 2$ is called the Euclidean distance, that is $L_2(x_i, x_j) = \left(\sum_{l=1}^{n} |x_i^{(l)} - x_j^{(l)}|^2 \right)^{\frac{1}{2}}$. In this study, the Euclidean distance $k = 5$, and the KNN were used since it is a fast, simple and common machine learning algorithm, which also has been widely used in feature selection research [158, 162, 163].

Artificial neural network (ANN) are extensive parallel networks comprised of adaptable basic units whose organization can be used to replicate the interactions of organic nervous systems with real-world objects [164, 165]. In this study, an ANN model with ten hidden layers was created under the condition of repeated model training and adjustment following the actual data, as the application of the ANN model in the current work was primarily skewed to increase the model's accuracy [46, 166]. The layers of the neural network are completely connected, that is, any neuron of the n-th layer must be connected to any neuron of the n+1 layer. Through forward propagation, the linear relation function and activation function continuously calculate the new values in a cycle from layer to layer, and finally obtain the model results. The linear relationship function of the model constructed in this study is: $z = \sum_{i=1}^{m} w_i x_i + b$, where the w_i is the connection weight of the i-th neuron, the x_i is the input from the i-th neuron. Take the input x and run it linearly to get z, and then the Sigmoid ($S = \frac{1}{1+e^{-x}}$) type activation function is used to get a [46].

Take the input x and run it linearly to get z, and then the hyperbolic tangent activation function is used to get a. Therefore, for the output of the 2-th layer, the a_1^2, a_2^2, a_3^2 can be obtained: $a_1^2 = \sigma(z_1^2) = \sigma(w_{11}^2 x_1 + w_{12}^2 x_2 + w_{13}^2 x_3 + b_1^2)$, $a_2^2 = \sigma(z_2^2) = \sigma(w_{21}^2 x_1 + w_{22}^2 x_2 + w_{23}^2 x_3 + b_2^2)$, $a_3^2 = \sigma(z_3^2) = \sigma(w_{31}^2 x_1 + w_{32}^2 x_2 + w_{33}^2 x_3 + b_3^2)$. For the output of the 3-th layer: $a_1^3 = \sigma(z_1^3) = \sigma(w_{11}^3 a_1^2 + w_{12}^3 a_2^2 + w_{13}^3 a_3^2 + b_1^3)$.

Finally, the neural network output a_i^{l+1} of the i-th neuron at layer $l+1$ is:

$$f(x) = a_i^{l+1} = \sigma(z_i^{l+1}) = \sigma\left(\sum_i a_i^{(l)} w_{ij}^{(l,l+1)} + b_j^{(l+1)} \right) \quad (3)$$

Where i is a neuron at the layer $l+1$, the $\sum_i \ldots$ runs over all lower layer neurons that are connected to neuron j, the $w_{ij}^{(l,l+1)}$, $b_j^{(l+1)}$ are specific parameters to pairs of adjacent neurons. The node of the input layer was determined according to the number of input features, the node of the hidden layer was determined according to the group number of input data, and the node of the output layer was determined based on the number of classes, and batch size was set as the 25, the max epoch was set to 3000

[46, 55, 165]. For the hidden layer setting of the ANN, its impact on the model performance was determined based on the experimental results.

The eight-fold cross-validation was used in all classification algorithms. The data were randomly divided into eight parts, and then six of them were selected as the training set, one of them was selected as the validation set, and the remaining parts were used as the test set, repeating a total of eight times [167, 168]. The final accuracy results obtained are based on the results generated from these eight training sessions, which greatly increases the accuracy of the results [167, 168]. ALL the classification algorithm implementation by self-written scripts based on the built-in function packages in MATLAB R2022a.

2.3 Experiments and methods for objective 2

The flow diagram of the whole study procedure is shown in Figure 12, which is mainly divided into three parts. This study selected two class landing datasets as the study input data, which were the single-leg landing between before fatigue intervention and after fatigue intervention (Figure 12A). Firstly, three classical and widely used classification and recognition algorithm models (SVM: Support Vector Machine; ANN: Artificial Neural Network; CNN: Convolutional Neural Network) were selected for automated landing pattern classification tasks based on the three-dimensional kinematics and kinetics data of landing leg during the landing phase (Figure 12B). At the same time, the ZeroR baseline was also computed by the ZeroR classifier for each classification task to verify the recognizability between classes. The classification task focuses on the recognizability of the differences between before fatigue and after fatigue landing patterns. Landing patterns represent the landing trends that subjects exhibit throughout the landing phase, which are usually specifically quantified by three-dimensional biomechanical data of the lower limbs.

Secondly, the ANN with the best performance in classification and recognition accuracy between classes was used as the forward propagation classifier, and the output of the ANN was used as the input of Layer-wise Relevance Propagation (LRP) to calculate the relevance score (RS) that can explain the difference of landing patterns through backward propagation (Figure 12C). The relevance scores were used to determine the degree to which each joint contributed to the differences in recognizing landing patterns in each plane, that is, interpretable results on the recognizability of the differences between before fatigue and after fatigue landing patterns. After that, these results were evaluated from the statistical perspective (Figure 12D) based on the approach of one-dimensional statistical parametric mapping (1d-SPM). Finally, the results of these two aspects were evaluated and discussed together (Figure 12E).

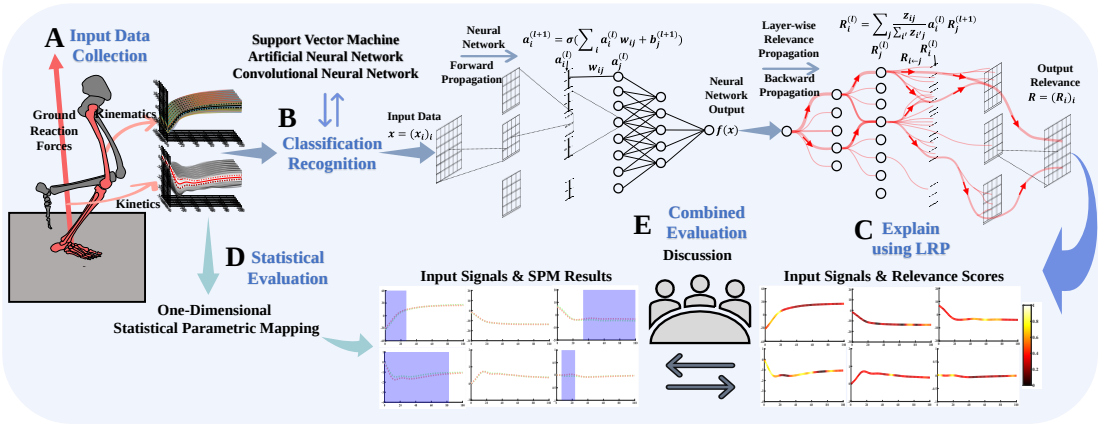

Figure 12 Overview of the proposed workflow for data collection, classification, and explanation in automated landing pattern recognition. (A) The single-leg landing movements of the subjects before and after the fatigue intervention were collected, and the three-dimensional kinematics and kinetics data of the landing leg during the landing phase were used as the input data of the model. (B) The three-dimensional kinematics and kinetics data as input signals to explore the recognizability of the two

class landing patterns by three classical classification and recognition algorithm models and ZeroR classifier. (C) The ANN with the best performance in classification and recognition accuracy between classes was used as the forward propagation classifier to compute the input signals, and the output signals of ANN were used as the input of LRP to calculate the RS that can explain the difference of landing patterns through backward propagation. (D) The application of 1d-SPM to evaluate the LRP results from a statistical perspective. (E) The results of these two aspects were evaluated and discussed together.

2.3.1 Landing pattern data

In landing movements, a large number of studies have shown that muscle fatigue will increase the risk of lower limb musculoskeletal injury during landing [14, 18, 64, 169]. In particular, the risk of lower extremity injury is generally increased in single-leg landings and can be detected from more pronounced changes in biomechanical data [1, 9, 64, 169]. In other words, single-leg landing may be more difficult to maintain a safe state of the lower extremity than double-leg landing, thereby more effectively identifying risky biomechanical patterns [30]. Thus, a highly recognizable difference in landing pattern can be expected for single-leg landing between before and after fatigue intervention. At the same time, predictive explainability analysis can also be carried out on the formation of injury risk and the results of injury factors based on the differences in this landing pattern. Therefore, this study collected the single-leg landing movements of the subjects before and after the fatigue intervention, and the three-dimensional kinematics and kinetics data of the landing leg during the landing phase were used as the input signals of the algorithms model. A total of 56 healthy male subjects (age: 22.56±5.13 years; body mass: 82.62±13.38 kg; height: 1.85±0.11 m) were recruited for this work to collect landing data before and after fatigue.

This study complies with the principles laid down in the Declaration of Helsinki. Ningbo University's Ethics Committee has accepted the study protocol (Approval Number: RAGH20210120), and all subjects supplied and signed written informed permission. Further details about landing data acquisition are provided in **Section 2.2**. Finally, the data matrices of landing pattern were obtained as follow:

(1) $M_{before\ fatigue} = 280(56_{subjects} \times 5_{trials}) \times 202(101_{kinematics} + 101_{kinetics}) \times 9(3_{joint} \times 3_{plane})$;

(2) $M_{after\ fatigue} = 280(56_{subjects} \times 5_{trials}) \times 202(101_{kinematics} + 101_{kinetics}) \times 9(3_{joint} \times 3_{plane})$.

2.3.2 Data classification

The main purpose of automated landing pattern classification is to detect high and low recognizability between different classes. To identify the single weights of each joint, each plane, kinematics, and kinetics in landing pattern recognition, the current study divides the input signal of the classification task into 9 algorithmic situations:

1) Both kinematics and kinetics signals: $M1_{before\ fatigue} = 280(56_{subjects} \times 5_{trials}) \times 202(101_{kinematics} + 101_{kinetics}) \times 9(3_{joint} \times 3_{plane})$, $M1_{after\ fatigue} = 280(56_{subjects} \times 5_{trials}) \times 202(101_{kinematics} + 101_{kinetics}) \times 9(3_{joint} \times 3_{plane})$;

2) Only kinematics signal: $M2_{before\ fatigue} = 280(56_{subjects} \times 5_{trials}) \times 101_{kinematics} \times 9(3_{joint} \times 3_{plane})$, $M2_{after\ fatigue} = 280(56_{subjects} \times 5_{trials}) \times 101_{kinematics} \times 9(3_{joint} \times 3_{plane})$;

3) Only kinetics signal: $M3_{before\ fatigue} = 280(56_{subjects} \times 5_{trials}) \times 101_{kinetics} \times 9(3_{joint} \times 3_{plane})$, $M3_{after\ fatigue} = 280(56_{subjects} \times 5_{trials}) \times 101_{kinetics} \times 9(3_{joint} \times 3_{plane})$;

4) Only ankle joint signal: $M4_{before\ fatigue} = 280(56_{subjects} \times 5_{trials}) \times 202(101_{kinematics} + 101_{kinetics}) \times 1_{ankle\ joint} \times 3_{plane}$, $M4_{after\ fatigue} = 280(56_{subjects} \times 5_{trials}) \times 202(101_{kinematics} + 101_{kinetics}) \times 1_{ankle\ joint} \times 3_{plane}$;

5) Only knee joint signal: $M5_{before\ fatigue} = 280(56_{subjects} \times 5_{trials}) \times 202(101_{kinematics} + 101_{kinetics}) \times 1_{knee\ joint} \times 3_{plane}$, $M5_{after\ fatigue} = 280(56_{subjects} \times 5_{trials}) \times 202(101_{kinematics} + 101_{kinetics}) \times 1_{knee\ joint} \times 3_{plane}$;

6) Only hip joint signal: $M6_{before\ fatigue} = 280(56_{subjects} \times 5_{trials}) \times 202(101_{kinematics} + 101_{kinetics}) \times 1_{hip\ joint} \times 3_{plane}$, $M6_{after\ fatigue} = 280(56_{subjects} \times 5_{trials}) \times 202(101_{kinematics} + 101_{kinetics}) \times 1_{hip\ joint} \times 3_{plane}$.

7) Only ankle joint signal: $M7_{before\ fatigue} = 280(56_{subjects} \times 5_{trials}) \times 202(101_{kinematics} + 101_{kinetics}) \times 1_{Sagittal\ plane} \times 3_{joint}$, $M7_{after\ fatigue} = 280(56_{subjects} \times 5_{trials}) \times 202(101_{kinematics} + 101_{kinetics}) \times 1_{Sagittal\ plane} \times 3_{joint}$;

8) Only ankle joint signal: $M8_{before\ fatigue} = 280(56_{subjects} \times 5_{trials}) \times 202(101_{kinematics} + 101_{kinetics}) \times 1_{Frontal\ plane} \times 3_{joint}$, $M8_{after\ fatigue} = 280(56_{subjects} \times 5_{trials}) \times 202(101_{kinematics} + 101_{kinetics}) \times 1_{Frontal\ plane} \times 3_{joint}$;

9) Only ankle joint signal: $M9_{before\ fatigue} = 280(56_{subjects} \times 5_{trials}) \times 202(101_{kinematics} + 101_{kinetics}) \times 1_{Transversal\ plane} \times 3_{joint}$, $M9_{after\ fatigue} = 280(56_{subjects} \times 5_{trials}) \times 202(101_{kinematics} + 101_{kinetics}) \times 1_{Transversal\ plane} \times 3_{joint}$;

At the same time, to ensure that the results of the LRP interpretation method employed after classification can be directly mapped to the original signal, the input signal was directly inputted into the classification model in this study. This was also done to better interpret the LRP results, thus not using techniques such as principal component analysis (PCA), which is commonly used in feature extraction and automatic pattern classification [33, 55, 170, 171].

For the nine input signals of the classification task, a total of three classical and widely used classification and recognition algorithm models were used in this study (SVM, ANN, CNN), which aims to give a more complete view of the problem under investigation and to make it possible to distinguish between task-specific and generic observations. The sample datasets of each task were randomly distributed uniformly to avoid errors during model training. Meanwhile, the data from the five successful trials for each subject were placed in the same subset during model training to ensure that the model performance was not affected by the same subject's data in different subsets. The eight-fold cross-validation was used in all classification algorithms. The data were randomly divided into eight parts, and then six of them were selected as the training set, one of them was selected as the validation set, and the remaining parts were used as the test set, repeating a total of eight times [167, 168]. The final accuracy results obtained are based on the results generated from these eight training sessions, which greatly increases the accuracy of the results [167, 168]. All the classification algorithm

implementation were by self-written scripts based on the built-in function packages in MATLAB R2022a. Further details about description of ANN, SVM classification methods are provided in **Section 2.2.6**.

For CNN, in neural networks, "weight sharing" is a strategy for saving training overhead by having a group of neurons use the same connection weights, and this strategy plays an important role in CNN [172, 173]. CNN is a feed-forward neural network, mainly inspired by natural biological visual cognitive mechanisms, which consists of the convolutional layer, pooling layer, and fully connected layer [172]. The current study processes the input signal by composing three successive convolutional and pooling layers, and then implements a mapping to the output target in a fully connected layer. Each convolutional layer contains multiple feature maps, each of which is a 'plane' of multiple neurons that extract a feature of the input through a convolutional filter. The Rectified Linear Unit was used as the activation function, the top of the fully connected layers activated using a SoftMax output, with the filter size and stride configuration of 1-4, and the number of filters in the convolutional layer was set to 32.

The dataset of each class is randomly distributed uniformly to avoid errors during model training. Meanwhile, the data from the five successful trials for each subject were placed in the same subset during model training to ensure that the model performance was not affected by the same subject's data in different subsets. The eight-fold cross-validation was used in all classification algorithms. The data were randomly divided into eight parts, and then six of them were selected as the training set, one of them was selected as the validation set, and the remaining parts were used as the test set, repeating a total of eight times [167, 168]. The final accuracy results obtained are based on the results generated from these eight training sessions, which greatly increases the accuracy of the results [167, 168]. For each classification task, this study also computed the Zero-R baseline (ZRB). ZRB is the theoretical accuracy resulting from assigning class labels based on the prior probability of the class. For ZRB, the targeted label is always set to the class with the largest base in the training dataset [49].

2.3.3 Prediction explanation

In this study, only the LRP analyzed with the ANN algorithm model is provided since it consistently outperformed SVM and CNN algorithm model in terms of classification performance, and because its computational efficiency is relatively high. The complexity of neural networks comes from the interconnection of a large number of basic units, and its output is obtained by feedforward evaluation of these neurons. As shown on the right side of **Figure 12C**, the RS that can explain the pattern recognition results is calculated by backward propagation, based on the local redistribution rule:

$$R_i^{(l)} = \sum_j \frac{z_{ij}}{\sum_{i'} z_{i'j}} a_i^{(l)} R_j^{(l+1)} \qquad (4)$$

and the $z_{ij} = x_i^{(l)} w_{ij}^{(l,l+1)}$, where the i is a neuron at the layer $l+1$, the $\sum_j \ldots$ runs over all upper layer neurons that are connected to neuron i. In general, LRP can compute the contribution of each feature to the classification result for dataset x, and

the degree of such contribution can be reliably assessed to a certain extent (Each input feature $x(d)$ contributes to a particular prediction $f(x)$, where d is the input data of $x(d)$ function). The l-th layer is modeled as a vector $z = \left(z_d^l\right)_{d=1}^{V(l)}$ with dimensionality $V(l)$. For each dimension $z_d^{(l+1)}$ of vector z at layer $l+1$, LRP has an RS $R_d^{(l+1)}$. Each dimension z_d^l of vector z towards the next layer l of the input layer contains an RS $R_d^{(l)}$.

$$f(x) = \cdots = \sum_{d \in l+1} R_d^{(l+1)} = \sum_{d \in l} R_d^{(l)} = \cdots = \sum_d R_d^{(1)} \quad (5)$$

The message $R_{i \leftarrow j}^{(l,l+1)}$ between neuron i and j represents the inter-hierarchical relevance, and these messages can be delivered along with each connection. The output $f(x)$ is then backward propagated from one neuron to the next. The sum of incoming messages defined the relevance of neurons, and the sum runs over the sinks at layer $l+1$ for a fixed neuron i at a layer l:

$$R_j^{(l)} = \sum_{k:\, i \text{ is input for neuron } j} R_{i \leftarrow j}^{(l,l+1)} \quad (6)$$

The next neuron's input is directed in the direction specified during classification, then the total is computed over the sources at layer l for a fixed neuron k at layer $l+1$. In general, it can be expressed as:

$$R_k^{(l+1)} = \sum_{i:\, i \text{ is input for neuron } k} R_{i \leftarrow k}^{(l,l+1)} \quad (7)$$

The relevance of the linear network $f(x) = \sum_i z_{ij}$ is $R_j = f(x)$, and the straightforward decomposition by $R_{i \leftarrow j} = z_{ij}$. Through two monotone increasing functions (rectification function and hyperbolic tangent function), the pre-activation function z_{ij} gives a reasonable method for determining the relative contribution of each neuron's x_i to R_j. The association decomposition is chosen based on the proportion of local and global pre-activation:

$$R_{i \leftarrow j}^{(l,l+1)} = \frac{z_{ij}}{z_j} * R_j^{(l+1)} \quad (8)$$

According to the $Eq.8$, through summing the correlations of all neurons in the upper layer i (combined $Eq.6$ and $Eq.7$), the overall relevance of all neurons in the following layer j can be determined:

$$R_i^{(l)} = \sum_j R_{i \leftarrow j}^{(l,l+1)} \quad (9)$$

The relevance propagates from the upper layer to the lower layer till it attains the input feature $x(d)$, where the hierarchical eigen-decomposition necessary for the

choice $f(x)$ is provided by the relevance $R_d^{(1)}$. More information is available in the previous study [54, 174]. Overall, LRP determined the RS between each variable and the model predicted results, and standardized the RS of LRP derived to their respective values for comparison. The average of all relevant modes was rectified by calculating the smoothing, where the previous and next points were weighted by 25% and the current point was weighted by 50% (total weight is 100%). The input landing pattern-related data was collected in the time domain, its adjacent values depend on each other, so applying the smoothing process can reduce the calculated RS fluctuation without affecting the general pattern [46]. The entire smoothing process was repeated three times (by Gaussian Filter) before scaling the smoothed correlation pattern to 0 (indicates the lowest correlation) - 1 (indicates the highest correlation). In this study, the algorithm implementation by self-written scripts was based on the LRP toolbox in MATLAB R2022a [175].

2.3.4 Statistical evaluation

In this study, Statistical Parametric Mapping (SPM) was used to evaluate the LRP results (derived RS), which has recently been widely used in the field of landing and gait analysis [1, 6, 89, 176]. SPM is a technique for conducting time series statistical analysis of continuous data collected over a period of time [62, 177]. Throughout the full performance, it can test and examine statistical differences in data that change over time. A comprehensive and objective statistical result is obtained through statistical analysis of the oversimplified vector trajectory, which can factually instruct the investigation of complex biomechanical structures [177]. The primary benefits of SPM are the presentation of statistical data in the original sampling space and the absence of the parameterization procedure [62, 177]. As SPM is entirely data-centric relative to interpretable machine learning algorithms, and the output results of SPM and LRP are both based on the same input signal space, it is entirely appropriate to use SPM as a model-independent method to assess the quality of LRP-derived results [49].

For the implementation of SPM, the open-source MATLAB script (paired-samples T-test) of One-Dimensional SPM (SPM 1D) was employed to test the statistical differences, and the significance threshold was set as 0.05 [62, 177]. The output of the SPM provides t-values for each time point of the explored one-dimensional time series input signal, as well as the time series interval corresponding to the determined significance threshold. A t-value above the significance threshold indicates that the difference in the corresponding part of the time series is statistically significant (as shown in the blue shaded part corresponding to Figure 4A, Figure 5A, and Figure 6A). In addition, the effect size was calculated by transforming the obtained t-values to the r of Pearson's correlation coefficient based on Rosenthal's study [178]. The effect size is independent of the significant size and is divided into three regions to provide an indicator to distinguish a given signal [179].

2.3.5 Clinical evaluation

To evaluate LRP-derived RS from a clinical perspective, a clinical expert with

nearly 20 years of experience in analyzing lower extremity landing injuries analyzed explainability results. Based on his own clinical experience, this expert assessed to what extent these areas with high RS were located matched the biomechanical data characteristics in clinical practice. On the one hand, the clinical experts analyzed the results using the LRP model and statistical analysis; on the other hand, they focused on the subjects' specific performance and joint changes during the drop test to compare the differences in the results.

2.4 Experiments and methods for objective 3

2.4.1 Subjects

Based on the results of previous experiments, 60 subjects were selected to cover a population of people with different physiological characteristics, ensuring statistical efficacy and representative results. Consequently, 60 healthy male subjects were recruited for this experiment, and their anthropometric parameters are: age 22.43±5.02 years, height 1.84±0.12 m, and body mass 81.93±12.81 kg. Subjects were screened based on 1) no history of serious lower limb surgery within the past 6 months; 2) no other injury variables that would affect the study; 3) no other problems that would affect sports performance. This study informed the subjects in advance of the experiment's purpose, requirements and procedures, and they signed the written informed consent form. The Ethics Committee of Ningbo University approved the study protocol.

2.4.2 Experimental protocol and procedures

Experiments were conducted in the biomechanics laboratory of Ningbo University. The instrument has a motion capture device with eight-camera (Vicon Metrics Ltd., UK), a wireless Electromyographic (EMG) with sixteen-channel (Delsys, Boston, MA, USA), and two force plates (AMTI, Watertown, USA), and the sampling frequencies were set as 200 Hz, 1000 Hz, and 1000 Hz, respectively. The current study carried out a lower limbs musculoskeletal modeling based on the pipeline constructed from previous models [36, 64, 77, 78]. This musculoskeletal model was mainly constructed and developed based on the 2392 generic musculoskeletal model [78, 89]. The current model contains a total of five main joints of the lower extremity (hip, knee, ankle, subtalar, and metatarsophalangeal joints), 10 rigid bodies, and 90 musculotendon actuators. Among them, the hip, knee and ankle joints have three degrees of freedom (DOF), and the subtalar joint and metatarsophalangeal joint only have sagittal plane DOF. For the 90 musculotendon actuators, based on the 92 musculotendon actuators of the 2392 model, 6 musculotendon actuators near the spine of the upper limbs were removed, and 4 ACL musculotendon actuators from the left and right knees were added.

As shown in Figure 13, thirty-eight reflective markers were placed on the body to track movement (Figure 13A), and ten wireless EMG sensors were used for the surface EMG signal acquisition (Figure 13B). During EMG signal acquisition, this study first treated the skin surface with alcohol cleaning and wiping to ensure that the electrodes could adhere well and record muscle activity accurately [64]. The EMG sensors were then placed jointly by two experimental operators to ensure that their electrodes were placed in the middle of the target muscle and aligned with the orientation of the muscle fibers [36]. Besides the use of EMG patches, this study used a bandage for secondary fixation of the EMG sensors to ensure that the electrodes would remain stable and in close contact with the muscles. Before starting the formal data acquisition, this study also performed signal testing to ensure that the electrodes were properly placed and could accurately record muscle activity. For the adjacent muscles, such as the soleus and lateral gastrocnemius, two experimental operators simultaneously observed the EMG signal data during the acquisition in real time. For the observed abnormal fluctuation signal, it is considered an acquisition failure, and the acquisition will be

carried out after debugging and checking again.

For these ten muscles, the corresponding maximal voluntary contraction (MVC) was also collected to calculate the muscle activation [89]. The placement of reflective markers was conducted by the same experimenter for all subjects and checked by a different experimenter. All subjects were required to wear leggings and uniform shoes. After the warm-up (run at their own pace for 10 minutes), the subjects were familiarized with the experimental procedures. Once the reflective markers and EMG sensors were attached, subjects were required to stand in a standard anatomical position on the force plate with their feet open, shoulder width apart and arms open to 45° diagonally downwards, and they were visually ahead and kept motionless until the experimenter completed static data collection.

The whole test process of the SL biomechanics test is outlined in Figure 13C. A 40 cm high jump platform was placed directly in front of the force plate, and the subject stood on the jump platform with his hands on his hips. After hearing the "begin" signal from the experimenter, the subject moves the dominant leg forward, and leans forward to fall vertically from the jump platform at no initial speed synchronously. All subjects were asked to try their best to pause briefly for half a second after leaning forward to ensure no initial velocity while falling from the platform. This study determined it in the Vicon Nexus software by observing the real-time spatial displacement changes of the medial and lateral ankle reflective markers. When the reflective marker is observed to have no obvious displacement change for 100-time points (0.5 seconds), the landing test is considered valid. Subjects were instructed to land with their dominant leg as close to the center of the force plate as possible, and then land on one leg for support and balance. A successful experiment was defined as the subject's ability to balance on the dominant leg for 3 seconds without any tendency to fall. 5 successful landing trial datasets were collected for each subject. The subjects rested for at least 30 seconds between each session in the landing test.

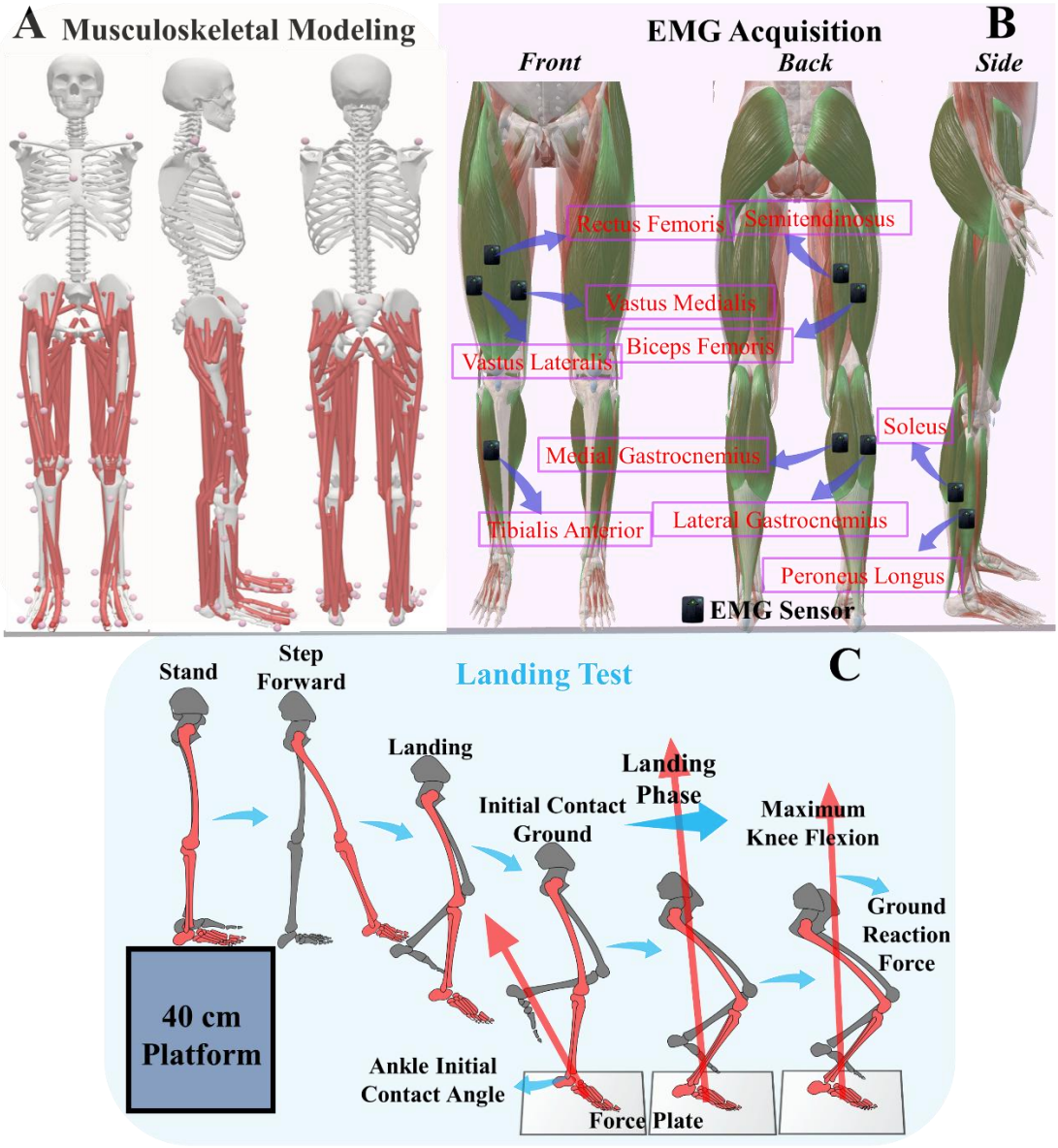

Figure 13 Overview of the data collection and the ACL model. (A) Illustration of the reflective mark's position about the updated musculoskeletal model. (B) Illustration of the surface EMG test's position on lower limbs. (C) Illustration of the process of SL biomechanics test.

2.4.3 Data initial processing and collection

The data of the landing phase from the initial contact force point (VGRF > 10N) to the maximum knee flexion was selected for analysis [2, 3]. Firstly, the data was processed in Vicon Nexus software: 1) name the captured reflective markers; 2) fix the missing reflective markers; 3) delete the redundant and wrong reflective markers. After that, the exported C3D files from Vicon Nexus were imported into Visual 3D 6.7.3 (C-Motion Inc., Germantown, US) software for the further modeling process. The joint kinematics and joint kinetics were calculated by using the built-in algorithms in Visual 3D. In the specific modeling, this study determined the anatomical bone position of the subject through the reflective marker points [1]. By combining the input height and

weight, this study can determine the specific rigid segment ratio for each subject. In the calculation process, lower limb joint angles and angular velocities were calculated based on the collected data of displacement changes of reflective marker points in space over time. In conjunction with the synchronized collected ground reaction force data, an inverse dynamics algorithm then calculated the joint reaction forces and joint moments. The joint power is defined as the product of the joint moment and the joint angular velocity [19].

Based on the calculated most appropriate signal-to-noise ratio, the fourth-order zero-phase lag Butterworth low-pass filters with frequencies of 10 and 20 Hz were conducted to filter the kinematic and kinetic data [19, 46]. Among them, each joint energy dissipation (joint negative/eccentric work) was calculated by the integral of joint power over time [6]. The total energy dissipation (TED) was defined as the sum of ankle, knee and hip joint energy dissipation. This work only considered joint energy dissipation in the sagittal plane, as the lower limb energy dissipation is mainly concentrated in the sagittal plane during SL [6, 19].

The EMG activation results were obtained from the EMG sensors, which were compared with the results obtained by OpenSim to validate the musculoskeletal model [64, 180]. First, the raw EMG signals were processed firstly by band-pass filtering with a Butterworth fourth-order filter (frequency range of 10-400 Hz). Then, the full-wave rectification was conducted. Based on the determined most appropriate signal-to-noise ratio, the low-pass filtered with a 6 Hz cut-off frequency was performed [64, 149]. The raw EMG signals were processed firstly by band-pass filtering with a Butterworth fourth-order filter (frequency range of 10-400 Hz). Then, the full-wave rectification was conducted. Based on the determined most appropriate signal-to-noise ratio, the low-pass filtered with a 6 Hz cut-off frequency was performed [149]. EMG signal was normalized by dividing the maximum EMG amplitude of maximal voluntary contraction (MVC) by the maximum root mean square amplitude to obtain the normalized signal $e_i(t)$. This study used a recursive non-linear model (second-order differential equation) to solve the muscle activation $a_i(t)$ by the obtained normalized signal $e_i(t)$ [36, 126, 180]. First, this study used the normalized signal $e_i(t)$ to solve the neural activation:

$$u_i(t) = \alpha e_i(t-d) - \beta_1 u_i(t-1) - \beta_2 u_i(t-2) \qquad (10)$$

Where the t represents the activation time point, and the $u_i(t)$ was related to the previous activations: $u_i(t-1)$, $u_i(t-2)$. The electromechanical delay d to be 10 milliseconds, and α, $\beta_1 = C_1 + C_2$, $\beta_2 = C_1 \times C_2$ ($|C_1| < 1$, $|C_2| < 1$) are the coefficients defining the second-order dynamics [36]. These parameters map $e_i(t)$ to $u_i(t)$, which is the key to forming a stable equation, and must satisfy the conditions $\alpha = 1 + \beta_1 + \beta_2$. Then, the muscle activation $a_i(t)$ was solved by the non-linear model [36, 126]:

$$a_i(t) = \frac{e^{A_i u_i(t)} - 1}{e^{A_i} - 1} \qquad (11)$$

Where the A_i is set to 1.5, which is the nonlinear shape coefficient and represents the degree of nonlinearity of the neural activation $u_i(t)$ and muscle activation $a_i(t)$ [36, 180]. All data were imported into MATLAB (Visual R2022a, MathWorks, United

States) to expand into 101 data point curves (0%-100% landing phase) by self-written MATLAB scripts.

2.4.4 Nonlinear ACL model creation and property setting

When evaluating the mechanism of ACL injury, the traditional ACL model primarily sets ligaments as having linear force-length characteristics and considers them independent of strain rate [77-79]. However, as dense connective tissue (DCT), ligaments are characterized by short-term viscoelastic strain, which affects their force-length characteristics [78, 80]. In order to more realistically revert and simulate the ACL injury mechanics, this study developed a knee musculoskeletal model that reverts the ACL ligament to a nonlinear short-term viscoelastic mechanical mechanism (strain rate-dependent) generated by the DCT as a function of strain. By implementing the structural constitutive model, this study calculated the compressive stress on the ligament at different strains [80, 81]. As presented in Figure 14, this study developed a graphical user interface (GUI) for OpenSim based on App Designer in MATLAB to assess the ligament material parameters. Meanwhile, ligament elongation and DCT forces were calculated based on the muscle and force analysis tools in the OpenSim analysis toolbox (Figure 14A). Considering the short-term viscoelastic behavior of ligament DCTs, the current study fits a sixth-order polynomial equation in the GUI to calculate the material parameters [80, 81]. The coefficient matrix $\bar{p}_{m,n}$ of this sixth-order polynomial equation is represented as follows:

$$\bar{p}_{m,n} = \frac{\sum_{m=1}^{K} p_{m,n}}{L} \ (n = 1, 2, \dots m) \quad (12)$$

Where the K is the sample size for this coefficient matrix equation, and the L is the number of coefficients. The coefficient matrix result is calculated from the coefficient term $p_{m,n}$ for each sample n. This study created a *C++* library (containing the $equation.h$ and $equation.cpp$ files) through the Win64 *C++* compiler to build and simulate the proposed intrinsic model of the ligament structure. In this process, an adaptive product algorithm is used to solve the numerical integration [181]. Build the NNL class in Visual Studio (Microsoft Ltd. 2017) and then create the NLSR.dll and NLSR.lib folders in the OpenSim plugin to register the NLL class into the OpenSim GUI. Based on the constructed structural constitutive model, this work inputs the material parameters and mechanical parameters of the ligament DCT in the GUI to define the properties of the DCT bundle (Figure 14B). Finally, the nonlinear characteristic strains and internal loading forces of the ligament under different strains were calculated based on the analysis tools in OpenSim.

The ACL length was defined as the resting length L_r based on the state when the knee was in the neutral position, and the extended length of the ACL when the knee was flexed during SL was defined as L_e, and the ligament strain was calculated by the percentage of L_e to L_r:

$$\varepsilon_s = \frac{L_e - L_r}{L_r} \quad (13)$$

Among them, there is a "ligament-class" property in OpenSim, which means that there is a defect in that the extension length cannot be calculated during the dynamic

simulation of SL [78]. Therefore, in this study, the instantaneous strain rate (ISR) $\dot{\varepsilon}$ was calculated by differentiating the strain with respect to time [80]:

$$\dot{\varepsilon} = \frac{d\varepsilon_s}{dt} \qquad (14)$$

Then, by assuming that the mean axial direction of the ACL collagen fibers is parallel to the loading direction of the stress (F_a), the probability density function defining the fiber orientation under the orientation coefficient m of the collagen fibers is:

$$R(m) = \delta(m - F_a) \qquad (15)$$

Where δ is the Dirac delta function. Constructing computational functions for nominal axial stress based on strain and strain rate [80, 81]:

$$\sigma_{af} = -p\lambda^{-1} + \sigma_e(\lambda) + \sigma_v\left(\lambda, \dot{\lambda}\right) \qquad (16)$$

The boundary conditions are set to no traction, that is, the pressure term p is equal to 0 [81]. The λ represents the ratio of ligament extension length L_e relative to resting length L_r: $\lambda = \frac{L_e}{L_r}$. And, the σ_e is the elastic stress generated in the collagen fibers of the ligament:

$$\begin{cases} \sigma_e(\lambda) = \int_1^{\lambda} R(\lambda_s)\overline{\sigma_e}\left(\frac{\lambda}{\lambda_s}\right)d\lambda_s \\ \overline{\sigma_e}(\lambda) = K\ln\lambda \end{cases} \qquad (17)$$

Where the $\overline{\sigma_e}$ is the elastic stress generated in each collagen fiber of the ligament. $R(\lambda_s)$ represents the probability density function of the fiber activity density of the ligament in the stretched state (λ_s). K is a constant, taken as 70 MPa, which is used to represent the collagen fiber's elastic modulus [182]. The σ_v is the viscous stress generated in the collagen fibers of the ligament:

$$\begin{cases} \sigma_v(\lambda) = \int_1^{\lambda} R(\lambda_s)\overline{\sigma_v}\left(\frac{\lambda}{\lambda_s}, \frac{\dot{\lambda}}{\lambda_s}\right)d\lambda_s \\ \overline{\sigma_v}\left(\lambda_r, \dot{\lambda_r}\right) = \eta\frac{D}{D_t}(\ln\lambda_r) \end{cases} \qquad (18)$$

Where λ_r is the stretch ratio of λ and λ_s, the η represents the absolute viscosity coefficient, taken as 20 MPa/S [182]. The term $\frac{D}{D_t}$ represents the time derivative of matter. Therefore, combining *Eqs.* 16, 18, and 19, the following equation can be obtained:

$$\sigma_{af} = \int_1^{\lambda} R(\lambda_s)\left\{K\ln\frac{\lambda}{\lambda_s} + \eta\frac{D}{D_t}\left(\ln\frac{\lambda}{\lambda_s}\right)\right\}d\lambda_s \qquad (19)$$

Based on previous studies [80, 81, 182, 183], distribution functions were used to solve for the uncoiled stretch of collagen fibers to obtain the probability distribution of their unwinding $R(\lambda)$:

$$R(\lambda) = \left(\frac{\ln\lambda - \gamma}{\beta}\right)\frac{\alpha}{\beta}\left(\frac{\ln\lambda - \gamma}{\beta}\right)^{\alpha-1}\exp\left(-\left(\frac{\ln\lambda - \gamma}{\beta}\right)^{\alpha}\right) \qquad (20)$$

Where $\alpha, \beta > 0$, are the shape, and scale with boundary conditions, respectively. The γ is the location parameter, when it converges to zero based on the Weibull model [81] $\lambda_s = e^{\varepsilon_s}$. So, the final calculation function of the nominal axial stresses developed based on the DCT is

$$\sigma_{af} = \int_0^{\varepsilon} \alpha\beta^{-\alpha}\varepsilon_S^{(\alpha-1)}e^{-\left(\frac{\varepsilon_s}{\beta}\right)^{\alpha}}[K(\varepsilon - \varepsilon_s) + \eta\dot{\varepsilon}]\, d\varepsilon_s \qquad (21)$$

Where $\alpha = 4.5$ and $\beta = 0.3$ are the shape and scale factors of the probability distribution function, respectively, for the sequential straightening of collagen fibers under stress loading in the 2-parameter Weibull model [80, 81, 182].

Based on the mechanical and material properties of ligaments, the ligament fiber bundle model is defined as a nonlinear viscoelastic unit [64, 80] When the ligament is in a resting or slack state, that is, the strain is equal to or less than zero, then the compressive stress within the ligament is zero. When the ligament is in tension, the strain is greater than 0, the internal ligament loading force is F_{af}:

$$F_{af} = \sigma_{af}A \qquad (22)$$

Where A is the average physiologic cross-sectional area of the DCTs. Based on our previous study, the anteromedial ACL (A-ACL) and posterolateral ACL (P-ACL) were modeled using the DCTs (Figure 14C), and a tunnel connecting the femur and tibia at both ends [64, 182]. The ACL was attached to the medial front of the tibial intercondylar eminence and extended to the medial side of the lateral condyle of the femur. For the A-ACL, the resting length is set to 30 mm, the cross-sectional area is set to 20.7 mm^2, and the max isometric force is set to 1500 N. For the P-ACL, the resting length is set to 23.36 mm, the cross-sectional area is set to 19.3 mm^2, and the max isometric force is set to 1600 N. The final calculated total ACL force was determined as the combination of the A-ACL force and the P-ACL force [64].

The lower limbs will dramatically change the acceleration and GRF of each segment during the landing phase, particularly in the early landing stage, which will prevent the optimization process from being convergent. As a result, during the whole modeling and simulation process, many attempts were performed to simulate the landing using the Computed Muscle Control (CMC) and Reduce Residuals Algorithm (RRA) for each segment. The strain of the ACL varies with the knee valgus angle under different flexion conditions. The ACL strain can be seen as a function of knee kinematics according to the simulation results after CMC, which is the function of the muscle optimization process. Therefore, this work sets the ratio of passive ACL strain to flexion-extension and varus-valgus angle to 15% by adjusting the ACL material properties for passive fiber strain at the maximum isometric force [78, 93, 96, 156]. As a maximum tolerance ratio, 15% is reasonable because the range of 9% to 15% has been shown to cause ACL rupture and microfiber damage [64, 96, 157]. If a passive ACL strain characteristic is specified as less than 1% in an individual model, additional adjustments are made to the models to ensure that the strain limit can be accurately

controlled. For the contact area between ligament and bone (junction of ligament together with bones), the maximum strain was limited to 2.5-3.0% to ensure that the isometric force could start from the lowest value in the simulation [93]. The length of bony osteoligamentous (tendons) and ligaments (muscles) will be examined during CMC based on the determined ACL strain when the presence of deformation of the entire muscle-tendon unit [64, 78].

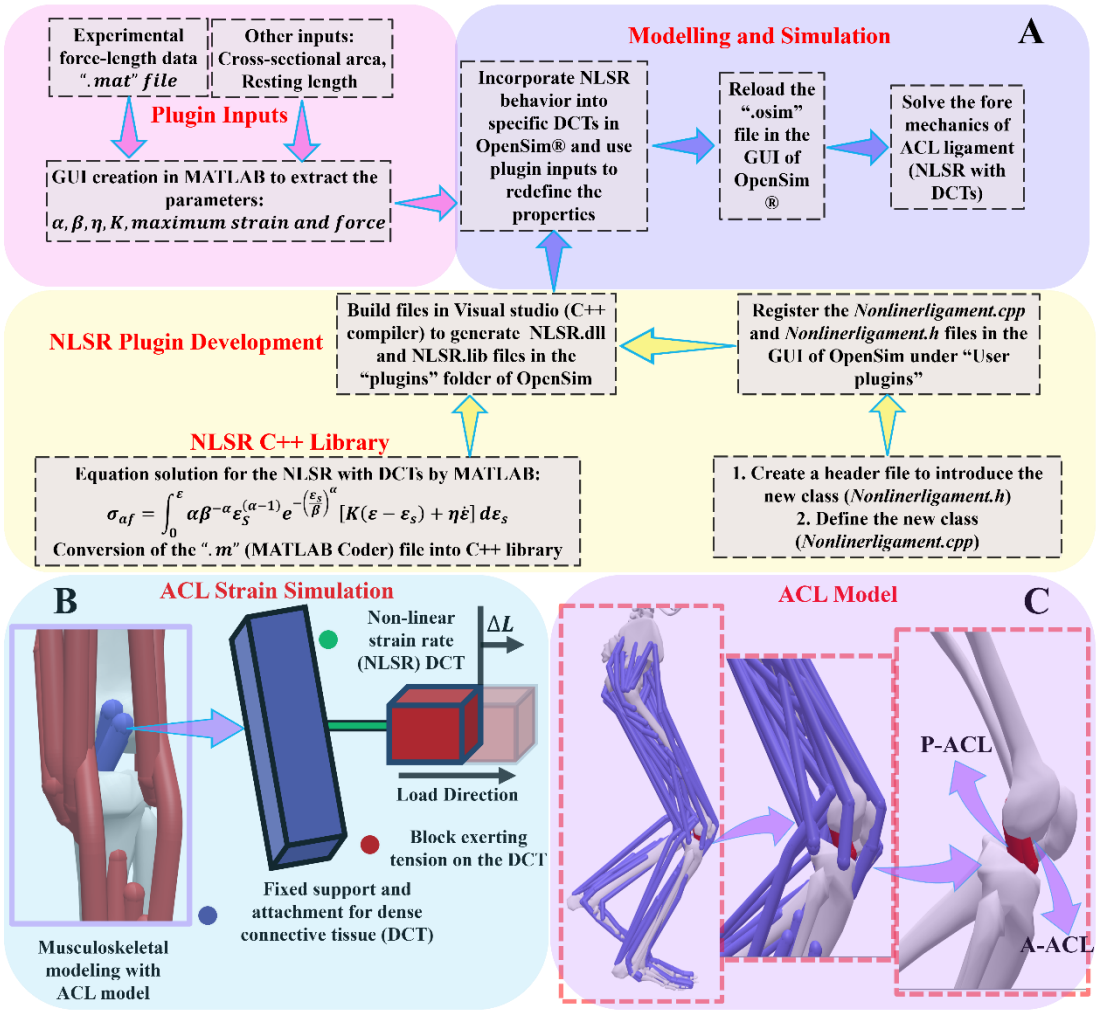

Figure 14 Illustration of the ACL model construction and property setting. (A) Flow diagram of the NLSR plugin creation and DCT model simulation. (B) Illustration of the ACL strain simulation (DCTs). (C) Illustration of the ACL model that was constructed in OpenSim and MATLAB.

2.4.5 Statistical analysis

Data analysis was conducted in SPSS 27.0 (IBM Corporation, NY, USA). Before formal analysis, the Kolmogorov-Smirnov test was performed to determine the normality of the data for each variable. All data obeyed a normal distribution. For the relationship between the ankle motion patterns (AICA, AROM) and lower limb injury risk (peak VGRF: PVGRF; total energy dissipation: TED; peak ankle dorsiflexion moment: PADM; peak knee flexion moment: PKFM; peak hip flexion moment: PHFM;

peak ACL force: PAF; peak ankle inversion angle: PAIA; peak ankle inversion moment: PAIM), the Pearson correlation and linear regression analysis were conducted to explore them (significant level $p < 0.05$). The value of Pearson correlation coefficient r ranges from -1 to 1. The $r > 0$, $r < 0$ and $|r| = 1$ represents the positive, negative and no correlation, respectively. The $|r| = 1$ indicates a perfectly linear correlation.

Meanwhile, the PAF and PAIA were standardized (0 to 1) to enable PAF and PAIA to be compared on the same frame of reference. This allows an effective assessment of the interaction between ACL injury and LAS risk. The corresponding maximum PAF and PAIA were estimated as the maximum likelihood of injury risk occurring, and the minimum PAF and PAIA were estimated as the minimum likelihood of injury risk occurring [64]. Therefore, the injury risk calculation formula is as follows:

$$R_{injury\ risk} = \frac{PAF/PAIA_{current\ value} - PAF/PAIA_{minimum\ value}}{PAF/PAIA_{maximum\ value} - PAF/PAIA_{minimum\ value}} \quad (23)$$

Where the $PAF/PAIA_{current\ value}$, $PAF/PAIA_{maximum\ value}$ and $PAF/PAIA_{minimum\ value}$ correspond to the current, maximum, and minimum values of PAF/PAIA, respectively.

2.5 Experiments and methods for objective 4

The overall experiment was conducted in two sessions, with the first test focusing on determining the trend of ankle plantarflexion angles when subjects landed on one leg in the natural state (Figure 15). The second test was to investigate the mechanical effects on the knee and ACL when SL with different ankle plantarflexion angles. The joint impact force and stresses (meniscus and femoral cartilage) were used to evaluate the impact loads on the knee at various landing angles, and the joint negative work was calculated to assess the ability of the knee to dissipate the energy impact. The ACL internal load forces (musculoskeletal modeling) and ACL stress (finite element analysis) were simulated and calculated to evaluate the ACL injury risk during SL. More detailed descriptions can be found in the corresponding sections.

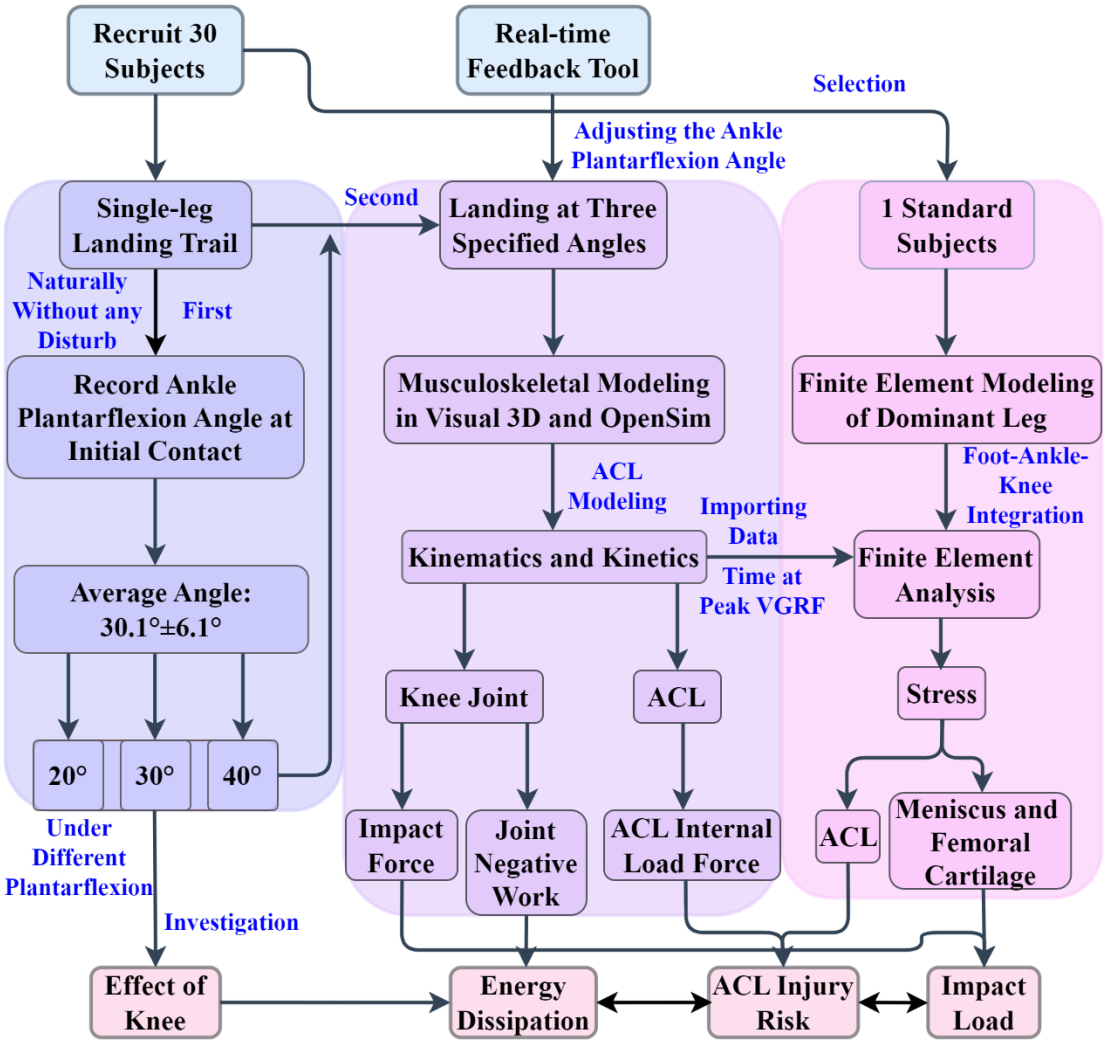

Figure 15 Overview of the whole work procedure.

2.5.1 Subjects

Thirty male subjects were recruited for this study (Age: 24.4±4.2 years; Height: 176.2±6.4 cm; Body Mass: 75.6±8.4 kg). The criteria for subject screening were: (1) no history of severe surgery within the previous six months; (2) no other injury variables that would affect the study; (3) no additional factors that would affect athletic

performance. All subjects were informed of the purpose, requirements and procedures of the experiment, and signed the written informed consent forms. Ningbo University Ethics Committee authorized the study protocol (Approval Number: RAGH20220415).

2.5.2 Experimental protocol and procedures

Experiments were conducted in the biomechanics laboratory of Ningbo University. As presented in Figure 16A, this study carried out musculoskeletal modeling according to the constructed pipeline of previous models [64]. The Vicon motion capture system (Vicon Metrics Ltd., UK) equipped with eight infrared cameras and the AMTI force plate (AMTI, Watertown, USA) were used to collect kinematic and kinetic data during landing, and the sampling frequency was set to 200 Hz and 1000 Hz respectively. Wireless Electromyographic (EMG) sensors (Delsys, Boston, MA, USA) were used to synchronically collect muscle activity data with a sampling frequency of 1000 Hz (Figure 16B). EMG signals of maximal voluntary contractions (MVC) of selected muscles were also collected to normalize the muscle activation degree [36, 64, 89]. Meanwhile, the Xsens sensor (Xsens, Henderson, USA) and the developed real-time feedback tool were used to determine the ankle plantarflexion angle during SL in real time (Figure 16C) [184]. All subjects wore uniform tight-fitting leggings and shoes, then performed a 10-minute warm-up run and familiarized themselves with the experimental procedures. The static acquisition was performed after the placement of the reflective marker points and EMG sensors, and then the formal experiment began [1, 64].

A jump platform (height: 40 cm) was set up in front of the force plate. The formal experiment was conducted in two sessions. For the first experiment, subjects were required to stand on the platform, and then lift the dominant leg and land on the downward single leg without any initial velocity [64]. The test was determined to be successful if the subjects maintained balance for 3 seconds without any tendency to fall after an SL for support. Five successful data sets were collected for each subject, with at least 30 seconds of rest between each test [1, 184]. In the first experiment, the experimenter did not provide any prompts to the subjects, and the subjects naturally landed on one leg based solely on their landing habits. The ankle plantarflexion angle of the landing leg during this process was recorded in real time. As shown in Figure 16D, the average ankle plantarflexion angle was 30.1°±6.1° (maximum: 42.7°; minimum: 16.2°) during SL in 30 subjects. Therefore, for the second experiment, subjects were asked to adjust their ankle plantarflexion angle to 20°, 30°, and 40° before conducting the SL task (Figure 16E). The tests for the three conditions were randomized. Subjects were required to use the real-time feedback tool to adjust the ankle plantarflexion angle to the specified position (20°, 30°, and 40°) and then execute the SL test. Other requirements for the second experiment were the same as the first, with five successful data collections in each case.

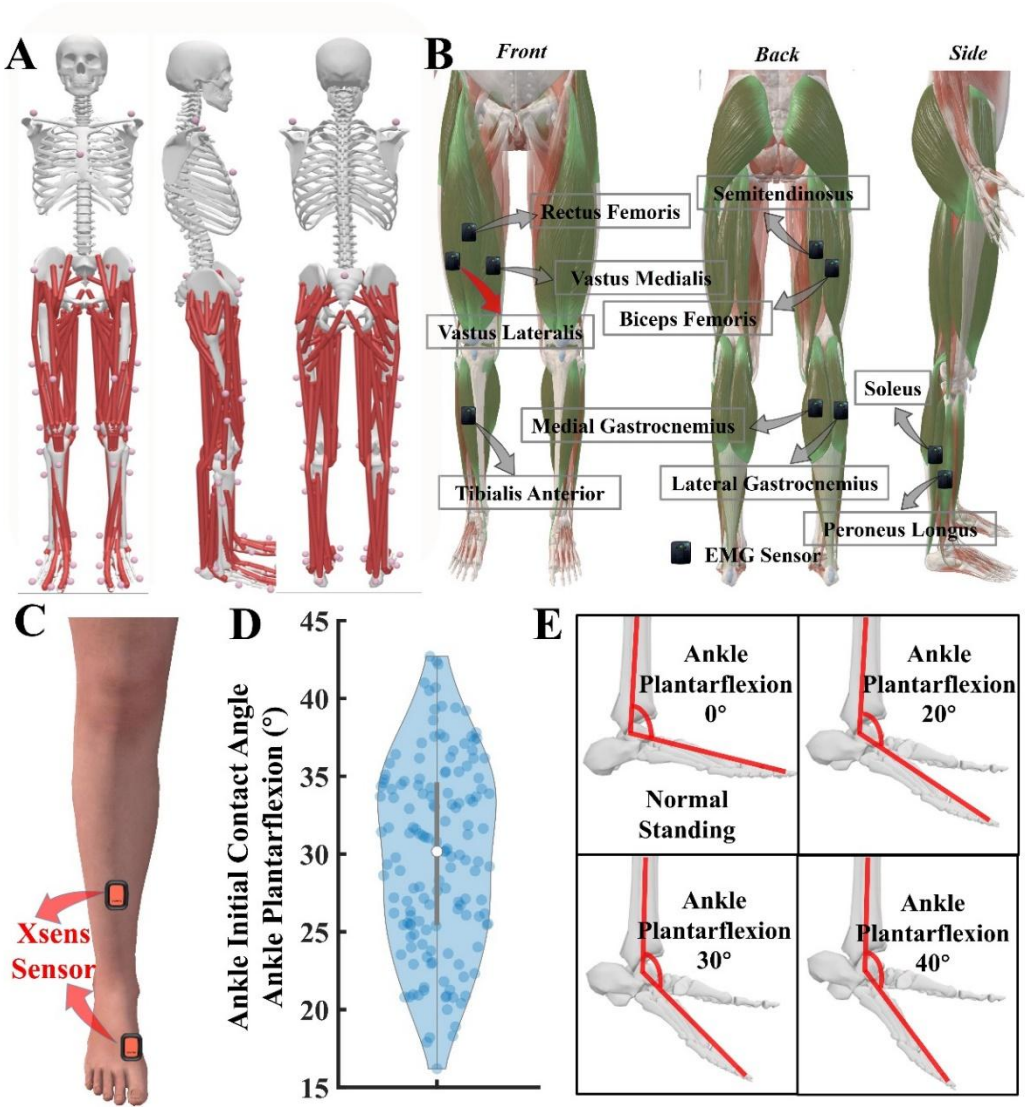

Figure 16 Overview of the musculoskeletal modeling and the determination of the ankle plantarflexion angle during landing. (A) Illustration of the constructed musculoskeletal model and the corresponding positions of 38 reflective markers. (B) Illustration of the position of the surface EMG test on the lower limb. (C) Illustration of the position of the Xsens sensor. Two sensors were placed ten centimeters up the distal tibia and at the distal end of the first metatarsal, respectively. The state of the subject's foot and ankle during normal standing was defined as the initial coordinate system of the sensor. The ankle plantarflexion angle was calculated in real time based on the change of the sensor in the sagittal plane relative to the initial coordinate system. (D) Results of ankle initial contact angle when subjects single-leg land in a natural state. (E) Illustration of the ankle plantarflexion angle for normal standing and three common ankle angles of initial contact during single-leg landing.

2.5.3 Data initial processing and collection

The time point of initial contact force ($F_{VGRF} > 10N$) to maximum knee flexion was defined as the landing phase [3]. This study first processed the data using Vicon Nexus software: 1) named the reflective markers; 2) fixed the missing reflective

markers; 3) deleted the wrong reflective markers. Then, based on the C3D file exported from Vicon Nexus, the initial modeling was conducted in Visual 3D 6.7.3 (C-Motion Inc., Germantown, US), and joint kinematics and kinetics data were calculated using its built-in algorithms. For the filtering of kinematics and kinetics, the Butterworth fourth-order filter (fourth-order zero-phase lag) with frequencies of 10 Hz and 20 Hz was selected according to the calculated most appropriate signal-to-noise ratio [46]. The magnitude of load impact on the knee joint was assessed by calculating its joint impact (contact) force [19]. The joint power is defined as the product of the joint moment and the joint angular velocity [19]. Meanwhile, the ability of the knee joint to dissipate impacts was assessed by calculating its joint negative work (the integral of joint power over time) [6]. The processed models of Visual 3D were saved in *".osim"* format and then imported into OpenSim 4.4 (Stanford University, Stanford, USA) for further musculoskeletal modeling and calculation [64].

The EMG activation results were obtained from the EMG sensors, which were compared with the results obtained by OpenSim to validate the musculoskeletal model [64, 180]. First, the raw EMG signals were processed firstly by band-pass filtering with a Butterworth fourth-order filter (frequency range of 10-400 Hz). Then, the full-wave rectification was conducted. Based on the determined most appropriate signal-to-noise ratio, the low-pass filtered with a 6 Hz cut-off frequency was performed [64, 149]. The raw EMG signals were processed firstly by band-pass filtering with a Butterworth fourth-order filter (frequency range of 10-400 Hz). Then, the full-wave rectification was conducted. Based on the determined most appropriate signal-to-noise ratio, the low-pass filtered with a 6 Hz cut-off frequency was performed [149]. EMG signal was normalized by dividing the maximum EMG amplitude of maximal voluntary contraction (MVC) by the maximum root mean square amplitude to obtain the normalized signal $e_i(t)$. This study used a recursive non-linear model (second-order differential equation) to solve the muscle activation $a_i(t)$ by the obtained normalized signal $e_i(t)$ [36, 126, 180].

$$a_i(t) = \frac{e^{A_i u_i(t)} - 1}{e^{A_i} - 1} \qquad (24)$$

Where the A_i is the nonlinear shape coefficient and represents the degree of nonlinearity of the neural activation $u_i(t)$ and muscle activation $a_i(t)$. This study takes A_i to be 1.5, the electromechanical delay to be 10 ms [180]. All data were expanded into 101 data point curves (0%-100% landing phase) by self-written MATLAB (Visual R2022a, MathWorks, United States) scripts.

2.5.4 ACL model creation and property setting

This study developed a graphical user interface (GUI) for OpenSim based on App Designer in MATLAB to assess the ligament material parameters. Meanwhile, ligament elongation and DCT forces were calculated based on the muscle and force analysis tools in the OpenSim analysis toolbox. The details of ACL model construction are provided in Section 2.4.4.

2.5.5 Finite element analysis of foot-ankle-knee integration model

2.5.5.1 Finite element model construction

A standard subject (height: 176 cm, weight: 75.5 kg, age: 25 years) was selected from 30 subjects to conduct FEA. The selection criteria for the standard subject were based on the average height and weight of all subjects. This study constructed a finite element model (FEM) of the foot-ankle-knee integration according to the medical imaging data of the subject's dominant limb (Figure 17). The MRI tomography and CT scanning of the lower limbs were performed (tube voltage: 120 kV, tube current: 125 mA, slice thickness: 2mm; no interval scanning) (Figure 17A). The segmentation of the two-dimensional image was performed using Mimics 21.0 (Materialise, Leuven, Belgium), while the creation and refinement of a three-dimensional model of the bone, ligaments, and bulk soft tissue was carried out using Geomagic Studio 2021 (Geomagic, Inc., Research Triangle Park, NC, United States) (Figure 17B). The SolidWorks 2017 software was utilized to convert the components into solids subsequent to their importing (SolidWorks Corporation, Waltham, MA, United States). The structure of cartilage was replicated through the construction of a solid material between the surfaces of two bones that are in contact with each other.

The contacts of all three models were meshed and established utilizing Workbench 2021 software (ANSYS, Inc., Canonsburg, PA, USA). Hexahedral meshes were employed to decompose each solid. The mesh sizes for the bulk soft tissue, bone, cartilage, and ACL were adjusted to 2 mm, 2 mm, 0.5 mm, and 0.5 mm, respectively. Furthermore, the process of refining at the local level was conducted with careful consideration of the geometric characteristics of the contact zone. The Workbench software facilitated the automated detection of component contacts. Possible contact pairings were generated using an algorithm that relies on surface proximity. The physical interaction between the surface of the foot bone and the cartilage was simulated through face-to-face contact. The coefficient of friction, defined as 0.04, was used to describe the sliding friction that occurs between the meniscus and femoral cartilage, as well as between the cartilage of the pinna and femoral cartilage [185, 186]. The cartilage has been determined to have undergone frictionless contact with both the bone surface and the ACL and PCL [187]. The soft tissue that was encapsulated served as an anchor for both the bones and cartilage (Figure 17C).

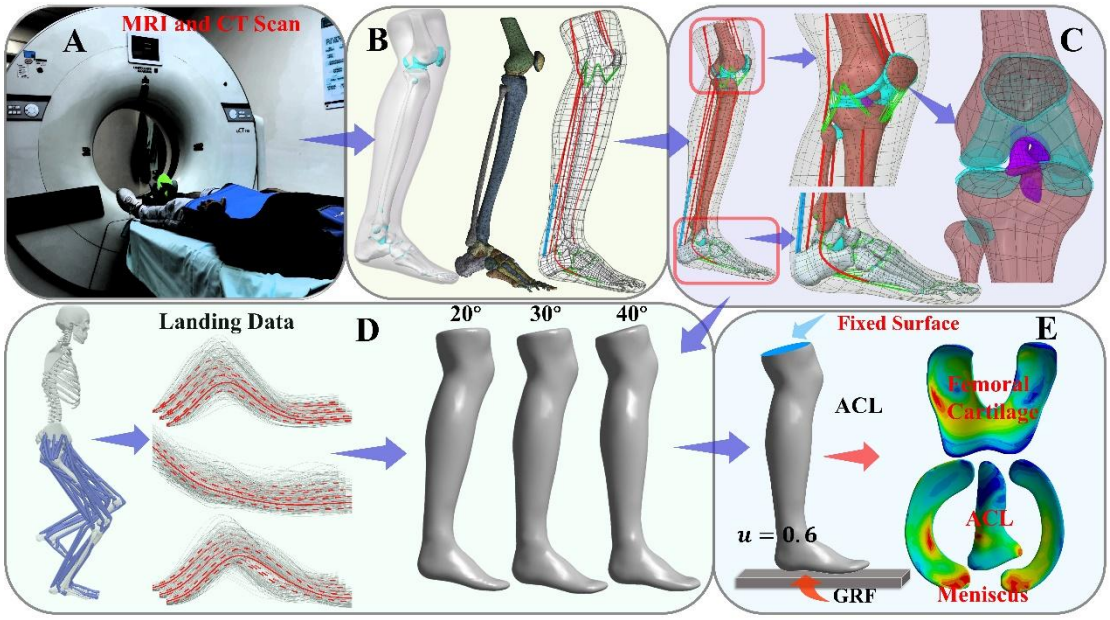

Figure 17 Illustration of the whole process of FEA. (A) Medical imaging data acquisition of the lower limb. (B) Three-dimensional finite element modeling process. (C) Detailed view of the constructed finite element model. (D) Illustration of the finite element model of the lower limb at three initial contact angles. (E) Illustration of the bounding in the computational process.

2.5.5.2 Material properties

All materials, except for the encapsulated soft tissue (refers to soft tissues encased by connective tissue, such as tendons, ligaments, adipose tissue, and synovial sacs) and ACL and PCL, were considered to be linear elastic materials. The elasticity of a material was represented by the selection of two material constants, namely Young's modulus (E) and Poisson's ratio (v). The soft tissue contained within was defined as a hyperelastic substance utilizing the Moonley Rivlin model. ACL and PCL are also assumed to be a hyperelastic material. Table 3 enumerates the material properties of each constituent. For the hyperelastic material, the strain energy formula is constructed based on the strain energy density function [188, 189]:

$$\Psi = \Psi_{vol}(J) + \Psi_{iso}^{m}(\overline{C}) + \Psi_{iso}^{f}(\lambda) \qquad (25)$$

Where the Ψ_{vol} is the volumetric component of ligament volume change, the Ψ_{iso} is the deviatoric component of the shape change (Ψ_{iso}^{m}: Stromal Fraction, Ψ_{iso}^{f}: fiber fraction). The J is the Jacques ratio of the deformation gradient tensor F, and the $\overline{C}$ is deviatoric component of the deformation gradient tensor C ($\overline{C} = J^{-\frac{2}{3}}C$). The centers of the attachment zones at both ends of the ligament were set as the initial direction of the fiber, and the elongation λ was calculated based on the deformation of the material and the initial direction of the fibers a_0 ($\lambda = \overline{C} \times a_0^2$).

This study conducted a Neo-Hooker model [190]. For the volumetric component

Ψ_{vol}:

$$\Psi_{vol}(J) = \frac{1}{2D}\ln J^2 \qquad (26)$$

For the deviatoric component $\Psi_{iso}^{m}(\overline{C})$:

$$\Psi_{iso}^{m}(\overline{C}) = C_1(\overline{I_1} - 3) \qquad (27)$$

Where the C_1 is the coefficient of the Neo-Hooke model, and the D is the inverse of the bulk modulus ($D = \frac{1}{2000}C_1$) [191]. The collagen fibers in the ligament can hardly withstand ballast, so the strain energy density function of the fiber fraction is defined as [189]:

$$\Psi_{iso}^{f}(\lambda) = F_2(\lambda) \qquad (28)$$

Therefore, the strain energy equation is determined as:

$$\Psi = \frac{1}{2D}\ln J^2 + C_1\left(\overline{I_1} - 3\right) + F_2(\lambda) \qquad (29)$$

Table 3 Material properties of the components in the finite element model.

Component	Elastic modules (MPa): E	Poisson's ratio: v	Destiny (kg/m^3)	Ref.
Skin	Hyperelastic (first-order Ogden model, $\mu = 0.122\ kPa, \alpha = 18$)	N/A	950	[192]
Bulk soft tissue	Hyperelastic (second-order polynomial strain, $C_{10} = 0.8556, C_{01} = 0.05841, C_{20} = 0.03900, C_{11} = 0.02319, C_{02} = 0.00851, D_1 = 3.65273$)	N/A	950	[5]
Aterior Crucial Ligament	Hyperelastic (first-order polynomial strain, $C_1 = 1.95, D = 0.00683$)	N/A	1000	[190]
Posterior Crucial Ligament	Hyperelastic (first-order polynomial strain, $C_1 = 3.25, D = 0.0041$)	N/A	1000	
Foot Bones	7300	0.3	1500	[193]
Foot Cartilages	1	0.4	1050	
Foot Ligaments	260	0.4	1000	[194]
Plantar Fascia	350	0.4	1000	[195]
Achilles	816	0.3	1000	[196]

Tendon				
Patellar Tendon	778	0.46	1000	[197]
Medial and Lateral Collateral Ligament	467	0.46	1000	[198]
Knee Cartilages	20	0.46	1000	[199]
Medial and Lateral Meniscus	59	0.49	2000	[200]
Fibula, Tibia, Femur and Patella	14220	0.3	1990	[201]
Plate	17000	0.4	1000	[202]

2.5.5.3 Boundary and loading condition

The establishment of the global coordinate system was carried out according to the OpenSim standard to maintain consistency in the reference frame [78]. The kinematic and kinetic data that corresponded to the time point of peak ground reaction force during SL were used for finite element analysis (Table 4). Ankle joint angulation was pre-set while positioning and orienting the foot model. In a short analytical step at the beginning of the simulation, the angle between the sagittal plane's femur axial line, tibial axial line, and foot longitudinal axis was adjusted to determine the ankle and knee angles [203]. Then, the corresponding kinetic data of three situations were taken into the adjusted three models (Figure 17D, Table 4). The ground plate and the interface of the femur were fixed to calculate (Figure 17E). A contact surface with a friction coefficient of 0.6 was employed to replicate the interaction between the foot and the ground [189]. All degrees of freedom of the patella, tibia, fibula, and foot were constrained to eliminate the effect of various loading points on simulation results. All contacts were set to frictionless finite sliding contacts, and the simulations were performed using a universal contact algorithm. The gravity and inertia forces on the tibia, fibula, and foot were excluded from the ground reaction forces [204, 205].

Table 4 Results of ground reaction force, ankle angle, knee angle, and muscle force data that corresponded to the time point of peak ground reaction force during SL.

Initial Contact Angle	Ankle Plantarflexion	20°	30°	40°
Ground Reaction Force (N)	Vertical	3601.2	3206.7	2897.6
	Medial	412.6	426.5	353.1
	Posterior	193.8	210.5	246.1
Ankle Angle (°)	Dorsiflexion	8.5	5.2	2.9

Knee Angle (°)	Flexion	38.6	35.9	33.2
Muscle Force (N)	Vastus Medialis	2085.4	1975.7	1811.1
	Vastus Lateralis	2140.3	2093.3	2030.6
	Rectus Femoris	1677.7	1491.1	1499.2
	Biceps Femoris	1865.9	1850.2	1677.7
	Semitendinosus	1650.2	1666.3	1590.8
	Tibialis Anterior	3559.3	3222.2	3104.4
	Medial Gastrocnemius	1458.2	1420.0	1293.6
	Lateral Gastrocnemius	1029.1	942.8	864.5
	Peroneus Longus	1489.2	1422.0	1425.6
	Soleus	989.3	978.5	1025.7

2.5.5.4 Model validation

With the knee in normal knee extension (knee flexion 0°), a backward force of 134 N was set to load at the midpoint of the midline of the femoral condyle to verify the validity of the model. This loading condition was able to simulate the anterior drawer test of the knee joint and clinically common force conditions [206-208]. The effectiveness of the ACL stress simulation was tested by the displacement of the knee joint model in the anterior-posterior, distal-proximal, and medial-lateral directions, as well as the angles of varus-valgus and external-internal [206-208]. Under the same load conditions, the results of this study were similar to those of other studies that used cadaveric specimens or finite element modeling and looked at joint displacement values and angles of movement. As shown in Table 5, the displacements of anterior-posterior, proximal-distal, and medial-lateral are 4.18 mm, 0.54 mm, and 0.62 mm, respectively; the angles of varus-valgus and external-internal are 0.1° and 1.6°.

Table 5 Comparative results of displacements and angles of knee models in different studies under the same loading conditions.

	Displacement (mm)			Angle (°)	
	Anterior-Posterior	Proximal-Distal	Medial-Lateral	Varus-Valgus	External-Internal
Gabriel [206]	4.0	0.3	0.6	0.2	1.7
Song [207]	4.3	0.62	0.39	0.09	1.9
Suggs [208]	4.16	/	/	/	/
Current study	4.18	0.54	0.62	0.1	1.6

In addition, the current study collected the knee fluoroscopic image data of the subjects in the landing state by the high-speed dual fluoroscopic imaging system (DFIS) (Ti-WISH-II, Ti-Motion ltd., Shanghai City, CN), and compared the calculated knee displacement results with the FEA results to verify the validity of FEM. Figure 18 illustrates the procedure and outcomes of knee displacement calculation based on DFIS.

By generating high voltage through a high voltage generator, the DFIS can accelerate the free electrons inside the X-ray tube towards the target surface to emit X-rays. Afterward, based on the principle that the X-rays emitted pass through different tissues and organs of the human body with different levels of attenuation, the X-rays that pass through the human body and carry enough information are projected onto a flat-panel detector. The computer processes the analog signals into digital signals through photoelectric conversion and analog-to-digital conversion, thereby providing reliable gray-scale medical image data for clinical diagnosis. The parameters setting of DFIS are as follows: source image distance 1350 mm, device voltage 60 kV, device current 500 mA, exposure time 3 seconds, laser wavelength 650 nm, dose range for the automatic exposure control 45 μGy, flat panel detector size 3072×3072 pixel, X-ray area 427×427 mm, nominal voltage of the ray tube 150 kV, laser power 3 mW, and sector angle 90°.

Subjects were asked to land vertically on one leg from a 20 cm high jumping platform, keeping the knee in a straight position (flexion 0°) during the process. The FEM was driven by kinematic and kinetic data collected during the landing via VICON and force platform equipment to calculate the degree of displacement in all three directions (anterior-posterior, proximal-distal, medial-lateral). The two fluoroscopes were placed in planes orthogonal to each other by 90° to enable simultaneous capture of knee fluoroscopy image data from two orthogonal projections (anterolateral and anteromedial). A cubic calibration frame spatially calibrated the shooting area, and the XMAlab software (Version 2.1.0, Brown University, Prov, USA) calculated the relative positions of the X-ray tube and the flat panel detector in space [209]. Subsequently, the environment calibration file generated by XMAlab was imported into the 3-D modeling software Rhinoceros (Version 7.4, Robert McNeel Ltd., WA, USA) to create a virtual bi-orthogonal perspective system [209, 210].

Two virtual cameras were created to represent the x-ray sources of the two fluoroscopes, based on the placement of orthogonal fluoroscopic images to restore the position of the fluoroscopic enhancers (Figure 18A). After that, the real knee model was imported into the virtual space, and the bone position was adjusted by rotation and translation in Rhinoceros to align the projected contour of the knee model with the actual bone position on the X-ray fluoroscopic images [211]. In this, the 3-D model reconstructed in Mimics based on previously acquired knee MRI/CT data was used as a standard framework for model correction and alignment (Section 2.5.5.1). Finally, the femoral, tibial, and fibular coordinate systems were established, and knee displacements were calculated using the coordinate system calculator plug-in in Rhinoceros [210]. As shown in Figure 18B, the knee displacement results obtained based on FEA and DFIS calculations in the three directions are basically consistent, which demonstrates the feasibility of the finite element model constructed in the current study.

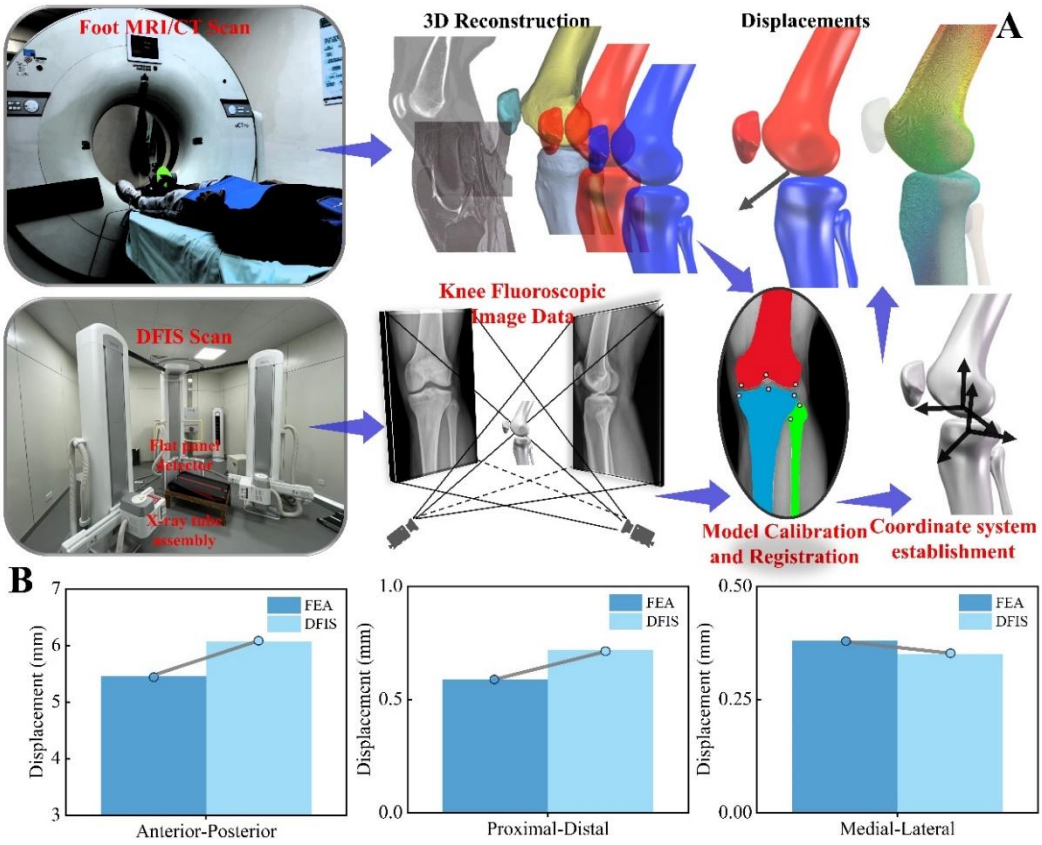

Figure 18 Illustration of the knee displacement process based on the DFIS calculation and its results. (A) Knee fluoroscopic image data collection and process based on the DFIS. (B) Comparison results for knee displacement calculated based on DFIS with finite element analysis.

2.5.6 Statistical analysis

Before formal analysis, the Kolmogorov-Smirnov test was performed to determine the normality of the data for each variable. All data obeyed a normal distribution. For the knee peak impact force, peak ACL forces and total negative work, a repeated-measures analysis of variance (ANOVA) was performed in SPSS 27.0 (SPSSs Inc., Chicago, IL, USA) to test for statistical differences between landing at different ankle plantarflexion angles. For the time-series curves of ACL forces during the landing phase, a repeated-measures analysis of variance (ANOVA) based on the statistical parametric mapping (SPM) was conducted in MATLAB to test statistical differences [1, 177]. Meanwhile, post hoc pairwise comparison analyses with Bonferroni adjustment were employed to test the difference between them (20° vs. 30°, 20° vs. 40°, and 30° vs. 40°). The significance threshold was set at 0.05.

2.6 Experiments and methods for objective 5

2.6.1 Landing biomechanical data

The landing biomechanics data for the prediction model are from Objective 1, details of which can be found in Section 2.2. A total of 112 samples datasets ($56_{Before-Fatigue} + 56_{After-Fatigue}$) for each variable is randomly distributed uniformly, and 80% of them were selected as the model training set ($90_{\text{samples}} \times 5_{\text{trials}}$), 20% of them were selected as the model testing set ($22_{\text{samples}} \times 5_{\text{trials}}$).

2.6.2 Prediction model of ACL force during the landing phase

This work constructed an ACL force prediction model based on machine learning algorithm to achieve effective and accurate prediction using simple and measurable kinematic data during the landing phase. The whole detailed workflow is presented in **Figure 19**, which mainly consists of 4 parts: 1) Optimized the parameters of the prediction model by the SSA of metaheuristic optimization algorithm (**Figure 19A**); 2) Predicted the PAF by the extreme learning machine (ELM) regression prediction model (**Figure 19B**); 3) Predicted the time-series waveform of ACL force during the whole landing phase by the LSTM neural network time series prediction model (**Figure 19C**); 4) Calibrated the predicted ACL force waveform by scaling equally to get the final optimized prediction result (**Figure 19D**). The simplified flow of the prediction model is shown in **Figure 19E**.

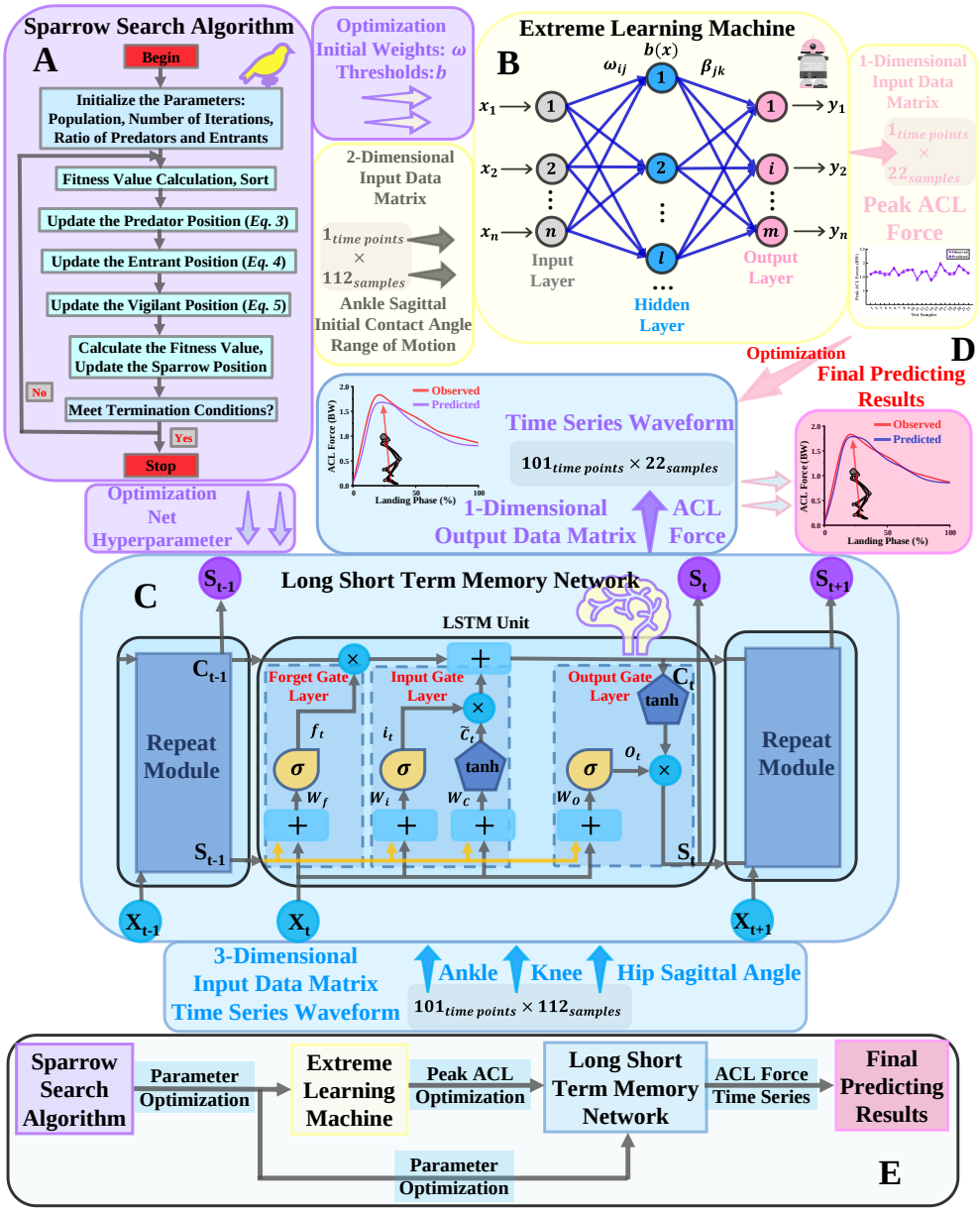

Figure 19 Overview of the proposed workflow for realizing the prediction of the ACL force during the landing phase. (A) Illustration of the realization flow of the SSA, which aims to optimize the parameters of the prediction model. (B) Illustration of the realization flow of ELM regression prediction model, which aims to predict the PAF. (C) Illustration of the realization flow of LSTM neural network time-series prediction model, which aims to predict the time-series waveform of ACL force during the whole landing phase. “+” indicates the operation of plus-by-element. "×" indicates the operation of multiply-by-element. "$\boldsymbol{\sigma}$" and "tanh" means the neural network layer. (D) Based on the predicted PAF, the predicted ACL force waveform is calibrated by scaling equally to get the final optimized prediction result. (E) Illustration of the schematic flow of the prediction model.

2.6.3 Parameter optimization by sparrow search algorithm

Sparrow search algorithm (SSA) was mainly proposed in 2020 by Xue et al., which

mainly inspired by the foraging behavior and anti-predation behavior of sparrows [107]. In this study, the main purpose of SSA is to find the optimal parameters of the prediction model to improve the accuracy of the ACL force prediction [107]. The implementation of the SSA mainly includes the following seven steps: 1) Initialize the population, the number of iterations, and the ratio of predators and entrants; 2) Calculate the fitness value and sort it; 3) Update the predator position; 4) Update the entrant position; 5) Update the Vigilant position; 6) Calculate the fitness value and update the sparrow position; 7) Determine whether the stop condition is met, if yes, exit and output the result, otherwise, repeat the execution (**Figure 19A**). SSA is novel and has been proved to have the advantages of strong searching ability and fast convergence speed [107].

At the time of modeling, the sparrow that is aware of the danger is assumed to be from 10% to 20% of the total population. The initial position of the sparrow is randomly generated in the population, which can be expressed as follows:

$$S_{i,j}^{t+1} = \begin{cases} S_{best}^{t} + \beta . \left| S_{i,j}^{t} - S_{best}^{t} \right|, & if\ f_i > f_g \\ S_{i,j}^{t} + K . \left(\dfrac{\left| S_{i,j}^{t} - S_{worst}^{t} \right|}{(f_i - f_w) + \varepsilon} \right), & if\ f_i = f_g \end{cases} \quad (30)$$

Where the S_{best} is the current global optimal position, indicating that sparrows in this position are the best position in the population and very safe. The β is a step control parameter, which follows the normal distribution of random numbers with mean 0 and variance 1. The $K \in [-1,1]$ is a random number, and the f_i is the fitness value of the current sparrow individual. The f_g and f_w are the current global best and worst fitness values, respectively. ε is the constant that avoids zero in the denominator. When $f_i > f_g$, indicates that the sparrow is at the edge of the population and is vulnerable to predators, and $f_i = f_g$ indicates that sparrows are aware of the danger and need to approach other sparrows to reduce the risk of predation. The K represents the step control parameter, which is also the direction of sparrow movement. For the setting of SSA related parameters, the number of hidden layers was set to 30, the safety value was set to 0.6, the ratio of finders to entrants was set at 7 to 3, the population of sparrow aware of danger was set at 0.2 of the total population.

No matter for the optimization of ELM (SSA-ELM) or LSTM (SSA-LSTM), the termination condition of optimization was determined by the defined fitness value:

$$fitness(x) = MSE\left(Y_{observed} - Y_{predicted}\right) \quad (31)$$

Where the $Y_{observed}$ is the true value of the predicted variable, the $Y_{predicted}$ is the predicted value of the predicted variable, the function of MSE is the squared of prediction error. The smaller the fitness value suggested that the higher the coincidence degree between the predicted data and the observed data. Finally, the optimal parameter was determined based on the parameter selection corresponding to the smallest fitness value.

A total of 112 samples dataset of each variable is randomly distributed uniformly, and 80% of them were selected as the model training set (90 groups), 20% of them were selected as the model testing set (22 groups). The input data were normalized before the model was established to reduce the influence of large variable differences on the

model prediction performance.

2.6.4 Peak ACL force prediction by SSA-ELM

For the SSA-ELM, the independent variables are the AICA and AROM (determined by the explored relationships), and the dependent variable is the PAF (**Figure 19B**). That is, two input variables correspond to two neurons in the input layer, and one output variable corresponds to one neuron in the output layer [212, 213]. The randomly generated initial weights w and thresholds b are full-eyed and do not allow the algorithm to achieve the best training performance. Therefore, the current study optimizes the initial weights w and thresholds b by SSA to determine the best parameters to achieve the best prediction results.

Extreme learning machine (ELM) is a feedforward neural network learning method composed of the input layer, hidden layer and output layer, and the neurons of the input layer and hidden layer, hidden layer and output layer are fully connected [212, 213]. ELM can randomly generate the connection weights between the input layer and the hidden layer and the threshold of the neurons in the hidden layer. It only needs to set the number of neurons in the hidden layer without adjustment in the training process, and has the advantages of fast learning speed and good generalization performance. The n input variables correspond to n neurons in the input layer, and l output variable corresponds to l neuron in the output layer. This study has two input variables and one output variable, and a total of 112 samples. In order not to lose generality, the connection weight w between the input layer and the hidden layer can be expressed as follows:

$$w = \begin{bmatrix} w_{11} & w_{12} & \cdots & w_{1n} \\ w_{21} & w_{22} & \cdots & w_{2n} \\ \vdots & \ddots & \ddots & \vdots \\ w_{l1} & w_{l2} & \cdots & w_{ln} \end{bmatrix} \quad (32)$$

Where the w_{ln} represents the connection weight between the i-th neuron in the input layer and the j-th neuron in the hidden layer. The connection weight β between the input layer and the hidden layer can be expressed as follows:

$$\beta = \begin{bmatrix} \beta_{11} & \beta_{12} & \cdots & \beta_{1m} \\ \beta_{21} & \beta_{22} & \cdots & \beta_{2m} \\ \vdots & \ddots & \ddots & \vdots \\ \beta_{l1} & \beta_{l2} & \cdots & \beta_{lm} \end{bmatrix} \quad (33)$$

Where the β_{lm} represents the connection weight between the l-th neuron in the hidden layer and the m-th neuron in the output layer. The threshold b of the neurons in the hidden layer can be expressed as follows:

$$b = \begin{bmatrix} b_1 \\ b_2 \\ \vdots \\ b_l \end{bmatrix} \quad (34)$$

The input matrix X and output matrix Y of the training set with $Q = 90$ samples are:

$$X = \begin{bmatrix} x_{11} & x_{12} & \cdots & x_{1Q} \\ x_{21} & x_{22} & \ldots & x_{2Q} \\ \vdots & \ddots & \ddots & \vdots \\ x_{n1} & x_{n2} & \cdots & x_{nQ} \end{bmatrix}, Y = \begin{bmatrix} y_{11} & y_{12} & \cdots & y_{1Q} \\ y_{21} & y_{22} & \ldots & y_{2Q} \\ \vdots & \ddots & \ddots & \vdots \\ y_{m1} & y_{m2} & \cdots & y_{mQ} \end{bmatrix} \quad (35)$$

The output T of the neural network can be expressed as follows:

$$T = [t_1, \ldots, t_Q]_{m\times Q}, t_j = [t_{1j}, \ldots, t_{mj}]^T = \begin{bmatrix} \sum_{i=1} t\,\beta_{i1} g(w_i x_j + b_i) \\ \sum_{i=1} t\,\beta_{i2} g(w_i x_j + b_i) \\ \vdots \\ \sum_{i=1} t\,\beta_{im} g(w_i x_j + b_i) \end{bmatrix}_{m\times 1}, (j = 1,2,\ldots,Q) \quad (36)$$

Where the $g(*)$ is an infinitely differentiable function as the activation function of the hidden layer. As the transpose matrix of the matrix T, $T' = H \times \beta$, so the output matrix H between the hidden layer and the output layer can be expressed as follows:

$$H(w_1, \ldots, w_i, b_1, \ldots, b_l, x_1, \ldots, x_Q) = \begin{bmatrix} g(w_1 x_1 + b_1) & g(w_2 x_1 + b_2) & \cdots & g(w_1 x_1 + b_l) \\ g(w_1 x_2 + b_1) & g(w_2 x_2 + b_2) & \ldots & g(w_1 x_2 + b_l) \\ \vdots & \ddots & \ddots & \vdots \\ g(w_1 x_Q + b_1) & g(w_2 x_Q + b_2) & \cdots & g(w_l x_Q + b_l) \end{bmatrix}_{Q\times l} \quad (37)$$

After that, the output matrix of the hidden layer was calculated, and the connection weight between the hidden layer and the output layer was calculated by the least square method, so as to obtain the final calculation result. Specifically, ELM can randomly generate connection weight w and the threshold b before training, and then connection weight β can be calculated by determining the number of hidden layer neurons and the activation function (infinitely differentiable function $g(*)$) between hidden layer and neuron. However, the randomly generated initial weights w and thresholds b are full-eyed and do not allow the algorithm to achieve the best training performance. Therefore, the current study optimizes the initial weights w and thresholds b by SSA to determine the best parameters to achieve the best prediction results. For the setting of ELM related parameters, the maximum number of iterations was set to 50, the number of hidden layers was set to 20.

2.6.5 ACL force waveform prediction by SSA-LSTM

For the SSA-LSTM, the independent variables are the time-series waveform of the ankle, knee, hip joints' sagittal angle, and the dependent variable is the time-series waveform of ACL force during the whole landing phase (**Figure 19C**). The selection of independent variables is mainly due to the sagittal plane angle is easy to measure, high accuracy and great influence on ACL [1]. Therefore, the LSTM structure in the current study is a 3-to-1 structure (3-dimensional input and 1-dimensional output) [214, 215].

Long short-term memory Network (LSTM) is a special structure of recurrent neural network (RNN) proposed by Hochreater and Schmidhuber, which can learn long-term dependent information and successfully solve the gradient explosion and gradient disappearance problems of traditional RNN in back propagation algorithm [214, 215]. For the LSTM detailed internal structure, as shown in **Figure 19C**, which introduces four interacting layers: three $\sigma(z) = \frac{1}{1+e^{-z}}$, one $tanh(z) = \frac{e^{z}-e^{-z}}{e^{z}+e^{-z}}$. In general, the training process has three main steps: 1) Calculated the output value of each neuron $(f_t, i_t, c_t, o_t, s_t)$ by forward calculation; 2) Calculated the error term value of each neuron by back propagation, which involves two directions: back propagation according to the time series, that is, calculation of the value of the error term at the previous moment $t-1$ from the current moment t; back propagation according to the spatial structure, that is, calculation of the value of the error term from the current layer l up one layer $l-1$; 3) Calculated the gradient value of each weight matrix and performed the update operation based on the two directional error term values.

However, the setting of some hyperparameters in traditional LSTM for time series prediction is likely to cause problems such as underfitting, overfitting, slow convergence or even failure to converge, thus affecting the model prediction performance. These hyperparameters include the number of hidden units, max epochs, initial learn rate and L2 regularization. Therefore, the current study used the error of the LSTM network as a fitness function to find an optimal set of hyperparameters to minimize the prediction error through the SSA model, and ultimately to accurately predict the ACL force during the whole landing phase.

2.6.6 Final optimization by combining the SSA-ELM and SSA-LSTM

The final calibration and optimization for the prediction results are shown in **Figure 19D**. Firstly, the peak value of ACL force (time series waveform) predicted by the SSA-LSTM model based on test samples was extracted, and then the peak value was compared with the peak ACL force predicted by SSA-ELM for corresponding test samples. Based on the comparison results (the multiple between the two), the ACL force predicted by SSA-LSTM was scaled equally to obtain the final predicted ACL force. The mean square error (MSE), root MSE (RMSE) and Pearson correlation coefficient R were calculated to evaluate the accuracy of the prediction model. ALL the algorithm implementation by self-written scripts based on the built-in function packages in MATLAB R2022a.

2.6.7 Performance evaluation of prediction results

The square of correlation coefficient (R^2), mean square error (MSE), and root mean square error (RMSE) were calculated to evaluate the performance evaluation of prediction results. For the value of MSE and RMSE, the magnitude of the value depends on the magnitude of the estimation error. Smaller values of MSE and RMSE (close to 0) indicate high accuracy. The equation is as follows:

$$MSE = \frac{1}{N}\sum_{i=1}^{N}(Y_i^{mea} - Y_i^{pre})^2 \qquad (38)$$

$$RMSE = \sqrt{MSE}$$

Where the N means the number of data points during the step-off landing phase, Y_i^{mea} and Y_i^{pre} are the measured and estimated results at data point i, Y_{max}^{mea} and Y_{min}^{mea} are the maximum and minimum values of the measured results.

The R^2 represents the degree of the correlation between the estimation outputs and the measured results, and its value closer to 1 implies a higher correlation and accuracy. The equation is as follows:

$$E_{R^2} = \frac{\sum_{i=1}^{N}(Y_i^{pre} - \overline{Y^{mea}})^2}{\sum_{i=1}^{N}(Y_i^{mea} - \overline{Y^{mea}})^2} \qquad (39)$$

Where the $\overline{Y^{mea}}$ is the average value of the measured results.

2.7 Experiments and methods for objective 6

The overall predictive modeling framework of the current study consists of a cascade of three models: 1) Muscle activation solution model based on second-order differential equation; 2) Muscle synergy extraction model based on NNMF; 3) estimation model of lower limb joint movement based on ANFIS. As shown in **Figure 20**, the work procedure was mainly divided into three parts. First, this study collected surface EMG and lower limb joint kinematic and kinetic data from healthy subjects and patients during step-off landing from stair steps. A total of twelve lower limb muscle groups were selected for this study to simulate the neuromuscular synergistic pattern of the lower limb during movement (**Figure 20A**). Second, this study pre-processed the acquired surface EMG data, such as filtering, and subsequently solved the pre-processed data based on the established recursive model of second-order differential equations to obtain the muscle activation matrix, and then imported it into the NNMF model to obtain the muscle synergy matrix (**Figure 20B**). Third, the lower limb neuromuscular synergy pattern during movement was obtained based on a combination of muscle synergy matrices, which were then imported into the developed ANFIS non-linear regression model to estimate the human movement intention during this movement pattern (**Figure 20C**). Finally, the estimated joint motion variable results were compared with the actual measured results, and the estimation errors between healthy subjects and patient groups were also analyzed to demonstrate the feasibility of the proposed detection system.

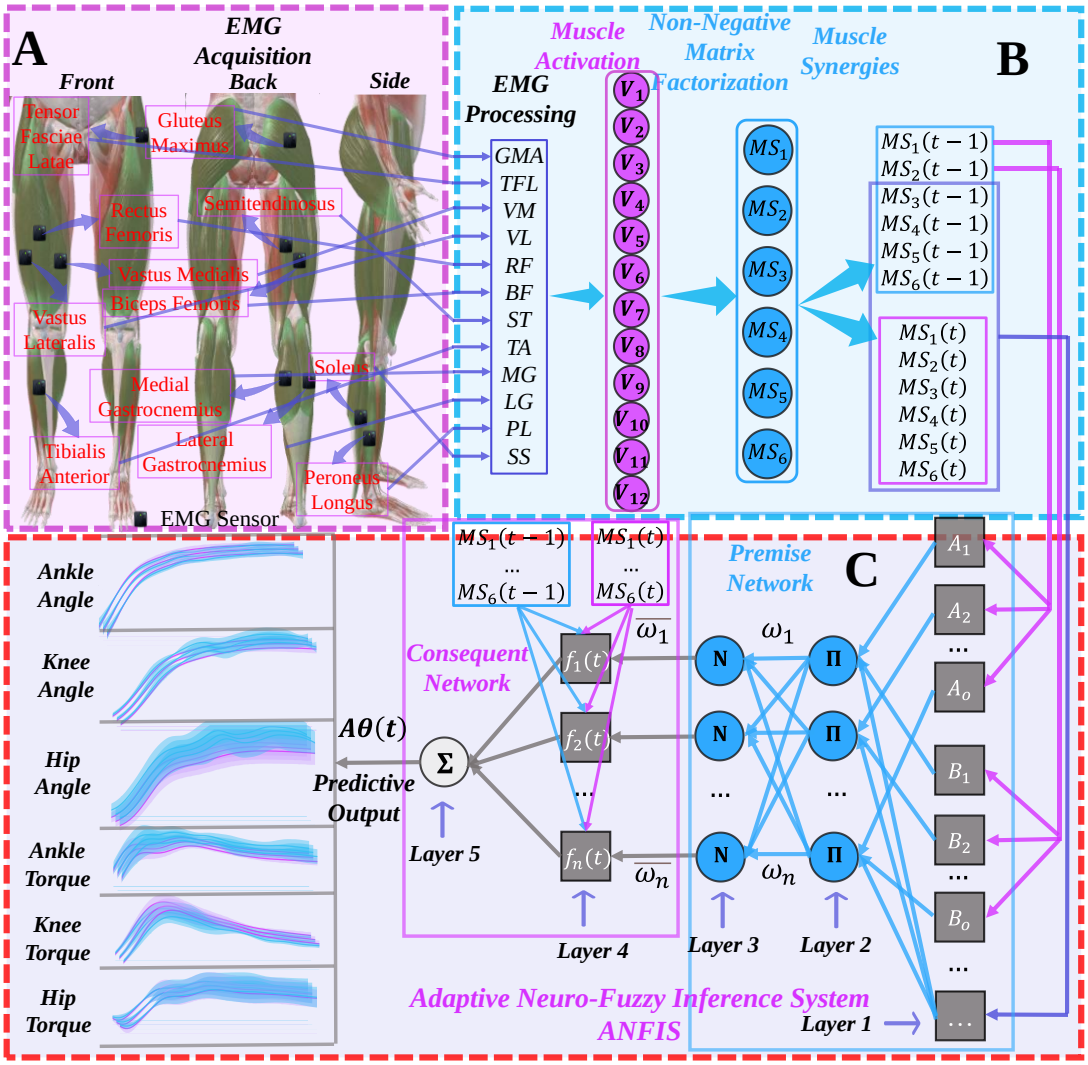

Figure 20 Overview of the study work procedure. (A) Surface EMG signal acquisition. (B) Surface EMG signal processing, muscle activation by the recursive model of the second-order differential equation, and muscle synergy extraction by the NNMF model. (C) ANFIS non-linear regression model estimates the human movement intention.

2.7.1 Experiment protocol and data collection

Sixteen healthy male subjects and sixteen male patients (symptomatic patellar tendinopathy) were recruited for this study (**Table 6**). For the healthy group, subjects reported no history of severe lower-extremity surgery or any other injury variables within the previous six months. For the patient group, subjects had to: 1) anterior knee pain that is felt in the inferior and lower poles of the patella; 2) a diagnosis that the superior patellar tendon is abnormal; 3) the existence of patellar tendon pain during landing tasks, but not sufficient to limit or affect performance levels; 4) history of activity-related pain, VISA-P score < 80; 5) patellar tendinopathy exists in the dominant leg [6, 216, 217]. The leg that is better suited for kicking the ball was defined as the dominant leg [1]. The subject was given a detailed explanation of the experiment's objectives, prerequisites and steps. This study was approved by Ningbo University's

Ethics Committee (Approval Number: RAGH20220310), and all subjects provided and signed written informed consent.

Table 6 Anthropometric parameters and VISA-P score between the healthy and patient groups.

	Healthy group	Patient group
Age (year)	22.6±3.1	23.5±3.6
Body Mass (kg)	79.2±7.0	77.5±6.2
Height (m)	1.80±0.06	1.79±0.05
VISA-P	/	59.1±8.7

Experiments were performed in the Ningbo University biomechanics laboratory, equipped with an eight-camera motion capture system (Vicon Metrics Ltd., UK), two force plates (AMTI, Watertown, UAS), sixteen-channel wireless EMG (Delsys, Boston, MA, USA), and the sampling frequencies were sampled at 200h Hz, 1000 Hz, and 1000 Hz, respectively. As shown in **Figure 21**, thirty-eight reflective markers were placed on the subject's body to track movement, and twelve wireless EMG sensors were used to measure the surface EMG signal (**Figure 21A**). The musculoskeletal modeling was performed based on the pipeline that had been constructed from previous models (**Figure 21B**) [77, 78, 89]. The maximal voluntary contraction (MVC) for selected twelve muscles was also collected to standardize the muscle activation [89]. The lower limb biomechanics data during stair descent were collected to validate the proposed estimation model (**Figure 21C**).

The placement of reflective markers in all subjects was performed by the same experimenter and checked by another experimenter. All subjects were required to wear tights, leggings, and uniform shoes, and warmed up for 10 minutes by running at their own pace in the laboratory, then they acquainted themselves with the experimental procedure. After the reflective markers and EMG sensors were affixed, subjects were asked to stand on the force plate in a standard anatomical posture with their feet open, shoulder width apart, arms open to 45° oblique downward, and they were visually ahead and kept motionless until the experimenter completed static data collection.

A jumping platform with three sections of stairs (30 cm high/section) was placed directly in front of the force plate, and the subject stood on the jump platform with his hands on his hips. After hearing the "begin" signal from the experimenter, the subject moves the dominant leg forward, and leans forward to walk down naturally to the stair descending. When the subject reached the third step, the dominant leg step-off lands on the center of the force plate, and then lands on one leg for support and balance. A successful experiment was defined as the subject's ability to balance on the dominant leg for 3 seconds without any tendency to fall. For each subject, the experimental test was completed in two days (Day 1, Day 2), and 5 successful trial datasets were collected for Day 1 and Day 2 according to the same steps.

The data of the step-off landing phase from the initial contact force point (vertical ground reaction force > 10N) to the maximum knee flexion was selected for analysis [2, 3]. The data was initially processed in Vicon Nexus software, then the exported C3D

files from Vicon Nexus were imported into Visual 3D 6.7.3 (C-Motion Inc., Germantown, US) software for further modeling process [1]. For the ankle knee hip joint, the joint angle and torque were calculated by using the built-in inverse kinematics and inverse dynamics algorithms in Visual 3D. Fourth-order zero-phase lag Butterworth low-pass filters with frequencies of 10 and 20 Hz were used to filter the angle and torque data [19].

For the collected EMG signal of the MVC and step-off landing test, the raw signals were band-pass filtered with a Butterworth fourth-order filter in the frequency range of 10-400 Hz firstly, followed by full-wave rectification, and finally low-pass filtered with a 6 Hz cut-off frequency (based on the determined most appropriate signal-to-noise ratio) [149]. All data were imported into MATLAB R2022a (Visual R2022a, MathWorks, United States) to expand into 101 data points (0%-100% landing phase).

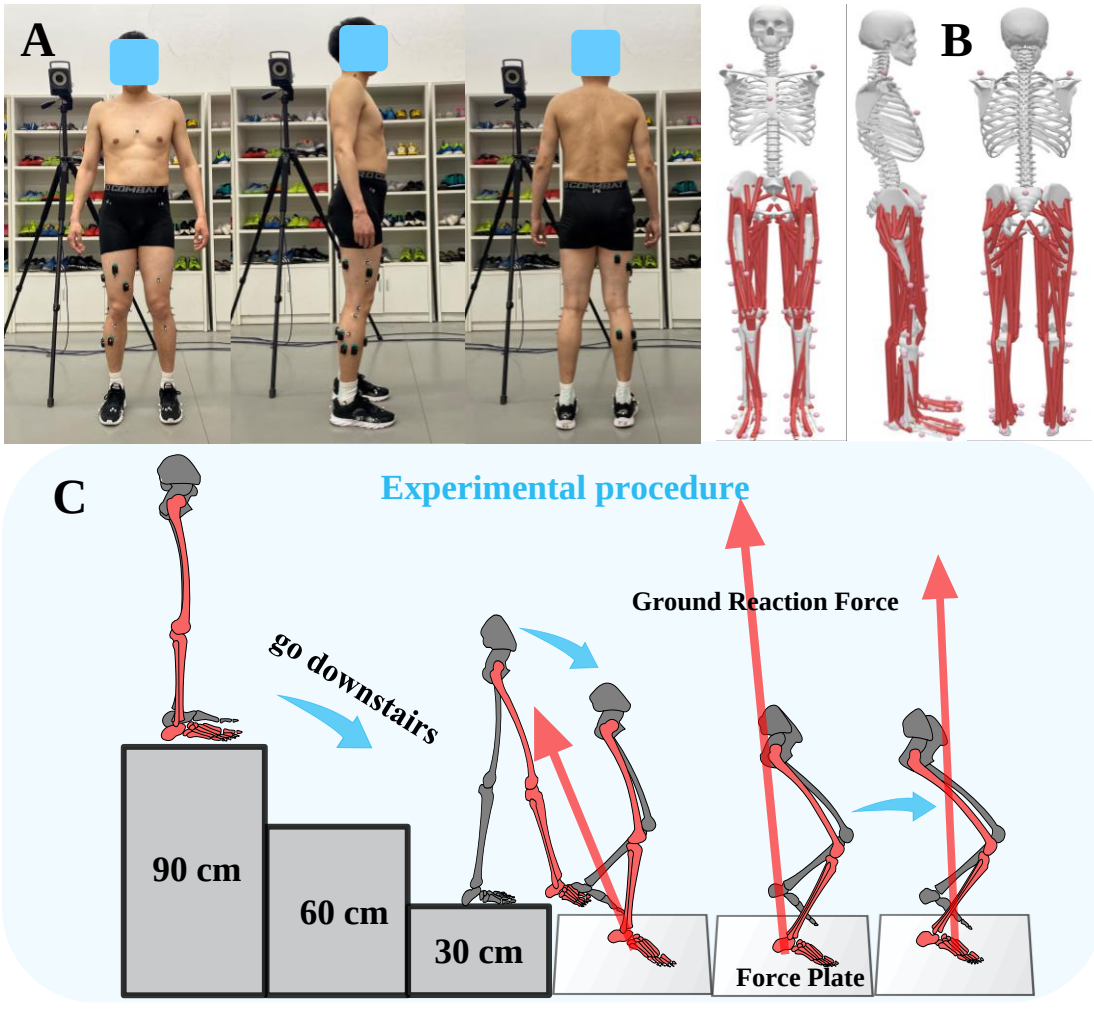

Figure 21 Overview of the musculoskeletal model and whole study experimental procedure. (A) Illustration of the position of the reflective marking points and EMG sensors. (B) Illustration of the constructed musculoskeletal model. (C) Illustration of the experimental procedure.

2.7.2 Muscle activation Model

EMG signal was normalized by dividing the maximum EMG amplitude of MVC by the maximum root mean square amplitude to obtain the normalized signal $e_i(t)$. Muscle activation mirrors the degree of active force generated by the muscle. This study used a recursive model (second-order differential equation) to solve the muscle activation $a_i(t)$ by the obtained normalized signal $e_i(t)$ (**Figure 20B**) [126, 180]. First, the neural activation $u_i(t)$ was solved by $e_i(t)$:

$$u_i(t) = \alpha e_i(t-d) - \beta_1 u_i(t-1) - \beta_2 u_i(t-2) \quad (40)$$

Where the t means the activation at time t, and the single neural activation $u_i(t)$ was related to the previous two activations $u_i(t-1)$ and $u_i(t-2)$. The $d = 10\,ms$ is the electromechanical delay, and α, $\beta_1 = C_1 + C_2$, $\beta_2 = C_1 \times C_2$ are the coefficients defining the second-order dynamics. These parameters map $e_i(t)$ to $u_i(t)$, which is the key to forming a stable equation, and must satisfy the following conditions:

$$\alpha = 1 + \beta_1 + \beta_2 \quad (41)$$

The C_1, C_2 satisfy $|C_1| < 1$, $|C_2| < 1$. Then, the muscle activation $a_i(t)$ was solved by the non-linear model [126]:

$$a_i(t) = \frac{e^{A_i u_i(t)} - 1}{e^{A_i} - 1} \quad (42)$$

Where the A_i is the nonlinear shape coefficient and represents the degree of nonlinearity of the neural activation $u_i(t)$ and muscle activation $a_i(t)$. The range of A_i is allowed from -3 (highly exponential) to 0 (linear relationship), and the current study takes A_i to be 1.5 [180].

2.7.3 Non-negative matrix factorization extracts muscle synergies

For the raw muscle activation matrix $V \in R_+^{i \times j}$, in which all the matrix elements decomposed under non-negative constraints [218]. In this study, the number of muscles $i = 12$ (12 Selected Muscles), the length of data points $j = 101$ (101 data points in each trial). The dataset for each successful trial in each subject corresponds to a set of V. By finding $W \in R_+^{i \times k}$ and $C \in R_+^{k \times j}$ satisfying the unconstrained condition, the raw muscle activation matrix V was abstracted as the product of the W and C:

$$V_{(i \times j)} = W_{(i \times k)} \times C_{(k \times j)} \quad (43)$$

W is the muscle synergy matrix, which represents the basis vectors of the synergy space. C is the synergy activation coefficient matrix, which represents the activation coefficients of the synergy space. The k is the number of muscle synergies ($k < i$). The current study set the activation coefficients of muscle synergy space C as inputs to drive the ANFIS model. In this process, each trial (10 trials) dataset for each subject is solved for a set of muscle synergy space data. In the process of solving W and C, the approximation error $E \in R_+^{i \times j}$ was introduced, then:

$$V_{(i \times j)} = W_{(i \times k)} \times C_{(k \times j)} + E_{(i \times j)} \quad (44)$$

By continuously reducing the error E, $W \times C$ is constantly approaching V, which transforms the problem into an approximate optimal solution [144]:

$$min_{W,H}\|V - W \times C\| \quad (45)$$

Based on the situation that the error E follows a Gaussian distribution and takes the natural logarithm, the log-likelihood function is obtained:

$$L(W,C) = \sum_{i,j} ln\frac{1}{\sqrt{2\pi}\sigma_{ij}} - \frac{1}{\sigma_{ij}} \times \frac{1}{2}\sum_{i,j}\left[V_{(i\times j)} - (WC)_{(i\times j)}\right]^2 \quad (46)$$

Here, the variance of the error E of each data point is the same, and the objective function is derived from the Euclidean distance measure:

$$J(W,C) = \frac{1}{2}\sum_{i,j}\left[V_{(i\times j)} - (WC)_{(i\times j)}\right]^2 \quad (47)$$

Then, substituting $(WC)_{(i\times j)} = \sum_k W_{(i\times k)} \times C_{(k\times j)}$ into Eq.8 and iterating W and C through the gradient descent can be obtained as follows:

$$W_{(i\times k)} = W_{(i\times k)} - \alpha_1 \times \left[(VC^T)_{(i\times k)} - (WCC^T)_{(i\times k)}\right] \quad (48)$$

$$C_{(k\times j)} = C_{(k\times j)} - \alpha_2 \times \left[(W^TV)_{(k\times j)} - (WCW^T)_{(k\times j)}\right] \quad (49)$$

Substitute $\alpha_1 = \frac{W_{(i\times k)}}{(WCC^T)_{(i\times k)}}$ and $\alpha_2 = \frac{C_{(k\times j)}}{(WCW^T)_{(k\times j)}}$ into Eq.5 and Eq.6, which is the multiplicative iteration rule, and finally obtain:

$$W_{(i\times k)} = W_{(i\times k)} \times \frac{(VC^T)_{(i\times k)}}{(WCC^T)_{(i\times k)}} \quad (50)$$

$$C_{(k\times j)} = C_{(k\times j)} \times \frac{(W^TV)_{(k\times j)}}{(WCW^T)_{(k\times j)}} \quad (51)$$

The data are then taken into the model for further calculations to determine the number of muscle synergies k. Because the different k has different accuracy for the reconstructed muscle activation matrix V_r, the reconstruction accuracy is determined by the Variability Accounted For (VAF):

$$\text{VAF} = 1 - \frac{\sum_{i,j}(V - V_r)^2_{i,j}}{\sum_{i,j} V^2_{i,j}} \quad (52)$$

The $\text{VAF} \in [0,1]$, a larger value of VAF represents that the reconstructed muscle activation matrix V_r from $W_{(i\times k)}$ and $C_{(k\times j)}$ is closer to the raw muscle activation matrix V. When the VAF value was greater than a certain threshold, it was considered that the selected muscle synergy numbers could fully reconstruct the raw muscle activation matrix V. This study set the $\text{VAF} > 90\%$ as the stopping condition for the calculation, and the number of muscle synergies determined by the current calculation was selected [128].

2.7.4 Muscle synergy driven adaptive network fuzzy inference system estimates lower limb joint movement

Taking the estimation of the ankle Angle $A\theta(t)$ as an example, this section describes in detail the modeling development process for estimating lower limb joint movements during step-off landing with muscle synergy driven ANFIS. As shown in **Figure 20C**, the ANFIS network has a total of five layers and consists of two parts: premise network and consequent network. The first layer of the premise network is the input layer, which is responsible for feeding the input variable S_n (extracted muscle synergies) to the next layer. This study integrated the muscle synergy space of the original time series $MS(t)$ and the muscle synergy space with the first-time data point removed $MS(t-1)$ as input variables, then:

$$MS_1(t-1), MS_2(t-1), \dots, MS_k(t-1) = S_1, S_2, \dots, S_6 \quad (53)$$

$$MS_1(t), MS_2(t), \dots, MS_k(t) = S_7, S_8, \dots, S_{12} \quad (54)$$

Where the $n = 1,2,\dots,12$ is the n-th input variables, $k = 1,2,\dots 6$ is the k-th muscle synergies. In the input layer, each input variable S_n is fuzzified based on the input parameters, and the membership function is assigned for the corresponding fuzzy set $(A_1, A_2, \dots, A_o)$:

$$O_n^1 = \mu_{A_1}(S_1)_n,\ \mu_{A_2}(S_2)_n, \dots, \mu_{A_o}(S_m)_n \quad (55)$$

Where o is the number of clusters, the m is the m-th fuzzy rules, $\mu_{A_o}(S_m)_n$ means the situation of the m-th fuzzy rules in the n-th input muscle synergy variables. The membership function follows the Gaussian membership function [145]:

$$\mu_{A_o}(S_m)_n = \exp - [\frac{s_n - (c_m)_n}{(\sigma_m)_n}]^2 \quad (56)$$

Where the s_n is the input parameter of the fuzzy system, $(c_m)_n$ and $(\sigma_m)_n$ form the set of premise parameters for ANFIS, representing the center and width of the membership function respectively.

The second layer of the premise network is the strength-release layer of the fuzzy rules. Each node Π represents a fuzzy rule to enable the operation on the fuzzy set of the first layer and the output represents the confidence level of the rule [145]:

$$O_n^2 = \omega_n = \mu_{A_1}(S_1)_n \times \mu_{A_2}(S_2)_n \times \dots \times \mu_{A_o}(S_m)_n = \prod_1^m \mu_{A_o}(S_m)_n \quad (57)$$

The third layer of the premise network normalizes the output of the second layer:

$$O_n^3 = \overline{\omega_n} = \frac{\omega_n}{\sum_n \omega_n} \quad (58)$$

The consequent network consists of several subnetworks, each of which produces an output variable. The first layer of the consequent network is the input layer, and each node in the second layer is the adaptive point, which matches the consequent of the fuzzy rule to calculate the output of each fuzzy logic:

$$O_n^4 = \overline{\omega_n} f_n(t) \quad (59)$$

The essence of fuzzy rules is the fuzzy implication relation, and the fuzzy implication relation R^m of the fuzzy set A_m^n is:

R^m: $if\ MS_1(t-1) is\ A_m^1, MS_2(t-1) is\ A_m^2, MS_3(t-1) is\ A_m^3, MS_4(t-1) is\ A_m^4, MS_5(t-1) is\ A_m^5, MS_6(t-1) is\ A_m^6,$
$and\ MS_1(t)\ is\ A_m^7, MS_2(t)\ is\ A_m^8, MS_3(t)\ is\ A_m^9, MS_4(t)\ is\ A_m^{10}, MS_5(t)\ is\ A_m^{11},$
$S_k(t)\ is\ A_m^{12};$
$then\ :\ f_n(t) = (\gamma_m)_1 \times MS_1(t-1) + (\gamma_m)_2 \times MS_2(t-1) + \cdots + (\gamma_m)_n \times S_k(t) + (\gamma_m)_{n+1}$

Where the $(\gamma_m)_n$ means the consequent parameter, the output of the fourth layer:

$$\overline{\omega_n} f_n(t) = \overline{\omega_n} \times [(\gamma_m)_1 \times MS_1(t-1) + (\gamma_m)_2 \times MS_2(t-1) + \cdots + (\gamma_m)_n \times S_k(t) + (\gamma_m)_{n+1}] \quad (60)$$

The fourth layer of the premise network is the output layer of the whole system, which is a fixed node and responsible for the calculation of the total output $A\theta(t)$:

$$O_n^5 = A\theta(t) = \sum_n \overline{\omega_n} f_n(t) = \overline{\omega_1} f_1(t) + \overline{\omega_2} f_2(t) + \cdots + \overline{\omega_n} f_n(t) \quad (61)$$

Substituting Eq. 8 to Eq. 11 into the above equation, the final estimation of ankle joint angle is obtained:

$$A\theta(t) = \sum_n \frac{\prod_1^m \mu_{A_o}(S_m)_n}{\sum_1^n \prod_1^m \mu_{A_o}(S_m)_n} \times [(\gamma_m)_1 \times MS_1(t-1) + (\gamma_m)_2 \times MS_2(t-1) + \cdots + (\gamma_m)_n \times S_k(t) + (\gamma_m)_{n+1}] \quad (13) \quad (62)$$

2.7.5 Parameters determination of ANFIS model

The parameters that need to be modified by learning in the ANFIS network are $(c_m)_n$, $(\sigma_m)_n$ of the membership function in the second layer of the premise network, and the consequent parameter $(\gamma_m)_n$. In this study, a hybrid Learning algorithm is used to continuously learn and modify these parameters [145]. First, the algorithm calculates the error by comparing the simulated outputs of the ANFIS network with the real result data (expected output):

$$E = \frac{1}{2} \sum_m [\widehat{A\theta(t)} - A\theta(t)]^2 \quad (63)$$

Where the $\widehat{A\theta(t)}$ is the expected output, the $A\theta(t)$ is the actual ANFIS system output. After that, the E was processed by backpropagation and the $(c_m)_n$ and $(\sigma_m)_n$ were modified by the gradient descent method [145].

2.7.6 Fuzzy rule determination of ANFIS model

The determination of fuzzy rule in the ANFIS network is based on the rules and properties of the input parameters, and the traditional method of Grid partitioning is generally adopted. After generating the first-order fuzzy inference system, this method continuously modifies its parameters to train the optimization network according to the above algorithmic model. It shows the following disadvantages: 1) The rules and properties of the original data cannot be completely described in the initial processing; 2) The constructed fuzzy inference system has a large computational volume, long computation time, low simulation accuracy error, and the model cannot converge [145].

Therefore, this study clustered the training samples by the subtractive clustering algorithm (SCA) [219]. After generating an optimized fuzzy inference system based on the clustering results, the optimal fuzzy rules and their number can be determined by the learning calculation of the neural network, which calculates the system more rapidly and accurately.

The essence of SCA belongs to density index clustering, which can adaptively determine the number of clusters at the density center to estimate the number of clusters and the location of cluster centers in the original data [219, 220]. The clustering results can be used in the fuzzy inference logic of the initial ANFIS. For the dataset $Z = \{X_1, X_2, \dots, X_U\}, X_U = [MS_k(t-1), MS_k(t)], k = 1,2, \dots 6$, the algorithm steps are as follows:

(1) Calculating the density values of all X_U in Z, the density function D_U:

$$D_U = \sum_{u=1}^{U} \exp\left[-\frac{\|X_v - X_u\|^2}{\frac{r_a{}^2}{4}}\right](u, v = 1,2, \dots U) \quad (64)$$

Where the r_a is the neighborhood radius of X_v: $r_a = \frac{1}{2} min_k[max_U(\|X_v - X_k\|)]$, X_v is made up of input and output data pairs. Then, the X_{c1} with the highest density value D_{c1} is selected as the first cluster center.

(2) When the X_{ck} with the highest density value D_{ck} is selected, the point value is used as the second cluster center: The formula for calculating the other elemental density indicators is updated as follows:

$$D_U = D_U - D_{ck}\exp[-\frac{\|X_v - X_{ck}\|^2}{\frac{r_b{}^2}{4}}](r_b = 1.2r_a) \quad (65)$$

(3) The above steps are repeated until the calculation results satisfy the threshold set for the likelihood of new cluster centers δ:

$$\delta > \frac{D_{k+1}}{D_1} \quad (66)$$

The number of fuzzy rules m is determined by the number of clusters, the $(c_m)_n$ and $(\sigma_m)_n$ are determined by the cluster center and radius respectively.

2.7.7 Performance evaluation of estimation outputs

The mean absolute percentage error ($MAPE$), root mean square error ($RMSE$), normalized RMSE ($NRMSE$), the square of correlation coefficient (R^2) were calculated to evaluate the accuracy of the estimation outputs. For the value of $MAPE$, $RMSE$, and $NRMSE$, the magnitude of the value depends on the magnitude of the estimation error, the larger the error the larger the value. The equation is as follows:

$$E_{MAPE} = \frac{1}{N}\sum_{i=1}^{N}\left|\frac{Y_i^{mea} - Y_i^{pre}}{Y_i^{mea}}\right| \quad (67)$$

$$E_{RMSE} = \sqrt{\frac{1}{N}\sum_{i=1}^{N}(Y_i^{mea} - Y_i^{pre})^2} \quad (68)$$

$$E_{NRMSE} = \frac{E_{RMSE}}{(Y_{max}^{mea} - Y_{min}^{mea})} \times 100\% \quad (69)$$

Where the N means the number of data points during the step-off landing phase, Y_i^{mea} and Y_i^{pre} are the measured and estimated results at data point i, Y_{max}^{mea} and Y_{min}^{mea} are the maximum and minimum values of the measured results.

The R^2 represents the degree of the correlation between the estimation outputs and the measured results, and its value closer to 1 implies a higher correlation and lower error. The equation is as follows:

$$E_{R^2} = \frac{\sum_{i=1}^{N}(Y_i^{pre} - \overline{Y^{mea}})^2}{\sum_{i=1}^{N}(Y_i^{mea} - \overline{Y^{mea}})^2} \quad (70)$$

Where the $\overline{Y^{mea}}$ is the average value of the measured results.

2.7.8 Model configurations and statistical analysis

As the current study sample did not cover the majority cases of muscle synergy patterns, the data from Day 1 were used as the training set, and the data from Day 2 were used as the testing set. For the estimation of sagittal joint angles and torques under each joint (ankle, knee, hip) in each subject group (healthy and patient), each estimation situation was input into the model separately. Data points from the different subjects of each estimation situation were combined together and shuffled.

Both in the training set and testing set, the data dimension for the muscle synergy space of the original time series $MS(t)$ is $\mathbb{M}^{k\times 8080}$ ($8080 = 101_{\text{data points}} \times 5_{trails} \times 16_{subjects}$). However, when solving for the joint torque in the dynamic scenario, it is considered that the torque at the current time data point needs to be determined based on the combined computation of variables such as the angle at the previous time data point, which can result in the joint torque lagging by one time data point [155]. Therefore, the current study integrated the muscle synergy space of the original time series $MS(t)$ and the muscle synergy space with the first-time data point removed $MS(t-1)$ as input variables, which allows the model to obtain more information about the time series variation. To maintain consistency with the dimension of the original $MS(t)$, this study also expanded the dimension of $MS(t-1)$ to 101 data points. Therefore, both in the training set and testing set, the final dimension of the input variable is $\mathbb{M}^{2k\times 8080}$.

For the estimation errors difference between the healthy and patient groups, the Independent-samples t-test was used (significant level $P < 0.05$). Pearson correlation analysis was conducted to explore the correlation of the synergy activation coefficient matrix between subjects.

3. Results

3.1 Influence of fatigue factors on lower limb biomechanical patterns during landing

3.1.1 Landing pattern variable difference between before-fatigue and after-fatigue

Figure 22A presents the comparison results of muscle activation between the results collected by the EMG sensor and the results obtained by musculoskeletal modeling simulation, both of which show a strong correlation with each other (Correlation coefficient greater than 0.85) [159]. Therefore, the activation of the six selected muscles remained consistent in most of the time and frequency domains in both conditions, which suggested that the simulation results obtained based on the established musculoskeletal model in the current study had high reliability [78, 89].

The raw data waveform of joint angle and joint moment of each joint (ankle, knee, hip) of each plane (sagittal, frontal, transversal) and sagittal joint power during the landing phase between before-fatigue and after-fatigue are presented in **Figure 23**. The raw data waveform of ACL force is presented in **Figure 22B**. Compared to before-fatigue SL, after-fatigue SL shows smaller knee and hip flexion, and greater ACL forces during the landing phase.

For the detailed results of AICA, AROM, PAF, AED, KED and HED, their distribution trends and recognizability between before-fatigue and after-fatigue are presented in **Figure 24**, and the specific values of the recognizability are presented in **Table 7**. The recognition accuracy of AICA, KED and PAF all exceeded 70%. All variables presented statistically significant differences (**Table 8**). Compared with the before-fatigue, the AICA (**Figure 24A**), AROM (**Figure 24B**), AED (**Figure 24D**), KED (**Figure 24E**), and HED (**Figure 24F**) are reduced in after-fatigue, but the PAF (**Figure 24C**) is increased. In general, there were significant differences in landing patterns between before-fatigue and after-fatigue.

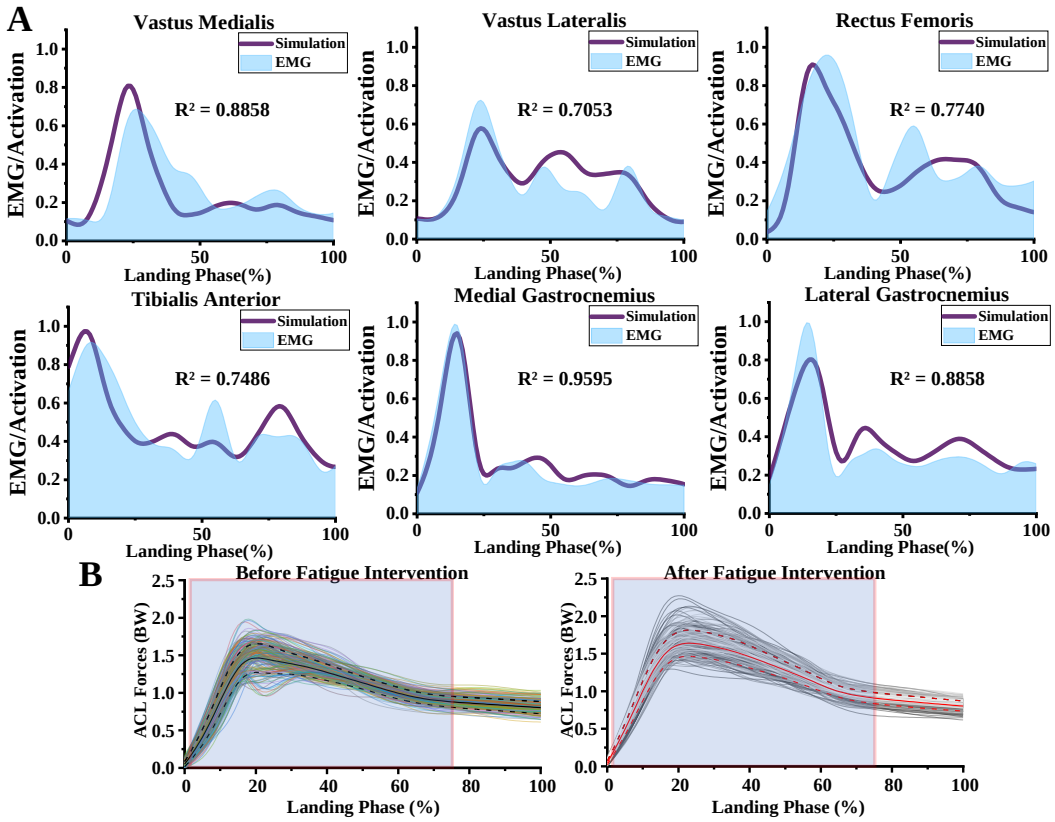

Figure 22 Detail results of EMG/Activation and ACL force. (A) Illustration of the EMG/Activation of selected muscles. The results of the simulation were calculated from the established musculoskeletal model in OpenSim software. The results of EMG were obtained from the EMG sensors. The muscle activation was normalized on a scale of 0 (no activation) to 1 (all activation). R^2 represents the square of the correlation coefficient. (B) Visualization of ACL force during the landing phase between before-fatigue and after-fatigue. The color curve is the full test data set for the SL test of before-fatigue, and the black curve and the line are the mean and standard deviation of these data sets. The gray curve is the full test data set for the SL test of AF, and the red curve and the line are the mean and standard deviation of these data sets. By comparing the magnitude of the ACL force, the shaded area within the red box indicates that the ACL force of after-fatigue is greater than that of before-fatigue during the landing phase at this stage.

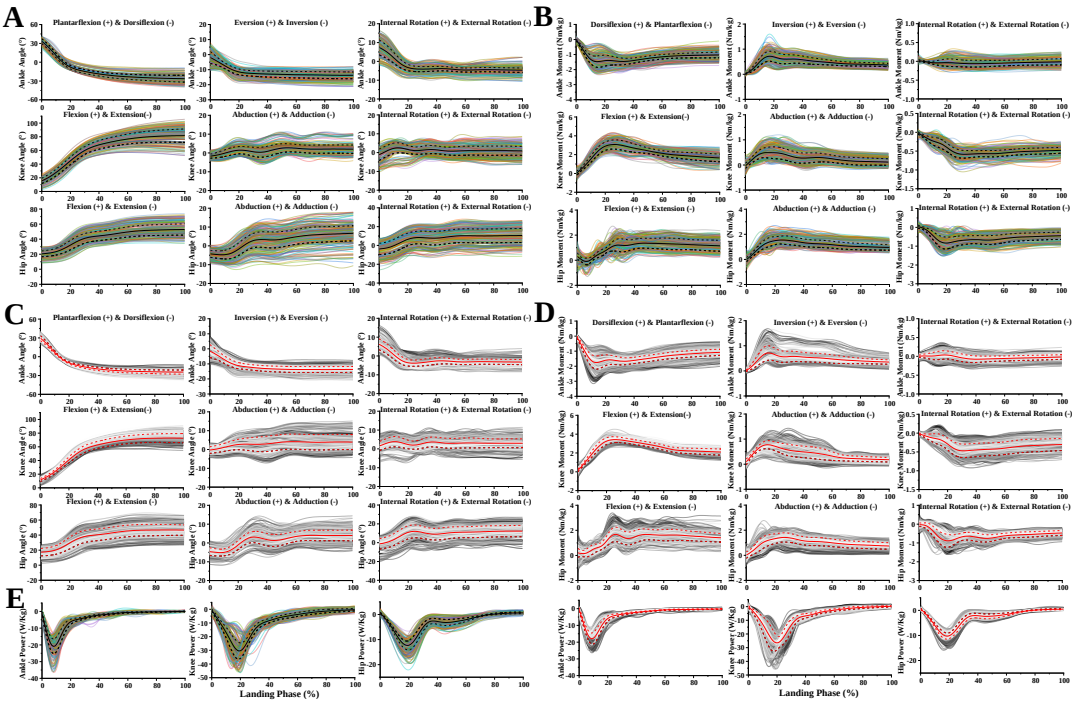

Figure 23 Visualization of joint angle and joint moment of each joint (ankle, knee, hip) of each plane (sagittal, frontal, transversal) and sagittal joint power during the landing phase between before-fatigue and after-fatigue SL. (A) The raw joint angle data waveform during the landing phase of the SL of before-fatigue. (B) The raw joint moment data waveform during the landing phase of the SL of before-fatigue. (C) The raw joint angle data waveform during the landing phase of the SL of after-fatigue. (D) The raw joint moment data waveform during the landing phase of the SL of after-fatigue. (E) The raw joint power data waveform during the landing phase. Y-axis means the 0%-100% landing phase. The anatomical definition is presented at the top of the Figure. The color curve is the full test data set for the SL of before-fatigue, and the black curve and the line are the mean and standard deviation of these data sets. The gray curve is the full test data set for the SL of after-fatigue, and the red curve and the line are the mean and standard deviation of these data sets.

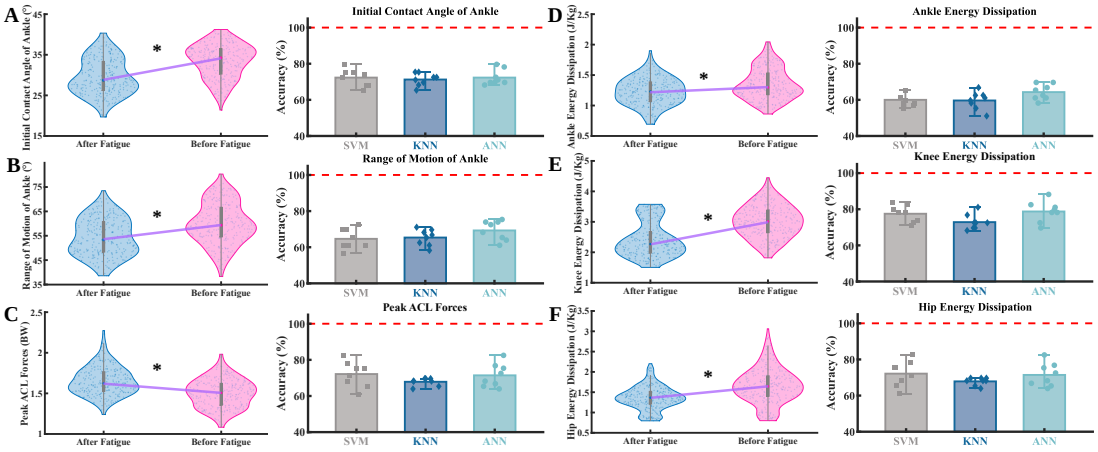

Figure 24 Detailed results of the distribution trends for six discrete variables, and their

recognizability and classification accuracy between before-fatigue and after-fatigue. (A) Results of AIC. (B) Results of AROM. (C) Results of PAF. (D) Results of AED. (E) Results of KED. (F) Results of HED. The left side is the violin plot of 560 discrete data distributions. The right side is the variables classification and recognition results based on the three different classification algorithm models. SVM: Support Vector Machine. KNN: K-Nearest Neighbor. ANN: Artificial Neural Network. "*" means the significance with $p < 0.05$.

Table 7 Detailed values of the recognizability and classification accuracy between before-fatigue and after-fatigue were obtained for the three different classification algorithm models (SVM, KNN, ANN) for six variables. Means and standard deviations were obtained based on eight-fold cross-validation.

Input Variables	SVM (%)	KNN (%)	ANN (%)	All (%)
Ankle Initial Contact Angle	72.32±4.73	71.25±3.45	72.32±4.28	71.96±4.04
Ankle Range of Motion	64.64±5.51	65.36±4.45	69.29±5.39	66.43±5.33
Ankle Energy Dissipation	60.00±3.72	59.64±4.83	64.28±4.23	61.31±4.63
knee Energy Dissipation	77.50±4.64	72.86±4.23	78.75±5.76	76.37±5.37
Hip Energy Dissipation	72.14±7.07	67.86±2.13	71.43±6.47	70.48±5.74
Peak ACL Force	70.18±7.26	69.82±7.32	70.18±6.59	70.06±6.75

Table 8 Detailed results of the significant difference for six variables.

Variables	After-Fatigue	Before-Fatigue	95% Confidence Interval	Mean Difference	P
AICA (°)	29.58±5.41	33.47±5.16	[-4.46,-3.32]	-3.89	<0.001
AROM (°)	54.38±8.59	59.99±8.35	[-6.75,-4.45]	-5.60	<0.001
AED (J/Kg)	1.23±0.32	1.35±0.36	[-0.16,-0.08]	-0.12	<0.001
KED (J/Kg)	2.41±0.66	3.01±0.63	[-0.70,-0.51]	-0.61	<0.001
HED (J/Kg)	1.36±0.38	1.66±0.53	[-0.35,-0.25]	-0.30	<0.001
PAF (BW)	1.65±0.23	1.50±0.17	[0.13,0.18]	0.15	<0.001

3.1.2 Relationship between each landing pattern variable

The linear relationship and scatter distribution between PAF and other variables are presented in **Figure 25**. With the increase of AIC, the PAF showed a downward trend, and the $R^2 = 0.4898$ (**Figure 25A**). With the increase of AROM, the PAF also showed a downward trend, and the $R^2 = 0.3768$ (**Figure 25B**). With the increase of TED, the PAF showed a downward trend, and the $R^2 = 0.6110$ (**Figure 25C**). With the increase in AED ($R^2 = 0.5387$), KED ($R^2 = 0.4685$), AED ($R^2 = 0.2527$), the PAF showed a downward trend (**Figure 25D**). There was almost no correlation between PAF and ACTED ($R^2 = 0.0032$), KCTED ($R^2 = 0.0037$), HCTED ($R^2 = 0.0077$) (**Figure 25E**).

The linear relationship and scatter distribution between AICA and other variables of energy dissipation are presented in **Figure 26**. With the increase of AIC, both the AED ($R^2 = 0.6455$), KED ($R^2 = 0.3606$), AED ($R^2 = 0.2198$) showed an upward

trend. There was almost no correlation between AICA and ACTED ($R^2 = 0.0594$), KCTED ($R^2 = 0.0021$), ACTED ($R^2 = 0.0098$).

The linear relationship and scatter distribution between AROM and other variables of energy dissipation are presented in **Figure 27**. With the increase of AROM, both the AED ($R^2 = 0.5850$), KED ($R^2 = 0.3037$), AED ($R^2 = 0.1538$) showed an upward trend. There was almost no correlation between ARM and ACTED ($R^2 = 0.0726$), KCTED ($R^2 = 0.0006$), ACTED ($R^2 = 0.0178$).

Detailed distributions of the absolute value of R between variables are presented in **Figure 28**. **Figure 28A** shows the results based on the SL data that combination of before-fatigue and after-fatigue, and the specific values are presented in **Table 9**. **Figure 7B** shows the results based on the SL data of before-fatigue, and the specific values are presented in **Table 10**. **Figure 7C** shows the results based on the SL data of after-fatigue, and the specific values are presented in **Table 11**. AICA and AROM are strongly correlated with other variables except for each joint contribution to total energy dissipation. PAF is most influenced by AICA and AROM.

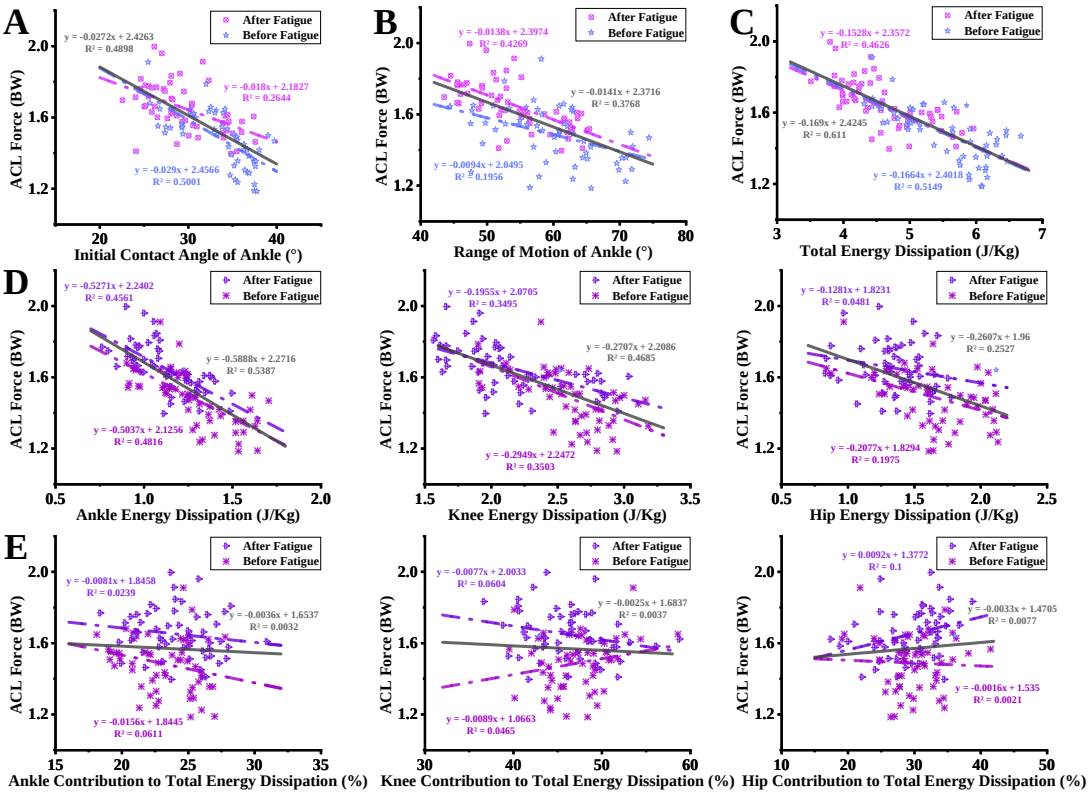

Figure 25 The linear relationship and scatter distribution between PAF and other variables. (A) The linear relationship and scatter distribution between PAF and AIC. (B) The linear relationship and scatter distribution between PAF and AROM. (C) The linear relationship and scatter distribution between PAF and TED. (D) The linear relationship and scatter distribution between PAF and AED, KED, HED. (E) The linear relationship and scatter distribution between PAF and ACTED, AKTED, AHTED. The gray line is the result of a linear fit based on the SL data of before-fatigue and after-fatigue.

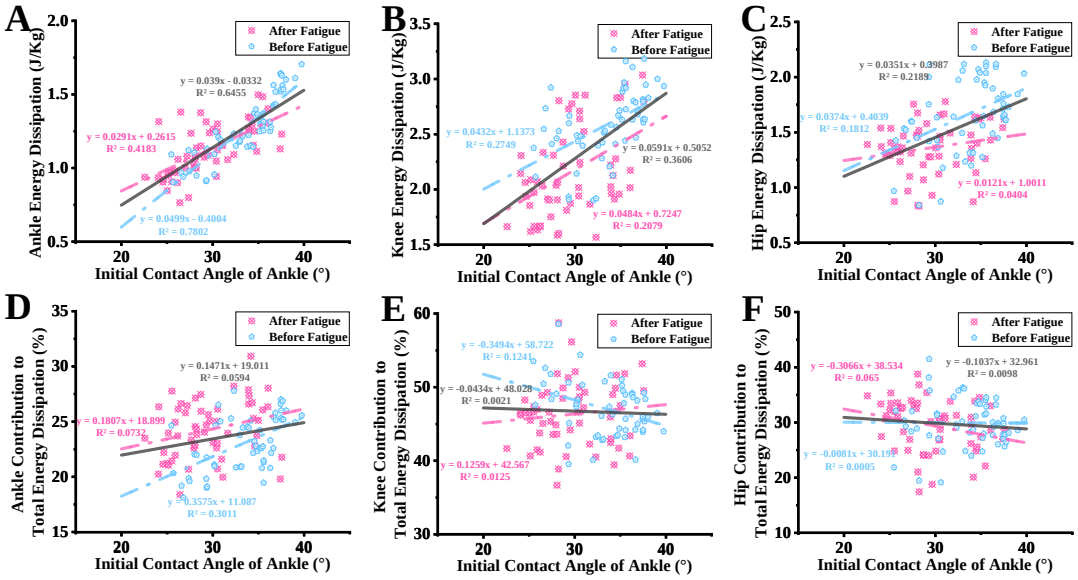

Figure 26 The linear relationship and scatter distribution between ankle initial contact angle and other variables of energy dissipation. (A) The linear relationship and scatter distribution between ankle initial contact angle and ankle energy dissipation. (B) The linear relationship and scatter distribution between ankle initial contact angle and knee energy dissipation. (C) The linear relationship and scatter distribution between ankle initial contact angle and hip energy dissipation. (D) The linear relationship and scatter distribution between ankle initial contact angle and ankle contribution to total energy dissipation. (E) The linear relationship and scatter distribution between ankle initial contact angle and knee contribution to total energy dissipation. (F) The linear relationship and scatter distribution between AICA and hip contribution to total energy dissipation. The gray line is the result of a linear fit based on the SL data of before-fatigue and after-fatigue.

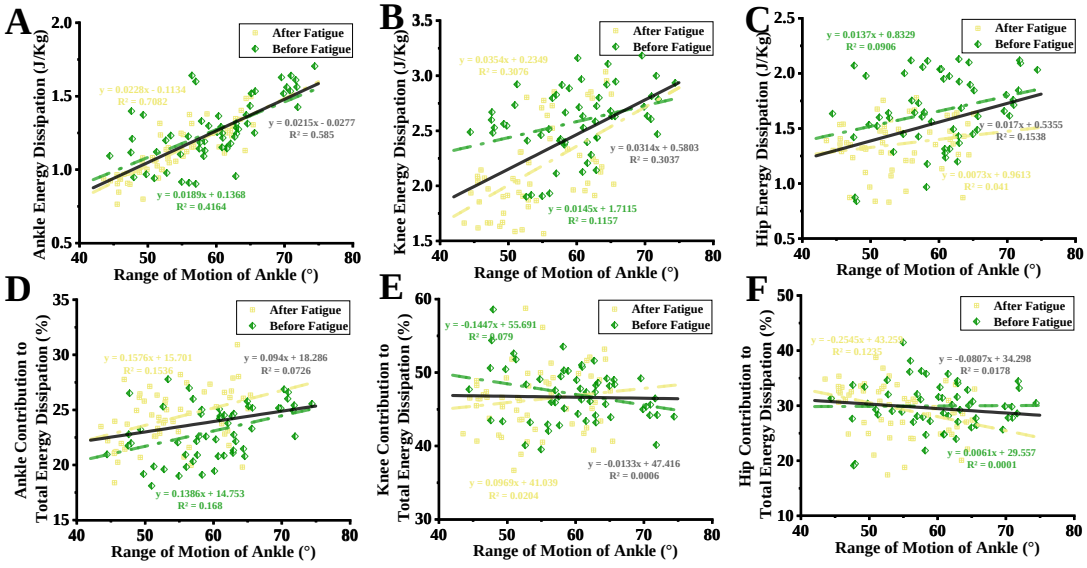

Figure 27 The linear relationship and scatter distribution between ankle range of

motion and other variables of energy dissipation. (A) The linear relationship and scatter distribution between ankle range of motion and ankle energy dissipation. (B) The linear relationship and scatter distribution between ankle range of motion and knee energy dissipation. (C) The linear relationship and scatter distribution between ankle range of motion and hip energy dissipation. (D) The linear relationship and scatter distribution between ankle range of motion and ankle contribution to total energy dissipation. (E) The linear relationship and scatter distribution between ankle range of motion and knee contribution to total energy dissipation. (F) The linear relationship and scatter distribution between ankle range of motion and hip contribution to total energy dissipation. The gray line is the result of a linear fit based on the SL data of before-fatigue and after-fatigue.

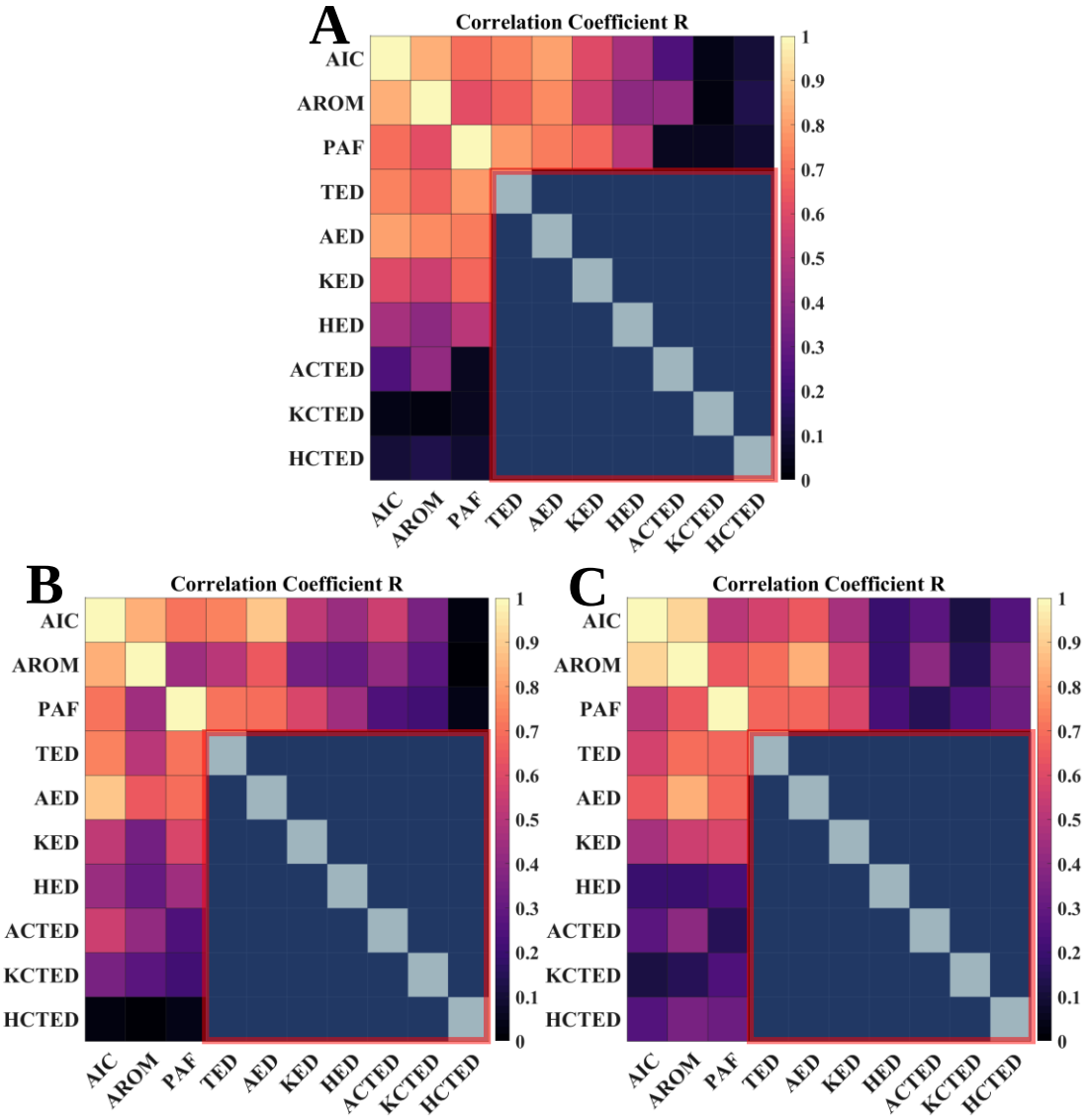

Figure 28 Detailed distributions of absolute value of the correlation coefficient R between variables. (A) Detailed distributions of correlation coefficient R between variables based on the SL data that combination of before-fatigue and after-fatigue. (B) Detailed distributions of correlation coefficient R between variables based on the SL

data of before-fatigue. (C) Detailed distributions of correlation coefficient R between variables based on the SL data of after-fatigue. The closer R-value is to 1, the greater the correlation between the two variables, and the closer R-value is to 0, the smaller the correlation between the two variables. The shaded area within the red box represents that the current study does not consider the correlation between the two variables.

Table 9 Detailed results of correlation coefficient R between variables, which combines the SL data of both before-fatigue and after-fatigue.

	AICA	AROM	PAF	TED	AED	KED	HED	ACTED	KCTED	HCTED
AICA	1.00	0.83	-0.70	0.74	0.80	0.60	0.47	0.24	-0.05	-0.10
AROM	0.83	1.00	-0.61	0.67	0.76	0.55	0.39	0.41	-0.02	-0.13
PAF	-0.70	-0.61	1.00	-0.78	-0.73	-0.68	-0.50	-0.06	-0.06	0.09
TED	0.74	0.67	-0.78	1.00	/	/	/	/	/	/
AED	0.80	0.76	-0.73	/	1.00	/	/	/	/	/
KED	0.60	0.55	-0.68	/	/	1.00	/	/	/	/
HED	0.47	0.39	-0.50	/	/	/	1.00	/	/	/
ACTED	0.24	0.41	-0.06	/	/	/	/	1.00	/	/
KCTED	-0.05	-0.02	-0.06	/	/	/	/	/	1.00	/
HCTED	-0.10	-0.13	-0.09	/	/	/	/	/	/	1.00

Note: The closer R-value is to 1, the greater the correlation between the two variables, and the closer R-value is to 0, the smaller the correlation between the two variables. "/" indicates that the current study does not consider the correlation between the two variables. AICA: Ankle Initial Contact Angle; AROM: Ankle Range of Motion; PAF: Peak ACL Force; TED: Total Energy Dissipation; AED: Ankle Energy Dissipation; KED: Knee Energy Dissipation; HED: Hip Energy Dissipation; ACTED: Ankle Contribution to Total Energy Dissipation; KCTED: Knee Contribution to Total Energy Dissipation; HCTED: Hip Contribution to Total Energy Dissipation.

Table 10 Detailed results of correlation coefficient R between variables, which only considers the SL data of before-fatigue.

	AICA	AROM	PAF	TED	AED	KED	HED	ACTED	KCTED	HCTED
AICA	1.00	0.83	-0.71	0.74	0.88	0.52	0.43	0.55	-0.35	-0.02
AROM	0.83	1.00	-0.44	0.51	0.65	0.34	0.30	0.41	-0.28	0.01

PAF	-0.71	-0.44	1.00	-0.72	-0.69	-0.59	-0.44	-0.25	0.22	-0.05
TED	0.74	0.51	0.72	1.00	/	/	/	/	/	/
AED	0.88	0.65	-0.69	/	1.00	/	/	/	/	/
KED	0.52	0.34	-0.59	/	/	1.00	/	/	/	/
HED	0.43	0.30	-0.44	/	/	/	1.00	/	/	/
ACTED	0.55	0.41	-0.25	/	/	/	/	1.00	/	/
KCTED	-0.35	-0.28	0.22	/	/	/	/	/	1.00	/
HCTED	-0.02	0.01	-0.05	/	/	/	/	/	/	1.00

Note: The closer R-value is to 1, the greater the correlation between the two variables, and the closer r value is to 0, the smaller the correlation between the two variables. "/" indicates that the current study does not consider the correlation between the two variables. AICA: Ankle Initial Contact Angle; AROM: Ankle Range of Motion; PAF: Peak ACL Force; TED: Total Energy Dissipation; AED: Ankle Energy Dissipation; KED: Knee Energy Dissipation; HED: Hip Energy Dissipation; ACTED: Ankle Contribution to Total Energy Dissipation; KCTED: Knee Contribution to Total Energy Dissipation; HCTED: Hip Contribution to Total Energy Dissipation.

Table 11 Detailed results of correlation coefficient R between variables, which only considers the SL data of after-fatigue.

	AICA	AROM	PAF	TED	AED	KED	HED	ACTED	KCTED	HCTED
AICA	1.00	0.92	-0.51	0.57	0.65	0.46	0.20	0.27	0.11	-0.25
AROM	0.92	1.00	-0.65	0.70	0.84	0.55	0.20	0.39	0.14	-0.35
PAF	-0.51	-0.65	1.00	-0.68	-0.68	-0.59	-0.22	-0.15	-0.25	0.32
TED	0.57	0.70	-0.68	1.00	/	/	/	/	/	/
AED	0.65	0.84	-0.68	/	1.00	/	/	/	/	/
KED	0.46	0.55	-0.59	/	/	1.00	/	/	/	/
HED	0.20	0.20	-0.22	/	/	/	1.00	/	/	/
ACTED	0.27	0.39	-0.15	/	/	/	/	1.00	/	/
KCTED	0.11	0.14	-0.25	/	/	/	/	/	1.00	/
HCTED	-0.25	0.35	0.32	/	/	/	/	/	/	1.00

Note: The closer R-value is to 1, the greater the correlation between the two variables,

and the closer r value is to 0, the smaller the correlation between the two variables. "/" indicates that the current study does not consider the correlation between the two variables. AICA: Ankle Initial Contact Angle; AROM: Ankle Range of Motion; PAF: Peak ACL Force; TED: Total Energy Dissipation; AED: Ankle Energy Dissipation; KED: Knee Energy Dissipation; HED: Hip Energy Dissipation; ACTED: Ankle Contribution to Total Energy Dissipation; KCTED: Knee Contribution to Total Energy Dissipation; HCTED: Hip Contribution to Total Energy Dissipation.

3.2 Exploring landing pattern differences before and after fatigue based on explainable machine learning

3.2.1 Kinematics and kinetics data waveform of landing pattern

The raw kinematics (joint angle) and kinetics (joint moment) data waveform of each joint (ankle, knee, hip) of each plane (sagittal, frontal, transversal) during the landing phase between before fatigue and after fatigue single-leg landing are shown in **Figure 2**. **Figure 2A** and **Figure 2B** display the raw joint angle and moment data waveform during the landing phase of the single-leg landing of before fatigue intervention, respectively. **Figure 2C** and **Figure 2D** show the raw joint angle and moment data waveform during the landing phase of the single-leg landing of after fatigue intervention, respectively.

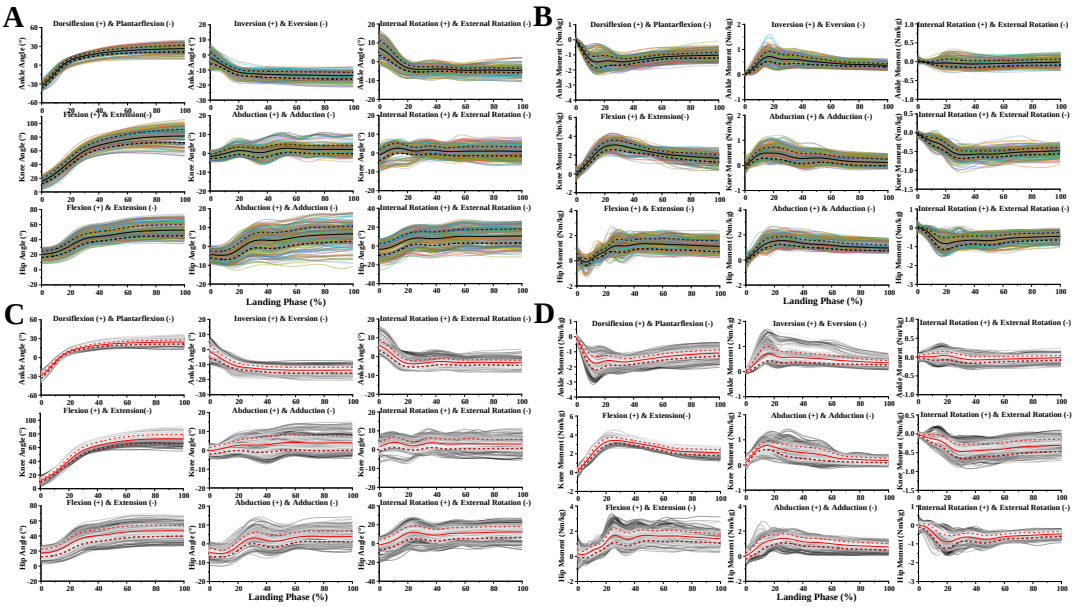

Figure 29 Visualization of joint angle and joint moment of each joint (ankle, knee, hip) of each plane (sagittal, frontal, transversal) during the landing phase between before fatigue and after fatigue single-leg landing. (A) The raw joint angle data waveform during the landing phase of the single-leg landing of before fatigue intervention. (B) The raw joint moment data waveform during the landing phase of the single-leg landing of before fatigue intervention. (C) The raw joint angle data waveform during the landing phase of the single-leg landing of after fatigue intervention. (D) The raw joint moment data waveform during the landing phase of the single-leg landing of after fatigue intervention. Y-axis means the 0%-100% landing phase. The anatomical definition is shown at the top of the figure. The color curve is the full test data set for the landing of before fatigue intervention, and the black curve and the line are the mean and standard deviation of these data sets. The gray curve is the full test data set for the landing of after fatigue intervention, and the red curve and the line are the mean and standard deviation of these data sets.

3.2.2 Classification results

The result distribution of prediction accuracy rate and ZRB was shown in **Figure**

30, and the details of means and standard deviations and ZRB were shown in **Table 12**. Comparison results of classification accuracy of nine classification tasks under three algorithm models were shown in **Figure 30A**. The ANN model showed better classification performance than SVM and CNN in all nine classification tasks, especially in the three classification tasks that took separate ankle, knee, and hip data as input signals. Comparison results of classification accuracy of three algorithm models under nine classification tasks were shown in **Figure 30B**. The classification performance that is based on both kinematics and kinetics as input signals are better than the classification performance that is based on only kinematics or only kinetics as input signals. The classification performance that is based on the knee data as input signals was better than the classification performance that is based on the ankle data or only hip data as input signals. The classification performance that is based on the sagittal plane data as input signals was better than the classification performance that is based on the frontal plane data or only transversal plane data as input signals. The prediction accuracy based on three classification algorithm models both were higher than the ZRB results.

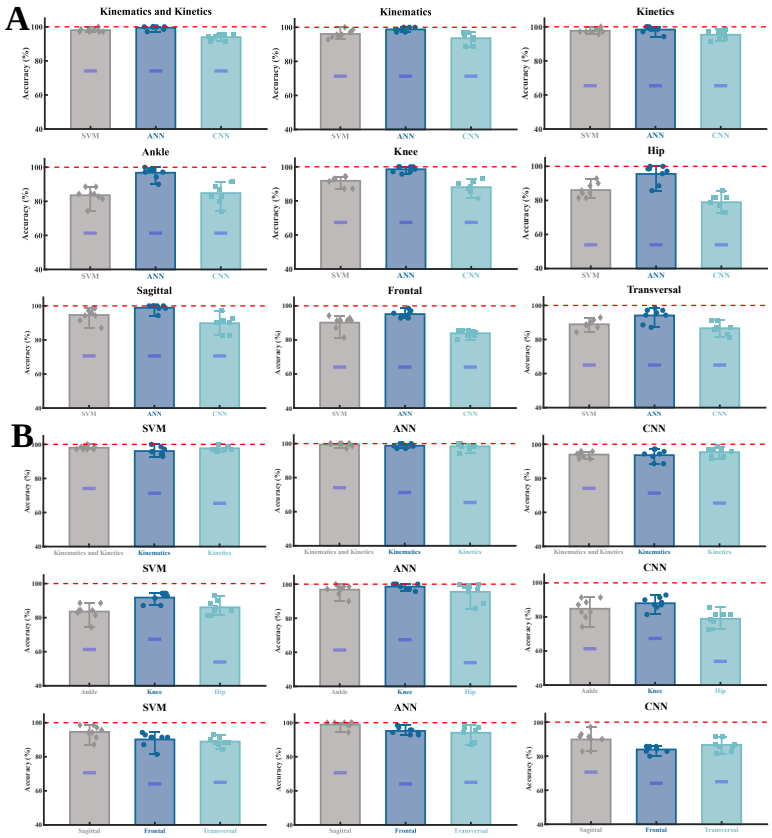

Figure 30 Detailed results of the prediction accuracy rate were obtained for the three different classification algorithm models (SVM, ANN, CNN). (A) Comparison results of classification accuracy of nine classification tasks under three algorithm models. (B) Comparison results of classification accuracy of three algorithm models under nine classification tasks. Bar graph with scatter points of the classification and recognition accuracy rate acquired through eight-fold cross-validation (a total of eight

individual scatter points).

Table 12 Detailed values of the prediction accuracy rate were obtained for the three different classification algorithm models (SVM, ANN, CNN) and ZRB in nine classification tasks. Means and standard deviations were obtained based on eight-fold cross-validation.

Input Signals	SVM (%)	ANN (%)	CNN (%)	ZRB (%)
Kinematics and Kinetics	98.04±1.06	99.46±1.06	93.93±1.83	74.11
Kinematics	96.07±2.38	98.75±1.19	93.57±3.41	71.30
Kinetics	97.68±1.31	98.39±1.94	95.36±2.62	65.41
Ankle	83.57±4.52	96.79±3.22	84.82±5.96	61.33
Knee	91.79±3.03	98.57±1.71	88.04±3.58	67.36
Hip	86.07±4.09	95.54±5.42	78.93±4.50	53.93
Sagittal	94.64±3.87	98.93±1.98	89.82±4.86	70.63
Frontal	90.18±4.07	95.18±2.01	83.93±1.98	64.08
Transversal	88.93±2.62	94.11±4.14	86.61±3.58	65.01

3.2.3 Explainability and statistical evaluation results

Detailed recognizability results and statistical evaluation of the differences between before fatigue and after fatigue single-leg landing patterns are shown in **Figures 30 to 32**. The classification and recognition results of the ankle joint kinematics and kinetics during the landing phase between two class landing patterns are shown in **Figure 31**. **Figure 31A** showed the comparison results of the two class landing patterns in ankle joint kinematics and kinetics, and SPM results show that the landing pattern differences are mainly concentrated in the sagittal and transversal plane (blue shaded part). **Figure 31B** showed the mean values of all test trial datasets, and the results of color-coded input RS for both classes acquired through LRP. **Figure 31C** shows the size of detailed RS during the landing phase, and the area with high RS in the ankle joint is consistent with the statistical results of SPM (red shaded part). **Figure 31D** shows the effect size for both classes during the landing phase, where the portion above 0.5 (red and orange lines) is also basically consistent with the high RS area, especially those parts above 0.8 (red lines). In general, the RS derived from LRP in identifying the differences between the two class landing patterns generally agreed with the statistical results in the ankle joint.

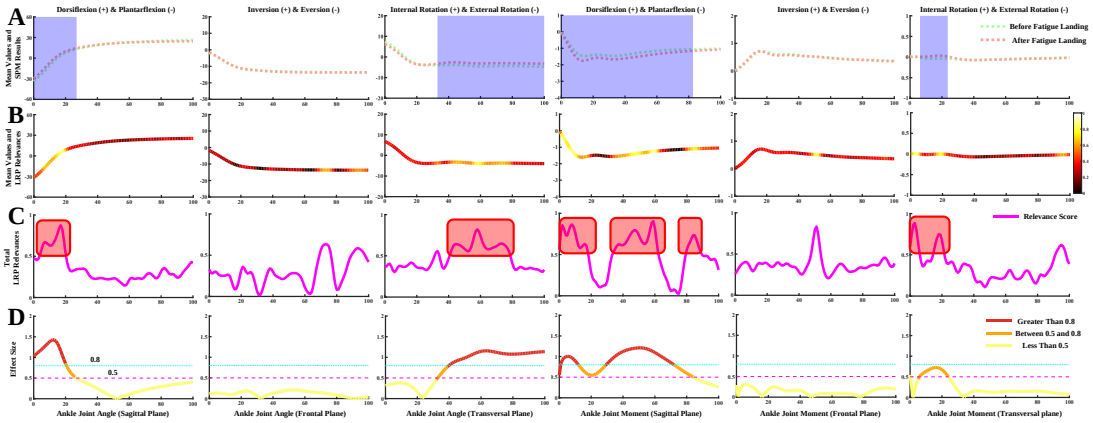

Figure 31 Detailed overview for the classification of the ankle joint kinematics and kinetics during the landing phase between before fatigue and after fatigue single-leg landing. (A) Comparison of the ankle joint kinematics and kinetics in the sagittal, frontal, and transversal plane between before fatigue and after fatigue single-leg landing. The anatomical definition is shown at the top of the picture. The blue shaded part indicates that there has a statistical difference in the landing phase in this section. (B) Mean values of all test trial datasets, color-coded by input RS for both classes acquired through LRP. The brighter colors mean high relevance variables, and the darker colors mean low relevance variables. The brighter the color, the greater the contribution to landing pattern recognition. (C) Detailed line plot of the RS for both classes acquired through LRP during the landing phase. The red shaded part represents the region where the RS obtained by LRP highly coincide with the SPM results. (D) Detailed line plot of the effect size for both classes during the landing phase. The situation description is shown at the bottom of the figure.

The classification and recognition results of the knee joint kinematics and kinetics during the landing phase between two class landing patterns are shown in **Figure 32**. **Figure 32A** shows the comparison results of the two class landing patterns in knee joint kinematics and kinetics. The SPM results indicated that the landing pattern differences are observed at all three anatomical planes (blue shaded part). **Figure 32B** shows the mean values of all test trial datasets, and the results of color-coded input RS for both classes acquired through LRP. **Figure 32C** shows the size of detailed RS during the landing phase, and the area with high RS in the knee joint is consistent with the statistical results of SPM (red shaded part). **Figure 32D** shows the effect size for both classes during the landing phase, where the portion above 0.5 (red and orange lines) is also consistent with the high RS area. In general, the RS derived from LRP in identifying the differences between the two class landing patterns also agreed with the statistical results in the knee joint.

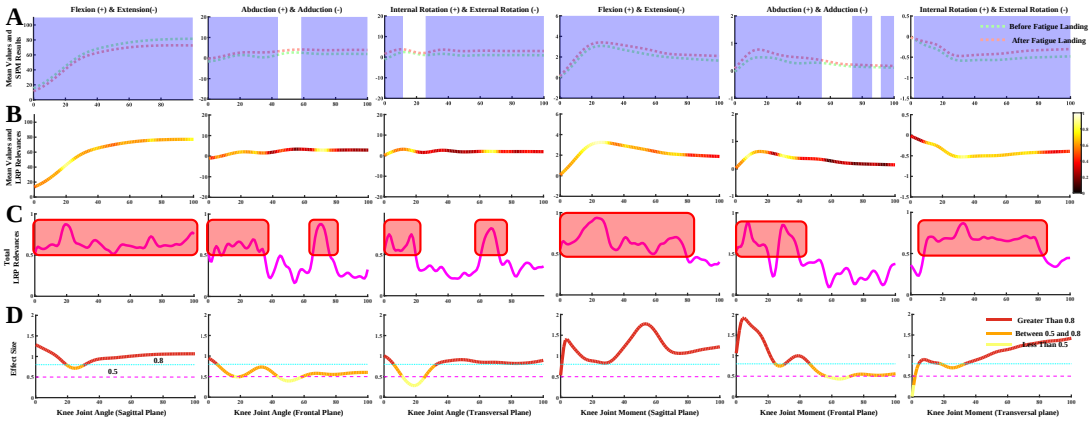

Figure 32 Detailed overview for the classification of the knee joint kinematics and kinetics during the landing phase between before fatigue and after fatigue single-leg landing. (A) Comparison of the knee joint kinematics and kinetics in the sagittal, frontal, and transversal plane between before fatigue and after fatigue single-leg landing. The anatomical definition is shown at the top of the picture. The blue shaded part indicates that there is a statistical difference in the landing phase in this section. (B) Mean values of all test trial datasets, color-coded by input RS for both classes acquired through LRP. The brighter colors indicate high relevance variables, and the darker colors indicate low relevance variables. The brighter the color, the greater the contribution to landing pattern recognition. (C) Detailed line plot of the RS for both classes acquired through LRP during the landing phase. The red shaded part represents the region where the RS obtained by LRP highly coincide with the SPM results. (D) Detailed line plot of the effect size for both classes during the landing phase. The situation description is shown at the bottom of the figure.

The classification and recognition results of the hip joint kinematics and kinetics during the landing phase between two class landing patterns were shown in **Figure 33**. **Figure 33A** shows the comparison results of the two class landing patterns in hip joint kinematics and kinetics, and SPM results show that the landing pattern differences are mainly concentrated in the sagittal and frontal plane (blue shaded part). **Figure 33B** shows the mean values of all test trial datasets, and the results of color-coded input RS for both classes acquired through LRP. **Figure 33C** shows the size of detailed RS during the landing phase, and the partial area with high RS in the hip joint was consistent with the statistical results of SPM (red shaded part). The RS derived from LRP in the hip sagittal and frontal planes during the late landing phase is inconsistent with the statistical results of SPM, although there was a statistical difference a high RS at this stage was not producted. **Figure 33D** shows the effect size for both classes during the landing phase, where the portion above 0.5 (red and orange lines) is partially consistent with the high RS area.

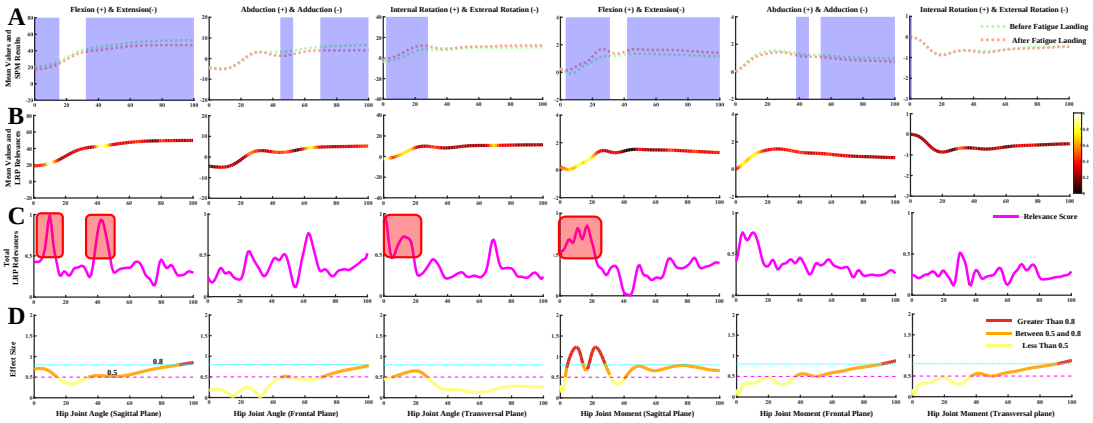

Figure 33 Detailed overview for the classification of the hip joint kinematics and kinetics during the landing phase between before fatigue and after fatigue single-leg landing. (A) Comparison of the hip joint kinematics and kinetics in the sagittal, frontal, and transversal plane between before fatigue and after fatigue single-leg landing. The anatomical definition is shown at the top of the picture. The blue shaded part indicates that there is a statistical difference in the landing phase of this section. (B) Mean values of all test trial datasets, color-coded by input RS for both classes acquired through LRP. The brighter colors reprent high relevance variables, and the darker colors reprent low relevance variables. The brighter the color, the greater the contribution to landing pattern recognition. (C) Detailed line plot of the RS for both classes acquired through LRP during the landing phase. The red shaded part represents the region where the RS obtained by LRP highly coincide with the SPM results. (D) Detailed line plot of the effect size for both classes during the landing phase. The situation description is shown at the bottom of the figure.

Detailed results of RS derived from LRP for explaining the landing pattern difference between before fatigue and after fatigue single-leg landing were shown in **Figure 34. Figure 34A** shows the relative contribution of variables during the overall landing phase, the variables recorded at every 1% of the landing phase interval were related to successfully matching the landing pattern between before fatigue and after fatigue single-leg landing. The variable contribution during the 1%-22% landing phase reached 27.06%, which indicated that the contribution of the early landing phase to the recognition of landing patterns was greater (black shaded area). **Figure 34B** shows the summed contribution of the RS of each joint of each plane of kinematics and kinetics trajectories. For each joint, the largest summed contribution rate of RS was 41.02% in the knee joint, followed by 30.62% in the ankle joint and 28.36% in the hip joint. For each plane, the largest summed contribution rate of RS was 37.78% in the sagittal plane, followed by 32.55% in the transversal plane and 29.67% in the frontal plane. The knee flexion–extension angle variable was the most relevant trajectory variable in landing pattern recognition, and the contribution rate of RS reached 8.31%. Secondly, the knee flexion–extension moment, knee internal–external rotation moment, ankle dorsiflexion-plantarflexion moment, ankle internal–external rotation angle, were the followed relevant trajectory variables in landing pattern recognition, and the

contribution rate of RS reached 8.03%, 7.86%, 6.58%, 6.13%, respectively. The RS contribution rates of other trajectory variables were detailed in **Figure 34B**.

Figure 34C shows the detailed distribution of RS during each joint of each plane of kinematics and kinetics. There was revealing information contributing to the distribution of the time points variables between the before fatigue and after fatigue single-leg landing during the overground landing movement patterns.

A total of 169 relevant variables (RS greater than 0.7) were extracted as the notable highly relevant variable to explore its distribution trend (**Figure 34D**). For the ankle kinematics, there was high RS in dorsiflexion-plantarflexion angle during the 15%-19% landing phase; in internal–external rotation angle during the 56%-60% landing phase. For the ankle kinetics, there was high RS in dorsiflexion-plantarflexion moment during the 2%-11%, 44%-50%, 56%-60%, 83%-85% landing phase; in inversion-eversion moment during the 50%-52% landing phase; in internal–external rotation moment during the 2%-5%, 18%-20% landing phase.

For the knee kinematics, there was high RS in flexion–extension angle during the 17%-24%, 72%-74%, 95%-99% landing phase; in abduction–adduction moment during the 29%, 67%-73% landing phase; in internal–external rotation angle during the 3%-5%, 17%-18%, 63%-69% landing phase. For the knee kinetics, there was high RS in flexion–extension moment during the 13%-30%, 41%, 72%-73% landing phase; in abduction–adduction moment during the 6%-10%, 28%-35% landing phase; in internal–external rotation moment during the 12%-14%, 28%-37%, 46%, 70%-73%, 77% landing phase.

For the hip kinematics, there was high RS in flexion–extension angle during the 9%-12%, 40%-45% landing phase; in abduction–adduction moment during the 62%-64% landing phase; in internal–external rotation angle during the 1%-3%, 12%-16% landing phase. For the hip kinetics, there was high RS in flexion–extension moment during the 11%-13%, 16%-19% landing phase; in abduction–adduction moment during the 4%-6%, 10%-13% landing phase. These high RS variables were also mainly concentrated in the early landing phase (red shaded area), which also suggested that the early stage landing phase was more important in landing pattern recognition.

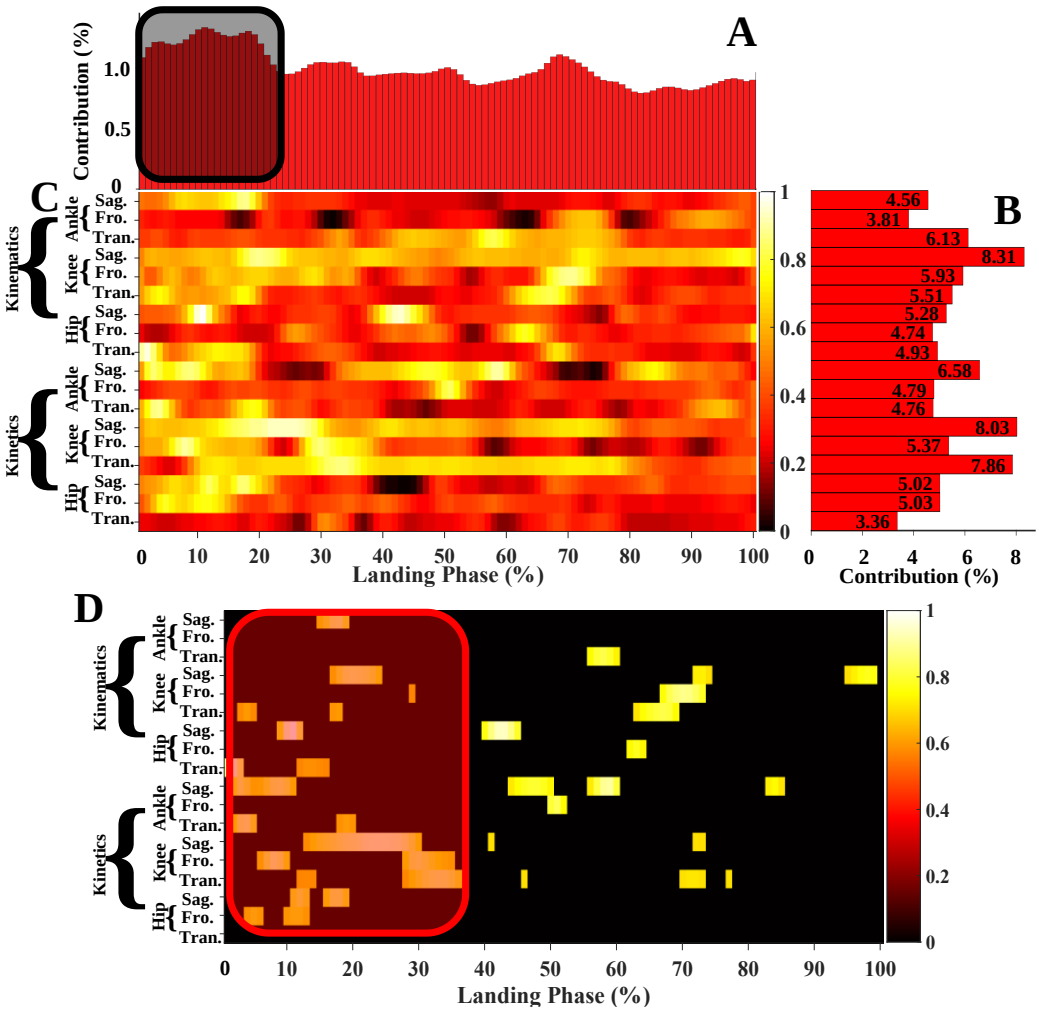

Figure 34 Detailed explanation results of landing pattern difference using LRP. (A) Relative contribution of variables during the overall landing phase. (B) Summed contribution of the relevance of each joint (ankle, knee, hip) of each plane (sagittal, frontal, transversal) of kinematics and kinetics trajectories. (C) Detailed distribution of RS during each joint of each plane of kinematics and kinetics. (D) Detailed distribution of the 169 highly relevant variables (RS greater than 0.7) during each joint of each plane of kinematics and kinetics. The brighter colors indicate high relevance variables, and the darker colors indicate low relevance variables. The model relied more on brighter color variables; the darker color variables had less relevance with correctly classified landing patterns.

3.2.4 Explainability and clinical evaluation results

"To what extent do these regions of input signals identified as most relevant for landing pattern recognition remain consistent with clinical assessment?" Based on the obtained results of the XML model, a specialist in analyzing lower extremity landing injuries with nearly 20 years of expertise provided the response to the query.

Firstly, for the single-leg landing task, it is generally accepted that the early landing phase is the main stage in which injury occurs. This is because the ground reaction force impact on the lower limbs increases rapidly after the foot initial contact with the ground,

resulting in a rapid transfer of impact loads within the musculoskeletal lower limb joints. During the landing process, the human body inevitably adopts the landing mode of transition from forefoot to midfoot and then to hindfoot (from plantarflexion to dorsiflexion). This process is often an unstable state. When the larger impact loads are piled up at the point of instability, the risk of lower limb injury naturally increases. As observed from the XML result that the variable contribution during the 1%-22% landing phase reached 27.06% (**Figure 34A**), and the high RS variables were also mainly concentrated in the early landing phase (**Figure 34D**). Therefore, the results obtained by the current XML model are consistent with the clinical feature that the input signals in the early landing phase have a greater contribution to landing pattern recognition.

During landing, the lower limb undergoes a load transfer pattern from distal to proximal, in which the foot and ankle first bear the impact of the ground reaction force, followed by the knee and hip joints. After the fatigue intervention, the degree of lower limb instability will be more severe during the landing phase. In response to this increased instability, the body subconsciously reduces knee and hip flexion during landing to maintain stability and avoid falling. This process inevitably increases the impact on the lower limb musculoskeletal, thus changing the landing pattern. The alteration of the hip during this whole coping process is minimal because the ankle and knee joints have already borne the main impact load by adjusting the landing strategy before impact is transmitted to the hip joint. As observed from the XML result that the classification performance based on the knee data as input signals was better than the classification performance based on the ankle data or hip data as input signals (**Figure 34B**), and the summed contribution of the RS of knee and ankle joint were higher than the hip joint (**Figure 34B**). Therefore, the input signals related to the hip joint showed worse classification performance in landing pattern classification compared with the ankle and knee joints, as well as contributed less to landing pattern recognition. This result is also consistent with clinical practice characteristics.

It is also worth noting that the classification performance based on the sagittal plane data as input signals was better than the classification performance based on the frontal plane data or transversal plane data as input signals (**Figure 34B**), and the summed contribution of the RS of sagittal plane was higher than the frontal and transversal plane (**Figure 34B**). From a clinical point of view, the most likely injury caused by landing after fatigue intervention is ACL injury. This is mainly due to the harder landing style after fatigue, namely the smaller knee and hip flexion mentioned above. The functional valgus collapse of the knee that traditionally leads to ACL injury is also directly related to the increased load impact caused by the stiffer landing mode. Because at a small flexion angle of the knee joint, compared with the longitudinal force, the transverse pull force caused by the load impact in the vertical direction is the main force on the ACL. In addition, the range of motion of each joint in the sagittal plane is much larger than that in the other planes, which is the main reason for the large variance in sagittal landing patterns between classes.

3.3 Effect of ankle motion patterns on reducing the lower limb injury risk during landing

3.3.1 Muscle activation and raw waveform data during the landing phase

Figure 35 presents the results of the comparison between the muscle activation results collected by the EMG sensor and the OpenSim musculoskeletal model simulation results. In both cases, the activation levels of the ten selected muscles remained essentially the same, suggesting that the model constructed in this study has a high degree of reliability [78, 89]. The raw data waveform of the relevant parameters during the landing phase is shown in **Figure 36**.

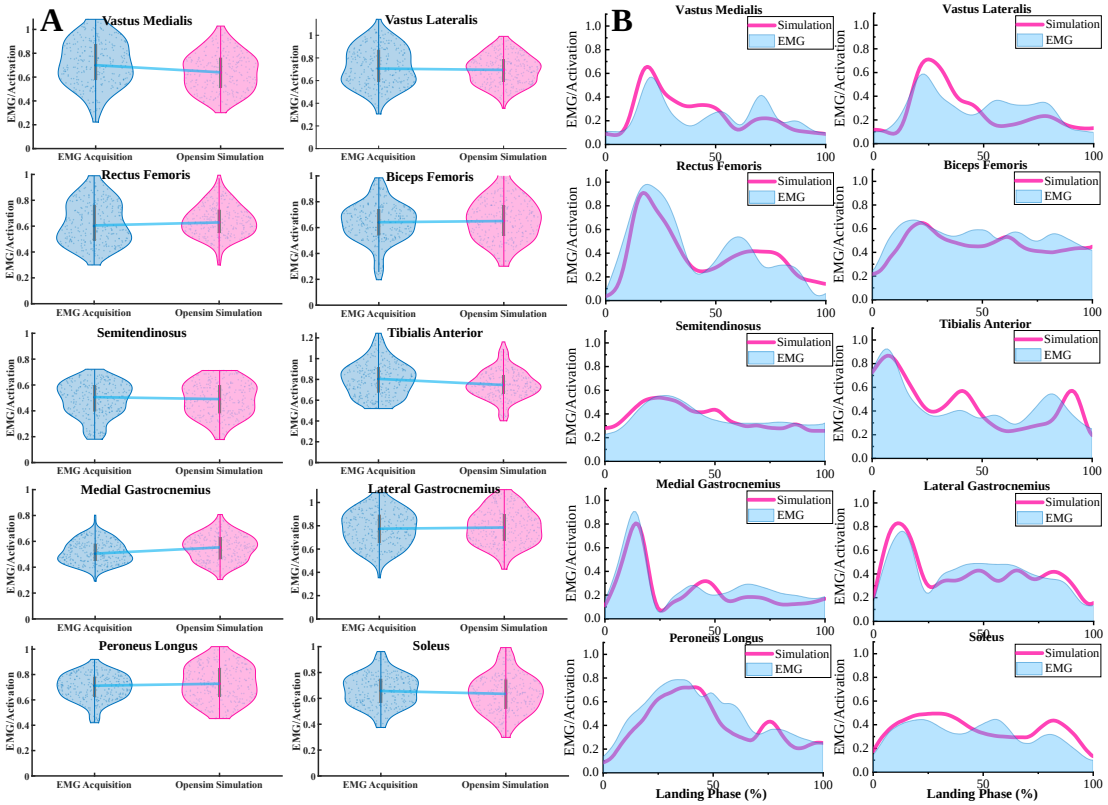

Figure 35 Illustration of the EMG/Activation of selected muscles. (A) Comparative results of muscle activation degrees for all subjects. (B) Comparative results of time-dependent muscle activation for a typical subject.

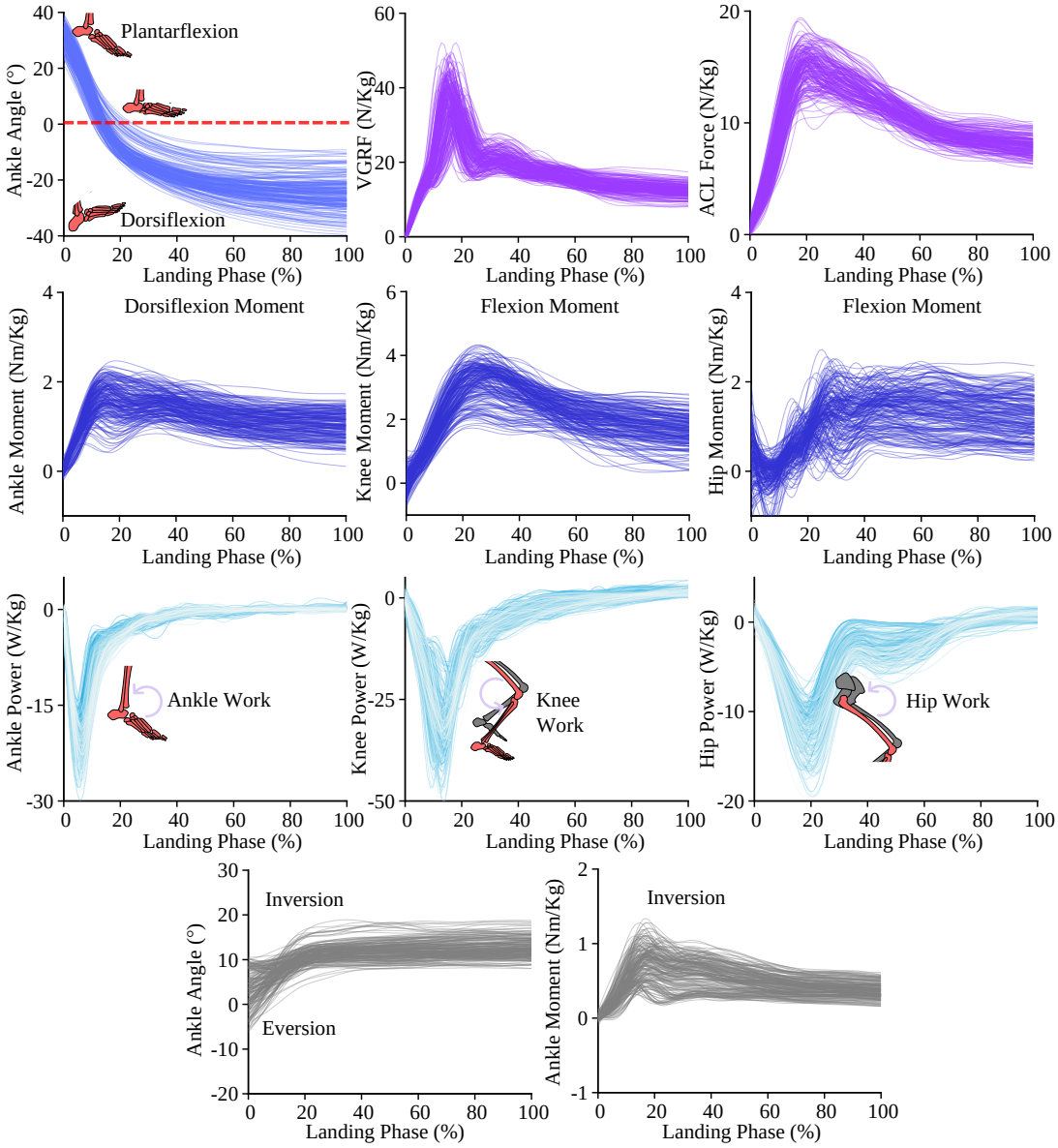

Figure 36 Visualization of the raw data waveform of the relevant parameters during the landing phase.

3.3.2 Relationship between the overall injury risk of lower limb and ankle motion patterns

There is a correlation between ankle movement patterns and overall injury risk (**Table 13, Figure 37, Figure 38**). The results of the AICA and AROM are 33.47±5.16° and 59.99±8.35° respectively (**Table 13**). The linear relationship and scatter distribution between PVGRF, TED and AICA, AROM are shown in **Figure 37**, and the detailed values are provided in **Table 13**. With the increase of AICA during SL, the PVGRF shows a downward trend ($r = -0.591$, $p < 0.001$). With the increase of AROM during landing, the PVGRF shows a downward trend ($r = -0.451$, $p < 0.001$). With the increase of AICA during landing, the TED shows an upward trend ($r = 0.490$, $p < 0.001$). With the increase of AROM during landing, the TED shows an upward trend ($r = 0.687$, $p < 0.001$).

The linear relationship and scatter distribution between peak ankle, knee, hip sagittal moment and AICA, AROM is shown in **Figure 38**. With the increase of AICA during landing, the peak ankle (r = -0.542), knee (r = -0.441), hip (r = -0.253) sagittal moment all show a downward trend (**Table 13**). With the increase of AROM during landing, the peak ankle (r = -0.357), knee (r = -0.284), hip (r = -0.357) sagittal moment all show a downward trend (**Table 13**).

Table 13 Detailed results of the Pearson correlation coefficients between ankle motion patterns and lower limb variables.

Variables	Mean±SD	Ankle Initial Contact Angle (33.47±5.16°)			Ankle Range of Motion (59.99±8.35°)		
		r	R^2	p	r	R^2	p
Peak VGRF (N/Kg)	36.61±5.10	-0.591	0.349	<0.001	-0.451	0.203	<0.001
Total Energy Dissipation (J/Kg)	6.01±0.77	0.490	0.241	<0.001	0.687	0.472	<0.001
Ankle Sagittal Moment (Nm/Kg)	1.61±0.32	-0.542	0.294	<0.001	-0.357	0.128	<0.001
Knee Sagittal Moment (Nm/Kg)	3.13±0.56	-0.441	0.194	<0.001	-0.284	0.081	<0.001
Hip Sagittal Moment (Nm/Kg)	1.58±0.40	-0.253	0.064	<0.001	-0.357	0.128	<0.001
Ankle Inversion Angle (°)	14.19±2.74	0.502	0.253	<0.001	0.600	0.360	<0.001
Ankle Inversion Moment (N/Kg)	0.75±0.23	-0.268	0.072	<0.001	-0.138	0.019	0.168
Peak ACL Force (N/Kg)	14.72±1.68	-0.554	0.307	<0.001	-0.332	0.110	<0.001

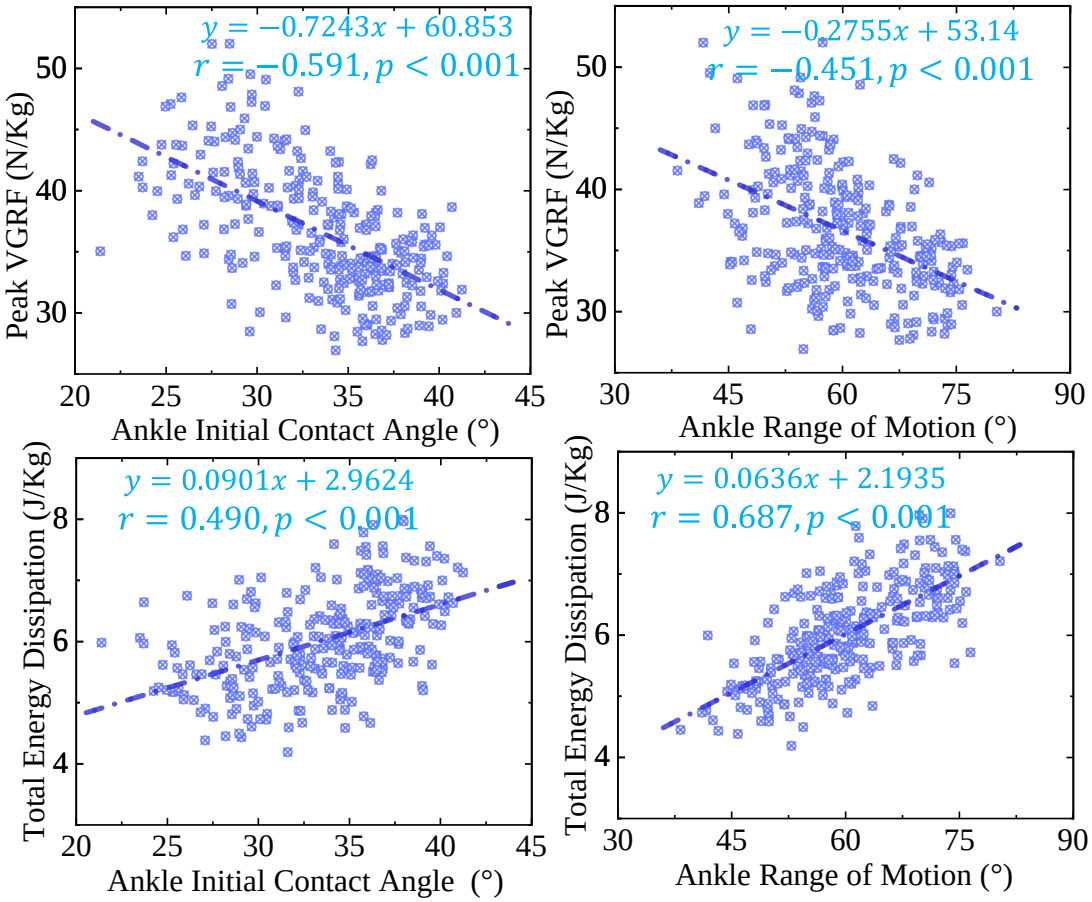

Figure 37 Visualization of the linear relationship and scatter distribution between PVGRF, TED and AICA, AROM.

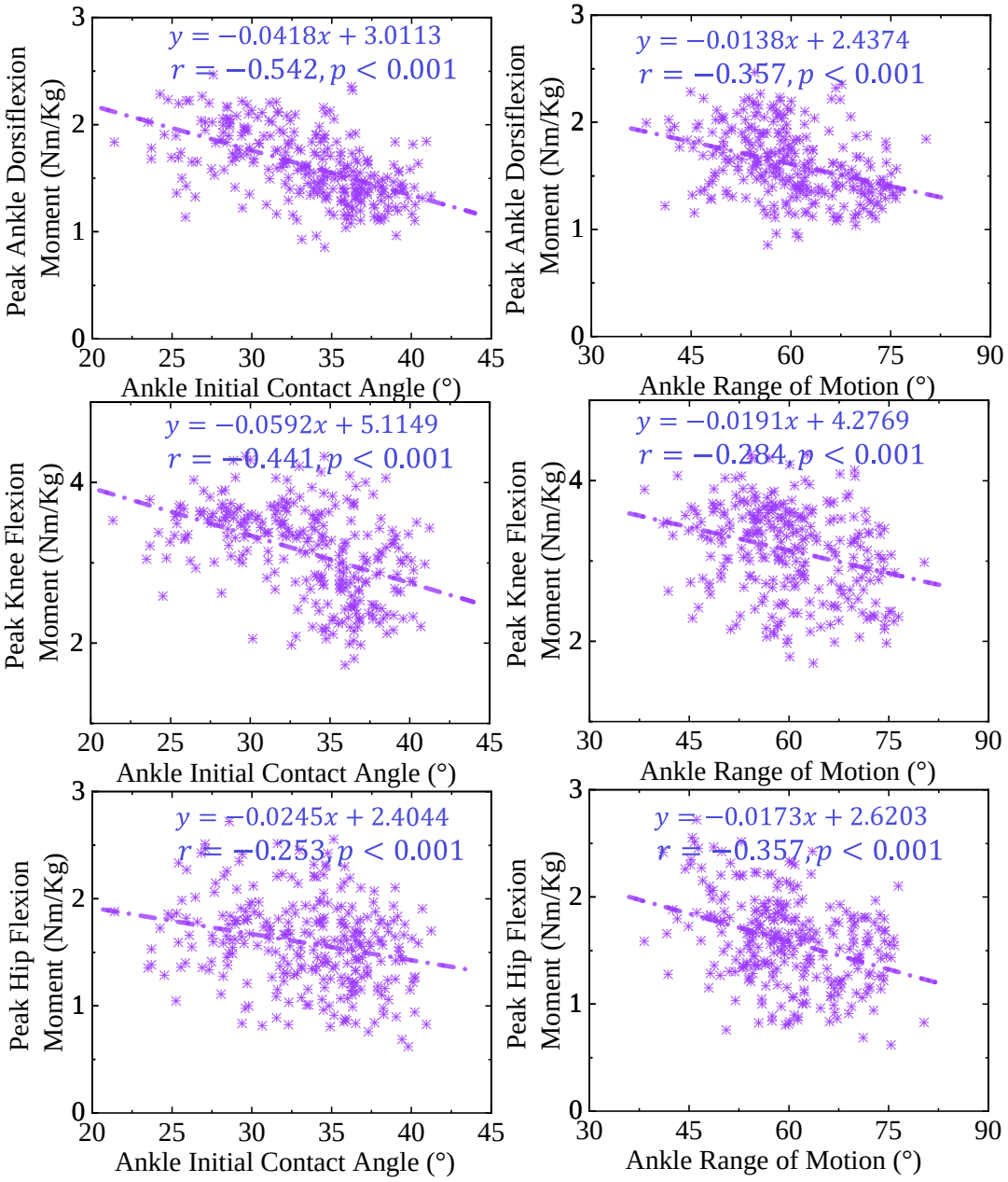

Figure 38 Visualization of the linear relationship and scatter distribution between peak ankle, knee, hip sagittal moment and AICA, AROM.

3.3.3 Relationship between the ACL injury risk and ankle motion patterns

AICA and AROM are negatively correlated with ACL injury risk (**Figure 39**). With the increase of AICA during landing, the PAF shows a downward trend (r = -0.554, p < 0.001). With the increase of AROM during landing, the PAF shows a downward trend (r = -0.332, p < 0.001) (**Table 13**).

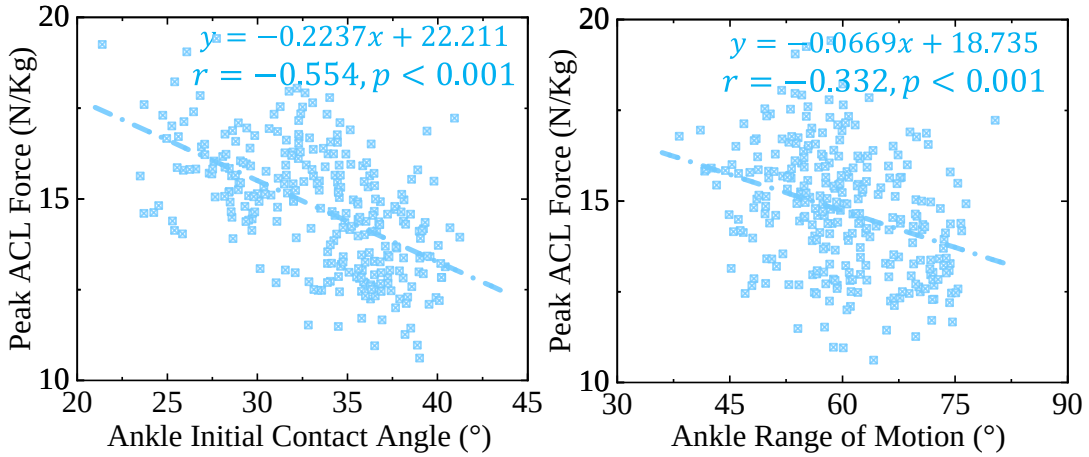

Figure 39 Visualization of the linear relationship and scatter distribution between peak ACL force and AICA, AROM.

3.3.4 Relationship between the LAS risk and ankle motion patterns

AICA and AROM are positively correlated with LAS risk (**Figure 40**). For the PAIA, it shows an upward trend with the increase of AICA (r = 0.502, p < 0.001) and AROM (r = 0.600, p < 0.001) (**Table 13**). For the PAIM, it shows a downward trend with the increase of AICA (r = -0.268, p < 0.001) and AROM (r = -0.138, p = 0.168) (**Table 13**).

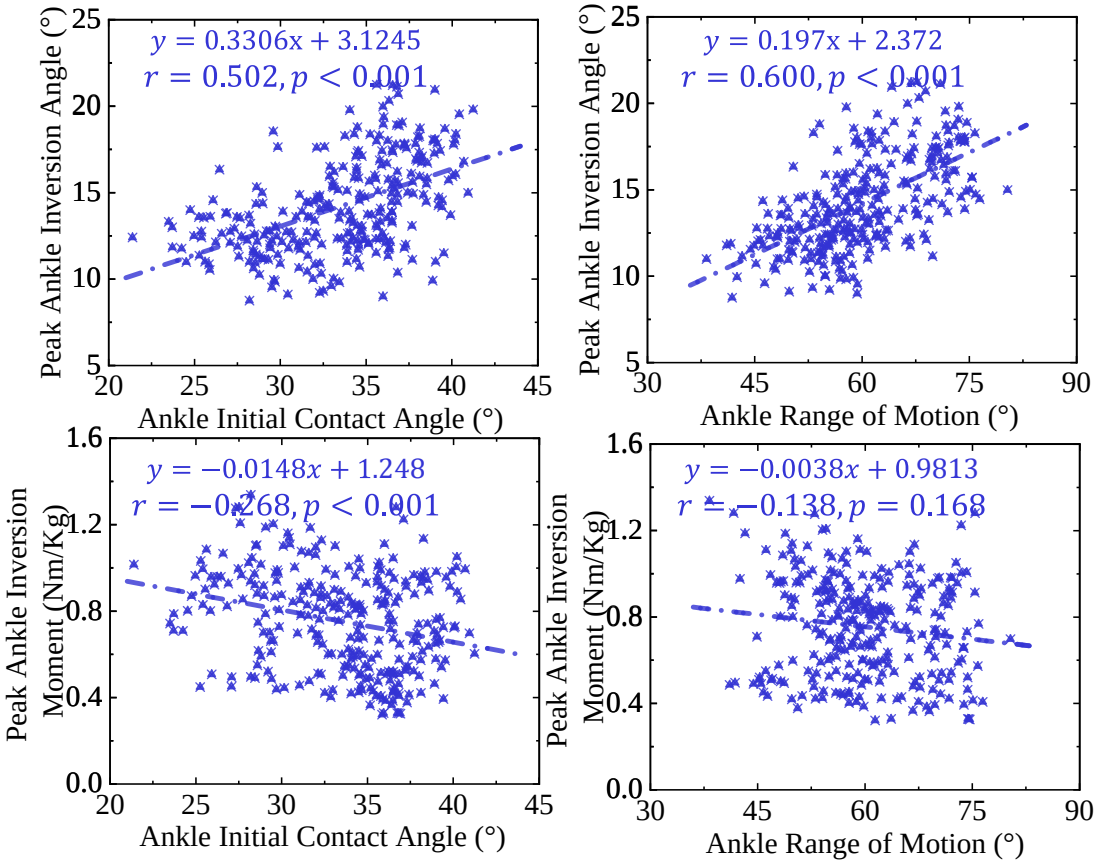

Figure 40 Visualization of the linear relationship and scatter distribution between peak ankle inversion angle, moment and AICA, AROM.

3.3.5 Interaction between LAS risk and ACL injury risk

As shown in **Figure 41**, the LAS risk is negatively correlated with ACL injury risk ($r = -0.330$, $p < 0.001$). For the AICA, the intersection of PAF and PAIA occurs at 34.09°, and the approximate range of balanced LAS and ACL injury risk may be 30° to 40°. For the AROM, the intersection of PAF and PAIA occurs at 61.18°, and the approximate range of balanced LAS and ACL injury risk may be 50° to 70°.

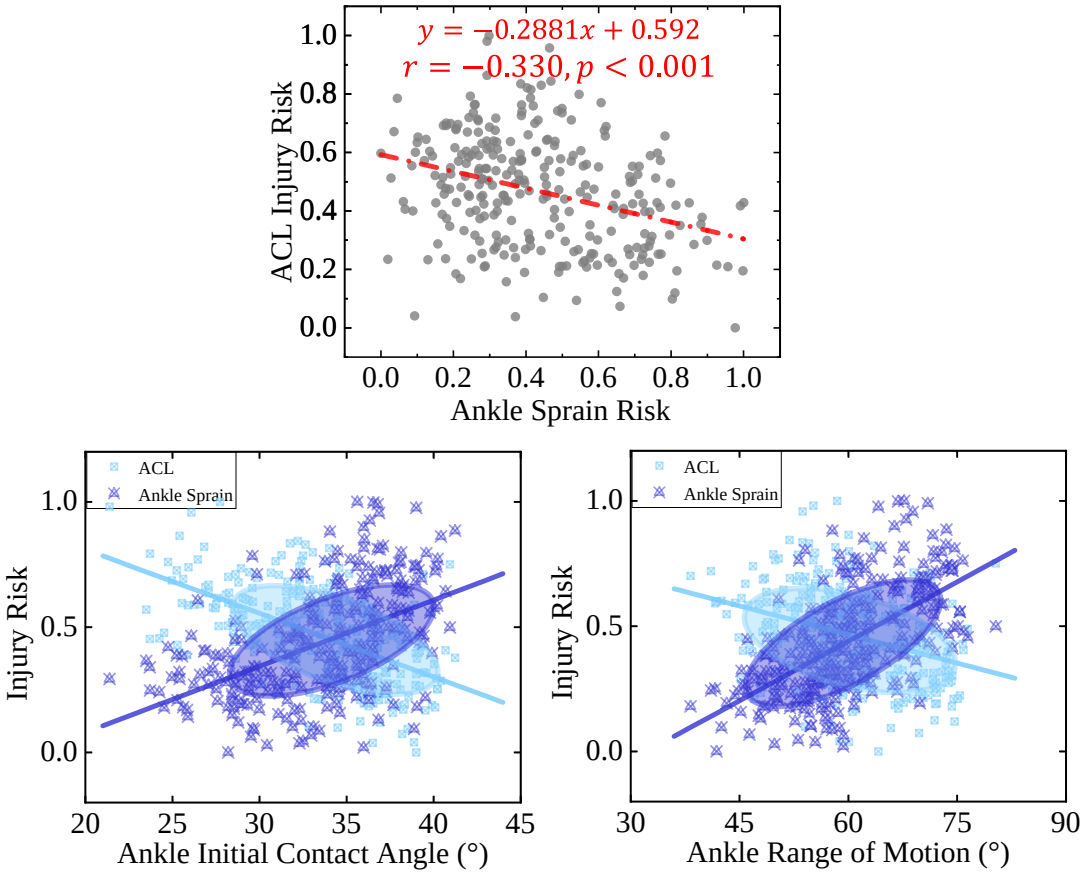

Figure 41 Visualization of the interaction between the risk of ACL injury, ankle sprain and AICA, AROM. The closer the injury risk is to 1, the greater the probability of corresponding injury.

3.4 Contribution of ankle initial contact angle during landing to reduce the knee-related injury risk

The degree of muscle activation of the ten selected muscles was similar in both cases (EMG collection and OpenSim simulation), which demonstrated the high reliability of the musculoskeletal model developed in this study (**Figure 42**). Results of peak impact forces and knee negative work (**Figure 43, Table 14**). There was no significant difference in the knee medial impact force at three landing angles. For the anterior impact force, there was no significant difference between 20° and 30°, and landing with 40° depicted a significantly smaller force than landing with 20° (p=0.003) and 30° (p=0.000). As the ankle plantarflexion angle increases during landing, the knee vertical impact force decreases significantly (20° vs. 30°: p=0.025; 20° vs. 40°: p=0.000; 30° vs. 40°: p=0.001). For the total negative work, there was a significant difference only between 20° (smaller) and 40° (p=0.018).

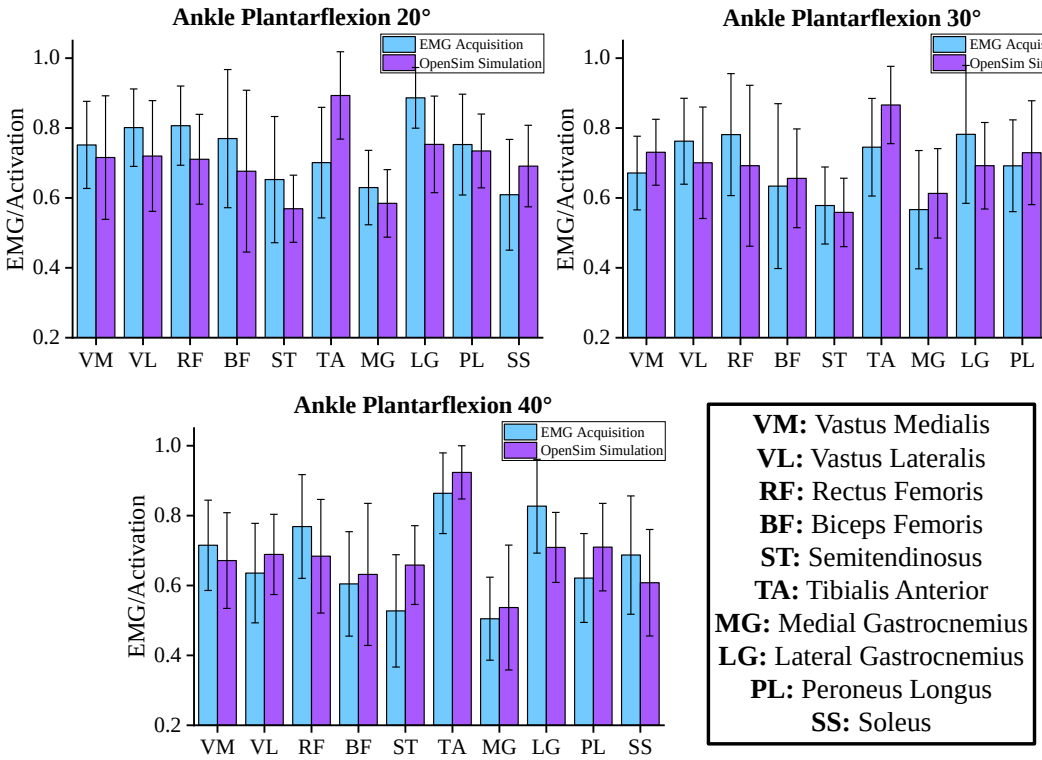

Figure 42 Illustration of the EMG/Activation of the lower limb muscles. The results of the EMG acquisition were calculated from the collected surface EMG signal. The results of the OpenSim simulation were calculated from the constructed musculoskeletal model. Muscle activation is normalized to 0-1, which represents no activation and full activation.

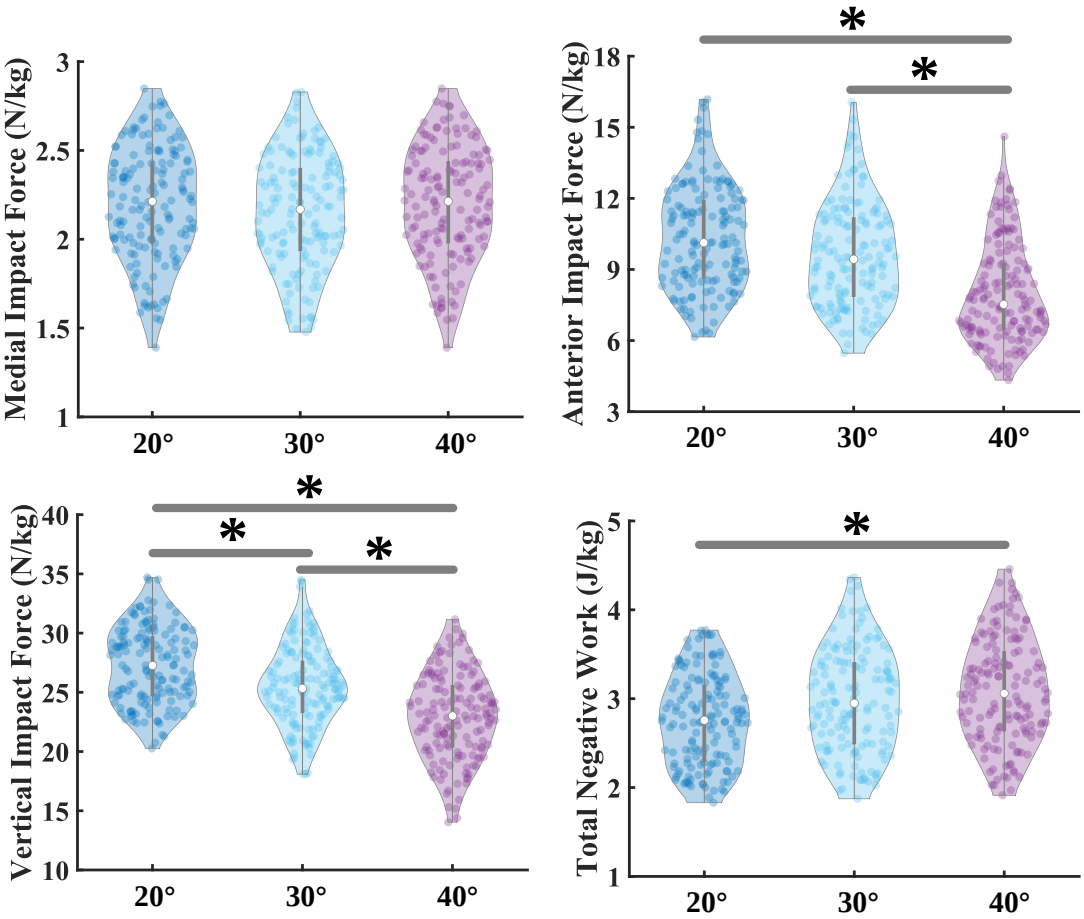

Figure 43 Detailed results of the distribution trends for peak impact force and negative work of the knee joint when landing with different ankle plantarflexion angles (20°, 30°, and 40°). "*" represents significance with $p < 0.05$.

Table 14 Detailed results of the peak impact force and negative work of the knee joint, ACL force when landing with different ankle plantarflexion angles (20°, 30°, and 40°).

Variables					Results					
		Mean ± Std			20° vs. 30°		20° vs. 40°		30° vs. 40°	
Initial Contact Angle (°)	Ankle Plantarflexion	20	30	40	95% Confidence Interval	*p*	95% Confidence Interval	*p*	95% Confidence Interval	*p*
Impact Loads on the Knee Joint	Medial Impact Force (N/kg)	2.20± 0.30	2.15± 0.28	2.21± 0.29	(-0.11, 0.20)	0.547	(-0.15, 0.15)	0.990	(-0.20, 0.11)	0.547
	Anterior Impact	10.31 ±2.17	9.62± 2.09	8.00± 1.77	(-0.33, 1.73)	0.182	(1.28, 3.35)	**0.000***	(0.58, 2.65)	**0.003***

	Force (N/kg) Vertical Impact Force (N/kg)	27.25 ±3.08	25.51 ±2.94	22.93 ±2.90	(0.23, 3.26)	**0.025***	(2.81, 5.84)	**0.000***	(1.06, 4.10)	**0.001***
Energy Dissipation in the Knee Joint	Total Negative Work (J/kg)	2.76± 0.49	2.98± 0.54	3.09± 0.54	(-0.49, 0.04)	0.100	(-0.60, -0.06)	**0.018***	(-0.37, 0.17)	0.451
ACL	ACL Force (N/kg)	17.50 ±2.73	16.06 ±2.79	13.76 ±2.27	(0.13, 2.43)	**0.032***	(2.43, 5.05)	**0.000***	(0.99, 3.61)	**0.001***

Note: "*" represents significance with $p < 0.05$.

For the ACL internal load force, SPM analysis revealed that there was a significant difference during the whole landing phase (**Figure 44**). The post hoc analyses suggested that: (1) there was no significant difference between 20° and 30°; (2) landing with 20° depicted a significantly greater ACL force than landing with 40° during the 1-100% landing phase ($p<0.001$); (3) landing with 30° depicted a significantly greater ACL force than landing with 40° during the 2-70% landing phase ($p<0.001$). As the ankle plantarflexion angle increases during landing, the peak ACL force decreases significantly (20° vs. 30°: $p=0.032$; 20° vs. 40°: $p=0.000$; 30° vs. 40°: $p=0.001$).

The stress distribution of the ACL, meniscus, and femoral cartilage is shown in **Figure 45**. The overall range of variation in ACL stress was small and was mainly distributed in the femoral and tibial attachment regions, as well as in the mid-lateral region. The maximum von Mises stress decreased as the ankle plantarflexion angle increase. When landing at 20°, 30°, and 40°, the maximum ACL stresses were 30.856 MPa, 27.053 MPa, and 24.592 MPa; the maximum meniscus stresses were 22.315 MPa, 20.073 MPa, and 17.972 MPa; and the maximum femoral cartilage stresses were 18.754 MPa, 17.012 MPa, and 15.429 MPa, respectively (**Figure 46**).

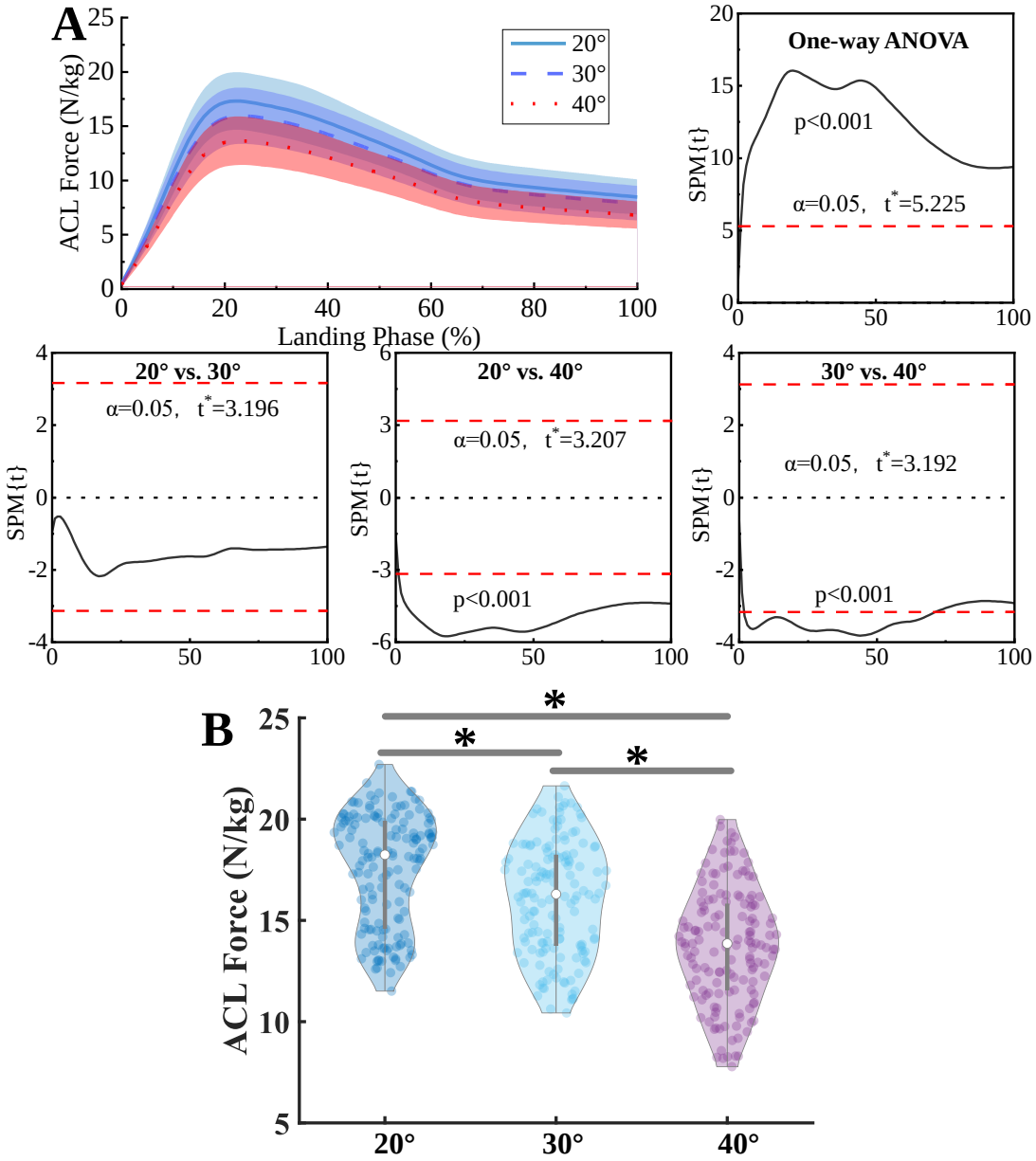

Figure 44 Detailed results of the ACL internal load force when landing with different ankle plantarflexion angles (20°, 30°, and 40°). (A) Visualization of force and its corresponding SPM results. (B) Detailed results of the distribution trends for peak ACL force, and the "*" represents significance with $p < 0.05$.

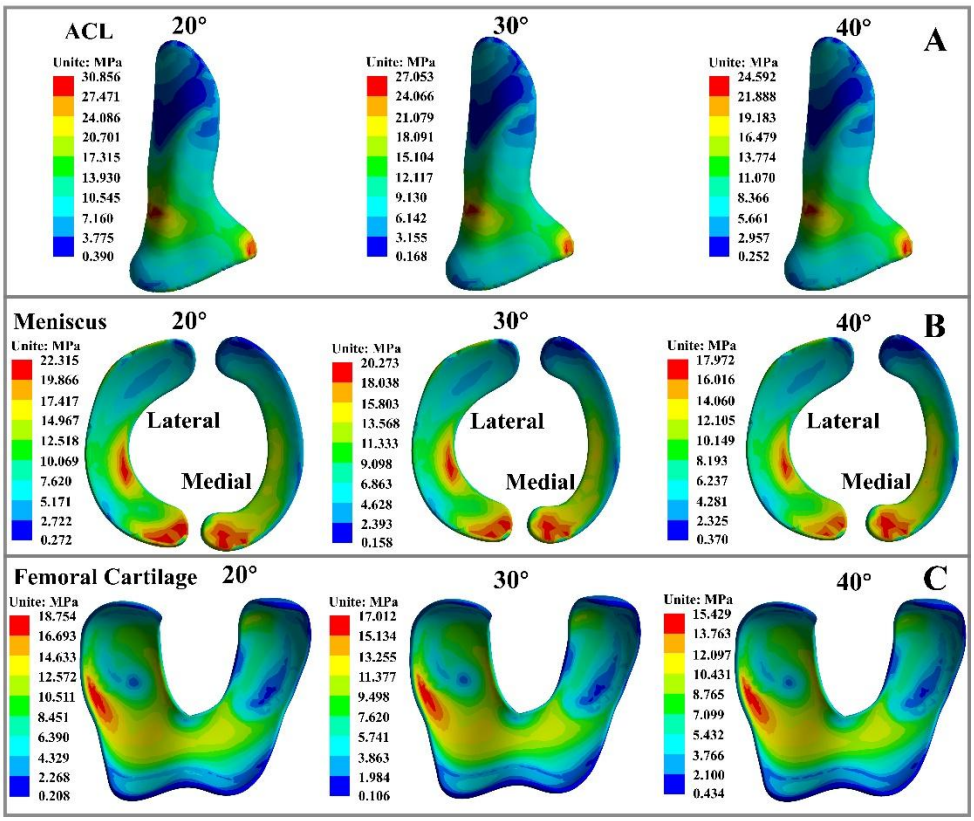

Figure 45 Visualization of ACL, meniscus, and femoral cartilage von Mises stress distribution when landing with different ankle plantarflexion angles (20°, 30°, and 40°). (A) Results of ACL stress. (B) Results of meniscus stress. (C) Results of femoral cartilage stress.

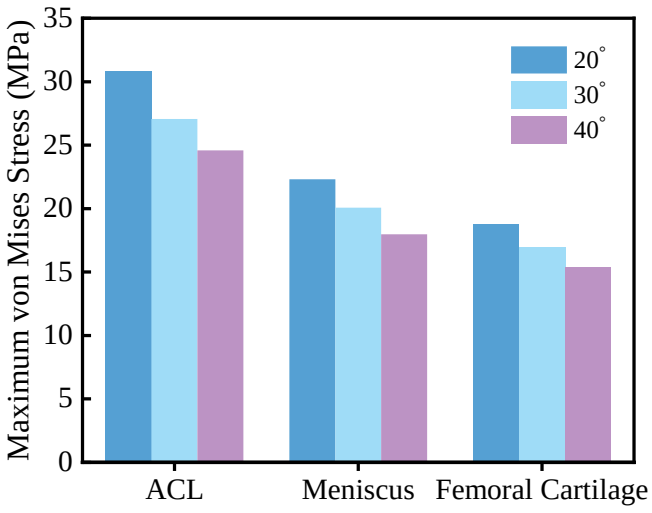

Figure 46 Illustration of the maximum von Mises stress results of ACL, meniscus, and femoral cartilage when landing with different ankle plantarflexion angles (20°, 30°, and 40°).

3.5 ACL dynamic loading force prediction based on lower limb joint movements

Detailed prediction results and errors of ACL force in 22 test samples based on the optimized prediction model are presented in **Figure 47**. For the prediction of PAF (**Figure 47A**), the SSA-ELM prediction model shows excellent prediction performance because of very strong correlation ($R^2 = 0.9992, MSE = 0.0023, RMSE = 0.0474$).

The prediction results and errors of ACL force waveform during the whole landing phase based on the SSA-LSTM prediction model are presented in **Figure 47B**, which achieves better performance in the overall waveform prediction ($R^2 = 0.9937, MSE = 0.0086, RMSE = 0.0928$), and the results during the 10%-35% landing phase ($R^2 = 0.9429, MSE = 0.0136, RMSE = 0.1166$) is worse than the whole landing phase (red shaded areas). The detailed comparison waveforms of ACL force for 22 test samples between the original observed results and the predicted values based on the SSA-LSTM prediction model are provided in **Figure 48**.

The prediction results and errors of ACL force waveform during the whole landing phase based on the equal scaling by combining the SSA-ELM and SSA-LSTM prediction model are presented in **Figure 47C**, which achieves a better performance in the overall waveform prediction ($R^2 = 0.9947, MSE = 0.0076, RMSE = 0.0873$), and the results during the 10%-35% landing phase ($R^2 = 0.9989, MSE = 0.0058, RMSE = 0.0762$) is good than the whole landing phase (red shaded areas). The detailed comparison waveforms of ACL force for 22 test samples between the original observed results and the predicted values based on the equal scaling by combining the SSA-ELM and SSA-LSTM prediction model are provided in **Figure 49**.

Detailed results of prediction errors and error distribution of ACL force are provided in **Figure 50**. During the 10%-35% landing phase, the absolute error of the final optimized prediction model (**Figure 47C**) is significantly lower than that of the SSA-LSTM prediction model (**Figure 47B**). The prediction error results are based on the data of the 10%-35% landing phase, which can see in **Table 15**.

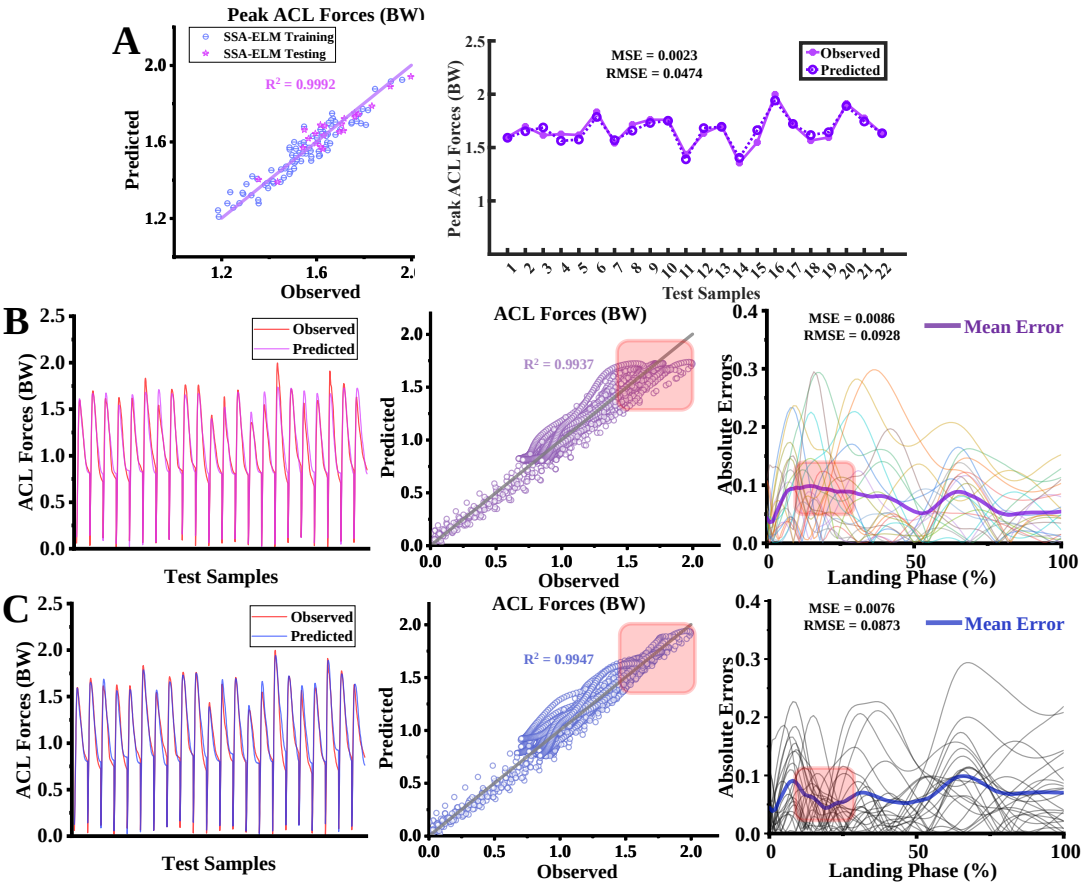

Figure 47 Detailed prediction results and errors of ACL force in 22 test samples based on the optimized prediction model. (A) The prediction results and errors of PAF based on the SSA-ELM prediction model. (B) The prediction results and errors of ACL force during the whole landing phase based on the SSA-LSTM prediction model. (C) The prediction results and errors of ACL force during the whole landing phase based on equal scaling by combining the SSA-ELM and SSA-LSTM prediction models.

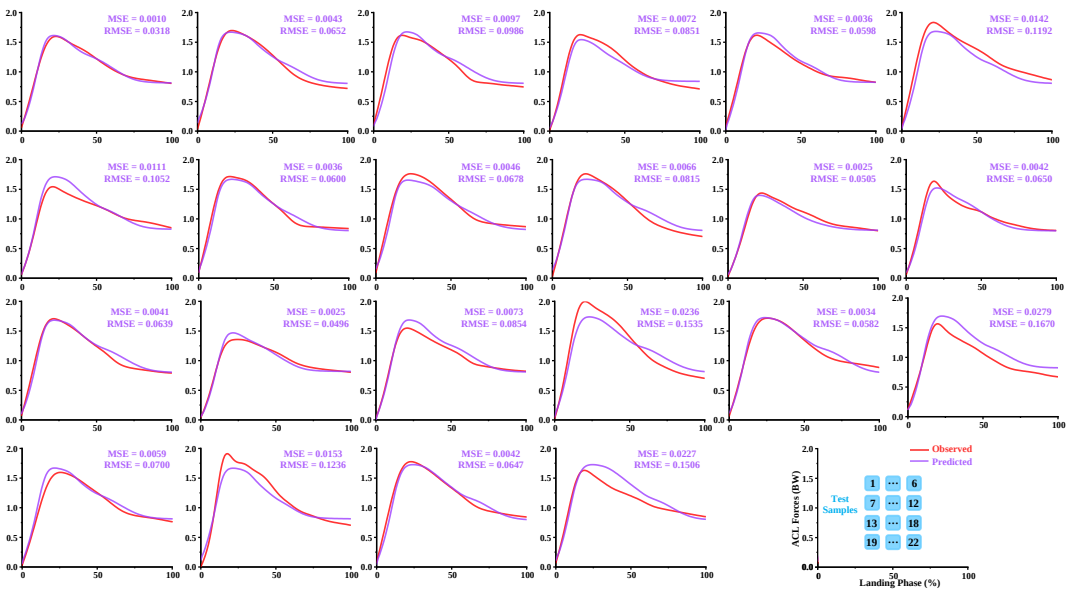

Figure 48 Comparison waveforms of ACL force for 22 test samples between the original observed results and the predicted values based on the SSA-LSTM prediction model.

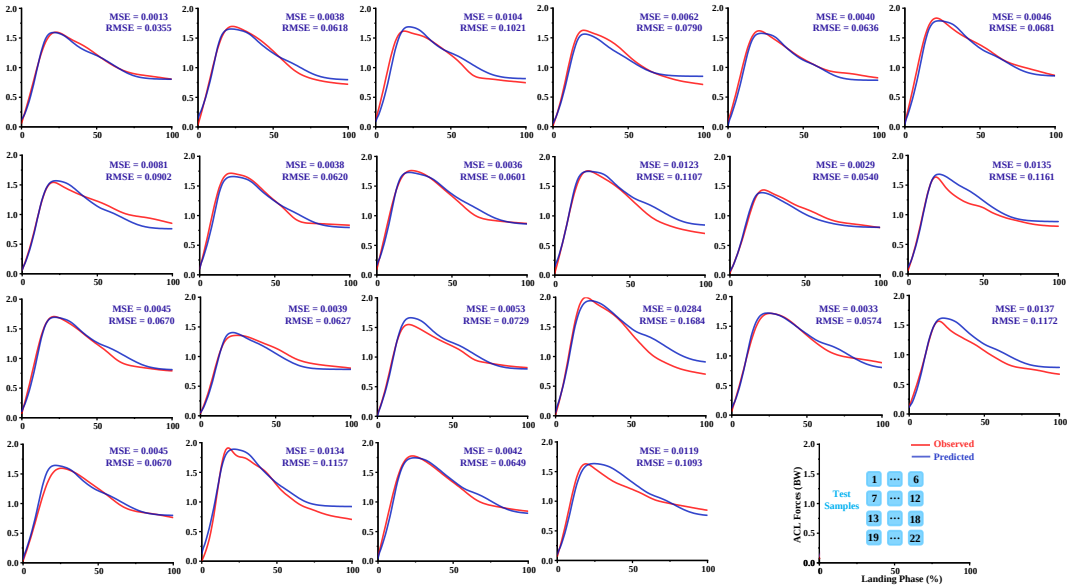

Figure 49 Comparison waveforms of ACL force for 22 test samples between the original observed results and the predicted values based on the equal scaling by combining the SSA-ELM and SSA-LSTM prediction model.

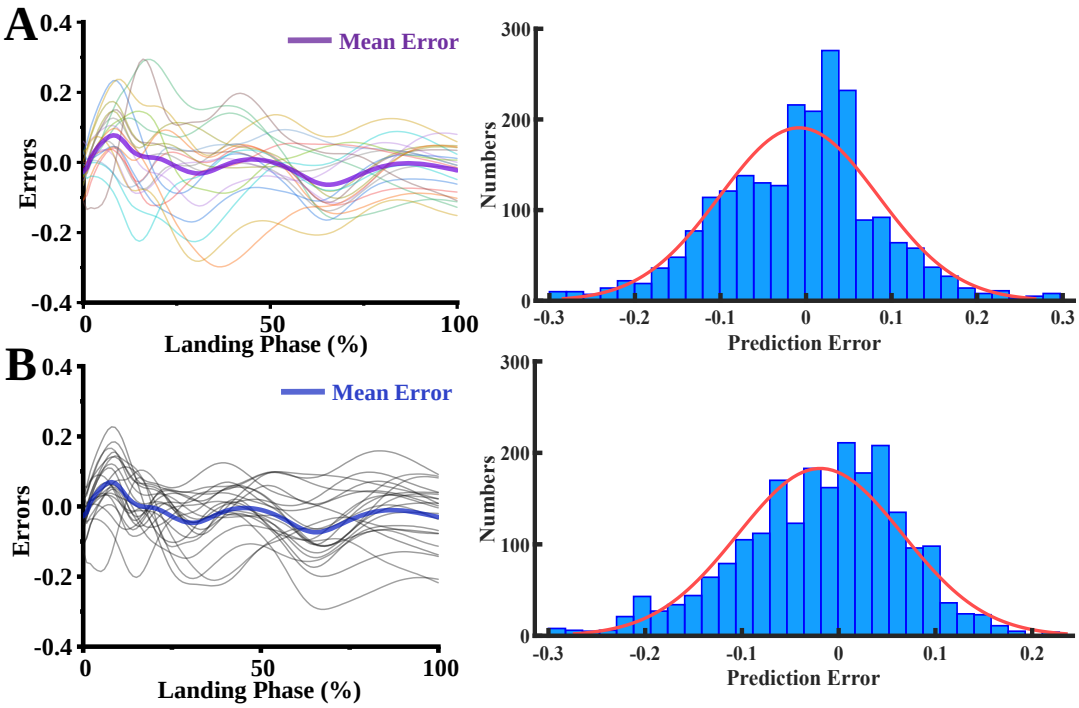

Figure 50 Detailed results of prediction errors and error distribution of ACL force. (A) The prediction errors and error distribution of ACL force during the whole landing phase based on the SSA-LSTM prediction model. (B) The prediction errors and error

distribution of ACL force during the whole landing phase based on equal scaling by combining the SSA-ELM and SSA-LSTM prediction model.

Table 15 Detailed prediction error results for 22 test samples.

Test Sample	Whole Landing Phase				10%-35% Landing Phase			
	MSE		RMSE		MSE		RMSE	
	Case1	Case2	Case1	Case2	Case1	Case2	Case1	Case2
1	0.0010	0.0013	0.0318	0.0355	0.0014	0.0009	0.0380	0.0295
2	0.0043	0.0038	0.0652	0.0618	0.0007	0.0010	0.0264	0.0311
3	0.0097	0.0104	0.0986	0.1021	0.0046	0.0058	0.0677	0.0760
4	0.0072	0.0062	0.0851	0.0790	0.0085	0.0055	0.0923	0.0745
5	0.0036	0.0040	0.0598	0.0636	0.0064	0.0019	0.0798	0.0438
6	0.0142	0.0046	0.1192	0.0681	0.0149	0.0034	0.1223	0.0584
7	0.0111	0.0081	0.1052	0.0902	0.0353	0.0033	0.1878	0.0578
8	0.0036	0.0038	0.0600	0.0620	0.0019	0.0027	0.0433	0.0522
9	0.0046	0.0036	0.0678	0.0601	0.0083	0.0007	0.0911	0.0260
10	0.0066	0.0123	0.0815	0.1107	0.0034	0.0017	0.0580	0.0416
11	0.0025	0.0029	0.0505	0.0540	0.0016	0.0019	0.0398	0.0432
12	0.0042	0.0135	0.0650	0.1161	0.0083	0.0256	0.0913	0.1600
13	0.0041	0.0045	0.0639	0.0670	0.0004	0.0004	0.0211	0.0210
14	0.0025	0.0039	0.0496	0.0627	0.0075	0.0015	0.0866	0.0389
15	0.0073	0.0053	0.0854	0.0729	0.0192	0.0138	0.1384	0.1175
16	0.0236	0.0284	0.1535	0.1684	0.0507	0.0040	0.2251	0.0632
17	0.0034	0.0033	0.0582	0.0574	0.0020	0.0018	0.0445	0.0426
18	0.0279	0.0137	0.1670	0.1172	0.0417	0.0188	0.2042	0.1370
19	0.0059	0.0045	0.0770	0.0670	0.0158	0.0114	0.1256	0.1067
20	0.0153	0.0134	0.1236	0.1157	0.0331	0.0077	0.1820	0.0875
21	0.0042	0.0042	0.0647	0.0649	0.0017	0.0009	0.0417	0.0299
22	0.0227	0.0119	0.1506	0.1093	0.0320	0.0138	0.1790	0.1174

Note: "Whole Landing Phase" represents the prediction error results based on the data of the whole landing phase (0%-100% landing phase). "10%-35% Landing Phase" represents the prediction error results based on the data of the 10%-35% landing phase. "Case1" represents the prediction error results based on the SSA-LSTM prediction model for 22 test samples. "Case2" represents the prediction error results based on equal scaling by combining the SSA-ELM and SSA-LSTM prediction model for 22 test samples.

3.6 Lower limb joint movements estimation based on muscle synergy patterns

3.6.1 Results of muscle synergy extraction by NNMF model

The relation between the number of synergies and the mean of VAF is shown in **Figure 51**. When the number of muscle synergies reached six, the VAF exceeded 90% in both the healthy (VAF = 92.83%) and patient groups (VAF = 92.04%). It showed only a small increase as the number of muscle synergies increased thereafter. Because of the computational cost of the estimation process and the accuracy of the estimation results, this study determined six muscle synergy numbers to construct the muscle synergy pattern driven ANFIS model.

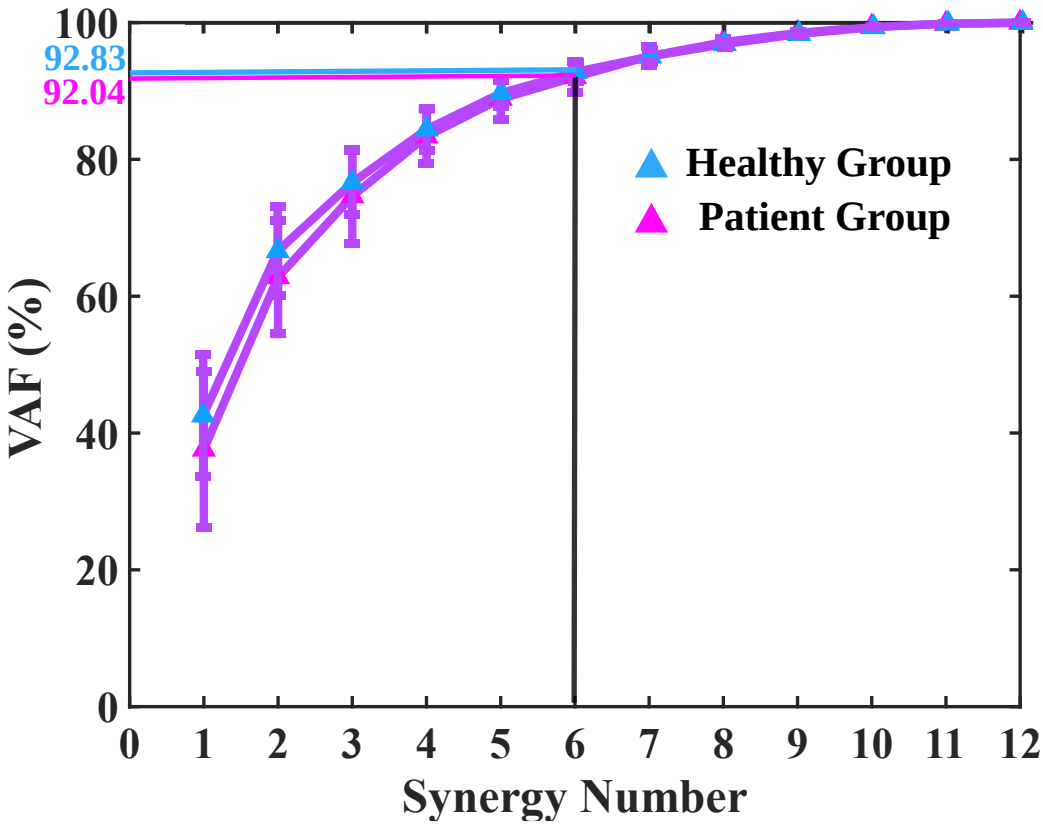

Figure 51 Relation between the number of synergies and mean of VAF. When the number of muscle synergies reached six, the VAF exceeded 90% in both the healthy (VAF = 92.83%) and patient groups (VAF = 92.04%).

The synergy matrix and synergy activation coefficient matrix of subjects 1 to 8 in muscle synergy 1 to synergy 6 in the healthy group are shown in **Figure 52**, and the results of subjects 9 to 16 are shown in **Figure 53**. For the results of the synergy matrix, this study can find that each subject's muscle activation pattern is unique, which also suggests that there is a unique muscle synergy pattern between individuals. The results of the correlation analysis of the muscle synergy activation coefficients showed that the correlation of the muscle synergy patterns across subjects was low. For example, the results of R^2 between subject 1 and subject 2 is 0.26, between subject 1 and subject 3 is 0.42, between subject 1 and subject 4 is 0.13. Also, for subject 1 in the healthy group, the synergy activation coefficient matrix revealed that their muscle synergy 1 was

mainly activated during the 10%-50% landing phase, and the corresponding synergy vectors showed higher activation of GMA, RF, PL, and SS in muscle synergy 1. In contrast, for subject 2 in the healthy group, the synergy activation coefficient matrix revealed that their muscle synergy 1 was mainly activated during the 0%-40% landing phase, and the corresponding synergy vectors showed higher activation of VM and RF in muscle synergy 1. This was also found in other subjects and the differences between the muscle synergies were more pronounced. However, from the view of the trend in the synergy activation scale factor, the integrative magnitude of muscle activation was more or less the same between subjects. That also explains the similarity in muscle activation expressed by different subjects when performing the same movement task. As shown in **Figure. 53** (subjects 1 to 8) and **Figure 55** (subjects 9 to 16), these findings were also seen in the patient group.

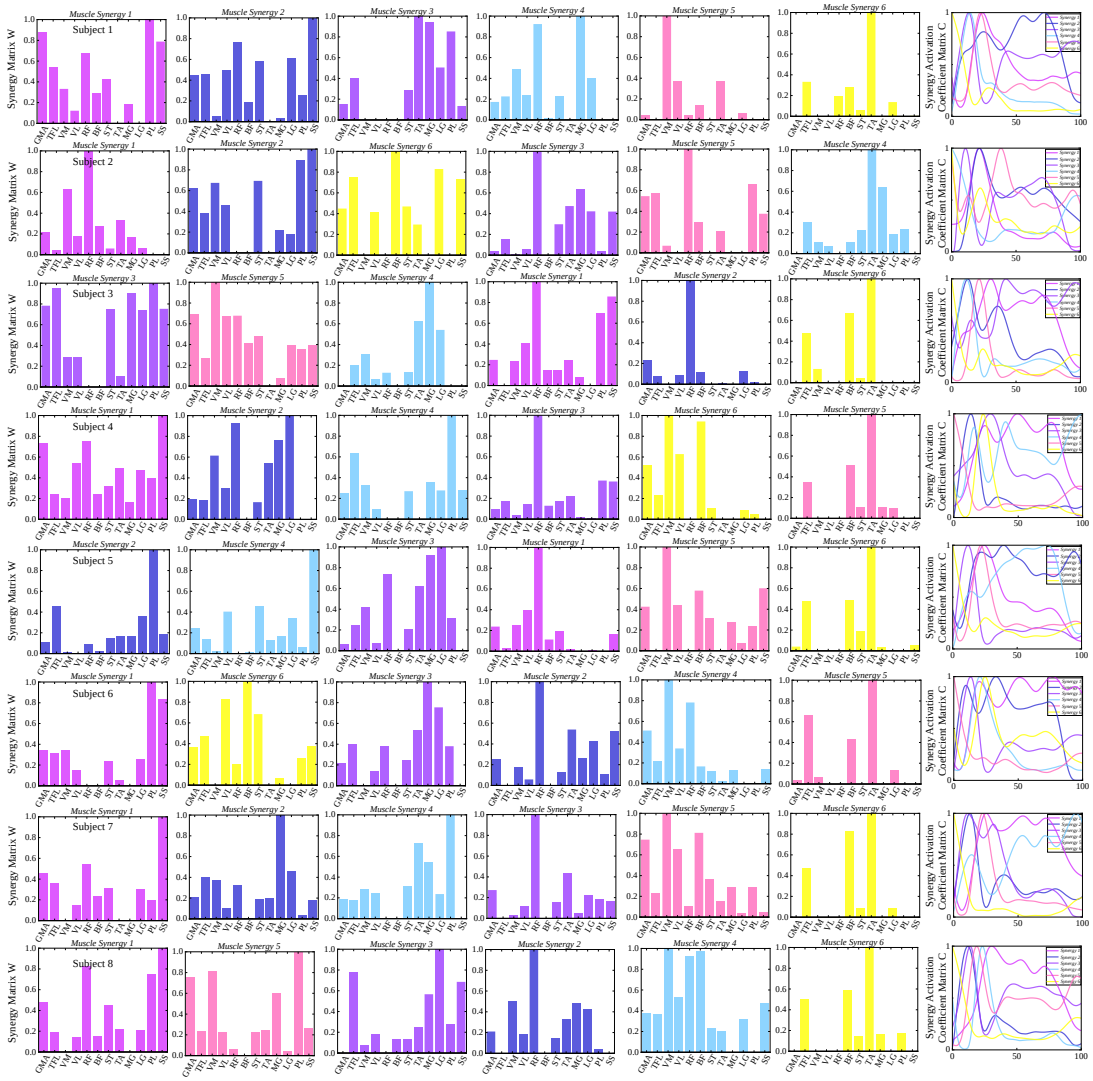

Figure 52 Synergy matrix and synergy activation coefficient matrix results (average of 10 trials) of subjects 1 to 8 in muscle synergy 1 to synergy 6 in the healthy group. From top to bottom are subjects 1 to 8, respectively.

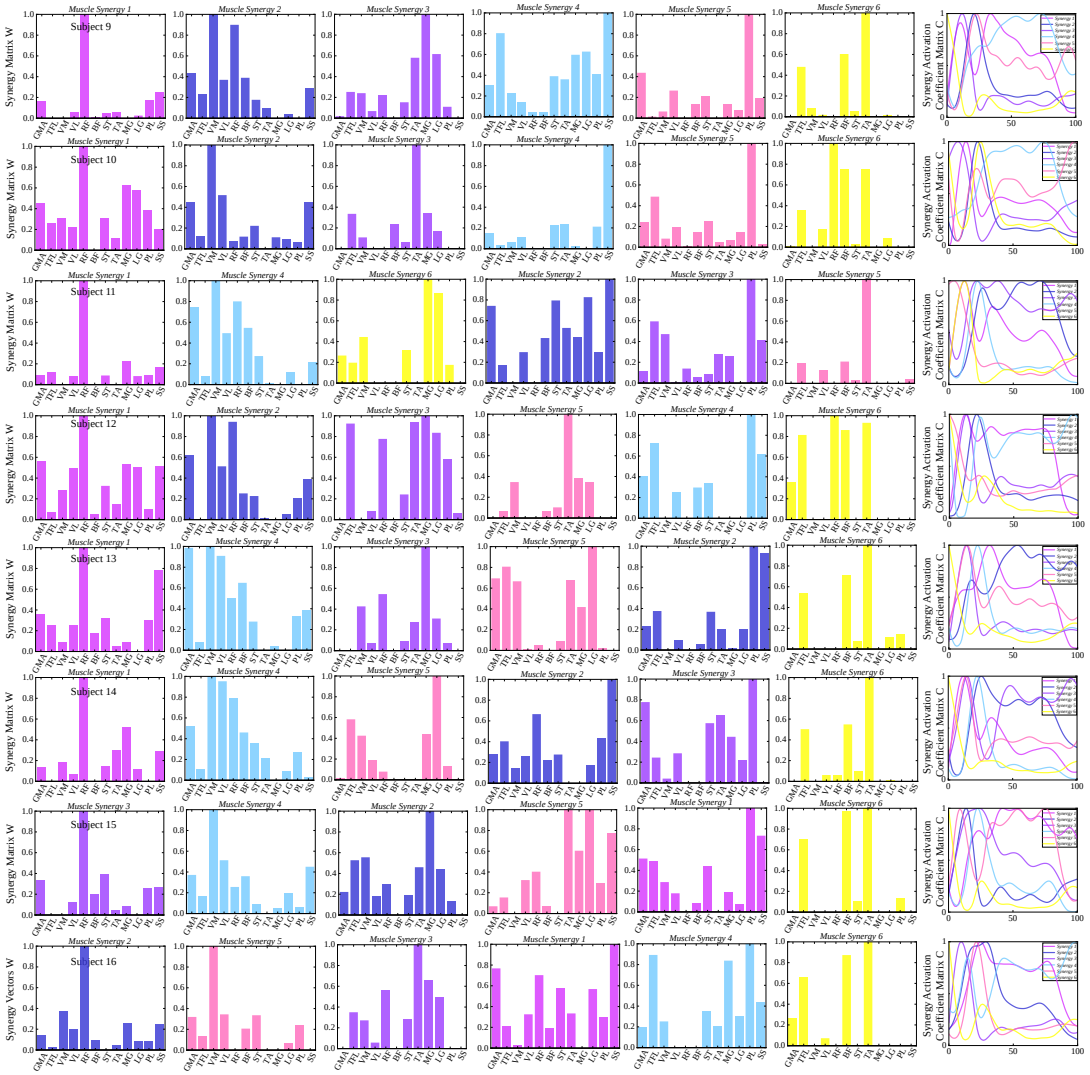

Figure 53 Synergy matrix and synergy activation coefficient matrix results (average of 10 trials) of subjects 9 to 16 in muscle synergy 1 to synergy 6 in the healthy group. From top to bottom are subjects 9 to 16, respectively.

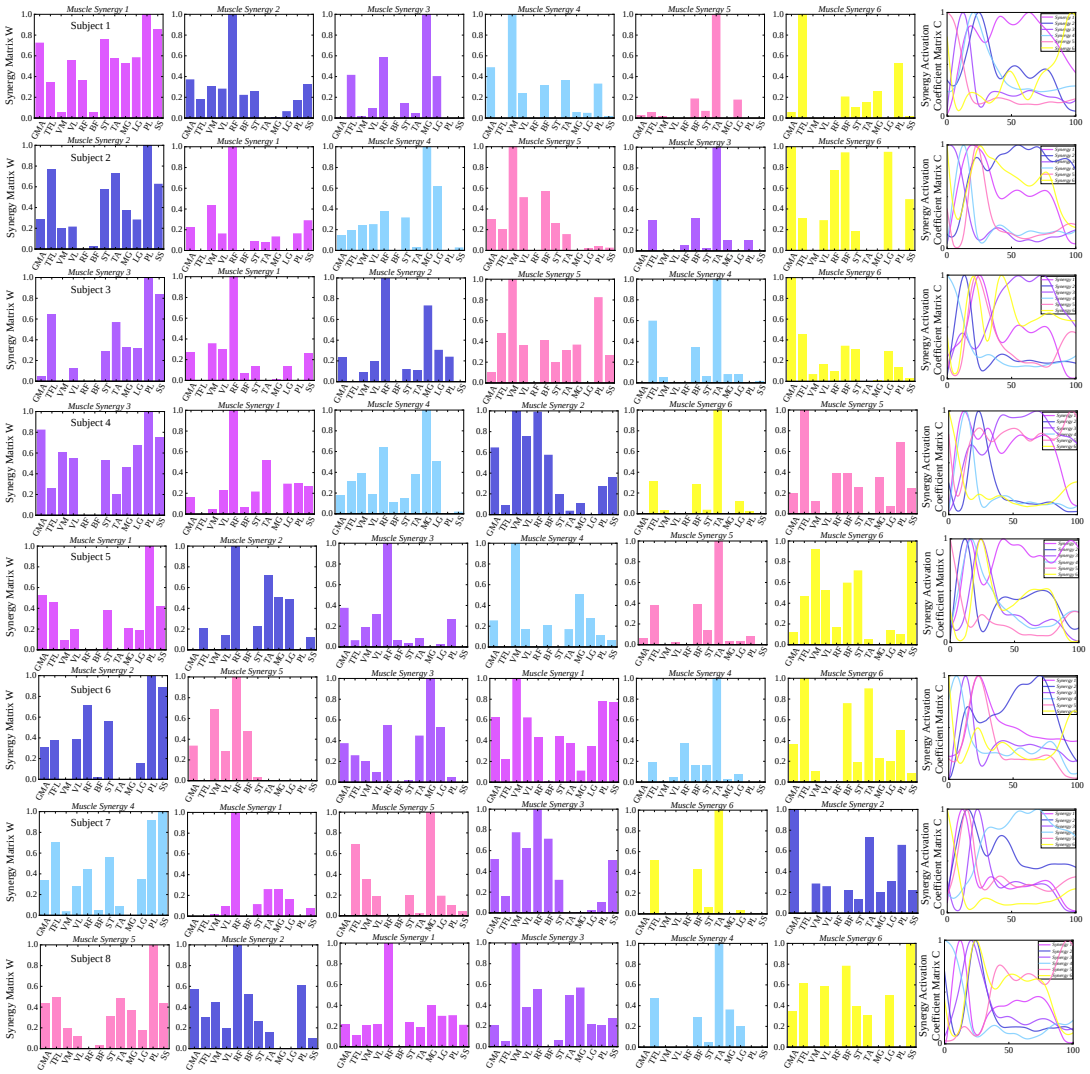

Figure 54 Synergy matrix and synergy activation coefficient matrix results (average of 10 trials) of subjects 9 to 16 in muscle synergy 1 to synergy 6 in the patient group. From top to bottom are subjects 1 to 8, respectively.

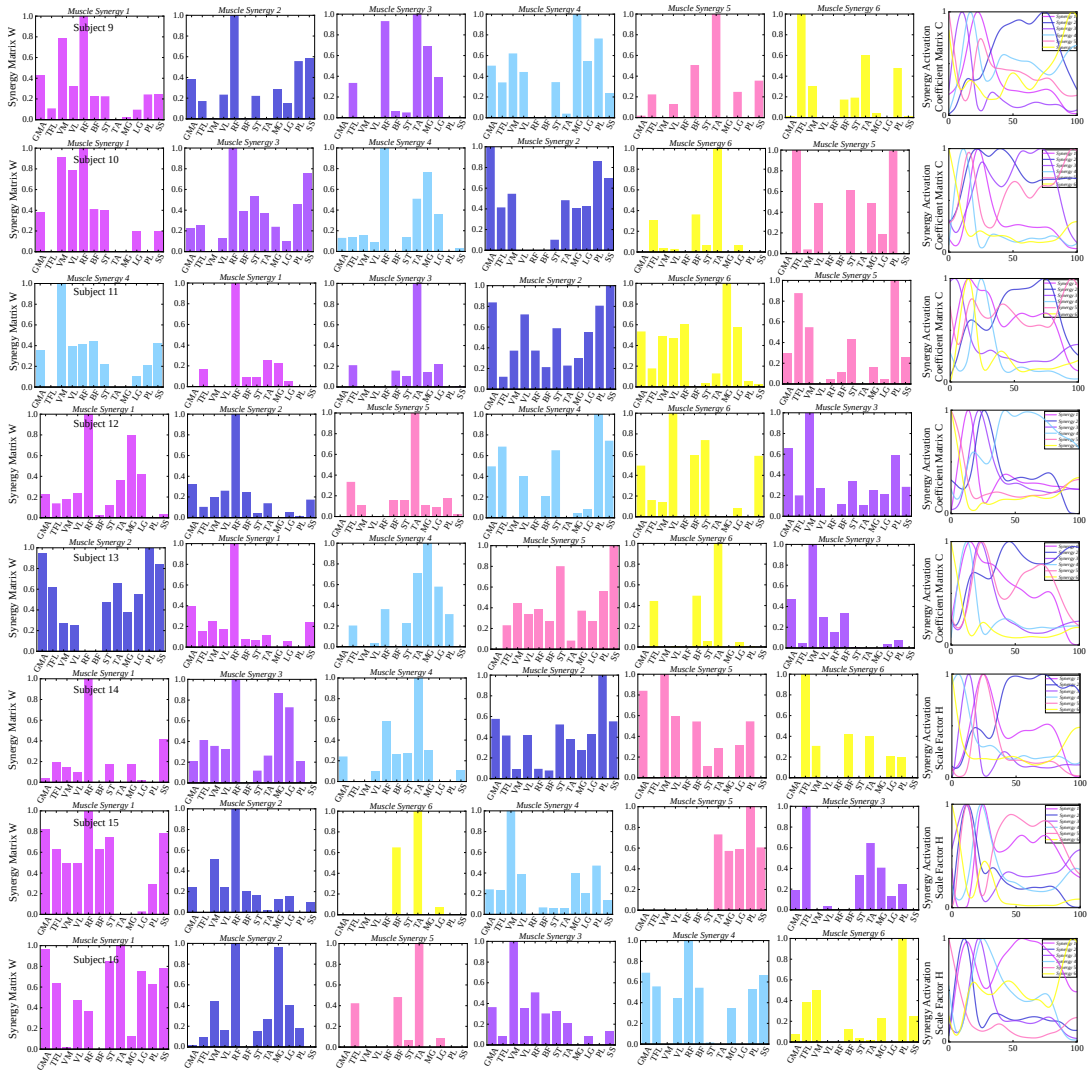

Figure 55 Synergy matrix and synergy activation coefficient matrix results (average of 10 trials) of subjects 9 to 16 in muscle synergy 1 to synergy 6 in the patient group. From top to bottom are subjects 9 to 16, respectively.

3.6.2 Results of ANFIS non-linear regression modeling

By integrating extracted six muscle synergy data $MS(t)$ and $MS(t-1)$, the $MS_1(t-1)$, $MS_2(t-1)$, $MS_3(t-1)$, $MS_4(t-1)$, $MS_5(t-1)$, $MS_6(t-1)$, and $MS_1(t)$, $MS_2(t)$, $MS_3(t)$, $MS_4(t)$, $MS_5(t)$, $MS_6(t)$ were used to drive the ANFIS model. For the estimation of sagittal joint angles and torques under each joint (ankle, knee, hip) in each subject group (healthy and patient), a total of 12 estimates were performed. Based on the Method description, the input variable $\mathbb{M}^{2\times6\times8079}$ and the corresponding estimated variable from Day 1 was used to determine the model parameters. Except for the hip torque estimation in the healthy group, where four fuzzy rules were determined, three fuzzy rules were determined in all the other estimation cases. The optimized fuzzy membership functions of the input variable in the healthy group are shown in **Figure 56** (joint angle) and **Figure 57** (joint torque). For the patient group, the optimized fuzzy membership functions are shown in **Figure 58** (joint angle) and **Figure 59** (joint torque). Take angle and torque as an example, the fuzzy rule of

ANFIS in estimating the ankle angle and torque in the healthy group are shown in **Table 16** and **Table 17**, respectively.

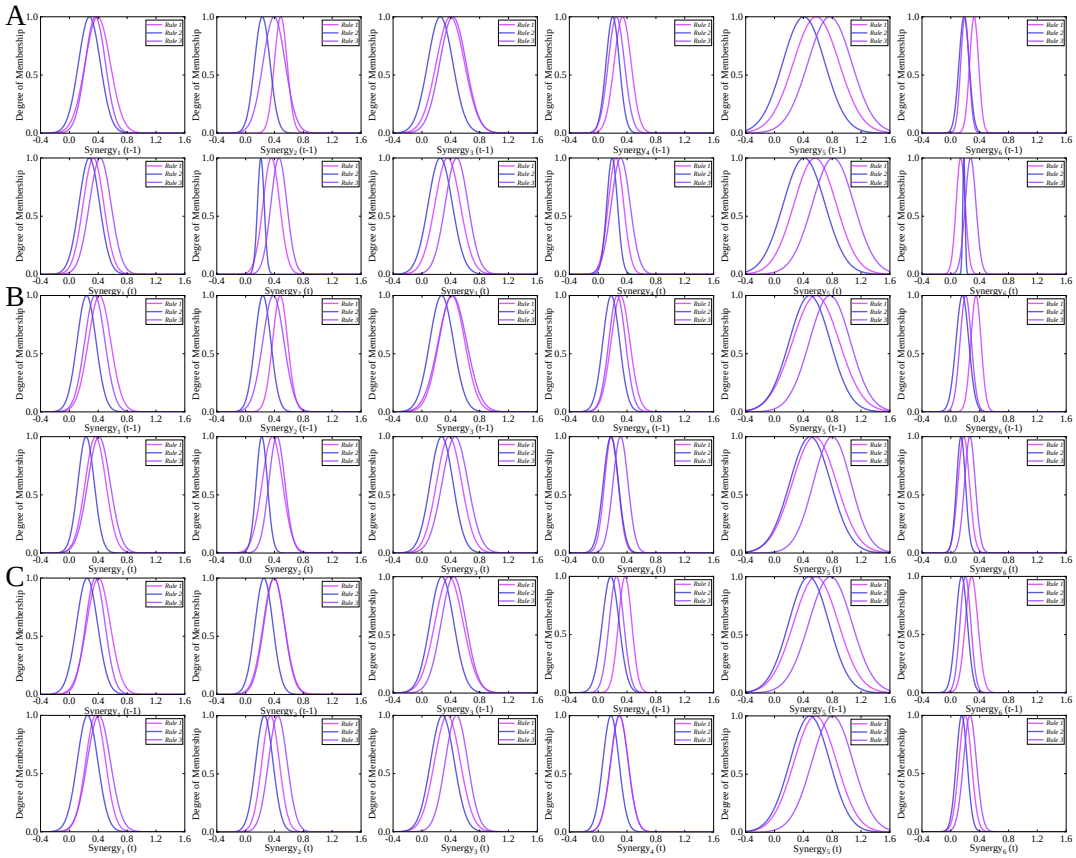

Figure 56 Optimized fuzzy membership functions of joint angle estimation of $MS_1(t-1)$, $MS_2(t-1)$, $MS_3(t-1)$, $MS_4(t-1)$, $MS_5(t-1)$, $MS_6(t-1)$, $MS_1(t)$, $MS_2(t)$, $MS_3(t)$, $MS_4(t)$, $MS_5(t)$, and $MS_6(t)$ in the healthy group. (A) Results based on the ankle joint sagittal angle estimation. (B) Results based on the knee joint sagittal angle estimation. (C) Results based on the hip joint sagittal angle estimation.

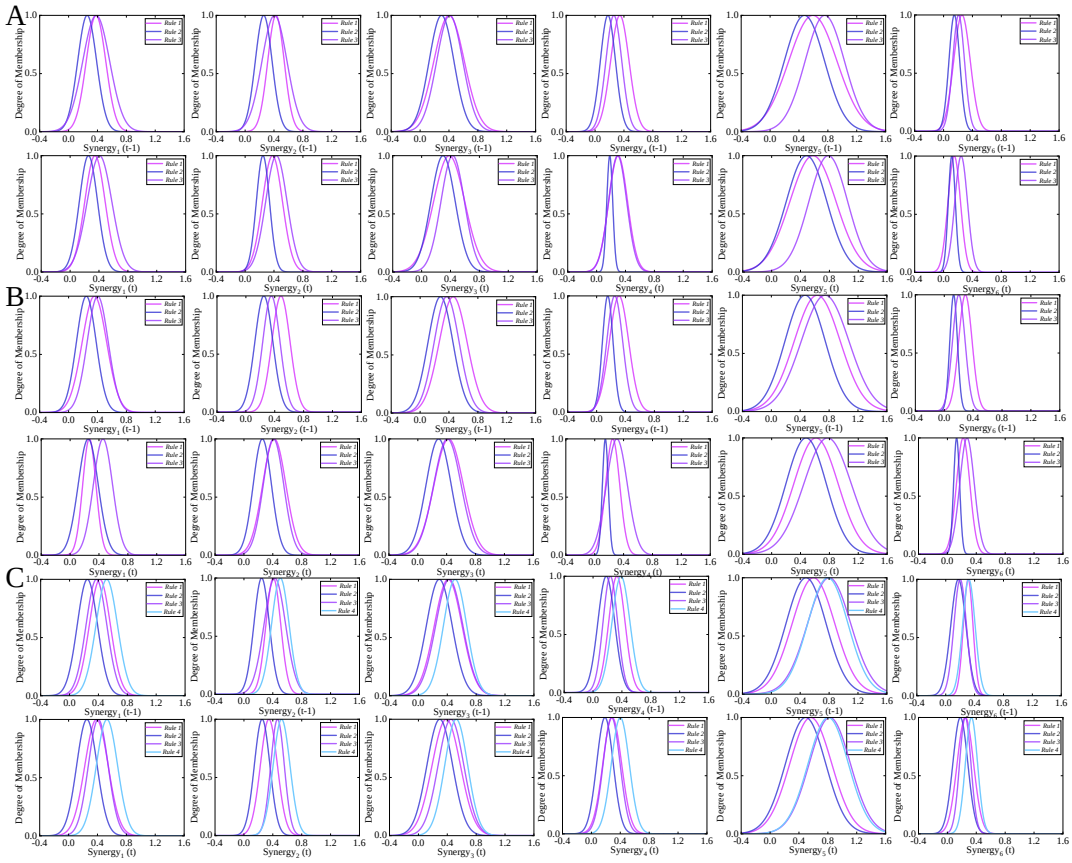

Figure 57 Optimized fuzzy membership functions of joint torque estimation of $MS_1(t-1)$, $MS_2(t-1)$, $MS_3(t-1)$, $MS_4(t-1)$, $MS_5(t-1)$, $MS_6(t-1)$, $MS_1(t)$, $MS_2(t)$, $MS_3(t)$, $MS_4(t)$, $MS_5(t)$, and $MS_6(t)$ in the healthy group. (A) Results based on the ankle joint sagittal torque estimation. (B) Results based on the knee joint sagittal torque estimation. (C) Results based on the hip joint sagittal torque estimation.

Table 16 Results of the fuzzy rule of ANFIS in estimating the ankle angle in the healthy group.

Fuzzy rules of ANFIS in estimating the ankle angle		
R^1	If $MS_1(t-1)$ is A_1^1, $MS_2(t-1)$ is A_1^2, $MS_3(t-1)$ is A_1^3, $MS_4(t-1)$ is A_1^4, $MS_5(t-1)$ is A_1^5, $MS_6(t-1)$ is A_1^6, $MS_1(t)$ is A_1^7, $MS_2(t)$ is A_1^8, $MS_3(t)$ is A_1^9, $MS_4(t)$ is A_1^{10}, $MS_5(t)$ is A_1^{11}, $MS_6(t)$ is A_1^{12}	Then $f_1(t) = -2396.36 \times MS_1(t-1) + 2343.01 \times MS_2(t-1) + 19787.28 \times MS_3(t-1) - 19159.79 \times MS_4(t-1) + 2172.15 \times MS_5(t-1) - 2183.78 \times MS_6(t-1) + 13263.27 \times MS_1(t) - 12909.78 \times MS_2(t) + 2006.84 \times MS_3(t) - 1630.35 \times MS_4(t) - 35555.65 \times MS_5(t) + 34037.59 \times MS_6(t) - 47.32$
R^2	If $MS_1(t-1)$ is A_2^1, $MS_2(t-1)$ is A_2^2, $MS_3(t-1)$ is A_2^3, $MS_4(t-1)$ is A_2^4,	Then $f_2(t) = -130.86 \times MS_1(t-1) + 108.40 \times MS_2(t-1) + 1084.72 \times MS_3(t-1) - 1046.73 \times MS_4(t-1) +$

	$MS_5(t-1)$ is A_2^5, $MS_6(t-1)$ is A_2^6, $MS_1(t)$ is A_2^7, $MS_2(t)$ is A_2^8, $MS_3(t)$ is A_2^9, $MS_4(t)$ is A_2^{10}, $MS_5(t)$ is A_2^{11}, $MS_6(t)$ is A_2^{12}	$1716.77 \times MS_5(t-1) - 1753.88 \times MS_6(t-1) + 1545.48 \times MS_1(t) - 1563.70 \times MS_2(t) - 762.50 \times MS_3(t) + 748.03 \times MS_4(t) - 1420.01 \times MS_5(t) + 1431.82 \times MS_6(t) + 31.50$
R^3	If $MS_1(t-1)$ is A_3^1, $MS_2(t-1)$ is A_3^2, $MS_3(t-1)$ is A_3^3, $MS_4(t-1)$ is A_3^4, $MS_5(t-1)$ is A_3^5, $MS_6(t-1)$ is A_3^6, $MS_1(t)$ is A_3^7, $MS_2(t)$ is A_3^8, $MS_3(t)$ is A_3^9, $MS_4(t)$ is A_3^{10}, $MS_5(t)$ is A_3^{11}, $MS_6(t)$ is A_3^{12}	Then $f_3(t) = 299.44 \times MS_1(t-1) - 294.48 \times MS_2(t-1) - 1586.12 \times MS_3(t-1) + 1549.42 \times MS_4(t-1) - 47.38 \times MS_5(t-1) + 58.26 \times MS_6(t-1) + 1557.23 \times MS_1(t) - 1467.15 \times MS_2(t) + 35.89 \times MS_3(t) - 61.80 \times MS_4(t) + 22.33 \times MS_5(t) - 44.49 \times MS_6(t) + 4.53$

Table 17 Results of the fuzzy rule of ANFIS in estimating the ankle torque in the healthy group.

Fuzzy rules of ANFIS in estimating the ankle torque		
R^1	If $MS_1(t-1)$ is A_1^1, $MS_2(t-1)$ is A_1^2, $MS_3(t-1)$ is A_1^3, $MS_4(t-1)$ is A_1^4, $MS_5(t-1)$ is A_1^5, $MS_6(t-1)$ is A_1^6, $MS_1(t)$ is A_1^7, $MS_2(t)$ is A_1^8, $MS_3(t)$ is A_1^9, $MS_4(t)$ is A_1^{10}, $MS_5(t)$ is A_1^{11}, $MS_6(t)$ is A_1^{12}	Then $f_1(t) = 37.23 \times MS_1(t-1) - 35.71 \times MS_2(t-1) + 178.14 \times MS_3(t-1) - 198.26 \times MS_4(t-1) - 51.87 \times MS_5(t-1) + 53.61 \times MS_6(t-1) - 59.92 \times MS_1(t) + 73.68 \times MS_2(t) + 22.42 \times MS_3(t) - 24.62 \times MS_4(t) - 143.41 \times MS_5(t) + 156.98 \times MS_6(t) + 0.74$
R^2	If $MS_1(t-1)$ is A_2^1, $MS_2(t-1)$ is A_2^2, $MS_3(t-1)$ is A_2^3, $MS_4(t-1)$ is A_2^4, $MS_5(t-1)$ is A_2^5, $MS_6(t-1)$ is A_2^6, $MS_1(t)$ is A_2^7, $MS_2(t)$ is A_2^8, $MS_3(t)$ is A_2^9, $MS_4(t)$ is A_2^{10}, $MS_5(t)$ is A_2^{11}, $MS_6(t)$ is A_2^{12}	Then $f_2(t) = 28.87 \times MS_1(t-1) - 27.83 \times MS_2(t-1) - 26.64 \times MS_3(t-1) + 30.56 \times MS_4(t-1) + 13.09 \times MS_5(t-1) - 14.06 \times MS_6(t-1) - 11.45 \times S_1(t) + 7.78 \times MS_2(t) - 3.06 \times MS_3(t) + 3.58 \times MS_4(t) + 37.53 \times MS_5(t) - 38.85 \times MS_6(t) + 0.65$
R^3	If $MS_1(t-1)$ is A_3^1, $MS_2(t-1)$ is A_3^2, $MS_3(t-1)$ is A_3^3, $MS_4(t-1)$ is A_3^4, $MS_5(t-1)$ is A_3^5, $MS_6(t-1)$ is A_3^6, $MS_1(t)$ is A_3^7, $MS_2(t)$ is A_3^8, $MS_3(t)$ is A_3^9, $MS_4(t)$ is A_3^{10}, $MS_5(t)$ is A_3^{11}, $MS_6(t)$ is A_3^{12}	Then $f_3(t) = -32.91 \times MS_1(t-1) + 35.32 \times MS_2(t-1) + 72.13 \times MS_3(t-1) - 66.34 \times MS_4(t-1) - 19.95 \times MS_5(t-1) + 18.70 \times MS_6(t-1) + 85.78 \times MS_1(t) - 99.68 \times MS_2(t) - 27.46 \times MS_3(t) + 29.76 \times MS_4(t) - 119.34 \times MS_5(t) + 119.78 \times MS_6(t) + 2.19$

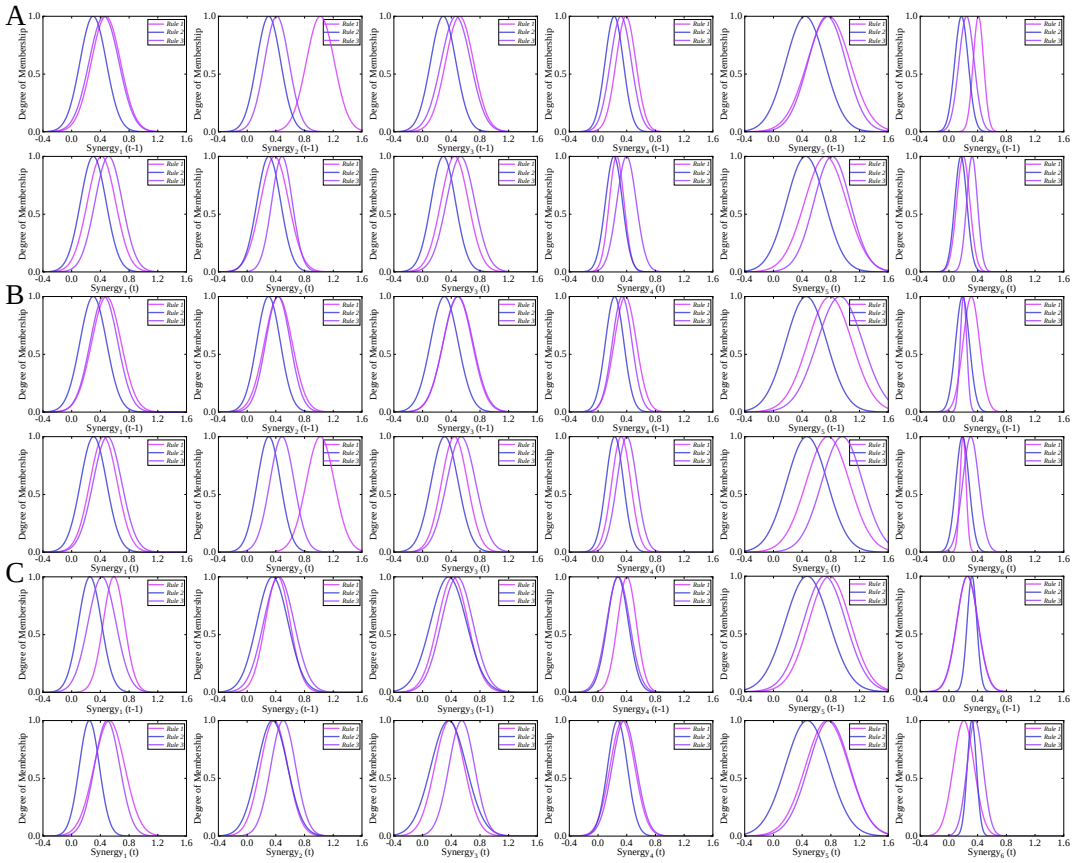

Figure 58 Optimized fuzzy membership functions of joint angle estimation of $MS_1(t-1)$, $MS_2(t-1)$, $MS_3(t-1)$, $MS_4(t-1)$, $MS_5(t-1)$, $MS_6(t-1)$, $MS_1(t)$, $MS_2(t)$, $MS_3(t)$, $MS_4(t)$, $MS_5(t)$, and $MS_6(t)$ in the patient group. (A) Results based on the ankle joint sagittal angle estimation. (B) Results based on the knee joint sagittal angle estimation. (C) Results based on the hip joint sagittal angle estimation.

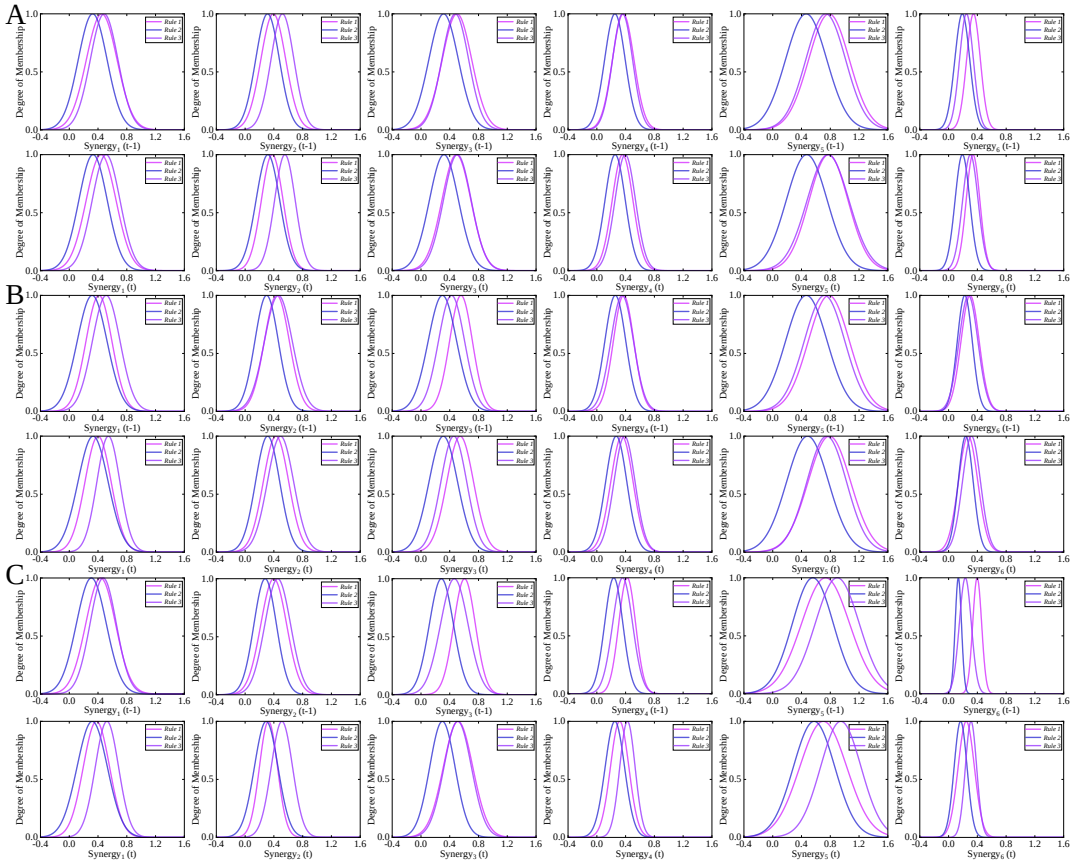

Figure 59 Optimized fuzzy membership functions of joint torque estimation of $MS_1(t-1)$, $MS_2(t-1)$, $MS_3(t-1)$, $MS_4(t-1)$, $MS_5(t-1)$, $MS_6(t-1)$, $MS_1(t)$, $MS_2(t)$, $MS_3(t)$, $MS_4(t)$, $MS_5(t)$, and $MS_6(t)$ in the patient group. (A) Results based on the ankle joint sagittal torque estimation. (B) Results based on the knee joint sagittal torque estimation. (C) Results based on the hip joint sagittal torque estimation.

3.6.3 Results of lower limb joint movement estimation

Comparison results of each joint (ankle, knee, hip) sagittal angle and torque between actual measurements (inverse kinematics/dynamics calculation) and estimated (muscle synergy driven ANFIS model) values of subjects 1 to 16 in the healthy group are shown in **Figure 60**. The comparison results of the patient group are shown in **Figure 61**. Error indicator results between the actual measured and estimated values of subjects 1 to 16 in the healthy group are shown in **Figure 62**, and error indicator results of the patient group are shown in **Figure 63**. By comparing the other relevant study results, this study showed a small estimation error (**Table 18**). Combining the results of the four error indicators across the estimated variables indicates that the current model has excellent predictive performance in estimating lower limb joint motion (**Table 19**). The statistical difference results of the error indicator between the healthy and patient groups are shown in **Table 19**. Their error indicator results are basically consistent, with only a few differences in knee joint angle (RMSE: P=0.007; R^2: P=0.004) and ankle joint torque (RMSE: P<0.001).

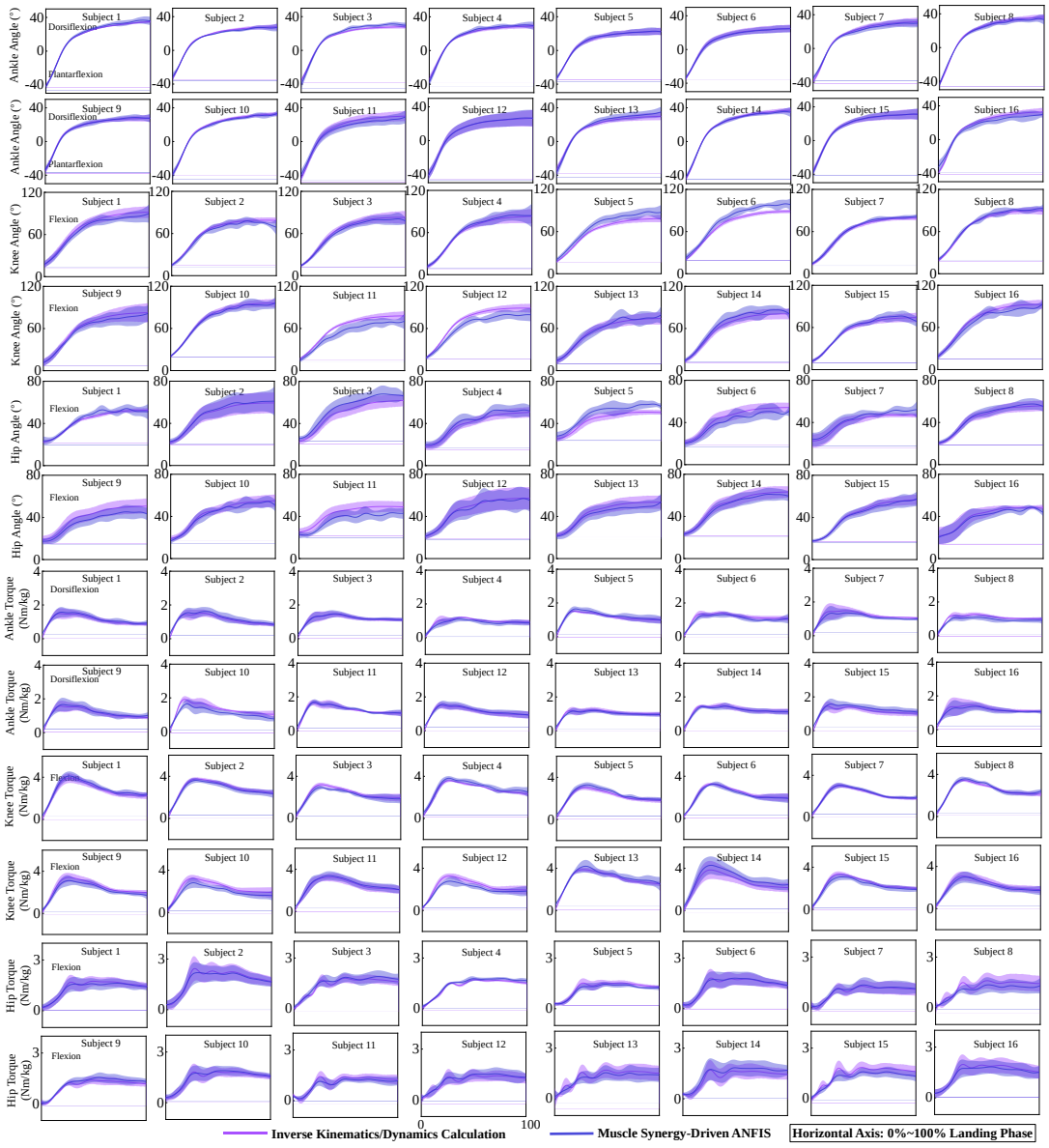

Figure 60 Comparison results of each joint (ankle, knee, hip) sagittal angle and torque between actual measurements (inverse kinematics/dynamics calculation) and estimated (muscle synergy driven ANFIS model) values of subjects 1 to 16 in the healthy group.

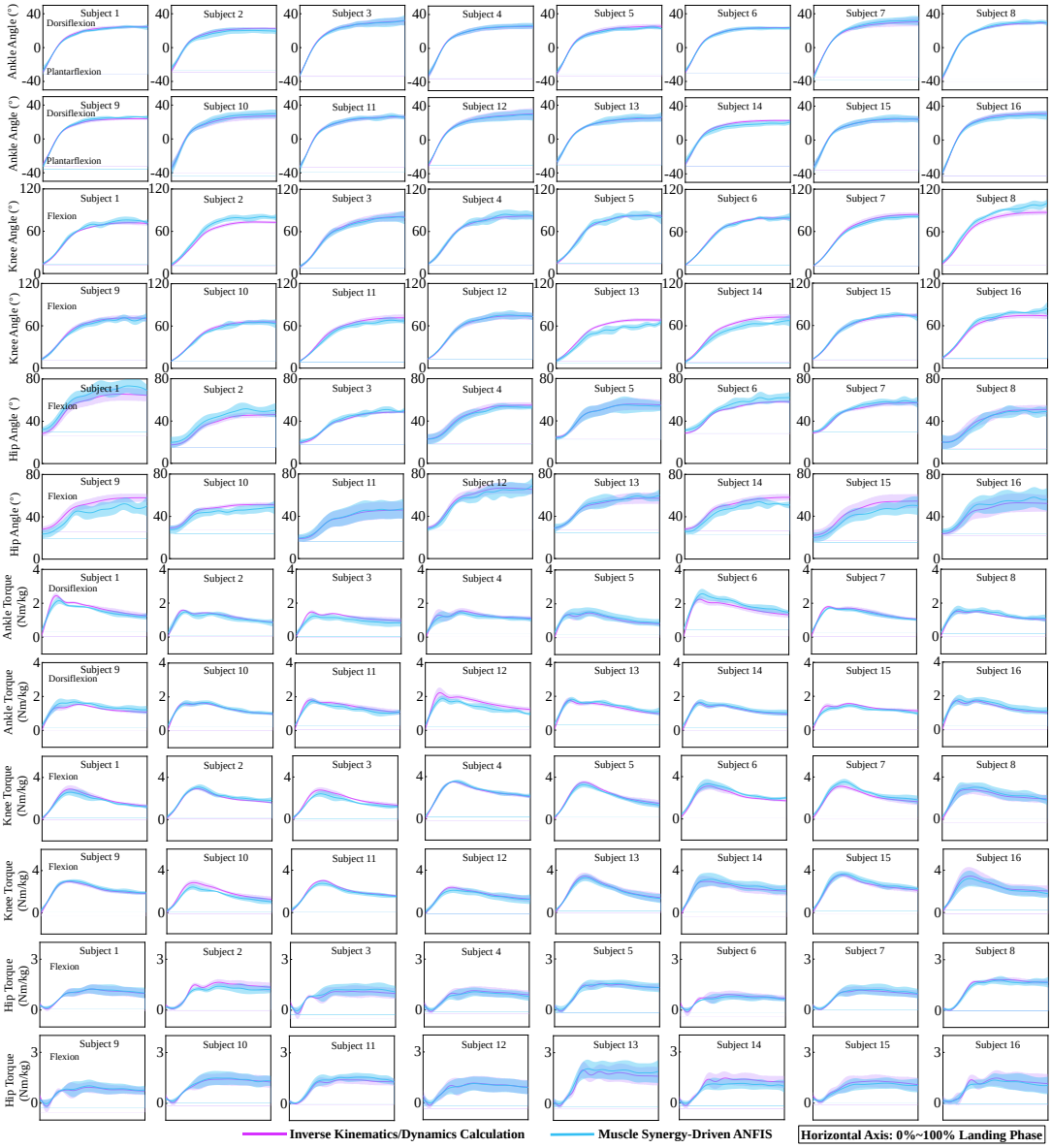

Figure 61 Comparison results of each joint (ankle, knee, hip) sagittal angle and torque between actual measurements (inverse kinematics/dynamics calculation) and estimated (muscle synergy driven ANFIS model) values of subjects 1 to 16 in the patient group.

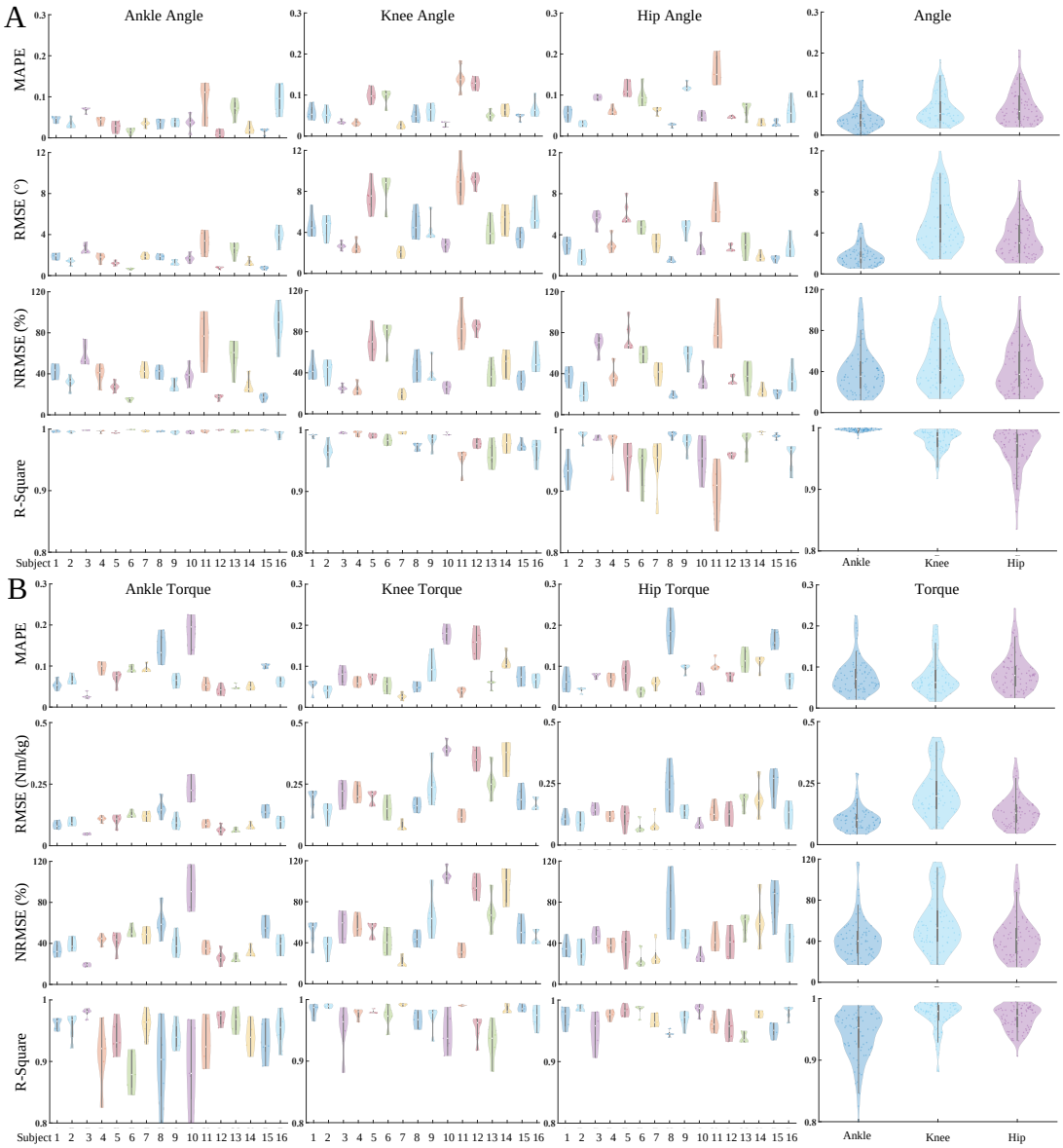

Figure 62 Error indicator results (violin plot) of each joint (ankle, knee, hip) sagittal angle and torque between actual measured (inverse kinematics/dynamics calculation) and estimated (muscle synergy driven ANFIS model) values of subjects 1 to 16 in the healthy group. (A) Error indicator results based on the joint angle estimation. (B) Error indicator results based on the joint torque estimation. The far right shows the results combining subjects 1 to 16.

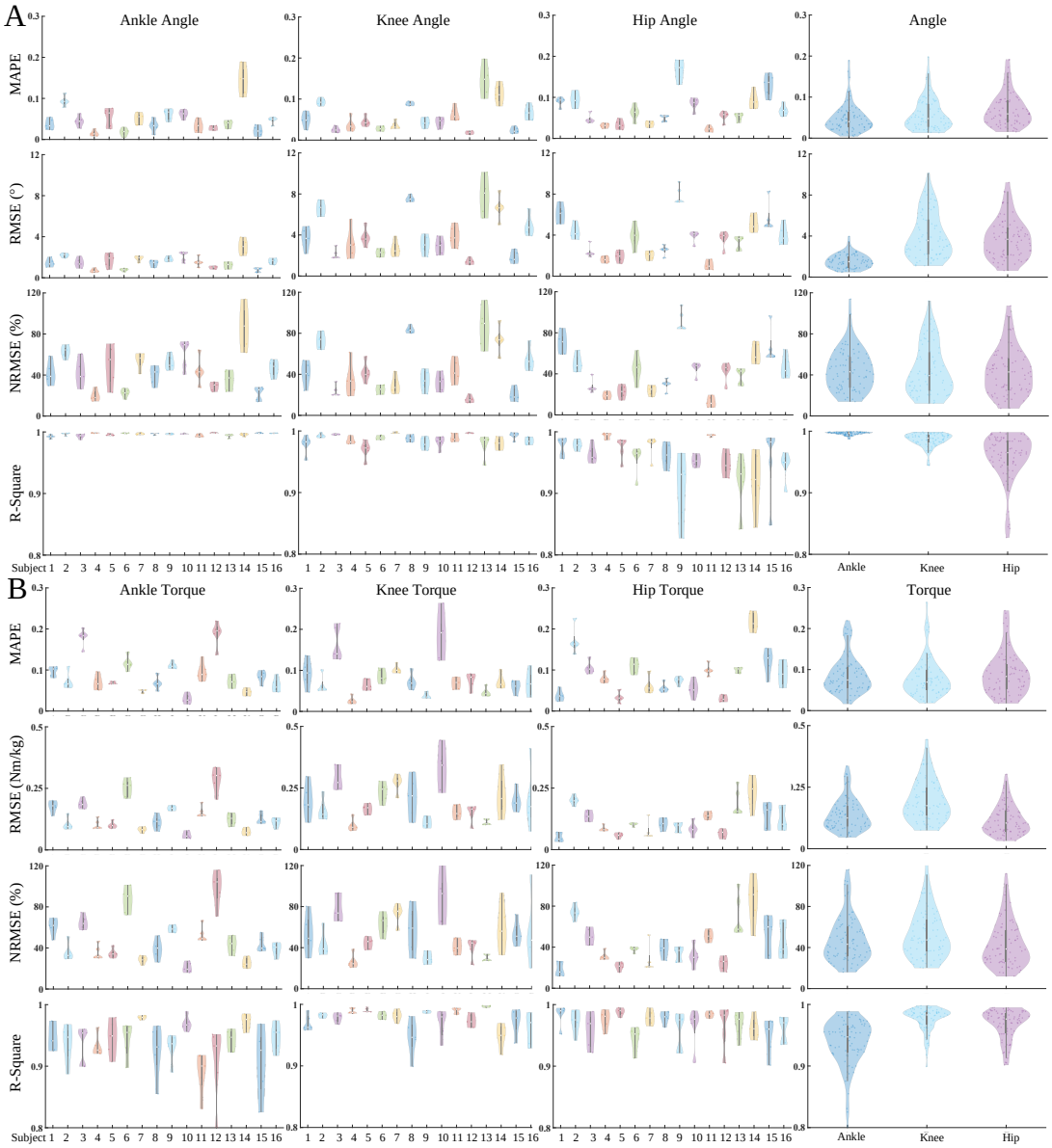

Figure 63 Error indicator results (violin plot) of each joint (ankle, knee, hip) sagittal angle and torque between actual measured (inverse kinematics/dynamics calculation) and estimated (muscle synergy driven ANFIS model) values of subjects 1 to 16 in the patient group. (A) Error indicator results based on the joint angle estimation. (B) Error indicator results based on the joint torque estimation. The far right shows the results combining subjects 1 to 16.

Table 18 Comparison with related research.

Ref.	Task	Method	Estimation method	Estimated target	Performance
Rohit et al.	Stair descent	Knee angle and surface	Nonlinear autoregressive	Ankle angle	RMSE=5.04±1.56

[221]		EMG data	Exogenous Model		R=0.85±0.05
Lu et al. [119]	Stair descent	Surface EMG data	Stacked convolutional and long–short term memory networks	Ankle angle	RMSE=6.791±0.3351
					R^2=0.908±0.0099
				Knee angle	RMSE=8.463±0.6105
					R^2=0.916±0.0120
				Hip angle	RMSE=2.657±0.806
					R^2=0.922±0.0158
Kaitlin et al. [120]	Stair descent	Sonomyography and surface EMG data	Gaussian process regression models	Ankle angle	RMSE=4.36±1.54
				Knee angle	RMSE=7.67±2.57
Liu et al. [98]	Stair descent	Whole-body kinematics data	Two bi-lateral long short-term memory neural networks	Vertical ground reaction forces	RMSE=0.055±0.005
					NRMSE=3.462±0.320
					R=0.991±0.002
Kaitlin et al. [222]	Stair descent	Sonomyography and surface EMG data	Gaussian process regression models	Hip angle	RMSE=4.57±2.01
					NRMSE=18.1
Zhang et al. [121]	Jump down from stair	Lower limb joint angles and surface EMG data	Long short-term memory neural networks and transfer learning	Ankle torque	RMSE=0.18
					NRMSE=10
				Knee torque	RMSE=0.16
					NRMSE=5
				Hip torque	RMSE=0.17
					NRMSE=9
Robert et al. [131]	Combination	surface EMG data	Convolutional neural network	Knee torque	NRMSE=9.2±4.4
Jonathan et al. [223]	Stair descent /ascent	IMU, surface EMG data and electrogoniometers	feedforward neural network and XGBoost	Ankle torque	MAE=0.15
				Knee torque	MAE=0.13
				Hip torque	MAE=0.09
Current	Stair descent	Six muscle synergies	ANFIS non-linear regression model	Ankle angle	RMSE=1.54±0.68
					R^2=1.00±0.00

research	were extracted from twelve surface EMG signals by the NNMF model	Knee angle	RMSE=4.01±2.18
			R^2=0.99±0.01
		Hip angle	RMSE=3.70±1.91
			R^2=0.96±.04
		Ankle torque	RMSE=0.14±0.06
			R^2=0.94±0.04
		Knee torque	RMSE=0.19±0.08
			R^2=0.98±0.02
		Hip torque	RMSE=0.12±0.06
			R^2=0.97±0.02

Table 19 Error indicator detailed results of each joint (ankle, knee, hip) sagittal angle and torque between actual measured (inverse kinematics/dynamics calculation) and estimated (muscle synergy driven ANFIS model) values, and the statistical difference results of error indicator between healthy group and patient group.

	Joint	Error Indicators	Healthy Group	Patient Group	*P*
Angle	Ankle	MAPE	0.04±0.03	0.05±0.03	*P*=0.247
		RMSE	1.78±0.98	1.54±0.68	*P*=0.074
		NRMSE	40.45±22.14	44.38±19.66	*P*=0.237
		R^2	1.00±0.00	1.00±0.00	*P*=0.756
	Knee	MAPE	0.06±.04	0.06±0.04	*P*=0.224
		RMSE	5.02±2.48	4.01±2.18	***P*=0.007**
		NRMSE	46.70±23.03	44.47±24.10	*P*=0.551
		R^2	0.98±0.02	0.99±0.01	***P*=0.004**
	Hip	MAPE	0.07±0.04	0.07±0.04	*P*=0.915
		RMSE	3.46±1.75	3.70±1.91	*P*=0.403
		NRMSE	42.90±21.75	43.13±22.24	*P*=0.946
		R^2	0.96±0.03	0.96±.04	*P*=0.305
	Lower limb joint	MAPE	0.06±0.04	0.06±0.04	*P*=0.962
		RMSE	3.42±2.26	3.09±2.03	*P*=0.089
		NRMSE	43.35±22.32	43.99±21.95	*P*=0.750
		R^2	0.98±0.03	0.98±0.02	*P*=0.929
Torque	Ankle	MAPE	0.08±0.04	0.09±0.05	*P*=0.144
		RMSE	0.11±0.05	0.14±0.06	***P*<0.001**
		NRMSE	42.76±19.18	47.99±22.15	*P*=0.112
		R^2	0.94±0.05	0.94±0.04	*P*=0.946
	Knee	MAPE	0.08±0.04	0.08±0.05	*P*=0.546
		RMSE	0.21±0.10	0.19±0.08	*P*=0.134
		NRMSE	57.63±25.69	52.44±22.39	*P*=0.175
		R^2	0.97±0.02	0.98±0.02	*P*=0.168
	Hip	MAPE	0.09±0.04	0.09±0.05	*P*=0.654
		RMSE	0.14±0.06	0.12±0.06	*P*=0.056
		NRMSE	44.34±20.46	43.43±22.04	*P*=0.786
		R^2	0.97±0.02	0.97±0.02	*P*=0.922

Lower limb joint	MAPE	0.08±0.04	0.08±0.05	*P*=0.154
	RMSE	0.15±0.08	0.15±0.08	*P*=0.749
	NRMSE	48.24±22.81	47.95±22.36	*P*=0.888
	R^2	0.96±0.04	0.96±0.03	*P*=0.548

4. Discussion

4.1 Influence of fatigue factors on lower limb biomechanical patterns during landing

This work investigated the landing pattern differences between before-fatigue and after-fatigue SL, as well as explored the relationship between AICA, AROM and PAF, lower limb joint energy dissipation. The main findings of this study: (1) The ACL dynamic load force will increase during after-fatigue SL, which suggested that the lower limb neuromuscular fatigue factor would increase the risk of ACL injury; (2) The increased risk of ACL injury during after-fatigue SL is related to the decrease of AICA and AROM, and the relationship between AICA, AROM and PAF is highly negatively correlated, the relationship with TED is highly positively correlated.

Previous studies have reported that lower limb muscle fatigue will exhibit less knee and hip flexion, greater GRF, and knee valgus angle during SL, then increasing the risk of ACL injury [1, 3, 15, 17, 18]. The results of the current study partially confirm previous research that after-fatigue SL is characterized by less knee and hip flexion than before-fatigue SL, which is an indication of a "hard" landing. The hard landing is considered to be a landing mode that increases the risk of lower limb injury, especially in non-contact ACL injuries [17]. This is because smaller flexion angles tend to exhibit greater joint reaction forces and joint moments, which will undoubtedly increase the risk of lower limb joint injury [1, 3, 7]. Echoing this, after-fatigue SL also showed greater knee and hip moments (**Figure 23**). During the SL mission, the shock is transmitted from the foot and ankle joints to the knee and hip joints, of which the knee joint plays the main shock absorption role [1, 224]. The degree of energy dissipation in the knee joint is significantly reduced when after-fatigue SL (**Figure 24E**), and insufficient energy dissipation directly increases the risk of knee injury [6]. More importantly, the results of simulations based on musculoskeletal modeling show that the ACL forces are also significantly increased during after-fatigue SL (**Figure 22B, Figure 22A**), which directly increases the risk of ACL injury. Combined with previous studies, this study hypothesized that this might be due to the body consciously reducing the knee and hip flexion angles to maintain postural stability during after-fatigue SL [1, 9]. Such a hard landing inevitably results in increased impact loading on the supporting leg during SL, thereby increasing the risk of lower limb injury, including ACL injury. Based on this, the current work hypothesized that this may be related to changes in ankle movement patterns and explored further.

Firstly, this study revealed that there was a significant difference in ankle motion patterns between before-fatigue and after-fatigue SL, in which the total recognition accuracy was 71.96% and 66.43% for variables ACI and AROM respectively under three classification recognition algorithms. As presented in **Figure 24**, both the AICA (**Figure 24A**) and AROM (**Figure 24B**) decreased during after-fatigue SL. During landing, the lower limbs experienced a distal to proximal load pattern dominated by the foot and ankle joints, and then the load dissipated to the knee and hip joints [1]. The foot and ankle joints, which are in contact with the ground, play a vital role in cushioning the impact loads during landing. Previous studies have reported that the

smaller the AICA (ankle plantarflexion angle) during SL, the shorter the time to reach the peak vertical GRF, and the lower the degree to which the plantar-flexor muscle is used to attenuate the impact load during this process. At the same time, the smaller plantarflexion angle means that the AED is also smaller during SL (**Figure 24D**), and further results showed that this also caused a decrease in the KED (**Figure 24E**). This demonstrates that the changes in AICA and AROM may affect the energy dissipation strategy of the lower limb joint.

The joint power of each joint of the lower limb during before-fatigue and after-fatigue SL is presented in **Figure 23E**, where each joint exhibited greater negative power in after-fatigue SL. Negative joint power indicates that the joint extensors consume the energy impact by doing eccentric work, with greater negative joint power implying greater eccentricity of the joint extensors [224]. By integrating the joint power to calculate the joint work, this study found that the TED, AED, KED and HED decreased in after-fatigue SL, and the relationship between them and PAF was highly negatively correlated (**Figure 25C, Figure 25D**). This provides ample evidence that inadequate joint energy dissipation caused by the decreased eccentricity of the lower limb extensor muscles during SL can lead to increased ACL forces, thereby increasing the risk of ACL injury.

This study also explored the relationship between AICA (**Figure 26**), AROM (**Figure 27**) and each joint energy dissipation and found that AICA showed a positive correlation with AED ($R^2 = 0.6455$), KED ($R^2 = 0.3606$) and HED ($R^2 = 0.2189$). Similar results were found for AROM, which also showed positive correlations with AED ($R^2 = 0.5850$), KED ($R^2 = 0.3037$), and HED ($R^2 = 0.1538$). This positive correlation with the AED, KED and HED diminishes as the impact during SL is transmitted from the ankle joint to the knee and hip joints, both for the AICA and AROM, which suggests that its effect on the energy dissipation of each joint diminishes. Therefore, the lower limb energy dissipation strategy during SL can be adjusted by consciously increasing AICA and AROM, which is specifically manifested as increasing the work by lower limb joints to reduce injuries. However, it is unclear whether increased AICA and AROM, and consequent changes in lower limb energy expenditure strategies, are also associated with ACL injury. As presented in **Figure 25**, the relationship between each variable and PAF was further explored. The results demonstrate a strong positive correlation between TED, AIC, AROM and PAF, with TED having the highest correlation $R^2 = 0.6110$ (**Figure 25C**), followed by AICA $R^2 = 0.4898$ (**Figure 25A**) and AROM $R^2 = 0.3768$ (**Figure 25B**). Combined with the decrease of AICA and AROM in after-fatigue SL, it is reasonable to believe that the increased ACL forces during after-fatigue landing may be caused by insufficient energy dissipation in the joints of the lower limbs due to reduced AICA and AROM.

Therefore, our results demonstrate that increasing the AICA and AROM during SL increases the lower limb joint energy dissipation, thereby reducing the impact loads on the lower limb joints, and thus reducing the risk of lower limb injuries, including ACL injuries. Previous studies have suggested that AICA is negatively correlated with peak knee valgus moment ($R^2 = 0.2500$) and with the sum of peak knee valgus and internal rotation moments ($R^2 = 0.3364$), thus indirectly suggesting that increasing AICA may

reduce the risk of ACL injury [225]. The current study directly demonstrates that AICA and AROM are highly negatively correlated with PAF and joint energy dissipation during SL. The findings may provide new insights for the optimized application of landing strategies, thus providing important theoretical support for the body to reduce the risk of lower limb injuries, including ACL injuries.

Therefore, this study suggest that the individual can consciously increase lower limb flexion angles, AIC, and AROM during SL, so as increase the energy dissipation in the joints of the lower limbs. This would decrease joint impact loads and ultimately reduce lower limb injury risk. For a conscious increase of AICA and AROM, the precondition is that the muscles and tissues around the ankle joint of the body have high strength [226, 227]. During SL, the ankle joint relies heavily on its surrounding tendon units when dissipating impact loads. Especially the ankle plantar-flexor muscle, which provides 30%-50% of the shock absorption during SL [1, 28]. Without a higher strength of the muscles and tissues around the ankle joint to cope with the increased AICA and AROM, the risk of injury to the ankle joint during dissipation of the energy impact is instead increased, which is a point to be balanced.

Some limitations should be considered in the current study. First, this study only collected data from male subjects, and whether the ACL injury law based on the results applies to female subjects needs to be further studied. At the same time, this study only selected a drop-off landing as the biomechanical test movement, which may reduce the generalizability of the application. Future studies should take into account test movements such as landings and cutting from different directions, as they may also contribute to ACL injuries. As a significant portion of the body mass, parameters related to the trunk may be an important property in predicting ACL force. The current study did not include the trunk in the analysis, which also needs to be improved in future studies.

4.2 Exploring landing pattern differences before and after fatigue based on explainable machine learning

The primary purpose of this work was to investigate whether XML can help with clinical landing pattern recognition and to what extent it can aid in the interpretation of prediction results. This work firstly compared the classification recognition performances of several classical classification models on two class landing tasks, and then constructed the XML model based on the neural network model with the best recognition performance combined with LRP to explain the model classification recognition results. Meanwhile, the RS results derived from LRP were evaluated from the statistical and clinical perspectives. Finally, this study completed the validation of the following two questions: 1) which areas of input signals in the two class landing patterns are most relevant to the landing pattern recognition? 2) To what extent do these regions of input signals identified as most relevant for landing pattern recognition remain consistent with statistical evidence and clinical assessment?

Before constructing the XML model, this study first selected three classical and widely used classification algorithm models (SVM, ANN, CNN) for automated landing pattern classification tasks. From the current results, both three classification algorithm models achieved high recognizability in the nine classification tasks (**Figure 30, Table 12**). In order to make a referenceable comparison of classification model performance to select the best classification model, this study also compared it with the calculated ZRB besides comparing the differences between the models. This kind of theoretical accuracy resulting from assigning class labels based on the prior probability of the class represents the minimum at which the input signals between classes can be identified. There are potential risks in analyzing an unreliable classification model, and high identifiability is the basis for further interpretability analysis and the key to providing important information [49]. In other terms, only when the selected classification model can robustly identify the differences between the target classes, the subsequent construction of XML combined with LRP for objective interpretability analysis will be more trustworthy. Among the three classification algorithm models, the classification performance level of ANN for the input signal is particularly outstanding in comparison to the other two models, so the current work only provided the LRP analyzed with the ANN algorithm model. For the binary classification task, this approach undoubtedly reduces the potential risk to a large extent, and its better recognition performance can make the XML model extract more robust features in the input signal.

Which areas of input signals in the two class landing patterns are most relevant to the landing pattern recognition? From the classification performance, this study found that based on the knee data as input signals the classification performance was better than the classification performance that was based on the ankle data or only hip data as input signals (**Figure 30B**). This result suggests that in the ankle knee hip joints, the knee related landing patterns vary more between classes, that is, the contribution of the knee to the successful classification of the two classes of landing patterns may be greater. As an intermediate joint connecting the distal (hip) and proximal (foot and ankle) joints, the knee joint plays a crucial role in the energy impact and transmission process of the lower limb movement chain [6]. Especially in single-leg landings, the energy

transfer and impact force can only be absorbed by the lower limb muscle tissue in contact with the ground (landing leg). At this time, the knee joint plays a dominant role in absorbing impact and energy consumption of the whole lower limb [63]. Therefore, the movement trend of the knee joint is most pronounced under different control conditions, which results from the adaptive adjustment strategy produced by the connecting joint in response to the landing impact. This also results in the classification performance based on knee data as input signals are significantly better than that of the ankle and hip joints.

In terms of the classification performance, this study found that the classification performance based on the sagittal plane data as input signals was better than the classification performance based on the frontal plane data or only transversal plane data as input signals (**Figure 30B**). This result suggests that in three planes (sagittal, frontal, transversal), the sagittal plane related landing patterns vary more between classes, that is, the contribution of the sagittal plane to the successful classification of the two classes of landing patterns may be greater. Compared with the frontal and transversal planes, the range of motion of lower limb joints in the sagittal plane is significantly larger, allowing for greater movement. Also for landing tasks, the energy dissipated in the sagittal plane can reach 10-20 times the energy dissipated in other planes [6, 63], so the main factor affecting the cushioning performance of the lower limb is the range of motion of the joints in the sagittal plane. Previous studies have shown that the most obvious change in landing pattern after fatigue intervention is a reduction in the degree of sagittal flexion of lower extremity joints, primarily in the knee joint [1, 12]. Therefore, it is convincing that there is a greater difference in sagittal landing patterns between classes in the three planes. This is also in line with the validation of clinical evaluation in terms of joints and planes: the features (input signals) in the knee joint and the sagittal plane are better able to identify landing patterns between classes. However, are these features also consistent with the predicted interpretation of the results?

Prediction interpretation aims to explain the local behavior of the model, that is, to predict a given input signal and then explain which part of the input signal has the greatest impact on the prediction of the classifier [53]. The LRP used in this study is one of the prediction interpretations, which propagates something importantly relevant to the prediction from the output layer of the model to the input layer by backward propagation to determine the relative contribution of each input feature, and finally completes the relevant evidence identification of a specific prediction [54]. For landing pattern recognition, XML can highlight signal regions and characteristic signal shapes in the input signal that are associated with a particular landing pattern. So, to what extent do these regions of input signals identified as most relevant for landing pattern recognition remain consistent with statistical evidence and clinical assessment? First, this study can observe two more interesting results from **Figure 34B**: 1) For each joint, the largest summed contribution rate of RS was 41.02% in the knee joint, followed by 30.62% in the ankle joint and 28.36% in the hip joint; 2) For each plane, the largest summed contribution rate of RS was 37.78% in the sagittal plane, followed by 32.55% in the transversal plane and 29.67% in the frontal plane. As discussed above, of the

three joints, the knee is probably the joint that contributes most to landing pattern recognition, and of the three planes, the sagittal plane is probably the plane that contributes most to landing pattern recognition. In statistical terms, the statistical differences between the two landing patterns are most significant in the sagittal plane and the knee joint (**Figure 31A, Figure 32A, Figure 33A**). In conclusion, the RS results derived from the XML model are consistent with the statistical and clinical analysis in at least two respects.

From detailed results of RS distribution, this study also found that the early landing phase contributed more to landing pattern recognition between classes (**Figure 34A**). This is difficult for us to evaluate from a statistical point of view, because the statistical results can only be partitioned for a given region and cannot be quantified to a specific value at each time point. Therefore, this is why the current research proposed the combination of interpretable machine learning to help solve the problem of clinical landing pattern recognition. The XML constructed by combining ANN and LRP is able to support the predicted explanatory output for each variable at different time points during the landing phase. However, from a clinical point of view, it is met with clinical validation. This is because the early landing phase of single-leg landing is an extremely unstable state, while that phase is often accompanied by large impact loads, which leads to a sharp change in landing patterns between classes [1, 2, 19, 30].

Combining the statistical and RS results during each joint of each plane, the RS in identifying the differences between the two class landing patterns generally agreed with the statistical results in the ankle and knee joints (**Figure 31, Figure 32**). However, the statistical results and RS results in the frontal plane of the hip joint were inconsistent. This may be related to the fact that the uniqueness of landing patterns of individual subjects is also taken into account in the calculation of RS [34, 54]. In contrast to statistical analyses where the input signal is based only on the average of individual subject characteristics, XML also takes into account the variability of the data for each test. This can lead to such discrepancies when the variability of the data is more disordered on a per-test basis. However, in most cases, when the XML model extracts general features of individual subjects for landing pattern recognition, its output RS can be convincing [228, 229].

At this stage, an understanding of ML and AI decision making seems inevitable for the application of ML and AI in clinical injury screening, intervention, and treatment. The lack of transparency is a major problem faced in the application of ML and AI in the clinic, and there is an increasing demand for clinical experts to further interpret the prediction results of ML [50, 228]. Here, this study demonstrated the feasibility of interpreting machine learning predictions in clinical landing pattern recognition by combining XML models constructed by LRP, which can not only satisfy the traditional decision problem between classes, but also largely solve the lack of transparency in clinical landing pattern recognition. However, two potential limitations still should be considered in this work. First, only male subject data was collected to train the XML models in the current study, future studies should take into account data from female subjects to more comprehensively validate the effectiveness of the XML models for landing pattern recognition in clinical diagnosis. In addition, the current work has

visualized the recognition results in the form of color-coded waveform. For clinical application by non-specialists, future research should consider translating predictive interpretation results into an easily understandable text format.

4.3 Effect of ankle motion patterns on reducing the lower limb injury risk during landing

This work aims to explore an optimized landing strategy to reduce the injury risk of the lower limb. Specifically, this study explored the relationship between ankle joint motion patterns and lower limb injury risk during SL, as well as investigated how to balance the association between the LAS and ACL injury risk under different ankle motion patterns. This study hypothesized that the overall injury risk of the lower limb, particularly ACL injury, can be minimized by appropriately increasing AICA and AROM during SL, but this increases the LAS risk. The current findings partially support the hypothesis that the larger AICA and AROM exhibit smaller PVGRF and PAF, as well as larger TED and PAIA. In addition, based on the interaction between PAIA and PAF, this study confirmed the range of the AICA and AROM that can balance the LAS and ACL injury risk.

During landing, the subject usually adopts ankle plantarflexion, and then transitions to dorsiflexion until reaching the steady state. In this study, the maximum ankle plantarflexion angle AICA was mainly distributed in the range of 20° to 40° (33.47 ± 5.16°) based on the ankle anatomical position in normal standing at 0°. With the increase of the AICA and AROM, PVGRF exhibited a negative correlation with them, and the correlation coefficient of AICA ($r = -0.591$) was higher than that of AROM ($r = -0.451$). This indicates that using a larger plantarflexion angle is an effective way to reduce lower limb impact loads during SL. It also supports previous findings that greater AICA and AROM reduced PVGRF and increased time to PVGRF [28, 76, 230]. Overall, a larger AICA during SL allows the body to use the plantar flexors to attenuate and cushion the impact load to a greater extent, with the accompanying larger AROM also dissipating more load impact [1, 76, 230].

In addition, the joint power is shown in **Figure 36**, the negative joint power represents that the joint extensor muscles dissipate the impact by producing eccentric work, and the higher negative joint power means a greater eccentric distance of the joint extensor muscle [6, 19]. By integrating and calculating the joint power and obtaining TED, this study found that TED presented a relatively obvious positive relation with AICA ($r = 0.490$) and AROM ($r = 0.687$) (**Figure 37**). Firstly, it is undeniable that the increase of AICA drives the increase of AROM to a certain extent, which also leads to an increased demand for active muscle contraction of the distal joints, with a consequent increase in TED of the lower limb joints. The increase in TED suggests that the lower limb is well cushioned against impact loads, and then the load is reduced based on the passive joint structures, thus reducing the lower limb injury risk [19, 63]. Therefore, the current results demonstrate that changes in ankle motion patterns during SL can influence the degree of impact loading on the lower limb, as well as alter the joint ability to dissipate energy during transfer.

To further radiate the specific effect on each joint, the relationships between AICA, AROM, peak ankle sagittal moment, peak knee sagittal moment, and peak hip sagittal moment were explored. The results showed that both AICA and AROM exhibited negative correlations with each joint moment, with a stronger correlation between AICA and PADM ($r = -0.542$), PKFM ($r = -0.441$). The magnitude of the sagittal joint

moment is directly related to the joint injury risk during landing [1]. As shown in **Figure 38**, this study can find that the increase of AICA and AROM may reduce the injury risk of each joint to a certain extent, which also confirms the conclusion that has been derived above.

The reduction of AICA could raise the energy dissipation demand of the proximal joint, which would result in an increased ACL injury risk. Previous studies have also speculated that larger body anteverted angle and ankle plantarflexion in contact with the ground during SL may show better lower limb cushioning ability with less ACL injury [28, 230]. According to Lee et al., there is a negative correlation between the AICA and both the peak knee valgus moment ($r = -0.5$) and the total of the internal rotation moments and peak knee valgus ($r = -0.58$) [225]. However, there are no relevant studies that directly demonstrate this from the dynamic loading of ACL itself, which often has a certain bias risk. Based on this, this study developed and constructed the ACL model in the OpenSim for musculoskeletal modeling simulations to calculate ACL dynamic loading forces during landing, and explored the relationship between ACL injury risk and ankle motion pattern.

As shown in **Figure 40**, the present work found that both AICA and AROM showed a negative correlation with PAF, with AICA (r = -0.554) showing a higher correlation than AROM (r = -0.332). The results suggested that increasing the AROM and AICA during SL would increase joint energy dissipation and lower the impact loads on the joints, thereby lowering the injury risk of the lower limb, including ACL injuries. Both AICA and AROM can be adjusted by autonomous awareness during SL, and larger AICA is often accompanied by larger AROM. As a result, this study propose that the individual can actively and consciously increase the AICA and AROM during SL to increase the TED, thus reducing lower limb injury risk. The muscles and tissues surrounding the ankle joint must be very strong in order to consciously increase AICA and AROM [64]. When dispersing impact stresses during SL, the ankle joint mostly depends on the muscle and tendon units surrounding it [1, 28, 64]. In the absence of strengthened tissues and muscles surrounding the ankle to accommodate the increased AICA and AROM, the LAS risk increases during energy impact dissipation [64].

In this study, AICA and AROM showed a strong positive correlation with PAIA, and a weak negative correlation with PAIM (**Figure 40**). The increased PAIA is believed to increase the LAS risk, which can further cause ankle instability and thus affect lower limb function [3, 75, 231]. Hence, it is essential to determine a feasible ankle motion pattern to balance the LAS and ACL injury. As shown in **Figure 41**, the results indicated that the LAS risk is negatively correlated with ACL injury risk (r = -0.330, $p < 0.001$). Based on the determined intersection points, this study found that 30° to 40° of AICA and 50° to 70° of AROM were the more appropriate range to balance the injury risk between them. This range can be referenced by individuals during SL, but it should also be adjusted according to the person's ankle dorsiflexion ability and the level of muscle function around the ankle joint. In addition, it is also necessary to strengthen the training of the muscles, the medial and lateral tissues, ligaments around the ankle joint, so as to increase the AICA and AROM to reduce lower limb injury risk while avoiding ankle joint injury.

Based on the actual situation in constructing ACL models, this study summarized the following optimization directions, hoping to make a breakthrough in future research. Throughout the simulation calculations, the model only considers the effect of knee motion on the ACL, but does not consider that as the knee joint movement changes, the attached ACL ligament will in turn affect the DOF of the knee joint. However, in the real human body, the knee DOF and ACL interact with each other. The changes in the knee joint can cause ACL strain, which is transmitted to the knee joint structure, and then affects the range of motion and stability of the knee joint [232]. Due to the complexity of the real human body environment, it is difficult for musculoskeletal modeling and simulation to completely restore the real state [233]. In our future research, I hope to further optimize and develop a more accurate and realistic musculoskeletal model by considering the interaction between various structures.

This study is a relatively short-term landing action simulation, so the ACL mainly exhibits a tensile strain state. This situation only needs to consider the viscoelastic properties of ACL under increasing tensile strain, without considering the viscoelastic response of ACL between stretching and shortening [1, 64]. Meanwhile, considering that setting ACL as a long-term viscoelastic property may increase model complexity and computational cost, the current study sets ACL as a nonlinear short-term viscoelastic property. Future research can focus on further deepening musculoskeletal modeling to develop an ACL model with long-term viscoelastic properties.

In this work, the parameters of the ACL, such as origin, insertion point, length and cross-sectional area of the ligament, were mainly based on data from previously published studies. In view of personalized differences, future research can consider combining medical imaging data (MRI and CT) to construct a subject-specific ACL model of the knee joint. This can make the musculoskeletal modeling simulation more closely match the real situation of the human body, and improve the accuracy and reliability of the simulation results [234]. On the other hand, researchers may also consider combining machine learning and data-driven approaches to optimize the model parameters with the help of a large amount of experimental and simulation data [64]. This can improve the accuracy and generalization ability of ACL force prediction models.

The current work also has the following two limitations and outlooks. First, only the male subjects were studied in this study, and it is not clear whether the movement laws explored based on the results are still applicable to females. Next work should consider exploring the inherent laws in the SL patterns of female subjects. In addition, when assessing the ankle injury risk, this study used only the indicator of ankle inversion angle. Although this indicator is largely indicative of the degree of LAS risk, future research should focus on more detailed indicators given the complexity of the medial and lateral ligaments around the ankle [1, 235].

4.4 Contribution of ankle initial contact angle during landing to reduce the knee-related injury risk

This study investigated the effects of different ankle plantarflexion angles during SL on knee impact loading and ACL injury risk. This study employed a joint impact force to evaluate the impact loads on the knee at various landing angles, and calculated the joint negative work to assess the ability of the knee to dissipate the energy impact. Additionally, the ACL internal load forces (musculoskeletal modeling) and ACL stress (finite element analysis) were simulated and calculated to evaluate the ACL injury risk. Based on the possible findings, I hoped to propose landing optimization strategies to reduce lower limb injuries.

During landing, the subject usually adopts ankle plantarflexion, and then transitions to dorsiflexion until reaching the steady state. In this study, the maximum ankle plantarflexion angle was mainly distributed in the range of 20° to 40° (30.1 ± 6.1°) based on the ankle anatomical position in normal standing at 0°. As the ankle plantarflexion angle increased during SL, this study found that the knee was under decreasing impact loads both in the anterior and vertical directions (**Figure 43**). Especially in the vertical direction, the impact force showed a significant decreasing trend. I suppose that this is related to the fact that the increased ankle plantarflexion angle will make the ankle joint have a greater range of motion and absorb more impact energy [28, 64, 76].

First, the contact between the talus and forefoot produces friction during the SL, and this friction can help absorb impact energy [236]. As the ankle plantarflexion angle increases, the area of the talus in contact with the forefoot increases, making friction increase as well. This contributes to the absorption of more impact energy by the foot, thus reducing the impact loads on the knee. Furthermore, the joint capsule between the talus and the tibia and fibula also helps to absorb impact energy [236, 237]. As the ankle plantarflexion angle increases, the volume and mobility of the joint capsule increase accordingly. The result allows for increased mobility and flexibility of the joint, which in turn helps to absorb the impact forces on the foot during landing [236, 237].

Additionally, greater ankle plantarflexion angles have been shown to increase the ankle joint's negative joint work, thereby increasing the ankle joint's contribution to the total energy dissipated [28, 64]. This naturally reduces the energy impact on the other joints of the lower extremity. Also, this study found that the knee joint negative work showed a tendency to increase, with significant differences occurring only between 20° and 40° (**Fig. 5**). In the case that the total energy of the impact load borne is reduced, the knee joint dissipates more energy by doing negative work, which undoubtedly reduces the joint impact force. Thus, the current findings revealed that the use of a larger ankle plantarflexion angle during landing may be an effective solution to reduce knee impact load.

Varying landing patterns might result in distinct loading impacts on the musculoskeletal, tendon and soft tissues of the lower limb joints [1, 5, 19]. The knee and associated components may sustain damage as a result of excessive impact. Of these, ACL injuries are notably prevalent and significant in terms of severity [1, 3, 9]. As one of the main ligaments around the knee joint, the ACL is extremely critical in

knee stabilization [10, 65]. The results of this study suggested that as the ankle plantarflexion angle increased during landing, the internal load force of the ACL decreased significantly (**Figure 44**). The current study avoids the possible risk of bias by starting with ACL dynamic loading, compared with previous studies that inferred ACL injury risk from other indicators such as knee internal and external rotation moments [28, 225, 230].

Moreover, to better reconstruct the real situation when landing, this study constructed a foot-ankle-knee integration finite element model to calculate the stress distribution of the knee joint and the surrounding structures. As shown in **Figure 45**, the ACL, meniscus, and femoral cartilage stress also decreases with increasing ankle plantarflexion angle. The overall range of variation in ACL stress was small and was mainly distributed in the femoral and tibial attachment regions, as well as in the mid-lateral region. The location of the maximum stress is mainly around the femoral attachment area, which quantitatively reveals that ACL ruptures frequently occur in the femoral attachment area in actual clinical situations [207, 238]. In conclusion, the results of this study revealed that a smaller ankle plantarflexion angle during landing may increase the risk of rupture of the medial femoral attachment area in the ACL, and other tissues around the knee joint. Meanwhile, the stresses on the meniscus and femoral cartilage increased with decreasing ankle plantarflexion angle during landing. Increased stress on the meniscus and femoral cartilage implies that the knee is exposed to increasing impact loads, which results in an increased risk of knee-related injuries. Therefore, a special landing mode by actively increasing the ankle plantarflexion angle at initial contact should be proposed to reduce the risk of knee-related injuries, particularly ACL injury.

Based on the actual situation in constructing ACL models, this study summarized the following optimization directions, hoping to make a breakthrough in future research. Throughout the simulation calculations, the model only considers the effect of knee motion on the ACL, but does not consider that as the knee joint movement changes, the attached ACL ligament will in turn affect the DOF of the knee joint. However, in the real human body, the knee DOF and ACL interact with each other. The changes in the knee joint can cause ACL strain, which is transmitted to the knee joint structure, and then affects the range of motion and stability of the knee joint [54]. Due to the complexity of the real human body environment, it is difficult for musculoskeletal modeling and simulation to completely restore the real state [55]. In the future research, I hope to further optimize and develop a more accurate and realistic musculoskeletal model by considering the interaction between various structures.

In this work, the parameters of the ACL, such as origin, insertion point, length and cross-sectional area of the ligament, were mainly based on data from previously published studies. In view of personalized differences, future research can consider combining medical imaging data (MRI and CT) to construct a subject-specific ACL model of the knee joint [56,57]. On the other hand, researchers may also consider combining machine learning and data-driven approaches to optimize the model parameters with the help of a large amount of experimental and simulation data [5]. This can improve the accuracy and generalization ability of ACL force prediction

models.

Also, other limitations should be noted. First, this study recruited only male subjects in this research, and further exploration is needed as to whether the intrinsic laws explored also occur in females. Second, based on the consensus of previous studies and estimates of computational costs, this study selected only one standard subject for finite element analysis. Considering the inherent inter-individual characteristics, future studies need to be further refined. In addition, this study simplified the medial and lateral collateral ligaments of the knee to a linear elastic material for simulation. which may reduce the accuracy of the simulation results for these ligaments. However, since the stress results of the medial-lateral collateral ligament of the knee were not considered in this study, and also as a method to improve computational efficiency, this setup has been adopted in most studies [5, 90].

4.5 ACL dynamic loading force prediction based on lower limb joint movements

Data-driven machine learning approaches are believed to perform modeling calculations faster than musculoskeletal models and also have higher prediction accuracy [99]. This study first introduces a metaheuristic optimization algorithm to optimize the prediction model based on existing machine learning models, and further optimizes the prediction results by combining the discovered linear relationship between AIC, AROM and PAF to achieve accurate prediction of the ACL dynamic load force during SL using simple and easy-to-measure kinematic data. Metaheuristic optimization algorithms are considered to be able to provide a practical and elegant solution in solving complex problems, and their implementation in optimization problems is specified in achieving an optimal solution with the shortest practical execution time [239]. In the current work, this study use a novel meta-heuristic optimization algorithm (SSA) to find the optimal parameter solution for a prediction model under a specific data set to improve the model prediction performance [107]. The SSA model constantly updates the fitness values to compute the optimal parameter solutions by comparing the prediction error between the actual output and the actual values [240]. Our work can provide some reference for other researchers in the process of constructing prediction models: Determine the optimal parameter solutions to optimize the prediction model based on metaheuristic algorithms.

It is considered that traditional machine learning prediction does not allow for personalized modeling like subject-specific musculoskeletal models, which affects the accuracy of the variable calculation. Based on this, this study revealed a high positive correlation between AIC, AROM and PAF, this study concluded that the regression forecasting model constructed by taking AIC, AROM as input variables to predict PAF could achieve excellent predictive performance. The results of the current study confirmed this conclusion, and the results of the SSA-ELM prediction model are presented in **Figure 47A**, with a high correlation coefficient between the observed and predicted values in the test set and a low prediction error ($R^2 = 0.9992, MSE = 0.0023, RMSE = 0.0474$). Furthermore, when predicting the ACL dynamic loading forces during the whole landing phase, this study used the simple and easy-to-measure ankle, knee and hip sagittal angles as input variables into the constructed SSA-LSTM prediction model, the output of which is presented in **Figure 47B**. The overall prediction results for the 22 test samples showed good prediction performance ($R^2 = 0.9937, MSE = 0.0086, RMSE = 0.0928$) and the individual prediction results for each test sample are presented in **Figure 48**.

However, this study found a greater prediction error during the 10%-35% landing phase (red shaded areas in **Figure 47B**), and the predictions at this stage are the key stage for evaluating the risk of ACL injury [1, 2]. Therefore, this study calibrated and optimized the ACL dynamic loading force predicted by the SSA-LSTM prediction model during the whole landing phase by the PAF predicted by the SSA-ELM prediction model, and the final prediction is presented in **Figure 47C**. In general, the overall prediction results after the final optimization showed excellent prediction performance because of a very strong correlation, and it also showed excellent prediction performance during the 10%-35% landing phase ($R^2 = 0.9989, MSE =$

$0.0058, RMSE = 0.0762$), and the prediction error for each test sample during the 10%-35% landing phase prediction results was also largely smaller than that of the SSA-LSTM results (**Table 15**). On the other hand, compared to previous related studies, Zou et al. developed a transfer learning model to estimate the knee contact medial force of knee valgus patients during rehabilitation gaits ($RMSE = 0.17$) [99]. Johnson et al. developed a convolutional neural network model to estimate the vertical GRF during running ($R^2 = 0.9409$) [241]. Liu et al. trained two bi-lateral LSTM neural networks to estimate the three-dimensional GRF during stair ascent ($R^2 = 0.9821$) and stair descent ($R^2 = 0.9742$) [98]. Therefore, the overall predictive performance of the current work is high accuracy ($R^2 = 0.9947, MSE = 0.0076, RMSE = 0.0873$). As for unavoidable prediction errors, the extremely small errors of the current work are certainly permitted in practical ACL injury risk assessment applications [242]. Especially for researchers who favor direct application, the computational method proposed in the current study avoids the high-cost, time-consuming, and complex process of biomechanical model construction and simulation calculations with extremely small errors.

In conclusion, the present study provides a method for constructing a prediction model for ACL dynamic loading forces during SL with input variables consisting of two discrete variables (AIC, AROM) and three time-series variables (ankle, knee and hip sagittal angles during the landing phase). All five variables are extremely simple and easy to measure in practice, which gives the prediction model excellent generalization capabilities. Furthermore, to ensure excellent performance of the prediction model, this study use the metaheuristic optimization algorithm SSA to optimize the model parameters and propose a secondary optimization by constructing a PAF prediction model, which ultimately results in a highly accurate and easily implemented ACL force prediction model. Given the feasibility and ease of operation of the prediction model, this study explored simple and easy-to-measure parameters as predictors whenever possible, but the data processing still requires users to have some basic skills. Therefore, I also plan to package the whole prediction model and gradually develop the supporting software for clinical application by routine personnel.

4.6 Lower limb joint movements estimation based on muscle synergy patterns

This study proposed a movement intention detection technology for estimating each joint continuous kinematic variable based on the lower limb muscle synergy pattern, with a view to developing applications for more efficient exoskeleton-assisted rehabilitation training. By extracting the lower limb muscle synergy patterns of healthy subjects and patients through NNMF, and then mapping the lower limb muscle synergy patterns to each joint continuous motion variable using the developed ANFIS non-linear regression model. It reveals that the proposed ANFIS model driven by the NNMF-extracted muscle synergy patterns will be able to accurately and reliably estimate lower limb joint movements, and that the effectiveness will also be radiated to patient subjects.

Lower limb-powered exoskeletons and orthoses play an essential role in the rehabilitation of patients [112, 113]. The basis for seamless control of exoskeleton robots and orthoses is to achieve accurate inference of the user's movement intentions in the human-machine interface [114, 115]. During this process, surface EMG signals, which are generated by muscle contractions during movement, and widely used as a tool for detecting movement intentions in rehabilitation robots [117, 118]. Due to the problems of insensitive responses and large estimation errors in traditional studies when using a single set of surface EMG signal information features as input variables to predict movement intention, this study substituted the reconstructed muscle synergy pattern based on the NNMF model extraction instead of a single set of surface EMG signals into the movement intention estimation system. Being a set of neural control information collections, muscle synergy contains coordinated information between each muscle and reveals the coordination of muscle recruitment [33, 34]. In the present study, this study extracted six muscle synergies from twelve muscle activation signals (**Figure 51**), and the muscle synergies obtained represent the variability of muscle coordination corresponding to the movement of each joint under a specific movement task. This study can find that each individual's muscle activation pattern is unique from the synergy vectors, which also suggests that there is a unique muscle synergy pattern between individuals (**Figure 52**). Meanwhile, from the view of the trend in the synergy activation coefficient matrix, the integrative magnitude of muscle activation was more or less the same between subjects, which also explains the similarity in muscle activation expressed by different subjects when performing the same movement task. In other words, the muscle synergy pattern recodes the muscle activation in a specific movement pattern, thus achieving the expression of joint movement.

Given the highly non-linear nature of the correlation between muscle synergy patterns and the movement variables to be estimated, this study propose the use of ANFIS neural networks that are both interpretable and non-linear to handle the complex non-linear information in the mapping of muscle synergy patterns to movement variables [145]. As shown in the Methods section, this study provides a comprehensive and detailed description of the entire modeling computational process of the ANFIS model driven by muscle synergy patterns extracted from the NNMF model. The ANFIS, which combines the autonomous learning mechanism of an artificial neural network with the fast inference capability of a fuzzy logic inference system, this study successfully connected the non-linear relationship between muscle synergistic patterns

and joint motion through its determined fuzzy rules and constructed membership functions (**Table 16**, **Figure 56**). From the results of the four error indicators across the estimated variables, this study demonstrated that the current model has excellent predictive performance in estimating lower limb joint motion (**Figure 62** and **Figure 63**). In the estimation of joint angle and torque, the square of the correlation coefficient R^2 between the model's estimation and the actual measurements reached 0.97 and 0.95, which is higher than the results of other related studies (**Table 18**).

In the previous study, Rohit et al. proposed a non-linear autoregressive model to estimate continuous ankle angles using surface EMG signals and knee angles as inputs [221]. Their results showed that the errors between the estimated and actual measured ankle angle during the movement of going down the stairs were: RMSE=5.04 ± 1.56, R^2=0.85±0.05 (this work: RMSE=1.54±0.68, R^2=1.00±0.00). Lu et al. proposed a stacked convolution and long short-term memory network to estimate continuous ankle, knee, and hip angles, and the estimation results are shown in **Table 18** [119]. Kaitlin et al. used Sonomyography and surface EMG data as input to estimate continuous ankle, knee, and hip angles with a Gaussian process regression model (**Table 18**) [120, 222]. For the estimation of joint torque, zhang et al. used Lower limb joint angles and surface EMG data as input, long short-term memory neural networks and transfer learning were used to estimate the continuous ankle (RMSE=0.18), knee (RMSE=0.16), and hip (RMSE=0.17) torque [121]. **Table 18** summarized the comparison results with other relevant studies, and **Table 19** provided the results of the estimation error indicators for the current study.

With movement disorders in patients, the surface EMG signals of their muscles during exercise are often different from those of healthy subjects. Abnormalities in neural function and deficits in muscle function result in a single set of surface EMG signal characteristics that hardly reflect the true physiological phenomenon. As a collection of neural control information, the muscle synergy pattern contains information on the coordinates between each muscle and can well restore the characteristics of muscle activation under a specific motor task [135, 136]. As shown in **Table 19**, the results of the error indicators in the patient group remained largely consistent with each other and the healthy group, both showing excellent estimation performance. This reveals the generalizability of mapping muscle synergy patterns to joint motion variables.

The extracted muscle synergy pattern shows a different approach to optimization theory, which distinguishes it from strictly neural hard-wired synergy. It can achieve the most advanced performance by using low-dimensional spatial synergy information. Considering the potential of artificial neural networks in solving the problem of non-linear relationships in mapping muscle synergy patterns to joint motion variables [46, 145], and the fast inference capability of fuzzy logic inference systems, this study developed ANFIS as the estimated model. Finally, the ANFIS model achieves superior performance in mapping muscle synergy patterns to joint motion variables from a specific movement task. Therefore, in clinical sports rehabilitation applications, muscle synergy patterns can be considered as input variables for movement intention detection, combined with the ANFIS model to achieve more flexible and precise movement

control in lower limb-powered exoskeletons.

Regrettably but inevitably, several limitations should be noted in the current work. First, the current work only selected the data on the movement of stairs descending to assess the accuracy of the proposed model. This is because the movements involved in stair descending are more complex than in other daily activities and the corresponding movement intentions are more difficult to estimate [112, 223]. Future work should consider the feasibility and accuracy of detecting other movement intentions. In addition, this study used only 16 subjects' movement data on the same day to train the model, which may result in poor generalization of the model when detecting other subjects' movement intentions [113]. Therefore, future research should also consider collecting a large sample of data to train the model in advance, so that the model can achieve a fast and accurate estimation of movement intention while having good generalization. This study integrated the muscle synergy space of the original time series $MS(t)$ and the muscle synergy space with the first-time data point removed $MS(t-1)$ as input variables. From the current prediction results, although the overall estimation performance of the model is excellent, future research should also explore the effect of different input variables on the estimation performance.

The objective function defines the magnitude of the error in solving for the muscle synergy matrix W. In the current study, the objective function is derived from the Euclidean distance measure, which is a widely used method. In the future, it should also compare the reconstruction errors under different objective functions so that the W can represent the muscle synergy matrix to the greatest degree possible. For the approximation methods, this study adopted simplified techniques in muscle synergy feature selection. The top 6 muscle synergies (VAF > 90%) were determined as inputs to the prediction model to reduce computational costs and increase computational efficiency. While this approach is generally accepted, the remaining six muscle synergies may also improve the estimation performance of the model. Therefore, future research should also consider combining both computational cost and model performance to determine the number of muscle synergies.

5. Conclusions and future work

5.1 Conclusions

This thesis explored the intrinsic laws of lower limb injury risk during landing by constructing an advanced musculoskeletal model, as well as developing a prediction model of lower limb biomechanics based on machine learning for accurate motion monitoring, which ultimately: 1) provide new insights for the optimization of landing strategies and thus provide important theoretical support for the development of ACL injury prevention training or related rehabilitation programs; 2) will enable applications in a wider range of sports training and injury monitoring to improve human performance and reduce sports injuries.

The first section of the thesis revealed that lower limb neuromuscular fatigue increases the ACL dynamic loading force during SL, thereby increasing the risk of ACL injury. After-fatigue SL is characterized by less knee and hip flexion than before-fatigue SL, this hard landing inevitably results in increased impact loading on the supporting leg during SL, thereby increasing the risk of lower limb injury. This result is associated with a smaller AICA (plantarflexion angle) and AROM movement pattern of the ankle joint during after-fatigue SL. There was a significant difference in ankle motion patterns between before-fatigue and after-fatigue SL. By increasing the AICA and AROM during SL, the energy dissipation of the lower limb joints can be increased and the PAF reduced, thus reducing the impact loads on the lower limb joints and reducing lower limb injuries, including ACL injuries. The findings of this section can provide new insights for the optimization of landing strategies and thus provide important theoretical support for the development of ACL injury prevention training or related rehabilitation programs.

The second section of the thesis revealed the applicability of XML methods that can interpret the results of ML decisions for clinical landing analysis, and their great promise for future application and implementation. This study explored the landing pattern recognition between classes, which provided a feasible framework for realizing the interpretability of ML decision results in clinical landing analysis, and provided methodological reference and a solid foundation for future clinical diagnosis and biomechanical analysis. This study can not only satisfy the traditional decision problem between classes, but also largely solve the lack of transparency in clinical landing pattern recognition. Also, in order to facilitate future clinical applications, in addition to the color-coded waveform figures presented in the current study, translation of the predictive interpretation results into an easy-to-understand text format should be considered. This will enable the research method to be understood by more people, and also provide clinical experts with more in-depth and intuitive explanations when analyzing landing patterns.

The third section of the thesis explored the relationship between ankle joint motion patterns and lower limb injury risk during SL. To more realistically revert and simulate the ACL injury mechanics, this study developed a knee musculoskeletal model that reverts the ACL ligament to a nonlinear short-term viscoelastic mechanical mechanism (strain rate-dependent) generated by the DCT as a function of strain. The current results

revealed that the appropriate increases in AICA and AROM may reduce the lower limb injury risk, particularly ACL injuries, but this may increase the LAS risk. AICA in the approximate range of 30° to 40° and AROM in the approximate range of 50° to 70° is likely to balance the association between the LAS and ACL injury risk. It is essential to strengthen the training of the muscles, the medial and lateral tissues, ligaments around the ankle. This can reduce lower limb injury risk while avoiding ankle joint injury when AICA and AROM are increased. This study has the potential to offer novel perspectives on the optimized application of landing strategies, thus giving crucial theoretical backing for decreasing the injury risk of the lower limb during SL.

The fourth section of the thesis concluded that the use of a larger ankle plantarflexion angle during landing may be an effective solution to reduce knee impact load. This study revealed that a smaller ankle plantarflexion angle during landing may increase the risk of rupture of the medial femoral attachment area in the ACL, and other tissues around the knee joint. Meanwhile, the stresses on the meniscus and femoral cartilage increased with decreasing ankle plantarflexion angle during landing. Increased stress on the meniscus and femoral cartilage implies that the knee is exposed to increasing impact loads, which results in an increased risk of knee-related injuries. Therefore, a special landing mode by actively increasing the ankle plantarflexion angle at initial contact should be proposed to reduce the risk of knee-related injuries, particularly ACL injury.

The fifth section of the thesis introduced a metaheuristic optimization algorithm to optimize the prediction model based on existing machine learning models, and further optimizes the prediction results by combining the discovered linear relationship between AICA, AROM and PAF to achieve accurate prediction of the ACL dynamic load force during SL using simple and easy-to-measure kinematic data. In general, the proposed prediction model has low input variable demands (sagittal joint angles), excellent generalization capabilities and superior performance in terms of high accuracy. For researchers who favor direct application, the computational method proposed in the current study avoids the high-cost, time-consuming, and complex process of biomechanical model construction and simulation calculations with extremely small errors. Furthermore, this study is expected to be promoted and applied to a wider range of sports training and injury monitoring to improve the body's sports performance and reduce sports injuries.

The sixth section of the thesis proposed a movement intention detection technology for estimating each joint continuous kinematic variable. We first extracted the lower limb muscle synergy patterns of healthy subjects and patients through NNMF, and then mapped the lower limb muscle synergy patterns to each joint continuous motion variable based on the constructed ANFIS non-linear regression model. It was demonstrated that the proposed ANFIS model driven by the NNMF-extracted muscle synergy patterns will be able to estimate the joint movements of the lower limb accurately and reliably, and that this effectiveness will also be radiated to patients. Future work from this study can be applied to sports rehabilitation in the clinical field by achieving more flexible and precise movement control of the lower limb assisted equipment to help the rehabilitation for patients.

5.2 Recommendations for future works

This thesis only collected data from male subjects, and whether the intrinsic laws based on the results applies to female subjects needs to be further studied. Throughout the simulation calculations, the model only considers the effect of knee motion on the ACL, but does not consider that as the knee joint movement changes, the attached ACL ligament will in turn affect the DOF of the knee joint. However, in the real human body, the knee DOF and ACL interact with each other. The changes in the knee joint can cause ACL strain, which is transmitted to the knee joint structure, and then affects the range of motion and stability of the knee joint. Due to the complexity of the real human body environment, it is difficult for musculoskeletal modeling and simulation to completely restore the real state. In our future research, we hope to further optimize and develop a more accurate and realistic musculoskeletal model by considering the interaction between various structures.

In addition, the parameters of the ACL, such as origin, insertion point, length and cross-sectional area of the ligament, were mainly based on data from previously published studies. In view of personalized differences, future research can consider combining medical imaging data (MRI and CT) to construct a subject-specific ACL model of the knee joint. On the other hand, researchers may also consider combining machine learning and data-driven approaches to optimize the model parameters with the help of a large amount of experimental and simulation data. This can improve the accuracy and generalization ability of ACL force prediction models. This study selected only one standard subject for finite element analysis. Considering the inherent inter-individual characteristics, future studies need to be further refined.

Given the feasibility and ease of operation of the prediction model, this study explored simple and easy-to-measure parameters as predictors whenever possible, but the data processing still requires users to have some basic skills. In the future, I plan to combine the proposed ACL force prediction model with a subject-specific musculoskeletal model, and use it as an effective and accurate ACL injury risk assessment tool. Furthermore, it will be promoted and applied to a wider range of sports training and injury monitoring to improve the body's sports performance and reduce sports injuries.

The current work highlights the applicability of XML methods that can interpret the results of ML decisions for clinical landing analysis, and their great promise for future application and implementation. In order to facilitate future clinical applications, in addition to the color-coded waveform figures presented in the current study, translation of the predictive interpretation results into an easy-to-understand text format should be considered. This will enable the research method to be understood by more people, and also provide clinical experts with more in-depth and intuitive explanations when analyzing landing patterns.

For the prediction model of lower limb joint movements, the current work only selected the data on the movement of stairs descending to assess the accuracy of the proposed model. This is because the movements involved in stair descending are more complex than in other daily activities and the corresponding movement intentions are more difficult to estimate. Future work should consider the feasibility and accuracy of

detecting other movement intentions. In addition, we used only 16 subjects' movement data on the same day to train the model, which may result in poor generalization of the model when detecting other subjects' movement intentions. Therefore, future research should also consider collecting a large sample of data to train the model in advance, so that the model can achieve a fast and accurate estimation of movement intention while having good generalization. This study integrated the muscle synergy space of the original time series $MS(t)$ and the muscle synergy space with the first-time data point removed $MS(t-1)$ as input variables. From the current prediction results, although the overall estimation performance of the model is excellent, future research should also explore the effect of different input variables on the estimation performance.

The objective function defines the magnitude of the error in solving for the muscle synergy matrix W. In the current study, the objective function is derived from the Euclidean distance measure, which is a widely used method. In the future, we should also compare the reconstruction errors under different objective functions so that the W can represent the muscle synergy matrix to the greatest degree possible. For the approximation methods, we adopted simplified techniques in muscle synergy feature selection. The top 6 muscle synergies (VAF > 90%) were determined as inputs to the prediction model to reduce computational costs and increase computational efficiency. While this approach is generally accepted, the remaining six muscle synergies may also improve the estimation performance of the model. Therefore, future research should also consider combining both computational cost and model performance to determine the number of muscle synergies.

Thesis points

1st Thesis points:

I explored whether there are recognizable differences in the ankle motion patterns between before-fatigue and after-fatigue SL, and further explore the relationship between AIC, AROM and lower limb energy dissipation and PAF.

As shown in Figure 64, the results suggested that the ACL dynamic load force will increase during after-fatigue SL, which suggested that the lower limb neuromuscular fatigue factor would increase the risk of ACL injury. There was a significant difference in ankle motion patterns between before-fatigue and after-fatigue SL, in which the total recognition accuracy was 71.96% and 66.43% for variables ACI and AROM respectively under three classification recognition algorithms. AICA showed a positive correlation with AED ($R^2 = 0.6455$), KED ($R^2 = 0.3606$) and HED ($R^2 = 0.2189$). Similar results were found for AROM, which also showed positive correlations with AED ($R^2 = 0.5850$), KED ($R^2 = 0.3037$), and HED ($R^2 = 0.1538$).

Therefore, the increased risk of ACL injury during after-fatigue SL is related to the decrease of AICA and AROM, and the relationship between AIC, AROM and PAF is highly negatively correlated, the relationship with TED is highly positively correlated. I concluded that lower limb neuromuscular fatigue increases the ACL dynamic loading force during SL, thereby increasing the risk of ACL injury. This result is associated with a smaller AICA (plantarflexion angle) and AROM movement pattern of the ankle joint during after-fatigue SL. By increasing the AICA and AROM during SL, the energy dissipation of the lower limb joints can be increased and the PAF reduced, thus reducing the impact loads on the lower limb joints and reducing lower limb injuries, including ACL injuries.

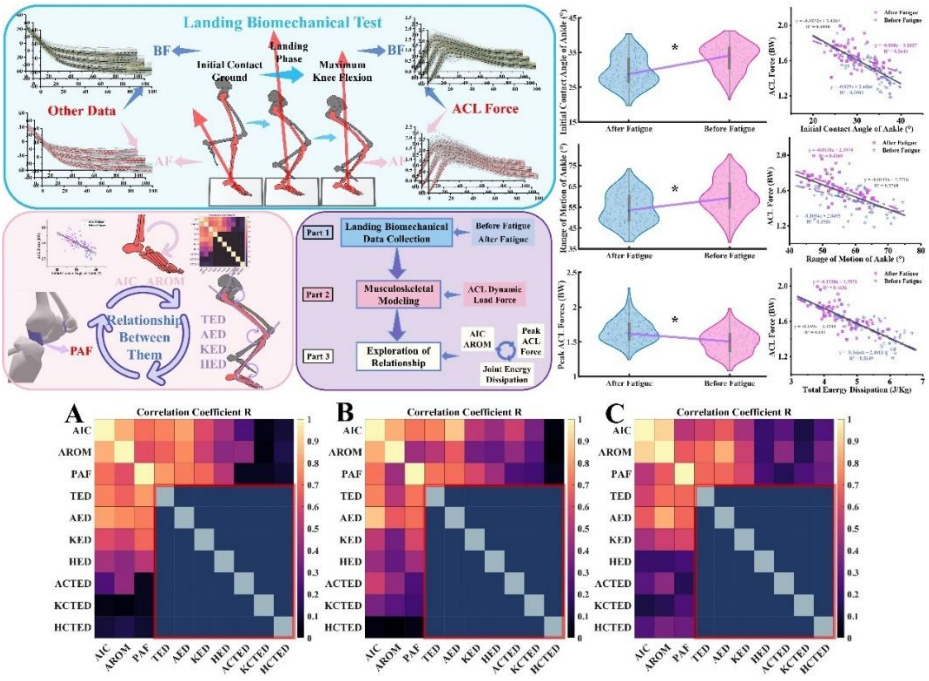

Figure 64 Recognizable differences in the ankle motion patterns and relevant results

between before-fatigue and after-fatigue SL.

Related articles to the 1st thesis point:

1. **Xu D**, Zhou H, Quan W, et al. Accurately and effectively predict the ACL force: Utilizing biomechanical landing pattern before and after-fatigue[J]. Computer Methods and Programs in Biomedicine, **2023,** 241: 107761. **Q1, IF=6.1**
2. **Xu D**, Lu J, Baker J S, et al. Temporal kinematic and kinetics differences throughout different landing ways following volleyball spike shots[J]. Proceedings of the Institution of Mechanical Engineers, Part P: Journal of Sports Engineering and Technology, 2022, 236(3): 200-208. **Q2, IF=1.1**
3. **Xu D**, Zhou H, Baker J S, et al. An investigation of differences in lower extremity biomechanics during single-leg landing from height using bionic shoes and normal shoes[J]. Frontiers in Bioengineering and Biotechnology, 2021, 9: 679123. **Q1, IF=4.3**
4. **Xu D**, Lu Z, Shen S, et al. The differences in lower extremity joints energy dissipation strategy during landing between athletes with symptomatic patellar tendinopathy (PT) and without patellar tendinopathy (UPT)[J]. Molecular & Cellular Biomechanics, 2021, 18(2): 107. **Q4, EI**

2nd Thesis points:

For the datasets of before-fatigue and after-fatigue landing, I investigated whether XML can help with landing pattern recognition and to what extent it can aid in the interpretation of prediction results. I compared the classification recognition performances of several classical classification models on two class landing tasks, and then constructed the XML model based on the neural network model with the best recognition performance combined with LRP to explain the model classification recognition results (Figure 65).

Meanwhile, the RS results derived from LRP were evaluated from the statistical and clinical perspectives. Both three classification algorithm models achieved high recognizability ($Accuracy > 90\%$) in the nine classification tasks, and the classification performance level of ANN for the input signal is particularly outstanding in comparison to the other two models. From the classification performance, I found that based on the knee data as input signals the classification performance was better ($Accuracy > 95\%$). There is a greater difference in sagittal landing patterns between classes in the three planes.

For the detailed results of RS distribution, I found that the early landing phase contributed more to landing pattern recognition between classes, and the variable contribution during the 1%–22% landing phase reached 27.06%. For each joint, the largest summed contribution rate of RS was 41.02% in the knee joint, followed by 30.62% in the ankle joint and 28.36% in the hip joint. For each plane, the largest summed contribution rate of RS was 37.78% in the sagittal plane, followed by 32.55% in the transversal plane and 29.67% in the frontal plane. The knee flexion-extension angle variable was the most relevant trajectory variable in landing pattern recognition, and the contribution rate of RS reached 8.31%. Secondly, the knee flexion-extension moment, knee internal-external rotation moment, ankle dorsiflexion-plantarflexion moment, ankle internal-external rotation angle, were the followed relevant trajectory variables in landing pattern recognition, and the contribution rate of RS reached 8.03%, 7.86%, 6.58%, 6.13%, respectively. In conclusion, I highlighted the applicability of XML methods that can interpret the results of ML decisions for clinical landing analysis, and their great promise for future application and implementation.

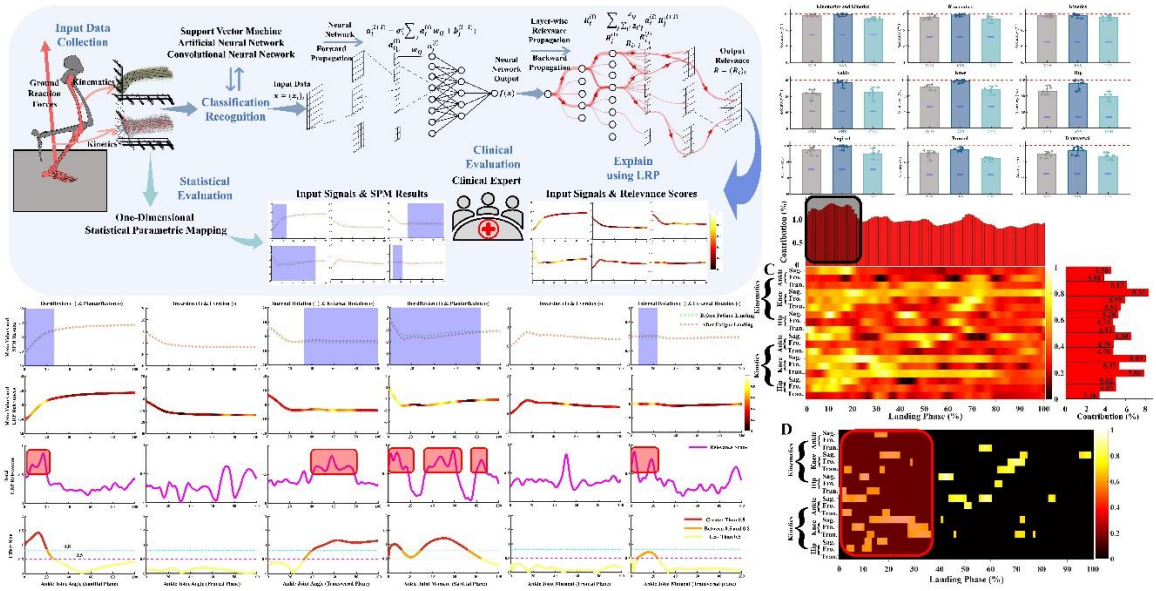

Figure 65 Explainable machine learning models for landing pattern recognition and its results.

Related articles to the 2nd thesis point:

1. **Xu D,** Zhou H, Quan W, et al. A new method applied for explaining the landing patterns: Interpretability analysis of machine learning[J]. Heliyon, **2024. Q1, IF=3.4**
2. **Xu D**, Quan W, Zhou H, et al. Explaining the differences of gait patterns between high and low-mileage runners with machine learning[J]. Scientific reports, **2022**, 12(1): 2981. **Q1, IF=3.8**
3. **Xu D**, Zhou H, Jiang X, et al. New insights for the design of bionic robots: Adaptive motion adjustment strategies during feline landings[J]. Frontiers in Veterinary Science, **2022**, 9: 836043. **Q1, IF=3.2**

3rd Thesis points:

Furthermore, I investigated the relationship between ankle motion patterns (AICA and AROM) and the lower limb injury risk during SL, and proposed an optimized landing strategy that can reduce the injury risk. As shown in Figure 66, to more realistically revert and simulate the ACL injury mechanics, I developed a knee musculoskeletal model that reverts the ACL ligament to a NLSV mechanical mechanism (strain rate-dependent) generated by the DCT as a function of strain.

As shown in Figure 66, the AICA exhibits a negative correlation with PVGRF (r = -0.591) and PAF (r = -0.554), a positive correlation with TED (r = 0.490) and PAIA (r = 0.502). The AROM exhibits a positive correlation with TED (r = 0.687) and PAIA (r = 0.600). The results indicated that the LAS risk is negatively correlated with ACL injury risk (r = -0.330, $p < 0.001$).

Based on the determined intersection points, I found that 30° to 40° of AICA and 50° to 70° of AROM were the more appropriate range to balance the injury risk between them. This range can be referenced by individuals during SL, but it should also be adjusted according to the person's ankle dorsiflexion ability and the level of muscle function around the ankle joint. In addition, it is also necessary to strengthen the training of the muscles, the medial and lateral tissues, ligaments around the ankle joint, so as to increase the AICA and AROM to reduce lower limb injury risk while avoiding ankle joint injury.

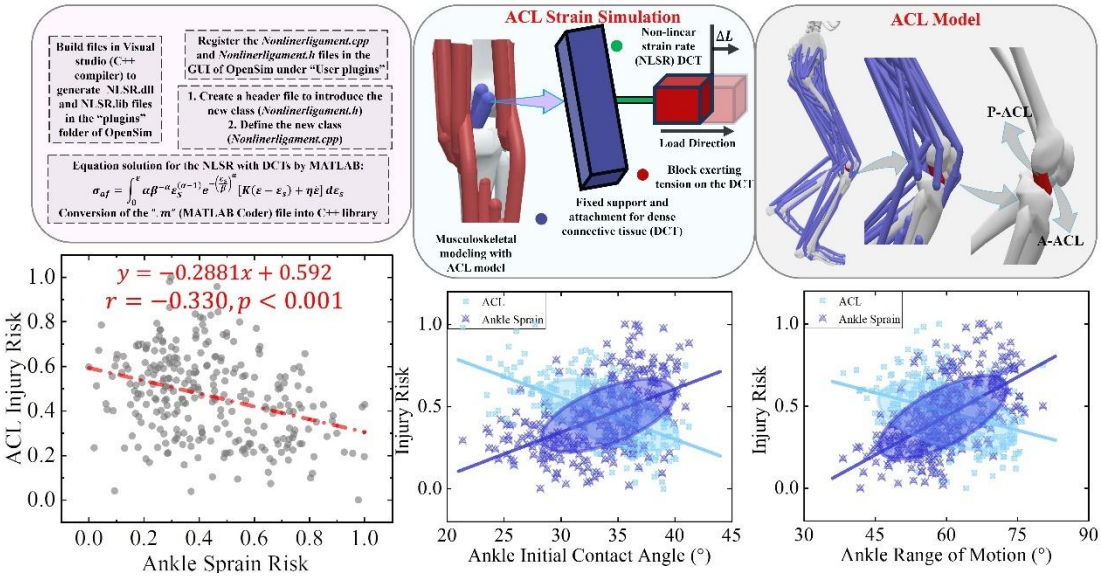

Figure 66 Illustration of the ACL model construction (DCTs with NLSR); Visualization of the interaction between the risk of ACL injury, ankle sprain and AICA, AROM.

Related articles to the 3rd thesis point:

1. **Xu D**, Zhou H, Quan W, et al. New insights optimize landing strategies to reduce lower limb injury risk[J]. Cyborg and Bionic Systems. **2024**, 5: 0126. **Q1, IF=10.5**

2. **Xu D**, Jiang X, Cen X, et al. Single-leg landings following a volleyball spike may increase the risk of anterior cruciate ligament injury more than landing on both-legs[J]. Applied Sciences, 2020, 11(1): 130. **Q1, IF=2.5**
3. **Xu D**, Cen X, Wang M, et al. Temporal kinematic differences between forward and backward jump-landing[J]. International Journal of Environmental Research and Public Health, 2020, 17(18): 6669. **Q1, IF=4.6**

4th Thesis points:

In addition, I explored the effects of different ankle plantarflexion angles during SL on the risk of knee-related injury. This study developed the finite element model of foot-ankle-knee integration and ACL musculoskeletal model with NLSV mechanical mechanism. The internal load forces (musculoskeletal modeling) and stress (finite element analysis) around the knee joint were simulated and calculated to evaluate the risk of knee-related injury during SL.

As the ankle plantarflexion angle increased during landing, both the peak knee vertical impact force (p=0.001) and ACL force (p=0.001) decreased significantly (Figure 67). The maximum von Mises stress of ACL, meniscus, and femoral cartilage decreased as the ankle plantarflexion angle increased. When landing at 20°, 30°, and 40°, the maximum ACL stresses were 30.856 MPa, 27.053 MPa, and 24.592 MPa; the maximum meniscus stresses were 22.315 MPa, 20.073 MPa, and 17.972 MPa; and the maximum femoral cartilage stresses were 18.754 MPa, 17.012 MPa, and 15.429 MPa, respectively (Figure 67).

The overall range of variation in ACL stress was small and was mainly distributed in the femoral and tibial attachment regions, as well as in the mid-lateral region. The current findings revealed that the use of larger ankle plantarflexion angles during landing may be an effective solution to reduce knee impact load and the risk of rupture of the medial femoral attachment area in the ACL.

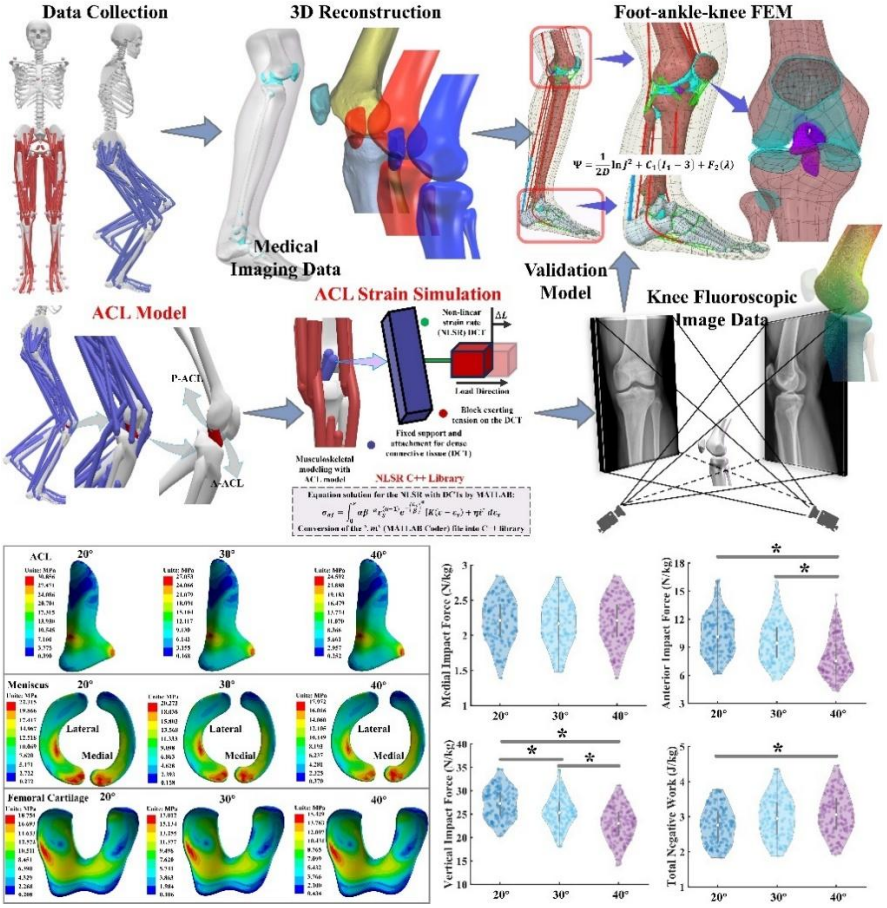

Figure 67 Overview of the model creation and impact load results.

Related articles to the 4th thesis point:

1. **Xu D**, Zhou H,Wang M, et al. Contribution of ankle motion pattern during landing to reduce the knee-related injury risk [J]. Computers in Biology and Medicine, **2024**, 180: 108965. **Q1, IF=7.0**
2. **Xu D**, Zhou H, Zhang Q, et al. A new method proposed to explore the feline's paw bones of contributing most to landing pattern recognition when landed under different constraints[J]. Frontiers in Veterinary Science, **2022**, 9: 1011357. **Q1, IF=3.2**
3. Zhou H, **Xu D,** Quan W, et al. Effects of different contact angles during forefoot running on the stresses of the foot bones: a finite element simulation study[J]. Frontiers in Bioengineering and Biotechnology, **2024,** 12. **Q1, IF=4.3**
4. Zhou H, **Xu D**, Quan W, et al. Can the Entire Function of the Foot Be Concentrated in the Forefoot Area during the Running Stance Phase? A Finite Element Study of Different Shoe Soles[J]. Journal of Human Kinetics, **2023**, 92. **Q1, IF=2.3**
5. Zhou Z, Zhou H, Jie T, **Xu D**, et al. Analysis of Stress Response Distribution in Patients with Lateral Ankle Ligament Injuries: A Study of Neural Control Strategies Utilizing Predictive Computing Models[J]. Frontiers in Physiology, 15: 1438194. **Q2, IF=3.2**

5th Thesis points:

Data-driven machine learning approaches are believed to perform modeling calculations faster than musculoskeletal models and also have higher prediction accuracy. I developed an ACL force prediction model by combining deep learning and the explored relationship between ACL force and ankle motion pattern.

By substituting AICA and AROM as independent variables in the SSA-ELM prediction model (Figure 68), the model shows excellent prediction performance because of very strong correlation ($R^2 = 0.9992, MSE = 0.0023, RMSE = 0.0474$). Based on the equal scaling by combining results of SSA-ELM and SSA-LSTM, the prediction model achieves excellent performance in ACL force prediction of the overall waveform ($R^2 = 0.9947, MSE = 0.0076, RMSE = 0.0873$).

Therefore, my study proposed a method for constructing a highly accurate and easy-to-implement ACL dynamic load force prediction model, which has low input variable demands (sagittal joint angles), excellent generalization capabilities and superior performance in terms of high accuracy.

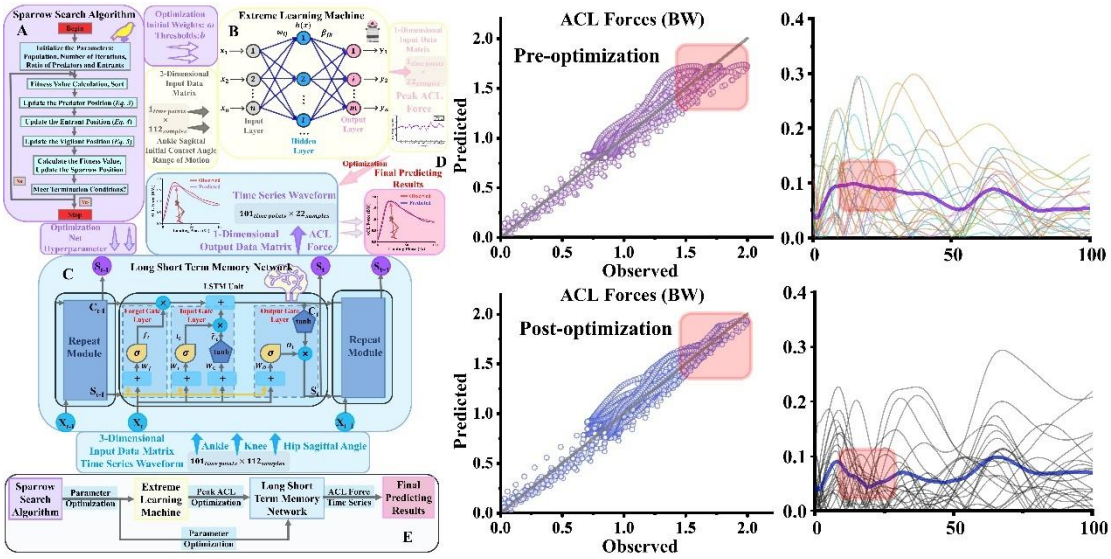

Figure 68 ACL dynamic load force prediction model and its prediction results.

Related articles to the 5th thesis point:

1. **Xu D**, Zhou H, Quan W, et al. Accurately and effectively predict the ACL force: Utilizing biomechanical landing pattern before and after-fatigue[J]. Computer Methods and Programs in Biomedicine, **2023,** 241: 107761. **Q1, IF=6.1**
2. **Xu D**, Zhou H, Quan W, et al. A new method proposed for realizing human gait pattern recognition: inspirations for the application of sports and clinical gait analysis[J]. Gait & Posture, **2024,** 107: 293-305. **Q1, IF=2.2**

6th Thesis points:

To achieve an accurate estimation of lower limb joint movements during landing, I further proposed a novel movement intention detection technology for estimating lower limb joint continuous kinematic variables following muscle synergy patterns, to develop applications for more efficient assisted rehabilitation training. The surface electromyography of 12 muscles and lower limb joint kinematic and kinetic data from healthy subjects and patients during step-off landings from 30 cm-high stair steps were collected. The lower limb neuromuscular synergy pattern was then imported into the developed adaptive neuro-fuzzy inference system non-linear regression model to estimate the human movement intention during this movement pattern (Figure 69).

Six muscle synergies were determined to construct the muscle synergy pattern driven ANFIS model. Three fuzzy rules were determined in most estimation cases. As shown in Figure 69, combining the results of the four error indicators across the estimated variables indicates that the current model has excellent estimated performance in estimating lower limb joint movement. The estimation errors between the healthy (Angle: R^2=0.98±0.03; Torque: R^2=0.96±0.04) and patient (Angle: R^2=0.98±0.02; Torque: R^2=0.96±0.03) groups are consistent.

The proposed model of this study can accurately and reliably estimate lower limb joint movements, and the effectiveness will also be radiated to the patient group. This revealed that the models also have certain advantages in the recognition of motor intentions in patients with relevant movement disorders.

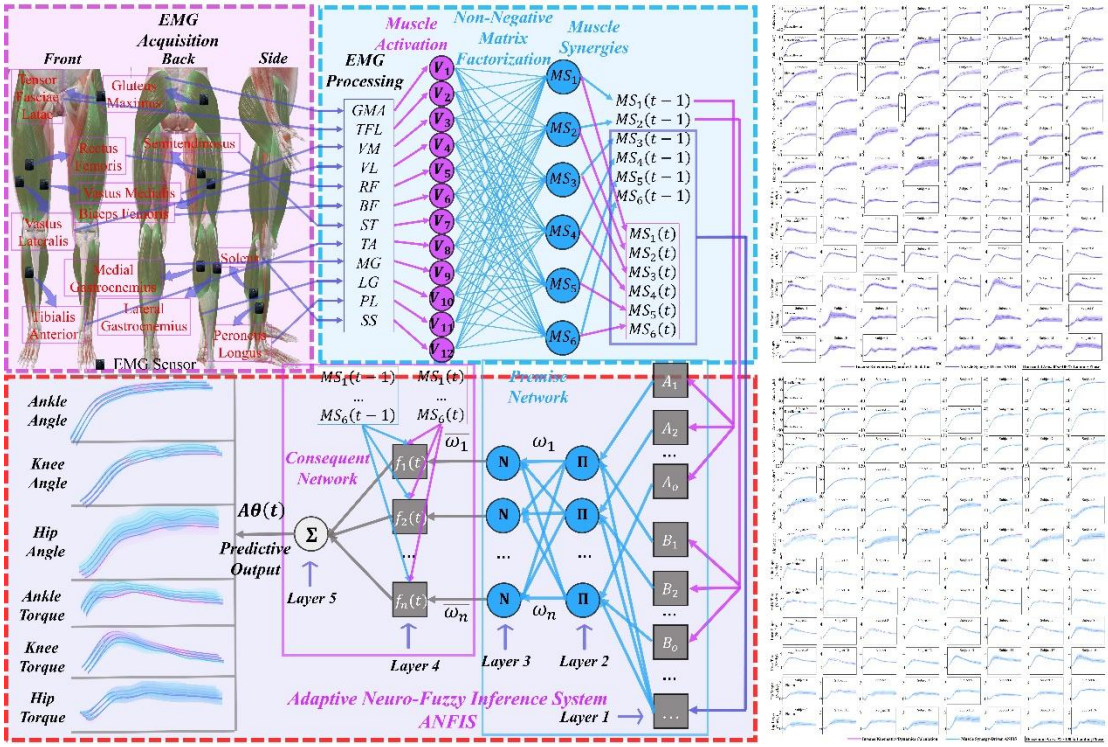

Figure 69 Overview of the NNMF-ANFIS model creation and prediction model results.

Related articles to the 6th thesis point:

1. **Xu D**, Zhou H, Quan W, et al. Adaptive neuro-fuzzy inference system model driven by the non-negative matrix factorization-extracted muscle synergy patterns to estimate lower limb joint movements[J]. Computer Methods and Programs in Biomedicine, **2023,** 242: 107848. **Q1, IF=6.1**
2. Jie T, **Xu D**, Zhang Z, et al. Structural and organizational strategies of locomotor modules during landing in patients with chronic ankle instability[J]. Bioengineering, **2024**, 11(5): 482. **Q2, IF=4.6**
3. Gao X, Jie T, **Xu D**, et al. Adaptive Adjustments in Lower Limb Muscle Coordination during Single-Leg Landing Tasks in Latin Dancers[J]. Biomimetics, 2024, 9(8): 489. **Q1, IF=3.4**

List of publications

Referred articles related to this thesis:

1. **Xu D**, Zhou H, Quan W, et al. New insights optimize landing strategies to reduce lower limb injury risk[J]. Cyborg and Bionic Systems. **2024**, 5: 0126. **Q1, IF=10.5**
2. **Xu D**, Zhou H, Quan W, et al. Accurately and effectively predict the ACL force: Utilizing biomechanical landing pattern before and after-fatigue[J]. Computer Methods and Programs in Biomedicine, **2023,** 241: 107761. **Q1, IF=6.1**
3. **Xu D**, Zhou H,Wang M, et al. Contribution of ankle motion pattern during landing to reduce the knee-related injury risk [J]. Computers in Biology and Medicine, **2024**, 180: 108965. **Q1, IF=7.0**
4. **Xu D**, Zhou H, Quan W, et al. Adaptive neuro-fuzzy inference system model driven by the non-negative matrix factorization-extracted muscle synergy patterns to estimate lower limb joint movements[J]. Computer Methods and Programs in Biomedicine, **2023,** 242: 107848. **Q1, IF=6.1**
5. **Xu D,** Zhou H, Quan W, et al. A new method applied for explaining the landing patterns: Interpretability analysis of machine learning[J]. Heliyon, **2024. Q1, IF=3.4**
6. **Xu D**, Zhou H, Quan W, et al. A new method proposed for realizing human gait pattern recognition: inspirations for the application of sports and clinical gait analysis[J]. Gait & Posture, **2024,** 107: 293-305. **Q1, IF=2.2**
7. **Xu D**, Quan W, Zhou H, et al. Explaining the differences of gait patterns between high and low-mileage runners with machine learning[J]. Scientific reports, **2022**, 12(1): 2981. **Q1, IF=3.8**
8. **Xu D**, Zhou H, Jiang X, et al. New insights for the design of bionic robots: Adaptive motion adjustment strategies during feline landings[J]. Frontiers in Veterinary Science, **2022**, 9: 836043. **Q1, IF=3.2**
9. **Xu D**, Zhou H, Zhang Q, et al. A new method proposed to explore the feline's paw bones of contributing most to landing pattern recognition when landed under different constraints[J]. Frontiers in Veterinary Science, **2022**, 9: 1011357. **Q1, IF=3.2**
10. **Xu D**, Zhou H, Baker J S, et al. An investigation of differences in lower extremity biomechanics during single-leg landing from height using bionic shoes and normal shoes[J]. Frontiers in Bioengineering and Biotechnology, **2021**, 9: 679123. **Q1, IF=4.3**
11. **Xu D**, Lu Z, Shen S, et al. The differences in lower extremity joints energy dissipation strategy during landing between athletes with symptomatic patellar tendinopathy (PT) and without patellar tendinopathy (UPT)[J]. Molecular & Cellular Biomechanics, **2021**, 18(2): 107. **Q4, EI**
12. **Xu D**, Jiang X, Cen X, et al. Single-leg landings following a volleyball spike may increase the risk of anterior cruciate ligament injury more than landing on both-legs[J]. Applied Sciences, **2020**, 11(1): 130. **Q1, IF=2.5**

13. **Xu D**, Cen X, Wang M, et al. Temporal kinematic differences between forward and backward jump-landing[J]. International Journal of Environmental Research and Public Health, **2020**, 17(18): 6669. **Q1, IF=4.6**
14. **Xu D**, Lu J, Baker J S, et al. Temporal kinematic and kinetics differences throughout different landing ways following volleyball spike shots[J]. Proceedings of the Institution of Mechanical Engineers, Part P: Journal of Sports Engineering and Technology, **2022**, 236(3): 200-208. **Q2, IF=1.1**
15. Jie T, **Xu D**, Zhang Z, et al. Structural and organizational strategies of locomotor modules during landing in patients with chronic ankle instability[J]. Bioengineering, **2024**, 11(5): 482. **Q2, IF=4.6**
16. Gao X, **Xu D,** Baker J S, et al. Exploring biomechanical variations in ankle joint injuries among Latin dancers with different stance patterns: utilizing OpenSim musculoskeletal models[J]. Frontiers in Bioengineering and Biotechnology, **2024,** 12: 1359337. **Q1, IF=4.3**
17. Zhou H, **Xu D,** Quan W, et al. Effects of different contact angles during forefoot running on the stresses of the foot bones: a finite element simulation study[J]. Frontiers in Bioengineering and Biotechnology, **2024,** 12. **Q1, IF=4.3**
18. Zhou H, **Xu D**, Quan W, et al. Can the Entire Function of the Foot Be Concentrated in the Forefoot Area during the Running Stance Phase? A Finite Element Study of Different Shoe Soles[J]. Journal of Human Kinetics, **2023**, 92. **Q1, IF=2.3**
19. Gao X, **Xu D**, Li F, et al. Biomechanical Analysis of Latin Dancers' Lower Limb during Normal Walking[J]. Bioengineering, **2023**, 10(10): 1128. **Q2, IF=4.6**
20. Zhou Z, Zhou H, Jie T, **Xu D**, et al. Analysis of Stress Response Distribution in Patients with Lateral Ankle Ligament Injuries: A Study of Neural Control Strategies Utilizing Predictive Computing Models[J]. Frontiers in Physiology, **2024**, 15: 1438194. **Q2, IF=3.2**
21. Zhou Z, **Xu D**, Zhou H, et al. Distinct Motion Control Strategy during Unanticipated Landing: Transitioning from Copers to Chronic Ankle Instability[J]. Journal of Biomimetics, Biomaterials and Biomedical Engineering[J], **2024**, 65: 15-32. **Q4, EI**
22. Gao X, Jie T, **Xu D**, et al. Adaptive Adjustments in Lower Limb Muscle Coordination during Single-Leg Landing Tasks in Latin Dancers[J]. Biomimetics, 2024, 9(8): 489. **Q1, IF=3.4**

International conference abstracts related to this thesis:

1. **Xu D**. NEW INSIGHTS FOR THE DESIGN OF BIONIC ROBOTS. 28th Congress of the European Society of Biomechanics, Maastricht, Netherlands. 2023
2. **Xu D**. Exploring Landing Pattern Differences with Machine Learning-Based Interpretability Analysis. 13th National Sports Science Conference, Tianjing, 2023

International conference full length article related to this thesis:

1. **Xu D**, Zhou H, Gu Y. Relationship between ankle motion pattern and lower limb injury risk during landing. 2023 International Academic Conference on Exercise and Health, Shanghai, China, 2023

Other publications

1. **Xu D**, Song Y, Meng Y, et al. Relationship between firefighter physical fitness and special ability performance: predictive research based on machine learning algorithms[J]. International journal of environmental research and public health, 2020, 17(20): 7689. **Q1, IF=4.6**
2. **Xu D**, Quan W, Zhou H, et al. Exploration of Gait Pattern Differences Between High-Mileage and Low-Mileage Runners Based on Deep Neural Network and Layer-Wise Relevance Propagation. Journal of Medical Biomechanics, **2022. Q4**
3. Jiang X, **Xu D**, et al. PCA of Running Biomechanics after 5 km between Novice and Experienced Runners[J]. Bioengineering, **2023**, 10(7): 876. **Q2, IF=4.6**
4. Li, F, **Xu D**, Zhou H, et al. The effect of heel height on the Achilles tendon and muscle activity in Latin dancers during a special-landing task[J]. International Journal of Biomedical Engineering and Technology, **2023**, 44(4): 303-323. **Q4, IF=0.8**
5. Quan W, Gao L, **Xu D**, et al. Simulation of Lower Limb Muscle Activation Using Running Shoes with Different Heel-to-Toe Drops Using Opensim[J]. Healthcare. **2023,** 11(9). **Q2, IF=2.4**
6. Li F, Zhou H, **Xu D**, et al. Comparison of Biomechanical Characteristics during the Second Landing Phase in Female Latin Dancers: Evaluation of the Bounce and Side Chasse Step[J]. Molecular & Cellular Biomechanics, **2022**, 19(3): 115. **Q4 EI**
7. Sun Z, Zhang Y, **Xu D**, et al. The Effects of Six-Month Subalpine Training on the Physical Functions and Athletic Performance of Elite Chinese Cross-Country Skiers[J]. Applied Sciences, **2022**, 12(1): 421. **Q1, IF=2.5**
8. Lu J, **Xu D,** Quan W, et al. Effects of forefoot shoe on knee and ankle loading during running in male recreational runners[J]. Molecular & Cellular Biomechanics, **2022,** 19(2): 61. **Q4 EI**
9. Zhou H, **Xu D**, Quan W, et al. A foot joint and muscle force assessment of the running stance phase whilst wearing normal shoes and bionic shoes[J]. Acta of Bioengineering Biomechanics, **2022**, 24: 191-202. **Q3, IF=1**
10. Lu Z, Sun D, **Xu D**, et al. Gait characteristics and fatigue profiles when standing on surfaces with different hardness: Gait analysis and machine learning algorithms[J]. Biology, 2021, 10(11): 1083.
11. Zhou H, **Xu D**, Quan W, et al. A pilot study of muscle force between normal shoes and bionic shoes during men walking and running stance phase using opensim[J]. Actuators, 2021, 10(10): 274. **Q2, IF=2.2**
12. Quan W, Zhou H, **Xu D**, et al. Competitive and recreational running kinematics examined using principal components analysis[J]. Healthcare, 2021, 9(10): 1321. **Q2, IF=2.4**

13. Quan W, Ren F, **Xu D**, et al. Effects of fatigue running on joint mechanics in female runners: A prediction study based on a partial least squares algorithm[J]. Frontiers in Bioengineering and Biotechnology, 2021, 9: 746761. **Q1, IF=4.3**
14. Zhou H, **Xu D**, Chen C, et al. Analysis of different stop-jumping strategies on the biomechanical changes in the lower limbs[J]. Applied Sciences, 2021, 11(10): 4633. **Q1, IF=2.5**
15. Zhou H, Chen C, **Xu D**, et al. Biomechanical characteristics between bionic shoes and normal shoes during the drop-landing phase: A pilot study[J]. International Journal of Environmental Research and Public Health, 2021, 18(6): 3223. **Q1, IF=4.6**
16. Xianjian C, **Datao X**. Effects of Tai Chi Chuan on the Physical and Mental Health of the Elderly: A Systematic Review[J]. Physical Activity & Health (2515-2270), 2021, 5(1). **Q1**
17. Cen X, **Xu D**, Baker J S, et al. Effect of additional body weight on arch index and dynamic plantar pressure distribution during walking and gait termination[J]. PeerJ, 2020, 8: e8998. **Q1, IF=2.3**
18. Xiang L, Mei Q, **Xu D**, et al. Multi-segmental motion in foot during counter-movement jump with toe manipulation[J]. Applied Sciences, 2020, 10(5): 1893. **Q1, IF=2.5**
19. Cen X, **Xu D**, Baker J S, et al. Association of arch stiffness with plantar impulse distribution during walking, running, and gait termination[J]. International Journal of Environmental Research and Public Health, 2020, 17(6): 2090. **Q1, IF=4.6**
20. Ji M, **Xu D**, Teo E C, et al. Biomechanical comparison of sagittal vertebral column bend change induced by backpacks in school-aged children and adolescents: Systematic review and network meta-analysis[J]. Molecular & Cellular Biomechanics, 2024, 21: 71-71. **Q4**, **EI**

Reviewer for International Journal Articles:

1. Computer Methods and Programs in Biomedicine
2. Computer Methods in Biomechanics and Biomedical Engineering
3. Sports Biomechanics
4. Journal of Bionic Engineering
5. International Journal of Mechanical Sciences
6. iScience
7. Journal of Sports Engineering and Technology
8. Frontiers in Bioengineering and Biotechnology
9. Applied Bionics and Biomechanics
10. Medical & Biological Engineering & Computing
11. BMC Sports Science Medicine and Rehabilitation
12. BMC Musculoskeletal Disorders
13. Scientific Reports
14. International Journal of Biomedical Engineering and Technology
15. Physical activity and health
16. Frontiers in Physiology

17. Expert Review of Medical Devices
18. Frontiers in Sports and Active Living
19. Physician and Sports Medicine
20. Plos One
21. Bioengineering
22. Molecular & Cellular Biomechanics
23. Applied Science
24. Heliyon
25. Journal of Functional Morphology and Kinesiology
26. Sensors
27. Diagnostics
28. Symmetry
29. Prosthesis
30. Life
31. Frontiers in Psychology
32. Rehabilitation

Guest Editor:

1. Molecular & Cellular Biomechanics
2. Physical activity and health

ORCID: https://orcid.org/0000-0002-1918-0756
Scopus Author ID: 57215841612
Scopus Link:
https://www.scopus.com/authid/detail.uri?authorId=57215841612&origin=AuthorEval
Google Scholar:
https://scholar.google.com.hk/citations?hl=zh-CN&user=GFx1v54AAAAJ&view_op=list_works
ResearchGate: https://www.researchgate.net/profile/Datao-Xu
h-index: 13 (Scopus); 15 (Google Scholar)
i10-index: 18 (Scopus); 20 (Google Scholar)
Total independent citations: 535 (Scopus); 658 (Google Scholar)
Total Impact Factor: 160 (Web of Science)

References

[1] D. Xu, X. Jiang, X. Cen, J.S. Baker, Y. Gu, Single-leg landings following a volleyball spike may increase the risk of anterior cruciate ligament injury more than landing on both-legs, Applied Sciences. 11 (1) (2020) 130.
[2] D. Xu, X. Cen, M. Wang, M. Rong, B. István, J.S. Baker, et al., Temporal kinematic differences between forward and backward jump-landing, International Journal of Environmental Research and Public Health. 17 (18) (2020) 6669.
[3] D. Xu, J. Lu, J.S. Baker, G. Fekete, Y. Gu, Temporal kinematic and kinetics differences throughout different landing ways following volleyball spike shots, Proceedings of the Institution of Mechanical Engineers, Part P: Journal of Sports Engineering and Technology. 236 (3) (2022) 200-208.
[4] K.L. Markolf, D.M. Burchfield, M.M. Shapiro, M.F. Shepard, G.A. Finerman, J.L. Slauterbeck, Combined knee loading states that generate high anterior cruciate ligament forces, Journal of orthopaedic research. 13 (6) (1995) 930-935.
[5] Y. Gu, X. Ren, J. Li, M. Lake, Q. Zhang, Y. Zeng, Computer simulation of stress distribution in the metatarsals at different inversion landing angles using the finite element method, International orthopaedics. 34 (2010) 669-676.
[6] D. Xu, Z. Lu, S. Shen, G. Fekete, U.C. Ugbolue, Y. Gu, The Differences in lower extremity joints energy dissipation strategy during landing between athletes with symptomatic patellar tendinopathy (PT) and without patellar tendinopathy (UPT), Mol. Cell. Biomech. 18 (2) (2021).
[7] B.P. Boden, J.S. Torg, S.B. Knowles, T.E. Hewett, Video analysis of anterior cruciate ligament injury: abnormalities in hip and ankle kinematics, The American journal of sports medicine. 37 (2) (2009) 252-259.
[8] T. Krosshaug, A. Nakamae, B.P. Boden, L. Engebretsen, G. Smith, J.R. Slauterbeck, et al., Mechanisms of anterior cruciate ligament injury in basketball: video analysis of 39 cases, The American journal of sports medicine. 35 (3) (2007) 359-367.
[9] C.E. Pfeifer, P.F. Beattie, R.S. Sacko, A. Hand, Risk factors associated with non-contact anterior cruciate ligament injury: a systematic review, International journal of sports physical therapy. 13 (4) (2018) 575.
[10] V. Duthon, C. Barea, S. Abrassart, J. Fasel, D. Fritschy, J. Ménétrey, Anatomy of the anterior cruciate ligament, Knee surgery, sports traumatology, arthroscopy. 14 (2006) 204-213.
[11] G.D. Myer, K.R. Ford, T.E. Hewett, Rationale and clinical techniques for anterior cruciate ligament injury prevention among female athletes, Journal of athletic training. 39 (4) (2004) 352.
[12] C.H. Yeow, P.V.S. Lee, J.C.H. Goh, An investigation of lower extremity energy dissipation strategies during single-leg and double-leg landing based on sagittal and frontal plane biomechanics, Human movement science. 30 (3) (2011) 624-635.
[13] E.A. Wikstrom, M.E. Powers, M.D. Tillman, Dynamic stabilization time after isokinetic and functional fatigue, Journal of Athletic Training. 39 (3) (2004) 247.
[14] A. Benjaminse, A. Habu, T.C. Sell, J.P. Abt, F.H. Fu, J.B. Myers, et al., Fatigue alters lower extremity kinematics during a single-leg stop-jump task, Knee Surgery,

Sports Traumatology, Arthroscopy. 16 (4) (2008) 400-407.
[15] N. Cortes, D. Quammen, S. Lucci, E. Greska, J. Onate, A functional agility short-term fatigue protocol changes lower extremity mechanics, Journal of sports sciences. 30 (8) (2012) 797-805.
[16] H. Kim, S. Son, M. Seeley, J. Hopkins, Functional fatigue alters lower-extremity neuromechanics during a forward-side jump, International Journal of Sports Medicine. 36 (14) (2015) 1192-1200.
[17] K. Sinsurin, R. Vachalathiti, W. Jalayondeja, W. Limroongreungrat, Altered peak knee valgus during jump-landing among various directions in basketball and volleyball athletes, Asian journal of sports medicine. 4 (3) (2013) 195.
[18] A. Tamura, K. Akasaka, T. Otsudo, Y. Sawada, Y. Okubo, J. Shiozawa, et al., Fatigue alters landing shock attenuation during a single-leg vertical drop jump, Orthopaedic journal of sports medicine. 4 (1) (2016) 2325967115626412.
[19] D. Xu, H. Zhou, J.S. Baker, B. István, Y. Gu, An investigation of differences in lower extremity biomechanics during single-leg landing from height using bionic shoes and normal shoes, Frontiers in Bioengineering and Biotechnology. 9 (2021) 679123.
[20] K.F. Orishimo, I.J. Kremenic, Effect of fatigue on single-leg hop landing biomechanics, Journal of applied biomechanics. 22 (4) (2006) 245.
[21] J.P. Buckley, G.A. Borg, Borg's scales in strength training; from theory to practice in young and older adults, Applied physiology, nutrition, and metabolism. 36 (5) (2011) 682-692.
[22] H. Mokhtarzadeh, C.H. Yeow, J.C.H. Goh, D. Oetomo, F. Malekipour, P.V.-S. Lee, Contributions of the soleus and gastrocnemius muscles to the anterior cruciate ligament loading during single-leg landing, Journal of biomechanics. 46 (11) (2013) 1913-1920.
[23] E. Coventry, K.M. O'Connor, B.A. Hart, J.E. Earl, K.T. Ebersole, The effect of lower extremity fatigue on shock attenuation during single-leg landing, Clinical Biomechanics. 21 (10) (2006) 1090-1097.
[24] H.-T. Peng, Changes in biomechanical properties during drop jumps of incremental height, The Journal of Strength & Conditioning Research. 25 (9) (2011) 2510-2518.
[25] M.J. Decker, M.R. Torry, T.J. Noonan, A. Riviere, W.I. Sterett, Landing adaptations after ACL reconstruction, Medicine and science in sports and exercise. 34 (9) (2002) 1408-1413.
[26] H. Zhou, U.C. Ugbolue, Is there a relationship between strike pattern and injury during running: a review, Physical Activity and Health. 3 (1) (2019).
[27] M.J. Decker, M.R. Torry, D.J. Wyland, W.I. Sterett, J.R. Steadman, Gender differences in lower extremity kinematics, kinetics and energy absorption during landing, Clinical biomechanics. 18 (7) (2003) 662-669.
[28] J. Lee, Y. Song, C.S. Shin, Effect of the sagittal ankle angle at initial contact on energy dissipation in the lower extremity joints during a single-leg landing, Gait & posture. 62 (2018) 99-104.
[29] D.M. Brazen, M.K. Todd, J.P. Ambegaonkar, R. Wunderlich, C. Peterson, The effect of fatigue on landing biomechanics in single-leg drop landings, Clinical Journal of Sport Medicine. 20 (4) (2010) 286-292.
[30] J.A. Hogg, J. Vanrenterghem, T. Ackerman, A.-D. Nguyen, S.E. Ross, R.J. Schmitz,

et al., Temporal kinematic differences throughout single and double-leg forward landings, Journal of biomechanics. 99 (2020) 109559.
[31] M.R. Patterson, E. Delahunt, A diagonal landing task to assess dynamic postural stability in ACL reconstructed females, The Knee. 20 (6) (2013) 532-536.
[32] C.J. Wright, B.L. Arnold, S.E. Ross, Altered kinematics and time to stabilization during drop-jump landings in individuals with or without functional ankle instability, Journal of athletic training. 51 (1) (2016) 5-15.
[33] A. Phinyomark, G. Petri, E. Ibáñez-Marcelo, S.T. Osis, R. Ferber, Analysis of big data in gait biomechanics: Current trends and future directions, Journal of medical and biological engineering. 38 (2) (2018) 244-260.
[34] F. Horst, S. Lapuschkin, W. Samek, K.-R. Müller, W.I. Schöllhorn, Explaining the unique nature of individual gait patterns with deep learning, Scientific reports. 9 (1) (2019) 2391.
[35] S. Das, A. Dey, A. Pal, N. Roy, Applications of artificial intelligence in machine learning: review and prospect, International Journal of Computer Applications. 115 (9) (2015).
[36] D. Xu, H. Zhou, W. Quan, F. Gusztav, J.S. Baker, Y. Gu, Adaptive Neuro-Fuzzy Inference System model driven by the Non-Negative Matrix Factorization-extracted muscle synergy patterns to estimate lower limb joint movements, Computer Methods and Programs in Biomedicine. (2023) 107848.
[37] A. Esteva, B. Kuprel, R.A. Novoa, J. Ko, S.M. Swetter, H.M. Blau, et al., Dermatologist-level classification of skin cancer with deep neural networks, nature. 542 (7639) (2017) 115-118.
[38] H.A. Haenssle, C. Fink, R. Schneiderbauer, F. Toberer, T. Buhl, A. Blum, et al., Man against machine: diagnostic performance of a deep learning convolutional neural network for dermoscopic melanoma recognition in comparison to 58 dermatologists, Annals of oncology. 29 (8) (2018) 1836-1842.
[39] S.M. McKinney, M. Sieniek, V. Godbole, J. Godwin, N. Antropova, H. Ashrafian, et al., International evaluation of an AI system for breast cancer screening, Nature. 577 (7788) (2020) 89-94.
[40] H.-y. Lau, K.-y. Tong, H. Zhu, Support vector machine for classification of walking conditions of persons after stroke with dropped foot, Human movement science. 28 (4) (2009) 504-514.
[41] F. Wahid, R.K. Begg, C.J. Hass, S. Halgamuge, D.C. Ackland, Classification of Parkinson's disease gait using spatial-temporal gait features, IEEE journal of biomedical and health informatics. 19 (6) (2015) 1794-1802.
[42] L. Van Gestel, T. De Laet, E. Di Lello, H. Bruyninckx, G. Molenaers, A. Van Campenhout, et al., Probabilistic gait classification in children with cerebral palsy: A Bayesian approach, Research in Developmental Disabilities. 32 (6) (2011) 2542-2552.
[43] C. Nüesch, V. Valderrabano, C. Huber, V. von Tscharner, G. Pagenstert, Gait patterns of asymmetric ankle osteoarthritis patients, Clinical Biomechanics. 27 (6) (2012) 613-618.
[44] D. Slijepcevic, M. Zeppelzauer, A.-M. Gorgas, C. Schwab, M. Schüller, A. Baca, et al., Automatic classification of functional gait disorders, IEEE journal of biomedical

and health informatics. 22 (5) (2017) 1653-1661.
[45] D. Xu, H. Zhou, W. Quan, X. Jiang, M. Liang, S. Li, et al., A new method proposed for realizing human gait pattern recognition: inspirations for the application of sports and clinical gait analysis, Gait & Posture. 107 (2024) 293-305.
[46] D. Xu, W. Quan, H. Zhou, D. Sun, J.S. Baker, Y. Gu, Explaining the differences of gait patterns between high and low-mileage runners with machine learning, Scientific Reports. 12 (1) (2022) 1-12.
[47] A. Adadi, M. Berrada, Peeking inside the black-box: a survey on explainable artificial intelligence (XAI), IEEE access. 6 (2018) 52138-52160.
[48] G. Montavon, W. Samek, K.-R. Müller, Methods for interpreting and understanding deep neural networks, Digital signal processing. 73 (2018) 1-15.
[49] D. Slijepcevic, F. Horst, S. Lapuschkin, B. Horsak, A.-M. Raberger, A. Kranzl, et al., Explaining machine learning models for clinical gait analysis, ACM Transactions on Computing for Healthcare (HEALTH). 3 (2) (2021) 1-27.
[50] M.A. Ahmad, C. Eckert, A. Teredesai, Interpretable machine learning in healthcare, Proceedings of the 2018 ACM international conference on bioinformatics, computational biology, and health informatics, 2018, pp. 559-560.
[51] W.J. Murdoch, C. Singh, K. Kumbier, R. Abbasi-Asl, B. Yu, Definitions, methods, and applications in interpretable machine learning, Proceedings of the National Academy of Sciences. 116 (44) (2019) 22071-22080. https://www.pnas.org/doi/abs/10.1073/pnas.1900654116.
[52] A. Holzinger, C. Biemann, C.S. Pattichis, D.B. Kell, What do we need to build explainable AI systems for the medical domain?, arXiv preprint arXiv:1712.09923. (2017).
[53] E. Tjoa, C. Guan, A survey on explainable artificial intelligence (xai): Toward medical xai, IEEE transactions on neural networks and learning systems. 32 (11) (2020) 4793-4813.
[54] S. Bach, A. Binder, G. Montavon, F. Klauschen, K.-R. Müller, W. Samek, On pixel-wise explanations for non-linear classifier decisions by layer-wise relevance propagation, PloS one. 10 (7) (2015) e0130140.
[55] D. Xu, H. Zhou, X. Jiang, S. Li, Q. Zhang, J.S. Baker, et al., New Insights for the Design of Bionic Robots: Adaptive Motion Adjustment Strategies During Feline Landings, Frontiers in Veterinary Science. 9 (2022).
[56] W. Samek, G. Montavon, S. Lapuschkin, C.J. Anders, K.-R. Müller, Explaining deep neural networks and beyond: A review of methods and applications, Proceedings of the IEEE. 109 (3) (2021) 247-278.
[57] J. Aeles, F. Horst, S. Lapuschkin, L. Lacourpaille, F. Hug, Revealing the unique features of each individual's muscle activation signatures, Journal of the Royal Society Interface. 18 (174) (2021) 20200770.
[58] W. Samek, A. Binder, G. Montavon, S. Lapuschkin, K.-R. Müller, Evaluating the visualization of what a deep neural network has learned, IEEE transactions on neural networks and learning systems. 28 (11) (2016) 2660-2673.
[59] I. Sturm, S. Lapuschkin, W. Samek, K.-R. Müller, Interpretable deep neural networks for single-trial EEG classification, Journal of neuroscience methods. 274

(2016) 141-145.
[60] S. Lapuschkin, S. Wäldchen, A. Binder, G. Montavon, W. Samek, K.-R. Müller, Unmasking Clever Hans predictors and assessing what machines really learn, Nature communications. 10 (1) (2019) 1-8.
[61] R.C. Fong, A. Vedaldi, Interpretable explanations of black boxes by meaningful perturbation, Proceedings of the IEEE international conference on computer vision, 2017, pp. 3429-3437.
[62] T.C. Pataky, Generalized n-dimensional biomechanical field analysis using statistical parametric mapping, Journal of biomechanics. 43 (10) (2010) 1976-1982.
[63] S.-N. Zhang, B.T. Bates, J.S. Dufek, Contributions of lower extremity joints to energy dissipation during landings, Medicine and science in sports and exercise. 32 (4) (2000) 812-819.
[64] D. Xu, H. Zhou, W. Quan, F. Gusztav, M. Wang, J.S. Baker, et al., Accurately and effectively predict the ACL force: Utilizing biomechanical landing pattern before and after-fatigue, Computer Methods and Programs in Biomedicine. 241 (2023) 107761.
[65] M. Odensten, J. Gillquist, Functional anatomy of the anterior cruciate ligament and a rationale for reconstruction, JBJS. 67 (2) (1985) 257-262.
[66] C.L. Ardern, N.F. Taylor, J.A. Feller, K.E. Webster, Fifty-five per cent return to competitive sport following anterior cruciate ligament reconstruction surgery: an updated systematic review and meta-analysis including aspects of physical functioning and contextual factors, British journal of sports medicine. 48 (21) (2014) 1543-1552.
[67] B.P. Boden, G.S. Dean, J.A. Feagin, W.E. Garrett, Mechanisms of anterior cruciate ligament injury, SLACK Incorporated Thorofare, NJ, 2000, pp. 573-578.
[68] J. Agel, E.A. Arendt, B. Bershadsky, Anterior cruciate ligament injury in national collegiate athletic association basketball and soccer: a 13-year review, The American journal of sports medicine. 33 (4) (2005) 524-531.
[69] F. Yan, F. Xie, X. Gong, F. Wang, L. Yang, Effect of anterior cruciate ligament rupture on secondary damage to menisci and articular cartilage, The Knee. 23 (1) (2016) 102-105.
[70] D.T.-P. Fong, Y. Hong, L.-K. Chan, P.S.-H. Yung, K.-M. Chan, A systematic review on ankle injury and ankle sprain in sports, Sports medicine. 37 (2007) 73-94.
[71] D.T. Fong, Y.-Y. Chan, K.-M. Mok, P.S. Yung, K.-M. Chan, Understanding acute ankle ligamentous sprain injury in sports, BMC Sports Science, Medicine and Rehabilitation. 1 (2009) 1-14.
[72] C. Doherty, C. Bleakley, J. Hertel, B. Caulfield, J. Ryan, E. Delahunt, Recovery from a first-time lateral ankle sprain and the predictors of chronic ankle instability: a prospective cohort analysis, The American journal of sports medicine. 44 (4) (2016) 995-1003.
[73] T.E. Andersen, T.W. Floerenes, A. Arnason, R. Bahr, Video analysis of the mechanisms for ankle injuries in football, The American journal of sports medicine. 32 (1_suppl) (2004) 69-79.
[74] E. Kristianslund, R. Bahr, T. Krosshaug, Kinematics and kinetics of an accidental lateral ankle sprain, Journal of biomechanics. 44 (14) (2011) 2576-2578.
[75] C.-M. Fong, J.T. Blackburn, M.F. Norcross, M. McGrath, D.A. Padua, Ankle-

dorsiflexion range of motion and landing biomechanics, Journal of athletic training. 46 (1) (2011) 5-10.
[76] A. Mason-Mackay, C. Whatman, D. Reid, The effect of reduced ankle dorsiflexion on lower extremity mechanics during landing: A systematic review, Journal of science and medicine in sport. 20 (5) (2017) 451-458.
[77] A. Sikidar, M. Marieswaran, D. Kalyanasundaram, Estimation of forces on anterior cruciate ligament in dynamic activities, Biomechanics and Modeling in Mechanobiology. 20 (2021) 1533-1546.
[78] S.L. Delp, F.C. Anderson, A.S. Arnold, P. Loan, A. Habib, C.T. John, et al., OpenSim: open-source software to create and analyze dynamic simulations of movement, IEEE transactions on biomedical engineering. 54 (11) (2007) 1940-1950.
[79] H. Xu, D. Bloswick, A. Merryweather, An improved OpenSim gait model with multiple degrees of freedom knee joint and knee ligaments, Computer methods in biomechanics and biomedical engineering. 18 (11) (2015) 1217-1224.
[80] A. Sikidar, D. Kalyanasundaram, An open-source OpenSim® ankle-foot musculoskeletal model for assessment of strains and forces in dense connective tissues, Computer Methods and Programs in Biomedicine. 224 (2022) 106994.
[81] R. De Vita, W.S. Slaughter, A structural constitutive model for the strain rate-dependent behavior of anterior cruciate ligaments, International Journal of Solids and Structures. 43 (6) (2006) 1561-1570.
[82] N.A. Bates, K.R. Ford, G.D. Myer, T.E. Hewett, Impact differences in ground reaction force and center of mass between the first and second landing phases of a drop vertical jump and their implications for injury risk assessment, Journal of biomechanics. 46 (7) (2013) 1237-1241.
[83] J.T. Podraza, S.C. White, Effect of knee flexion angle on ground reaction forces, knee moments and muscle co-contraction during an impact-like deceleration landing: implications for the non-contact mechanism of ACL injury, The Knee. 17 (4) (2010) 291-295.
[84] Y. Shimokochi, S.J. Shultz, Mechanisms of noncontact anterior cruciate ligament injury, Journal of athletic training. 43 (4) (2008) 396-408.
[85] D. Xu, H. Zhou, W. Quan, X. Ma, T.-E. Chon, J. Fernandez, et al., New insights optimize landing strategies to reduce lower limb injury risk, Cyborg and Bionic Systems. 5 (2024) 0126.
[86] C. Yeow, P. Lee, J. Goh, Effect of landing height on frontal plane kinematics, kinetics and energy dissipation at lower extremity joints, Journal of biomechanics. 42 (12) (2009) 1967-1973.
[87] M. Majewski, H. Susanne, S. Klaus, Epidemiology of athletic knee injuries: A 10-year study, The knee. 13 (3) (2006) 184-188.
[88] J. Lerat, B. Moyen, F. Cladiere, J. Besse, H. Abidi, Knee instability after injury to the anterior cruciate ligament: quantification of the Lachman test, The Journal of Bone & Joint Surgery British Volume. 82 (1) (2000) 42-47.
[89] H. Zhou, D. Xu, W. Quan, M. Liang, U.C. Ugbolue, J.S. Baker, et al., A pilot study of muscle force between normal shoes and bionic shoes during men walking and running stance phase using opensim, Actuators, MDPI, 2021, p. 274.

[90] Q. Zhang, T. Chon, Y. Zhang, J.S. Baker, Y. Gu, Finite element analysis of the lumbar spine in adolescent idiopathic scoliosis subjected to different loads, Computers in Biology and Medicine. 136 (2021) 104745.
[91] Q. Zhang, Y. Zhang, T.E. Chon, J.S. Baker, Y. Gu, Analysis of stress and stabilization in adolescent with osteoporotic idiopathic scoliosis: Finite element method, Computer Methods in Biomechanics and Biomedical Engineering. 26 (1) (2023) 12-24.
[92] B. Szabó, I. Babuška, Finite Element Analysis: Method, Verification and Validation, (2021).
[93] J. Kar, P.M. Quesada, A numerical simulation approach to studying anterior cruciate ligament strains and internal forces among young recreational women performing valgus inducing stop-jump activities, Annals of biomedical engineering. 40 (8) (2012) 1679-1691.
[94] A. Seth, J.L. Hicks, T.K. Uchida, A. Habib, C.L. Dembia, J.J. Dunne, et al., OpenSim: Simulating musculoskeletal dynamics and neuromuscular control to study human and animal movement, PLoS computational biology. 14 (7) (2018) e1006223.
[95] W.A. Laughlin, J.T. Weinhandl, T.W. Kernozek, S.C. Cobb, K.G. Keenan, K.M. O'Connor, The effects of single-leg landing technique on ACL loading, Journal of biomechanics. 44 (10) (2011) 1845-1851.
[96] C.S. Shin, A.M. Chaudhari, T.P. Andriacchi, The effect of isolated valgus moments on ACL strain during single-leg landing: a simulation study, Journal of biomechanics. 42 (3) (2009) 280-285.
[97] C.S. Shin, A.M. Chaudhari, T.P. Andriacchi, Valgus plus internal rotation moments increase anterior cruciate ligament strain more than either alone, Med Sci Sports Exerc. 43 (8) (2011) 1484-1491.
[98] D. Liu, M. He, M. Hou, Y. Ma, Deep learning based ground reaction force estimation for stair walking using kinematic data, Measurement. (2022) 111344.
[99] J. Zou, X. Zhang, Y. Zhang, J. Li, Z. Jin, Prediction on the medial knee contact force in patients with knee valgus using transfer learning approaches: Application to rehabilitation gaits, Computers in Biology and Medicine. 150 (2022) 106099.
[100] Y. Ma, D. Liu, L. Cai, Deep learning-based upper limb functional assessment using a single kinect v2 sensor, Sensors. 20 (7) (2020) 1903.
[101] E. Shao, Q. Mei, J. Ye, U.C. Ugbolue, C. Chen, Y. Gu, Predicting Coordination Variability of Selected Lower Extremity Couplings during a Cutting Movement: An Investigation of Deep Neural Networks with the LSTM Structure, Bioengineering. 9 (9) (2022) 411.
[102] J. Snoek, H. Larochelle, R.P. Adams, Practical bayesian optimization of machine learning algorithms, Advances in neural information processing systems. 25 (2012).
[103] A.E. Maxwell, T.A. Warner, F. Fang, Implementation of machine-learning classification in remote sensing: An applied review, International Journal of Remote Sensing. 39 (9) (2018) 2784-2817.
[104] J. Wang, T. Kumbasar, Parameter optimization of interval Type-2 fuzzy neural networks based on PSO and BBBC methods, IEEE/CAA Journal of Automatica Sinica. 6 (1) (2019) 247-257.
[105] S. Loussaief, A. Abdelkrim, Convolutional neural network hyper-parameters

optimization based on genetic algorithms, International Journal of Advanced Computer Science and Applications. 9 (10) (2018).
[106] E. Bochinski, T. Senst, T. Sikora, Hyper-parameter optimization for convolutional neural network committees based on evolutionary algorithms, 2017 IEEE international conference on image processing (ICIP), IEEE, 2017, pp. 3924-3928.
[107] J. Xue, B. Shen, A novel swarm intelligence optimization approach: sparrow search algorithm, Systems Science & Control Engineering. 8 (1) (2020) 22-34.
[108] D. Xu, H. Zhou, W. Quan, F. Gusztav, J.S. Baker, Y. Gu, Adaptive neuro-fuzzy inference system model driven by the non-negative matrix factorization-extracted muscle synergy patterns to estimate lower limb joint movements, Computer Methods and Programs in Biomedicine. 242 (2023) 107848.
[109] P.S. Lum, C.G. Burgar, P.C. Shor, M. Majmundar, M. Van der Loos, Robot-assisted movement training compared with conventional therapy techniques for the rehabilitation of upper-limb motor function after stroke, Archives of physical medicine and rehabilitation. 83 (7) (2002) 952-959.
[110] J.H. Carr, R.B. Shepherd, Neurological rehabilitation: optimizing motor performance, Elsevier Health Sciences2010.
[111] B.E. Fisher, A.D. Wu, G.J. Salem, J. Song, C.-H.J. Lin, J. Yip, et al., The effect of exercise training in improving motor performance and corticomotor excitability in people with early Parkinson's disease, Archives of physical medicine and rehabilitation. 89 (7) (2008) 1221-1229.
[112] A. Plaza, M. Hernandez, G. Puyuelo, E. Garces, E. Garcia, Lower-limb medical and rehabilitation exoskeletons: A review of the current designs, IEEE Reviews in Biomedical Engineering. (2021).
[113] A. Rodríguez-Fernández, J. Lobo-Prat, J.M. Font-Llagunes, Systematic review on wearable lower-limb exoskeletons for gait training in neuromuscular impairments, Journal of neuroengineering and rehabilitation. 18 (1) (2021) 1-21.
[114] W. Meng, Q. Liu, Z. Zhou, Q. Ai, B. Sheng, S.S. Xie, Recent development of mechanisms and control strategies for robot-assisted lower limb rehabilitation, Mechatronics. 31 (2015) 132-145.
[115] R.S. Calabrò, A. Cacciola, F. Bertè, A. Manuli, A. Leo, A. Bramanti, et al., Robotic gait rehabilitation and substitution devices in neurological disorders: where are we now?, Neurological Sciences. 37 (2016) 503-514.
[116] M.R. Tucker, J. Olivier, A. Pagel, H. Bleuler, M. Bouri, O. Lambercy, et al., Control strategies for active lower extremity prosthetics and orthotics: a review, Journal of neuroengineering and rehabilitation. 12 (1) (2015) 1-30.
[117] A. Furui, S. Eto, K. Nakagaki, K. Shimada, G. Nakamura, A. Masuda, et al., A myoelectric prosthetic hand with muscle synergy–based motion determination and impedance model–based biomimetic control, Science Robotics. 4 (31) (2019) eaaw6339.
[118] Y.H. Yin, Y.J. Fan, L.D. Xu, EMG and EPP-integrated human–machine interface between the paralyzed and rehabilitation exoskeleton, IEEE Transactions on Information Technology in Biomedicine. 16 (4) (2012) 542-549.
[119] Y. Lu, H. Wang, B. Zhou, C. Wei, S. Xu, Continuous and simultaneous estimation

of lower limb multi-joint angles from sEMG signals based on stacked convolutional and LSTM models, Expert Systems with Applications. 203 (2022) 117340.
[120] K.G. Rabe, N.P. Fey, Continuous prediction of leg kinematics during ambulation using peripheral sensing of muscle activity and morphology, 2021 International Symposium on Medical Robotics (ISMR), IEEE, 2021, pp. 1-7.
[121] D. Soselia, R. Wang, E.M. Gutierrez-Farewik, Lower-limb joint torque prediction using LSTM neural networks and transfer learning, IEEE Transactions on Neural Systems and Rehabilitation Engineering. 30 (2022) 600-609.
[122] C. Morbidoni, A. Cucchiarelli, V. Agostini, M. Knaflitz, S. Fioretti, F. Di Nardo, Machine-learning-based prediction of gait events from EMG in cerebral palsy children, IEEE Transactions on Neural Systems and Rehabilitation Engineering. 29 (2021) 819-830.
[123] A. Phinyomark, F. Quaine, S. Charbonnier, C. Serviere, F. Tarpin-Bernard, Y. Laurillau, Feature extraction of the first difference of EMG time series for EMG pattern recognition, Computer methods and programs in biomedicine. 117 (2) (2014) 247-256.
[124] J. Chen, X. Zhang, Y. Cheng, N. Xi, Surface EMG based continuous estimation of human lower limb joint angles by using deep belief networks, Biomedical Signal Processing and Control. 40 (2018) 335-342.
[125] L. Zhang, Z. Li, Y. Hu, C. Smith, E.M.G. Farewik, R. Wang, Ankle joint torque estimation using an EMG-driven neuromusculoskeletal model and an artificial neural network model, IEEE Transactions on Automation Science and Engineering. 18 (2) (2020) 564-573.
[126] D.G. Lloyd, T.F. Besier, An EMG-driven musculoskeletal model to estimate muscle forces and knee joint moments in vivo, Journal of biomechanics. 36 (6) (2003) 765-776.
[127] C.P. Cop, A.C. Schouten, B. Koopman, M. Sartori, Electromyography-driven model-based estimation of ankle torque and stiffness during dynamic joint rotations in perturbed and unperturbed conditions, Journal of biomechanics. 145 (2022) 111383.
[128] W. Zhong, X. Fu, M. Zhang, A muscle synergy-driven anfis approach to predict continuous knee joint movement, IEEE Transactions on Fuzzy Systems. 30 (6) (2022) 1553-1563.
[129] C. Yi, F. Jiang, S. Zhang, H. Guo, C. Yang, Z. Ding, et al., Continuous prediction of lower-limb kinematics from multi-modal biomedical signals, IEEE Transactions on Circuits and Systems for Video Technology. 32 (5) (2021) 2592-2602.
[130] A.J. Young, L.J. Hargrove, T.A. Kuiken, The effects of electrode size and orientation on the sensitivity of myoelectric pattern recognition systems to electrode shift, IEEE Transactions on Biomedical Engineering. 58 (9) (2011) 2537-2544.
[131] R.V. Schulte, M. Zondag, J.H. Buurke, E.C. Prinsen, Multi-Day EMG-Based Knee Joint Torque Estimation Using Hybrid Neuromusculoskeletal Modelling and Convolutional Neural Networks, Frontiers in Robotics and AI. 9 (2022).
[132] P. Maceira-Elvira, T. Popa, A.-C. Schmid, F.C. Hummel, Wearable technology in stroke rehabilitation: towards improved diagnosis and treatment of upper-limb motor impairment, Journal of neuroengineering and rehabilitation. 16 (1) (2019) 1-18.
[133] N. Jiang, S. Dosen, K.-R. Muller, D. Farina, Myoelectric control of artificial

limbs—is there a need to change focus?[In the spotlight], IEEE Signal Processing Magazine. 29 (5) (2012) 152-150.
[134] I. Vujaklija, A.D. Roche, T. Hasenoehrl, A. Sturma, S. Amsuess, D. Farina, et al., Translating research on myoelectric control into clinics—Are the performance assessment methods adequate?, Frontiers in neurorobotics. 11 (2017) 7.
[135] M.C. Tresch, P. Saltiel, E. Bizzi, The construction of movement by the spinal cord, Nature neuroscience. 2 (2) (1999) 162-167.
[136] A. d'Avella, P. Saltiel, E. Bizzi, Combinations of muscle synergies in the construction of a natural motor behavior, Nature neuroscience. 6 (3) (2003) 300-308.
[137] N. Yang, Q. An, H. Kogami, H. Yamakawa, Y. Tamura, K. Takahashi, et al., Temporal features of muscle synergies in sit-to-stand motion reflect the motor impairment of post-stroke patients, IEEE Transactions on Neural Systems and Rehabilitation Engineering. 27 (10) (2019) 2118-2127.
[138] J.M.N. Essers, A. Peters, K. Meijer, K. Peters, A. Murgia, Superficial shoulder muscle synergy analysis in facioscapulohumeral dystrophy during humeral elevation tasks, IEEE Transactions on Neural Systems and Rehabilitation Engineering. 27 (8) (2019) 1556-1565.
[139] G. Averta, G. Valenza, V. Catrambone, F. Barontini, E.P. Scilingo, A. Bicchi, et al., On the time-invariance properties of upper limb synergies, IEEE Transactions on Neural Systems and Rehabilitation Engineering. 27 (7) (2019) 1397-1406.
[140] A.J. Young, D.P. Ferris, State of the art and future directions for lower limb robotic exoskeletons, IEEE Transactions on Neural Systems and Rehabilitation Engineering. 25 (2) (2016) 171-182.
[141] S.K. Dwivedi, J. Ngeo, T. Shibata, Extraction of nonlinear synergies for proportional and simultaneous estimation of finger kinematics, IEEE Transactions on Biomedical Engineering. 67 (9) (2020) 2646-2658.
[142] D. Xiong, D. Zhang, X. Zhao, Y. Chu, Y. Zhao, Synergy-based neural interface for human gait tracking with deep learning, IEEE Transactions on Neural Systems and Rehabilitation Engineering. 29 (2021) 2271-2280.
[143] D.D. Lee, H.S. Seung, Learning the parts of objects by non-negative matrix factorization, Nature. 401 (6755) (1999) 788-791.
[144] Y.-X. Wang, Y.-J. Zhang, Nonnegative matrix factorization: A comprehensive review, IEEE Transactions on knowledge and data engineering. 25 (6) (2012) 1336-1353.
[145] J.-S. Jang, ANFIS: adaptive-network-based fuzzy inference system, IEEE transactions on systems, man, and cybernetics. 23 (3) (1993) 665-685.
[146] W. Caesarendra, T. Tjahjowidodo, Y. Nico, S. Wahyudati, L. Nurhasanah, EMG finger movement classification based on ANFIS, Journal of Physics: conference series, IOP Publishing, 2018, p. 012005.
[147] R. Raj, K. Sivanandan, Comparative study on estimation of elbow kinematics based on EMG time domain parameters using neural network and ANFIS NARX model, Journal of Intelligent & Fuzzy Systems. 32 (1) (2017) 791-805.
[148] J.-S.R. Jang, C.-T. Sun, E. Mizutani, Neuro-fuzzy and soft computing-a computational approach to learning and machine intelligence [Book Review], IEEE

Transactions on automatic control. 42 (10) (1997) 1482-1484.
[149] H. Zhou, D. Xu, W. Quan, U.C. Ugbolue, N.F. Sculthorpe, J.S. Baker, et al., A foot joint and muscle force assessment of the running stance phase whilst wearing normal shoes and bionic shoes, Acta Bioeng. Biomech. 24 (2022) 191-202.
[150] L. Yu, Q. Mei, N.I. Mohamad, Y. Gu, J. Fernandez, An exploratory investigation of patellofemoral joint loadings during directional lunges in badminton, Computers in Biology and Medicine. 132 (2021) 104302.
[151] R. Haddas, C.R. James, T.L. Hooper, Lower extremity fatigue, sex, and landing performance in a population with recurrent low back pain, Journal of athletic training. 50 (4) (2015) 378-384.
[152] D.A. Padua, B.L. Arnold, D.H. Perrin, B.M. Gansneder, C.R. Carcia, K.P. Granata, Fatigue, vertical leg stiffness, and stiffness control strategies in males and females, Journal of athletic training. 41 (3) (2006) 294-304.
[153] S. Steib, A. Zech, C. Hentschke, K. Pfeifer, Fatigue-induced alterations of static and dynamic postural control in athletes with a history of ankle sprain, Journal of athletic training. 48 (2) (2013) 203-208.
[154] D. Quammen, N. Cortes, B.L. Van Lunen, S. Lucci, S.I. Ringleb, J. Onate, Two different fatigue protocols and lower extremity motion patterns during a stop-jump task, Journal of Athletic Training. 47 (1) (2012) 32-41.
[155] D.A. Winter, Biomechanics and motor control of human movement, John Wiley & Sons2009.
[156] F.R. Noyes, Functional properties of knee ligaments and alterations induced by immobilization: a correlative biomechanical and histological study in primates, Clinical Orthopaedics and Related Research (1976-2007). 123 (1977) 210-242.
[157] S.L.-Y. Woo, J.M. Hollis, D.J. Adams, R.M. Lyon, S. Takai, Tensile properties of the human femur-anterior cruciate ligament-tibia complex: the effects of specimen age and orientation, The American journal of sports medicine. 19 (3) (1991) 217-225.
[158] D. Xu, H. Zhou, Q. Zhang, J.S. Baker, U.C. Ugbolue, Z. Radak, et al., A new method proposed to explore the feline's paw bones of contributing most to landing pattern recognition when landed under different constraints, Frontiers in Veterinary Science. 9 (2022).
[159] P. Schober, C. Boer, L.A. Schwarte, Correlation coefficients: appropriate use and interpretation, Anesthesia & analgesia. 126 (5) (2018) 1763-1768.
[160] C. Cortes, V. Vapnik, Support-vector networks, Machine learning. 20 (3) (1995) 273-297.
[161] S. Suthaharan, Support vector machine, Machine learning models and algorithms for big data classification, Springer2016, pp. 207-235.
[162] T. Cover, P. Hart, Nearest neighbor pattern classification, IEEE transactions on information theory. 13 (1) (1967) 21-27.
[163] L.E. Peterson, K-nearest neighbor, Scholarpedia. 4 (2) (2009) 1883.
[164] O.I. Abiodun, A. Jantan, A.E. Omolara, K.V. Dada, N.A. Mohamed, H. Arshad, State-of-the-art in artificial neural network applications: A survey, Heliyon. 4 (11) (2018) e00938.
[165] T. Kohonen, An introduction to neural computing, Neural networks. 1 (1) (1988)

3-16.
[166] W. Liu, Z. Wang, X. Liu, N. Zeng, Y. Liu, F.E. Alsaadi, A survey of deep neural network architectures and their applications, Neurocomputing. 234 (2017) 11-26.
[167] J.D. Rodriguez, A. Perez, J.A. Lozano, Sensitivity analysis of k-fold cross validation in prediction error estimation, IEEE transactions on pattern analysis and machine intelligence. 32 (3) (2009) 569-575.
[168] P. Refaeilzadeh, L. Tang, H. Liu, Cross-validation, Encyclopedia of database systems. 5 (2009) 532-538.
[169] L.J. Santamaria, K.E. Webster, The effect of fatigue on lower-limb biomechanics during single-limb landings: a systematic review, Journal of orthopaedic & sports physical therapy. 40 (8) (2010) 464-473.
[170] W. Quan, H. Zhou, D. Xu, S. Li, J.S. Baker, Y. Gu, Competitive and recreational running kinematics examined using principal components analysis, Healthcare, MDPI, 2021, p. 1321.
[171] B.M. Nigg, J. Baltich, C. Maurer, P. Federolf, Shoe midsole hardness, sex and age effects on lower extremity kinematics during running, Journal of biomechanics. 45 (9) (2012) 1692-1697.
[172] Y. LeCun, Y. Bengio, Convolutional networks for images, speech, and time series, The handbook of brain theory and neural networks. 3361 (10) (1995) 1995.
[173] Y. LeCun, L. Bottou, Y. Bengio, P. Haffner, Gradient-based learning applied to document recognition, Proceedings of the IEEE. 86 (11) (1998) 2278-2324.
[174] G. Montavon, A. Binder, S. Lapuschkin, W. Samek, K.-R. Müller, Layer-wise relevance propagation: an overview, Explainable AI: interpreting, explaining and visualizing deep learning. (2019) 193-209.
[175] S. Lapuschkin, A. Binder, G. Montavon, K.-R. Müller, W. Samek, The LRP toolbox for artificial neural networks, The Journal of Machine Learning Research. 17 (1) (2016) 3938-3942.
[176] W. Quan, F. Ren, D. Xu, F. Gusztav, J.S. Baker, Y. Gu, Effects of Fatigue Running on Joint Mechanics in Female Runners: A Prediction Study Based on a Partial Least Squares Algorithm, Frontiers in Bioengineering and Biotechnology. (2021) 880.
[177] T.C. Pataky, M.A. Robinson, J. Vanrenterghem, Vector field statistical analysis of kinematic and force trajectories, Journal of biomechanics. 46 (14) (2013) 2394-2401.
[178] R. Rosenthal, Meta-Analytic Procedures for Social Science Research Sage Publications: Beverly Hills, 1984, 148 pp, Educational Researcher. 15 (8) (1986) 18-20.
[179] C.J. Ferguson, An effect size primer: a guide for clinicians and researchers, (2016).
[180] T.S. Buchanan, D.G. Lloyd, K. Manal, T.F. Besier, Neuromusculoskeletal modeling: estimation of muscle forces and joint moments and movements from measurements of neural command, Journal of applied biomechanics. 20 (4) (2004) 367-395.
[181] L.F. Shampine, Vectorized adaptive quadrature in MATLAB, Journal of Computational and Applied Mathematics. 211 (2) (2008) 131-140.
[182] A. Sikidar, D. Kalyanasundaram, An open-source plugin for OpenSim® to model

the non-linear behaviour of dense connective tissues of the human knee at variable strain rates, Computers in Biology and Medicine. 110 (2019) 186-195.
[183] R. Sopakayang, R. De Vita, A mathematical model for creep, relaxation and strain stiffening in parallel-fibered collagenous tissues, Medical engineering & physics. 33 (9) (2011) 1056-1063.
[184] K.M. Rowley, J.G. Richards, Increasing plantarflexion angle during landing reduces vertical ground reaction forces, loading rates and the hip's contribution to support moment within participants, Journal of sports sciences. 33 (18) (2015) 1922-1931.
[185] A. Godest, M. Beaugonin, E. Haug, M. Taylor, P. Gregson, Simulation of a knee joint replacement during a gait cycle using explicit finite element analysis, Journal of biomechanics. 35 (2) (2002) 267-275.
[186] J.P. Halloran, A.J. Petrella, P.J. Rullkoetter, Explicit finite element modeling of total knee replacement mechanics, Journal of biomechanics. 38 (2) (2005) 323-331.
[187] M.Z. Bendjaballah, A. Shirazi-Adl, D. Zukor, Biomechanics of the human knee joint in compression: reconstruction, mesh generation and finite element analysis, The knee. 2 (2) (1995) 69-79.
[188] Y.-c. Fung, Biomechanics: mechanical properties of living tissues, Springer Science & Business Media2013.
[189] J.A. Weiss, B.N. Maker, S. Govindjee, Finite element implementation of incompressible, transversely isotropic hyperelasticity, Computer methods in applied mechanics and engineering. 135 (1-2) (1996) 107-128.
[190] E. Pena, B. Calvo, M. Martinez, M. Doblare, A three-dimensional finite element analysis of the combined behavior of ligaments and menisci in the healthy human knee joint, Journal of biomechanics. 39 (9) (2006) 1686-1701.
[191] J.A. Weiss, J.C. Gardiner, C. Bonifasi-Lista, Ligament material behavior is nonlinear, viscoelastic and rate-independent under shear loading, Journal of biomechanics. 35 (7) (2002) 943-950.
[192] C. Pailler-Mattei, S. Bec, H. Zahouani, In vivo measurements of the elastic mechanical properties of human skin by indentation tests, Medical engineering & physics. 30 (5) (2008) 599-606.
[193] J.T.-M. Cheung, M. Zhang, A.K.-L. Leung, Y.-B. Fan, Three-dimensional finite element analysis of the foot during standing—a material sensitivity study, Journal of biomechanics. 38 (5) (2005) 1045-1054.
[194] S. Siegler, J. Block, C.D. Schneck, The mechanical characteristics of the collateral ligaments of the human ankle joint, Foot & ankle. 8 (5) (1988) 234-242.
[195] W.-M. Chen, T. Lee, P.V.-S. Lee, J.W. Lee, S.-J. Lee, Effects of internal stress concentrations in plantar soft-tissue—a preliminary three-dimensional finite element analysis, Medical engineering & physics. 32 (4) (2010) 324-331.
[196] W.-M. Chen, J. Park, S.-B. Park, V.P.-W. Shim, T. Lee, Role of gastrocnemius–soleus muscle in forefoot force transmission at heel rise—A 3D finite element analysis, Journal of biomechanics. 45 (10) (2012) 1783-1789.
[197] M.A. Baldwin, C.W. Clary, C.K. Fitzpatrick, J.S. Deacy, L.P. Maletsky, P.J. Rullkoetter, Dynamic finite element knee simulation for evaluation of knee replacement

mechanics, Journal of biomechanics. 45 (3) (2012) 474-483.
[198] J.C. Gardiner, J.A. Weiss, T.D. Rosenberg, Strain in the human medial collateral ligament during valgus loading of the knee, Clinical Orthopaedics and Related Research®. 391 (2001) 266-274.
[199] G. Li, O. Lopez, H. Rubash, Variability of a three-dimensional finite element model constructed using magnetic resonance images of a knee for joint contact stress analysis, J. Biomech. Eng. 123 (4) (2001) 341-346.
[200] M.A. LeRoux, L.A. Setton, Experimental and biphasic FEM determinations of the material properties and hydraulic permeability of the meniscus in tension, J. Biomech. Eng. 124 (3) (2002) 315-321.
[201] T.L. Haut Donahue, M. Hull, M.M. Rashid, C.R. Jacobs, A finite element model of the human knee joint for the study of tibio-femoral contact, J. Biomech. Eng. 124 (3) (2002) 273-280.
[202] L. Xiang, Q. Mei, A. Wang, V. Shim, J. Fernandez, Y. Gu, Evaluating function in the hallux valgus foot following a 12-week minimalist footwear intervention: A pilot computational analysis, Journal of Biomechanics. 132 (2022) 110941.
[203] E.S. Grood, W.J. Suntay, A joint coordinate system for the clinical description of three-dimensional motions: application to the knee, (1983).
[204] S. Checa, M. Taylor, A. New, Influence of an interpositional spacer on the behaviour of the tibiofemoral joint: a finite element study, Clinical Biomechanics. 23 (8) (2008) 1044-1052.
[205] T. Nagura, C.O. Dyrby, E.J. Alexander, T.P. Andriacchi, Mechanical loads at the knee joint during deep flexion, Journal of Orthopaedic Research. 20 (4) (2002) 881-886.
[206] M.T. Gabriel, E.K. Wong, S.L.Y. Woo, M. Yagi, R.E. Debski, Distribution of in situ forces in the anterior cruciate ligament in response to rotatory loads, Journal of orthopaedic research. 22 (1) (2004) 85-89.
[207] Y. Song, R.E. Debski, V. Musahl, M. Thomas, S.L.-Y. Woo, A three-dimensional finite element model of the human anterior cruciate ligament: a computational analysis with experimental validation, Journal of biomechanics. 37 (3) (2004) 383-390.
[208] J. Suggs, C. Wang, G. Li, The effect of graft stiffness on knee joint biomechanics after ACL reconstruction—a 3D computational simulation, Clinical biomechanics. 18 (1) (2003) 35-43.
[209] B.J. Knörlein, D.B. Baier, S.M. Gatesy, J. Laurence-Chasen, E.L. Brainerd, Validation of XMALab software for marker-based XROMM, Journal of Experimental Biology. 219 (23) (2016) 3701-3711.
[210] G. Li, S.K. Van de Velde, J.T. Bingham, Validation of a non-invasive fluoroscopic imaging technique for the measurement of dynamic knee joint motion, Journal of biomechanics. 41 (7) (2008) 1616-1622.
[211] R.J. De Asla, M. Kozánek, L. Wan, H.E. Rubash, G. Li, Function of anterior talofibular and calcaneofibular ligaments during in-vivo motion of the ankle joint complex, Journal of Orthopaedic Surgery and Research. 4 (2009) 1-6.
[212] G.-B. Huang, Q.-Y. Zhu, C.-K. Siew, Extreme learning machine: a new learning scheme of feedforward neural networks, 2004 IEEE international joint conference on

neural networks (IEEE Cat. No. 04CH37541), Ieee, 2004, pp. 985-990.
[213] G.-B. Huang, Q.-Y. Zhu, C.-K. Siew, Extreme learning machine: theory and applications, Neurocomputing. 70 (1-3) (2006) 489-501.
[214] S. Hochreiter, J. Schmidhuber, Long short-term memory, Neural computation. 9 (8) (1997) 1735-1780.
[215] F.A. Gers, J. Schmidhuber, F. Cummins, Learning to forget: Continual prediction with LSTM, Neural computation. 12 (10) (2000) 2451-2471.
[216] A. Rudavsky, J. Cook, Physiotherapy management of patellar tendinopathy (jumper's knee), Journal of physiotherapy. 60 (3) (2014) 122-129.
[217] P.J. Visentini, K.M. Khan, J.L. Cook, Z.S. Kiss, P.R. Harcourt, J.D. Wark, et al., The VISA score: an index of severity of symptoms in patients with jumper's knee (patellar tendinosis), Journal of science and medicine in sport. 1 (1) (1998) 22-28.
[218] S. Ranaldi, C. De Marchis, G. Severini, S. Conforto, An objective, information-based approach for selecting the number of muscle synergies to be extracted via non-negative matrix factorization, IEEE Transactions on Neural Systems and Rehabilitation Engineering. 29 (2021) 2676-2683.
[219] D.-W. Kim, K. Lee, D. Lee, K.H. Lee, A kernel-based subtractive clustering method, Pattern Recognition Letters. 26 (7) (2005) 879-891.
[220] M. Panella, A.S. Gallo, An input-output clustering approach to the synthesis of ANFIS networks, IEEE Transactions on fuzzy systems. 13 (1) (2005) 69-81.
[221] R. Gupta, I.S. Dhindsa, R. Agarwal, Continuous angular position estimation of human ankle during unconstrained locomotion, Biomedical Signal Processing and Control. 60 (2020) 101968.
[222] K.G. Rabe, N.P. Fey, Evaluating electromyography and sonomyography sensor fusion to estimate lower-limb kinematics using Gaussian process regression, Frontiers in Robotics and AI. 9 (2022).
[223] J. Camargo, D. Molinaro, A. Young, Predicting biological joint moment during multiple ambulation tasks, Journal of Biomechanics. 134 (2022) 111020.
[224] P. Devita, W.A. Skelly, Effect of landing stiffness on joint kinetics and energetics in the lower extremity, Med Sci Sports Exerc. 24 (1) (1992) 108-115.
[225] J. Lee, C.S. Shin, Association between ankle angle at initial contact and biomechanical ACL injury risk factors in male during self-selected single-leg landing, Gait & Posture. 83 (2021) 127-131.
[226] A. Rabin, S. Portnoy, Z. Kozol, The association of ankle dorsiflexion range of motion with hip and knee kinematics during the lateral step-down test, Journal of orthopaedic & sports physical therapy. 46 (11) (2016) 1002-1009.
[227] J. Brazier, S. Maloney, C. Bishop, P.J. Read, A.N. Turner, Lower extremity stiffness: considerations for testing, performance enhancement, and injury risk, The Journal of Strength & Conditioning Research. 33 (4) (2019) 1156-1166.
[228] J. Figueiredo, C.P. Santos, J.C. Moreno, Automatic recognition of gait patterns in human motor disorders using machine learning: A review, Medical engineering & physics. 53 (2018) 1-12.
[229] W. Zeng, F. Liu, Q. Wang, Y. Wang, L. Ma, Y. Zhang, Parkinson's disease classification using gait analysis via deterministic learning, Neuroscience letters. 633

(2016) 268-278.
[230] Y. Shimokochi, J.P. Ambegaonkar, E.G. Meyer, S.Y. Lee, S.J. Shultz, Changing sagittal plane body position during single-leg landings influences the risk of non-contact anterior cruciate ligament injury, Knee Surgery, Sports Traumatology, Arthroscopy. 21 (2013) 888-897.
[231] P. Yu, Q. Mei, L. Xiang, J. Fernandez, Y. Gu, Differences in the locomotion biomechanics and dynamic postural control between individuals with chronic ankle instability and copers: a systematic review, Sports Biomechanics. 21 (4) (2022) 531-549.
[232] G. Li, J. Suggs, T. Gill, The effect of anterior cruciate ligament injury on knee joint function under a simulated muscle load: a three-dimensional computational simulation, Annals of biomedical engineering. 30 (2002) 713-720.
[233] J.L. Hicks, T.K. Uchida, A. Seth, A. Rajagopal, S.L. Delp, Is my model good enough? Best practices for verification and validation of musculoskeletal models and simulations of movement, Journal of biomechanical engineering. 137 (2) (2015) 020905.
[234] G. Valente, G. Crimi, N. Vanella, E. Schileo, F. Taddei, nmsBuilder: Freeware to create subject-specific musculoskeletal models for OpenSim, Computer methods and programs in biomedicine. 152 (2017) 85-92.
[235] J.F. Baumhauer, D.M. Alosa, P.A. Renström, S. Trevino, B. Beynnon, A prospective study of ankle injury risk factors, The American journal of sports medicine. 23 (5) (1995) 564-570.
[236] A.S. Kelikian, S.K. Sarrafian, Sarrafian's anatomy of the foot and ankle: descriptive, topographic, functional, Lippincott Williams & Wilkins2011.
[237] P.A. Rockar Jr, The subtalar joint: anatomy and joint motion, Journal of Orthopaedic & Sports Physical Therapy. 21 (6) (1995) 361-372.
[238] M.F. Sherman, L. Lieber, J.R. Bonamo, L. Podesta, I. Reiter, The long-term followup of primary anterior cruciate ligament repair: defining a rationale for augmentation, The American journal of sports medicine. 19 (3) (1991) 243-255.
[239] T. Dokeroglu, E. Sevinc, T. Kucukyilmaz, A. Cosar, A survey on new generation metaheuristic algorithms, Computers & Industrial Engineering. 137 (2019) 106040.
[240] F.S. Gharehchopogh, M. Namazi, L. Ebrahimi, B. Abdollahzadeh, Advances in sparrow search algorithm: a comprehensive survey, Archives of Computational Methods in Engineering. 30 (1) (2023) 427-455.
[241] W.R. Johnson, A. Mian, M.A. Robinson, J. Verheul, D.G. Lloyd, J.A. Alderson, Multidimensional ground reaction forces and moments from wearable sensor accelerations via deep learning, IEEE Transactions on Biomedical Engineering. 68 (1) (2020) 289-297.
[242] B. Mahesh, Machine learning algorithms-a review, International Journal of Science and Research (IJSR).[Internet]. 9 (1) (2020) 381-386.